

# **Pine Island Glacier - a 3D full-Stokes model study**

Dissertation  
zur Erlangung des Doktorgrades  
der Naturwissenschaften im Fachbereich  
Geowissenschaften  
der Universität Hamburg

vorgelegt von

**Nina Wilkens**

aus Berlin

Hamburg

2014

Als Dissertation angenommen vom Fachbereich Geowissenschaften  
der Universität Hamburg

auf Grund der Gutachten von Prof. Dr. Angelika Humbert  
und Prof. Dr. Jörn Behrens

Hamburg, den 4. April 2014

Prof. Dr. Christian Betzler  
Leiter des Fachbereichs Geowissenschaften

# Contents

<b>List of Figures</b>	<b>VII</b>
<b>List of Tables</b>	<b>XI</b>
<b>Abstract</b>	<b>XII</b>
<b>1 Introduction</b>	<b>1</b>
1.1 The Antarctic Ice Sheet . . . . .	2
1.1.1 Geologic history . . . . .	2
1.1.2 The marine ice sheet instability . . . . .	3
1.1.3 Basal properties . . . . .	5
1.2 Ice sheet models . . . . .	7
1.2.1 Approximations . . . . .	8
1.2.2 Basal motion . . . . .	9
1.2.3 Grounding line migration . . . . .	10
1.3 Pine Island Glacier . . . . .	11
1.3.1 Observations . . . . .	12
1.3.2 Model studies . . . . .	13
1.4 Objectives and structure of this study . . . . .	14
<b>2 Theory</b>	<b>17</b>
2.1 Balance equations . . . . .	17
2.1.1 Mass balance - Continuity equation . . . . .	18
2.1.2 Momentum balance - Momentum equation . . . . .	19
2.1.3 Energy balance - Heat transfer equation . . . . .	20
2.2 Constitutive relation - Rheology of ice . . . . .	22
2.2.1 Glen's flow law . . . . .	22
2.2.2 Rate factor . . . . .	24
2.2.3 Enhancement factor . . . . .	25
2.3 Overview of equations . . . . .	26
2.4 Boundary conditions . . . . .	26
2.4.1 Ice surface . . . . .	27
2.4.2 Ice base . . . . .	28
2.4.3 Lateral boundaries - Ice divide, calving front and inflow . . . . .	30
2.5 Finite element method - FEM . . . . .	32
2.5.1 Meshing . . . . .	32
2.5.2 Approximation functions - Basis functions . . . . .	33
2.5.3 Weighted-integral form . . . . .	34
2.5.4 Boundary conditions . . . . .	35
2.5.5 Assembly . . . . .	35

2.5.6	Solution . . . . .	36
<b>3</b>	<b>The 3D full-Stokes model for Pine Island Glacier</b>	<b>39</b>
3.1	Data . . . . .	39
3.1.1	Ice geometry . . . . .	40
3.1.2	Grounding line position . . . . .	41
3.1.3	Ice rises . . . . .	42
3.1.4	Surface temperature . . . . .	43
3.1.5	Geothermal heat flux . . . . .	43
3.1.6	Surface velocity . . . . .	45
3.2	Implementation . . . . .	46
3.2.1	Model geometry . . . . .	48
3.2.2	Ice flow model . . . . .	49
3.2.3	Thermal model . . . . .	53
3.2.4	Mesh . . . . .	55
3.2.5	Solver . . . . .	57
3.3	Verification and validation . . . . .	58
3.3.1	Ice shelf ramp . . . . .	58
3.3.2	MISMIP 3D . . . . .	63
<b>4</b>	<b>Identification of dominant local flow mechanisms</b>	<b>67</b>
4.1	No-slip simulations . . . . .	68
4.1.1	Driving stress . . . . .	69
4.1.2	Heat conduction . . . . .	71
4.1.3	Strain heating . . . . .	72
4.1.4	Internal deformation . . . . .	76
4.2	Reference simulations . . . . .	78
4.2.1	Quasi-inversion technique . . . . .	79
4.2.2	Reference simulation . . . . .	81
4.2.3	Temperate layer . . . . .	84
4.2.4	Water content . . . . .	85
4.2.5	Full-Stokes vs. SIA . . . . .	86
4.2.6	Sensitivity to geothermal heat flux . . . . .	88
4.3	Hydraulic potential . . . . .	90
4.4	Basal roughness . . . . .	91
4.5	Discussion . . . . .	92
<b>5</b>	<b>Basal sliding</b>	<b>97</b>
5.1	Theory - Basal sliding . . . . .	97
5.1.1	Hard beds . . . . .	98
5.1.2	Deformable beds . . . . .	101
5.2	Evaluation method of results . . . . .	102
5.3	Constant sets of sliding parameters $p$ , $q$ and $C_b$ . . . . .	104
5.3.1	Simulations . . . . .	104
5.3.2	Discussion . . . . .	107
5.4	Matching of roughness measure $\xi$ and sliding parameter $C_b$ . . . . .	110
5.4.1	Simulations . . . . .	112

---

5.4.2	Discussion . . . . .	116
5.5	Li-sliding . . . . .	117
5.5.1	The two parameter roughness index - $\xi_2$ and $\eta_2$ . . . . .	118
5.5.2	Assumptions - Controlling obstacle size - Constant $C_L$ . . . . .	119
5.5.3	Simulations . . . . .	120
5.5.4	Discussion . . . . .	123
5.6	Discussion . . . . .	123
<b>6</b>	<b>Conclusions and outlook</b>	<b>127</b>
<b>A</b>		<b>131</b>
A.1	Integration theorems . . . . .	131
A.1.1	Reynold's transport theorem . . . . .	131
A.1.2	Integral formula of Gauss - Divergence theorem . . . . .	131
A.1.3	Integration by parts - Green-Gauss theorem . . . . .	131
	<b>Bibliography</b>	<b>133</b>
	<b>Acknowledgements</b>	<b>147</b>



# List of Figures

1.1	Bedrock topography of Antarctica . . . . .	3
1.2	Schematic of a marine ice sheet on a retrograde bed . . . . .	4
1.3	Bed roughness distribution below the Antarctic Ice Sheet . . . . .	6
1.4	Surface velocity and grounding line positions at Pine Island Glacier . . . . .	13
2.1	Stress-strain relationships . . . . .	23
2.2	Theory - Boundary conditions - Ice surface . . . . .	27
2.3	Theory - Boundary conditions - Ice base - floating . . . . .	28
2.4	Theory - Boundary conditions - Ice base - grounded . . . . .	29
2.5	Theory - Boundary conditions - Ice divide . . . . .	30
2.6	Theory - Boundary conditions - Calving front . . . . .	31
2.7	Example of a non-uniform FEM mesh on a complex geometry . . . . .	33
2.8	Linear basis functions . . . . .	34
2.9	Quadratic basis functions . . . . .	34
3.1	Model region on Antarctica . . . . .	39
3.2	Model domain of Pine Island Glacier on a mosaic of satellite images . . . . .	40
3.3	Surface elevation of Pine Island Glacier . . . . .	41
3.4	Bed topography of Pine Island Glacier . . . . .	41
3.5	Different grounding line and ice rise positions at Pine Island Glacier . . . . .	42
3.6	Surface temperature of Pine Island Glacier . . . . .	43
3.7	Geothermal heat flux from Shapiro 2004 of Pine Island Glacier . . . . .	44
3.8	Geothermal heat flux from Fox Maule 2005 of Pine Island Glacier . . . . .	44
3.9	Geothermal heat flux from Purucker 2012 of Pine Island Glacier . . . . .	44
3.10	Location of volcanic center at Pine Island Glacier . . . . .	44
3.11	Observed surface velocity field of Pine Island Glacier . . . . .	46
3.12	Screenshot of the COMSOL GUI . . . . .	47
3.13	Difference between interpolated data and geometry object at surface . . . . .	49
3.14	Difference between interpolated data and geometry object at base . . . . .	49
3.15	Model - Boundary conditions - Ice surface . . . . .	51
3.16	Model - Boundary conditions - Ice base . . . . .	51
3.17	Model - Boundary conditions - Ice divide . . . . .	52
3.18	Model - Boundary conditions - Calving front . . . . .	52
3.19	Model - Boundary conditions - Inflow . . . . .	53
3.20	Function for implementation of the thermal basal boundary condition . . . . .	55
3.21	FEM mesh on the 3D Pine Island Glacier model geometry . . . . .	56
3.22	Mesh quality on the 3D Pine Island Glacier model geometry . . . . .	56
3.23	Ice shelf ramp - 3D geometry with the flow field . . . . .	60
3.24	Ice shelf ramp - Horizontal velocities . . . . .	61
3.25	Ice shelf ramp - Vertical velocities . . . . .	62

3.26	Ice shelf ramp - Mass balance . . . . .	63
3.27	MISMIP 3D - Perturbed basal friction parameter . . . . .	64
3.28	MISMIP 3D - Geometry with velocity field . . . . .	65
3.29	MISMIP 3D - Horizontal surface velocity $u$ at grounding line . . . . .	65
3.30	MISMIP 3D - Horizontal surface velocity $v$ at grounding line . . . . .	65
3.31	MISMIP 3D - Horizontal surface velocity field $u$ . . . . .	66
3.32	MISMIP 3D - Horizontal surface velocity field $v$ . . . . .	66
3.33	MISMIP 3D - Vertical surface velocity field $w$ . . . . .	66
4.1	Numbering of tributaries on observed surface flow field . . . . .	67
4.2	SIA basal drag on Pine Island Glacier . . . . .	70
4.3	Simulated basal drag on Pine Island Glacier . . . . .	70
4.4	Homologous basal temperature due to heat conduction . . . . .	71
4.5	Homologous basal temperature - Without strain heating term . . . . .	72
4.6	Homologous basal temperature - With strain heating term . . . . .	72
4.7	Source term at base . . . . .	73
4.8	Viscosity at base . . . . .	74
4.9	Effective strain rate at base . . . . .	74
4.10	First term in source term at base - D1 . . . . .	75
4.11	Second term in source term at base - D2 . . . . .	75
4.12	Third term in source term at base - D3 . . . . .	75
4.13	Fourth term in source term at base - D4 . . . . .	75
4.14	Fifth term in source term at base - D5 . . . . .	75
4.15	Sixth term in source term at base - D6 . . . . .	75
4.16	Surface velocity field - No sliding - Constant temperature . . . . .	77
4.17	Difference to observed surface velocity - No sliding - Constant temperature . . . . .	77
4.18	Surface velocity field - No sliding - Temperature field - Purucker 2012 . . . . .	77
4.19	Difference to observed - No sliding - Temperature field - Purucker 2012 . . . . .	77
4.20	Surface velocity field - No sliding - Temperature field - Fox Maule 2005 . . . . .	77
4.21	Difference to observed - No sliding - Temperature field - Fox Maule 2005 . . . . .	77
4.22	Surface velocity field - No sliding - Temperature field - Shapiro 2004 . . . . .	78
4.23	Difference to observed - No sliding - Temperature field - Shapiro 2004 . . . . .	78
4.24	Spatial distribution of basal sliding parameter $\beta^2$ . . . . .	81
4.25	Surface velocity field - Reference simulation - Purucker 2012 . . . . .	81
4.26	Difference to observed field - Reference simulation - Purucker 2012 . . . . .	81
4.27	Observed surface velocity vs. reference surface velocity . . . . .	82
4.28	Observed surface velocity vs. angle difference (observed-reference) . . . . .	82
4.29	Homologous basal temperature field - Reference simulation - Purucker 2012 . . . . .	83
4.30	Basal velocity/Surface velocity - Reference simulation - Purucker 2012 . . . . .	83
4.31	3D homologous temperature field - Reference simulation - Purucker 2012 . . . . .	84
4.32	Temperate layer thickness - Reference simulation - Purucker 2012 . . . . .	85
4.33	Normed ice thickness vs. homologous temperature and source term . . . . .	85
4.34	Difference with including water content in temperate layer . . . . .	86
4.35	Difference with including water content everywhere . . . . .	86
4.36	Location of extracted profiles on reference surface velocity field . . . . .	87
4.37	Horizontal and vertical derivatives of extracted profiles . . . . .	87
4.38	Homologous basal temperature field - Fox Maule 2005 . . . . .	89

4.39	Homologous basal temperature field - Shapiro 2004 . . . . .	89
4.40	Homologous basal temperature field - Constant $q_{geo}$ . . . . .	89
4.41	Homologous basal temperature field - Constant $q_{geo}$ - No friction heating . . . . .	89
4.42	Homologous basal temperature field - Constant $q_{geo}$ - No friction heating - No source . . . . .	89
4.43	Homologous basal temperature field - Artificial $q_{geo}$ - Volcano . . . . .	89
4.44	Hydraulic potential at Pine Island Glacier . . . . .	90
4.45	Hydraulic potential gradient at Pine Island Glacier . . . . .	91
4.46	Single parameter roughness measure $\xi$ at Pine Island Glacier . . . . .	92
4.47	Bed topography at Pine Island Glacier . . . . .	92
5.1	Weertman's original obstacle size and spacing . . . . .	98
5.2	Basal velocity due to regelation . . . . .	100
5.3	Basal velocity due to enhanced creep . . . . .	100
5.4	Surface velocity field - Reference simulation . . . . .	102
5.5	Homologous basal temperature field - Reference simulation . . . . .	102
5.6	Partitioning of the surface flow field into subregions for evaluation . . . . .	103
5.7	Surface velocity field - p1q2 . . . . .	105
5.8	Difference to reference field - p1q2 . . . . .	105
5.9	Surface velocity field - p2q0 . . . . .	105
5.10	Difference to reference field - p2q0 . . . . .	105
5.11	Surface velocity field - p3q1 . . . . .	105
5.12	Difference to reference field - p3q1 . . . . .	105
5.13	Surface velocity field - p3q2 . . . . .	106
5.14	Difference to reference field - p3q2 . . . . .	106
5.15	Surface velocity field - p1q0 . . . . .	106
5.16	Difference to reference field - p1q0 . . . . .	106
5.17	RMS value vs. sliding law Nr. - Constant parameters . . . . .	107
5.18	Effective basal pressure at Pine Island Glacier . . . . .	108
5.19	Reduced effective basal pressure at Pine Island Glacier . . . . .	108
5.20	Simulated basal drag vs. observed surface velocity . . . . .	109
5.21	Simulated basal drag vs. simulated basal velocity . . . . .	109
5.22	Spatial distribution of basal sliding parameter $C_b$ . . . . .	110
5.23	Arcuate surface crevasses on satellite image . . . . .	110
5.24	Normed and inverted single parameter roughness measure $\xi_n$ . . . . .	111
5.25	Inverted basal sliding parameter $C_b$ for $q = 0$ . . . . .	111
5.26	Inverted basal sliding parameter $C_b$ for $q = 1$ . . . . .	111
5.27	Inverted basal sliding parameter $C_b$ for $q = 2$ . . . . .	111
5.28	RMS value vs. simulation Nr. - Matched parameters . . . . .	113
5.29	Surface velocity field - Matched parameters - p1q0_2 . . . . .	114
5.30	Homologous basal temperature field - Matched parameters - p1q0_2 . . . . .	114
5.31	Temperate layer thickness - Matched parameters - p1q0_2 . . . . .	115
5.32	Temperate layer thickness - Matched parameters - p1q2_11 . . . . .	115
5.33	Surface velocity field - Matched parameters - p1q1_7 . . . . .	115
5.34	Homologous basal temperature field - Matched parameters - p1q1_7 . . . . .	115
5.35	Surface velocity field - Matched parameters - p1q2_11 . . . . .	116
5.36	Homologous basal temperature field - Matched parameters - p1q2_11 . . . . .	116

5.37	Two parameter roughness measure $\xi_2$ at Pine Island Glacier . . . . .	118
5.38	Two parameter roughness measure $\eta_2$ at Pine Island Glacier . . . . .	118
5.39	RMS value vs. $C_L$ . . . . .	121
5.40	Surface velocity field and difference to reference - $C_L = 1 \text{ Pa}^{-2} \text{ m a}^{-1}$ . . . .	121
5.41	Surface velocity field and difference to reference - $C_L = 31.56 \text{ Pa}^{-2} \text{ m a}^{-1}$ . .	122
5.42	RMS value vs. results from simulations with constant, matched and Li- parameters . . . . .	124

# List of Tables

3.1	Overview of parameters for the coupled flow model . . . . .	47
3.2	Overview of variables for the flow model . . . . .	50
3.3	Overview of variables for the thermal model . . . . .	54
3.4	Overview of parameters for the ice shelf ramp . . . . .	59
3.5	Mesh specifications for the ice shelf ramp . . . . .	60
3.6	Velocity results for the ice shelf ramp . . . . .	61
3.7	Mass balance results for the ice shelf ramp . . . . .	63
4.1	Overview of simulations conducted for Section "No-slip simulations" . . . . .	69
4.2	Overview of simulations conducted for Section "Reference simulations" . . . . .	79
4.3	Overview of results for discussion in Chapter 4 . . . . .	93
5.1	Overview of simulations with constant parameter sets . . . . .	104
5.2	Overview of simulations with matched sliding parameters . . . . .	112

## Abstract

Mass loss from the Antarctic Ice Sheet is found to significantly contribute to eustatic sea level rise, due to a dynamic response in the system. Pine Island Glacier, a fast flowing outlet glacier in the West Antarctic Ice Sheet, is located in the Amundsen Sea Embayment Area, where the present Antarctic mass loss is concentrated. The observed mass loss in the area coincides with acceleration and thinning of the glacier, accompanied by a retreat of the grounding line, which is the line of separation between grounded and floating ice. The bed beneath the glacier lies in large parts below sea level, with the bed sloping down away from the ocean. This setting makes the glacier especially vulnerable to increasing and possibly accelerating retreat.

Remote sensing techniques allow only for the surface conditions of glacial systems to be nowadays monitored over reasonable temporal and spatial scales. The conditions at the base, however, are still widely unknown, due to their inaccessibility. This poses a challenge, as basal conditions are a very important component for understanding glacier dynamics. A key technique to bridge this challenge is given by numerical modelling. In glaciological studies flow models are developed, that can either be used to solve in a prognostic manner over long time scales, being based on approximations to the full system of equations, or to solve diagnostically in high resolution for the full system, to study processes in more detail.

Here we present a model of the later category, a thermo-mechanically coupled 3D full-Stokes ice flow model, which is set up to the region of Pine Island Glacier. It is solved with the finite element method, and the prismatic mesh is refined horizontally across the grounding line, where high resolution is needed. With this coupled flow model we assess the present thermal and dynamical state of the coupled ice sheet - ice shelf system. Furthermore, we develop a method to include measured basal properties into the formulation of the basal sliding law.

We find the glacier to be predominantly cold, with most parts of the base being temperate, thus at pressure melting point. The temperate base is a prerequisite for basal sliding, which controls the faster flowing central stream of the glacier. The dominant mechanisms driving the flow of the different tributaries are diverse. Some are controlled by a strong bed and according high driving stresses. Others are steered by the basal topography and likely the presence of water saturated marine sediments. Only minor areas are identified with a significantly thick temperate basal layer. Furthermore, we show a connection between the basal roughness and the sliding behaviour of the glacier. A reduced effective pressure is a key necessity to explain the fast flow towards the grounding line. Thus, a thermo-mechanically coupled model, as we presented here, is essential for the inference of interrelations between the thermal regime, the basal roughness structure and the flow and sliding conditions.

## Zusammenfassung

Der Massenverlust des Antarktischen Eisschildes hat auf Grund einer dynamischen Komponente im System, einen wesentlichen Einfluss auf den Anstieg des eustatischen Meeresspiegels. Der Pine Island Gletscher, ein schnell fließender Auslassgletscher im Westantarktischen Eisschild, liegt in einer Region, die an das Amundsen Meer anschließt, und in der sich der aktuelle antarktische Massenverlust konzentriert. Der beobachtete Massenverlust wird begleitet von einer zunehmenden Beschleunigung des Gletschers, Abnahme der Oberflächenhöhe und einem Rückzug der Aufsatzlinie, wo gegründetes in schwimmendes Eis übergeht. Der Boden unter dem Gletscher liegt zu einem großen Teil unterhalb des Meeresspiegels und neigt sich zum Inland. Diese Situation macht den Gletscher besonders anfällig für zunehmenden, und eventuell sogar sich beschleunigenden, Rückzug.

Allein die Oberflächeneigenschaften der glazialen Gebiete können heute durch Fernerkundungsmethoden in relativ hoher räumlicher und zeitlicher Auflösung abgeschätzt werden. Die Bodeneigenschaften unter den eisbedeckten Gebieten hingegen sind weitgehend unbekannt, weil sie schwer zugänglich sind. Da basale Eigenschaften einen großen Einfluss auf die Dynamik des Gletschers haben, stellt dies eine Herausforderung dar. Numerische Modellierung ist eine wichtige Technik, um diese Herausforderungen zu meistern. In glaziologischen Studien werden meist entweder Modelle entwickelt, die prognostisch über lange Zeitskalen lösen können, basierend auf einer Näherungslösung, oder diagnostisch in hoher Auflösung das volle Gleichungssystem lösen, um detaillierter Prozesse zu studieren.

Hier stellen wir ein Modell der letzteren Sorte vor. Es ist ein thermo-mechanisch gekoppeltes 3D full-Stokes Fließmodell, welches wir auf den Pine Island Gletscher anwenden. Es wird mit der Methode der Finiten Elemente gelöst. Das zugrunde liegende prismatische Gitter wird horizontal über der Aufsatzlinie verfeinert, wo besonders hohe Auflösung gefordert ist. Mit diesem gekoppelten Fließmodell berechnen wir den aktuellen thermischen und dynamischen Zustand des Gletschersystems, bestehend aus gegründetem und schwimmendem Eis. Außerdem entwickeln wir eine Methode, mit der gemessene basale Eigenschaften in der Formulierung des basalen Gleitens berücksichtigt werden können.

Wir stellen fest, dass der Pine Island Gletscher vornehmlich von kaltem Eis bestimmt ist, wobei große Teile der Basis temperiert, also am Druckschmelzpunkt, sind. Die temperierte Basis ist eine Voraussetzung für basales Gleiten, welches das Fließfeld im zentralen Strom des Gletschers kontrolliert. Die dominierenden Mechanismen, die die einzelnen Zuströme antreiben, sind divers. Einige sind durch einen festen Untergrund und dadurch durch große Antriebskräfte bestimmt. Unter anderen wird marines Sediment vermutet, und ihre Existenz wird durch die basale Topographie und die Fließwege des basalen Wassers bestimmt. Nur in sehr wenigen Regionen wird eine temperierte basale Schicht von nennenswerter Dicke vermutet. Außerdem zeigen wir eine Verbindung zwischen der basalen Rauigkeit und der Gleitgeschwindigkeit auf. Ein reduzierter effektiver Druck ist eine Erklärung für das schnelle Gleiten des Gletschers in der Nähe der Aufsatzlinie. Demnach ist ein thermo-mechanisch gekoppeltes Fließmodell, wie wir hier präsentieren, gefordert, um die Wechselwirkungen zwischen dem thermalen Regime, der basalen Rauigkeitsstruktur und der Fließ- und Gleitbewegungen, zu analysieren.



# Chapter 1

## Introduction

A topic that will become increasingly important in the future is that of global sea-level rise and its resulting impact on the coastal zone. A major reservoir of fresh water exists presently in form of the ice sheets on Greenland and Antarctica. The Antarctic Ice Sheet alone holds the potential to raise global sea level by 58 m, if fully melted (*Fretwell et al.*, 2013). The contribution to present global sea level rise of  $3.1 \pm 0.4 \text{ mm a}^{-1}$  (1993-2006, *Nerem et al.* (2006)) from the Greenland and Antarctic Ice Sheets is  $0.59 \pm 0.2 \text{ mm a}^{-1}$  (1992-2011, *Shepherd et al.* (2012)). Ice sheets have long been seen to vary substantially only on timescales of centuries to millennia. This view is changing as observations show a much faster response of ice sheets to climatic change. The cause is believed to be a dynamic response of ice streams and outlet glaciers in the ice sheet. Hereby not the flow acceleration due to changes in accumulation or surface temperature is dominant, but due to a response to changing basal conditions or changes in the buttressing of ice shelves (*Scambos et al.*, 2004). The ability to make accurate projections for sea level rise with modelling studies is among other things limited by uncertainties about basal conditions, basal sliding behaviour, ice deformation and interactions with the surrounding ocean (*IPCC-AR4*, 2007).

Ice moves due to a combination of internal deformation and basal sliding. The internal deformation of ice is nonlinear, increasing approximately proportional to the cube of the applied stress. For computational efficiency, most simulations over long time scales use a simplified stress distribution. Some of the recent changes observed in ice sheet margins and fast flowing ice streams can not be reproduced by these models. Thus models considering all stress terms in the momentum balance are needed (*IPCC-AR4*, 2007), and have recently gathered more and more attention, additionally fostered by growing computational resources.

Strongly affected by changes in flow velocities, grounding line retreat and surface lowering in the past decades is the Amundsen Sea Embayment Area (ASEA) in West Antarctica. While the ASEA only holds an area fraction of about 3% of the entire Antarctic Ice Sheet, and about 17.5% of the West Antarctic Ice Sheet (WAIS) (*Rignot*, 2001; *Vaughan et al.*, 2006; *Bindschadler*, 2006), it accounted for over 50% of the total mass loss from Antarctica between 2002 and 2008 (*Horwath and Dietrich*, 2009). Associated with this mass loss are two glacier systems located in this area, Thwaites and Pine Island Glacier. While Thwaites Glacier mainly widened, Pine Island Glacier accelerated, thinned and showed retreat of the grounding line, which separates grounded from floating ice.

In the following we will give an introduction to the Antarctic Ice Sheet (Section 1.1) and its geologic history (Section 1.1.1) to understand the special setting of the WAIS. A summary of the major aspects of the Marine Ice Sheet Instability hypothesis is given in Section 1.1.2, followed by a section about the basal properties under the WAIS (1.1.3).

The instrument to conduct this study is a 3D full-Stokes thermo-mechanically coupled ice flow model. To put this into perspective, we give a general introduction to ice sheet models (Section 1.2), with a special focus on approximations commonly applied (Section 1.2.1) and how basal sliding (Section 1.2.2) and grounding line motion are incorporated (Section 1.2.3).

Finally, the study area of Pine Island Glacier is introduced (Section 1.3), with observations and model studies described in Sections 1.3.1 and 1.3.2, respectively. The objectives and structure of this study are given in Section 1.4.

## 1.1 The Antarctic Ice Sheet

The Antarctic continent is almost entirely covered by an ice sheet of varying thickness. This ice sheet is, with an area of  $\sim 13.5 \times 10^6 \text{ km}^2$  and a volume of  $25.4 \times 10^6 \text{ km}^3$ , which includes the fringing ice shelves, the world's largest fresh water store (*Benn and Evans, 2010*). The Pacific side of the Transantarctic Mountains roughly divides the Antarctic Ice Sheet into two unequal parts, the smaller West Antarctic Ice Sheet (WAIS), with a grounded ice volume of  $3 \times 10^6 \text{ km}^3$ , and the bigger East Antarctic Ice Sheet (EAIS), with a grounded ice volume of  $21.7 \times 10^6 \text{ km}^3$  (*Benn and Evans, 2010*). The remainder of  $0.7 \times 10^6 \text{ km}^3$  of the ice volume is found in the ice shelves surrounding the grounded ice.

### 1.1.1 Geologic history

West and East Antarctica are geologically distinct. East Antarctica is believed to be primarily a Precambrian craton older than 500 Ma, while the WAIS is believed to rest on a cluster of four major crustal blocks (Antarctic Peninsula, Thurston Island, Ellsworth-Whitmore mountains and Marie Byrd Land) (*Dalziel and Lawver, 2001*). These blocks have moved relative to each other and relative to the East Antarctic craton during breakup of Gondwanaland in the Mesozoic, 251 – 65.5 Ma ago (*Dalziel and Elliot, 1982; Walker and Geissman, 2009*). The force driving these blocks apart was given by a combination of ridge-crest subduction and a magmatic plume. The crust was stretched and thinned and crustal gaps were created that filled with mafic intrusions, a magnesium and iron rich rock. The modification continued in the Cenozoic, starting 65.5 Ma ago, possibly caused by plume-driven extensional rifting of the Central West Antarctic basin and led to continuing volcanic activity and crustal fracturing (*Bindschadler, 2006*). *Jordan et al. (2009)* currently find the thinnest crust of the WAIS with  $\sim 19 \pm 1 \text{ km}$  beneath Pine Island Glacier, a potential source of enhanced heat flow and thus modification of the ice flow dynamics above.

The distinct formation history of East and West Antarctica is currently also noticeable at the bed below the ice sheet, shown in Figure 1.1 with the data from *Timmermann et al. (2010)*. The tectonic processes described above created a geologic 'cradle' under the WAIS (*Bindschadler, 2006*), such that the bedrock under most of the WAIS lies below sea level. Also some areas under the EAIS lie below sea level, but would rebound above sea level, if the ice sheet would be removed (*Joughin and Alley, 2011*). In total around 8.5% of the present day grounded ice sheet volume of Antarctica lies below sea level (*Benn and Evans, 2010*). There are several indications for the WAIS to have completely or partially disappeared during past interglacial periods (*Scherer et al., 1998; Naish et al., 2009; Pollard and DeConto, 2009*). This could be connected to the hypothetical instability

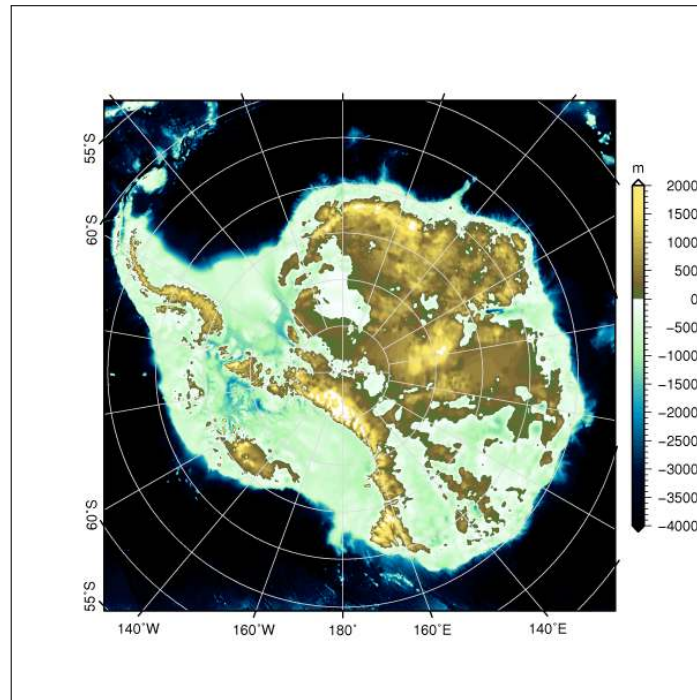


Figure 1.1: Bedrock topography of Antarctica

of marine ice sheets, described in Section 1.1.2, and would explain the existence of sediment filled basins below the present day WAIS (refer to Section 1.1.3) (*Jordan et al.*, 2009; *Smith et al.*, 2012).

### 1.1.2 The marine ice sheet instability

Because most of the bedrock under the WAIS lies below sea level, it is classified as a so called marine ice sheet. Some areas lie as deep as 2000 m below sea level (*Vaughan et al.*, 2006). A marine ice sheet is anchored to its bed only because it is too thick to float. The WAIS is the only significant marine ice sheet still present today. A past marine ice sheet was for example present in the Barents Sea during the Last Glacial Maximum ( $\sim 20$  ka ago) (*Landvik et al.*, 1998; *Benn and Evans*, 2010). The disappearance of all marine ice sheets but the WAIS encouraged the hypothesis that marine ice sheets are intrinsically unstable (*Vaughan*, 2008). A variety of studies arose discussing the validity of this hypothesis.

Figure 1.2 shows a sketch of a marine ice sheet based on a bed with a retrograde slope, of which the importance will be pointed out in the subsequent text.

*Hughes* (1973) evaluated a variety of measurements taken on the Antarctic Ice Sheet from the International Geophysical Year 1957-1958 onwards. He found, that the WAIS shows several signs of non equilibrium flow conditions, being currently in a retreating state. This made him suspect that a marine ice sheet may be inherently unstable and that the possibility of a surge like retreat of the WAIS exists.

*Weertman* (1974) approached the stability question from a more theoretical side, based on a idealised flow-line model. He analysed stable grounding line positions for a variety of bed slope profiles and concluded, that a marine ice sheet placed on a flat bed is inherently

unstable. A stable situation can only be achieved on a bed that slopes away from the center. When he applied his analysis to bed slope values representative for the WAIS, a stable position was found at about half-width of the present WAIS. *Weertman* (1974) already stated the importance of including lateral drag and buttressing, caused by ice shelves, into the analysis.

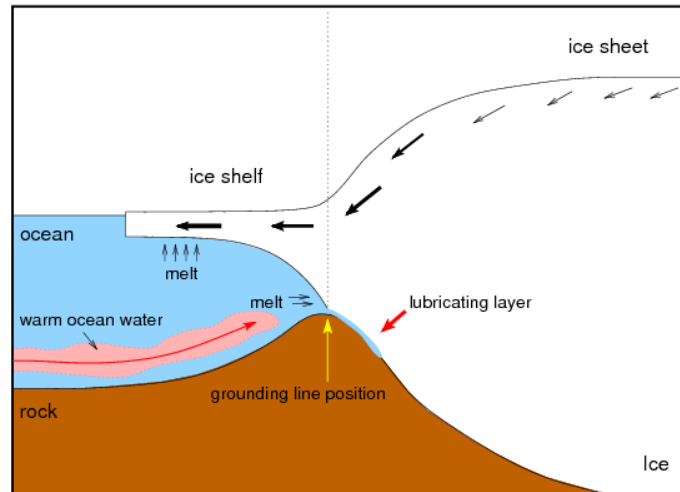


Figure 1.2: Schematic of a marine ice sheet on a retrograde bed

*Thomas and Bentley* (1978) described a feedback cycle that leads to an unstable retreat of marine grounding lines on a retrograde bed as the following: If for example sea level rise causes the grounding line to retreat inland it will move into thicker ice due to the retrograde bed. This will lead to enhanced mass flux across the grounding line and, as an effect, to dynamic thinning. This thinning will then lead to a further retreat of the grounding line, closing the feedback cycle. *Thomas and Bentley* (1978) emphasised the importance of ice shelves for stabilising the retreat scenario.

While the earlier studies believe the cause for an unstable retreat or even collapse of the WAIS to be unconnected to anthropogenic climate change, *Mercer* (1978) was the first to combine the actual threat of greenhouse warming with the collapse of the WAIS and a induced sea level rise of 5 m globally (this value was later revised to 3.3 m by *Bamber et al.* (2009)). *Mercer* (1978) centred his reasoning around the buttressing effect of ice shelves. He argues that, if climatic warming would disintegrate ice shelves by percolating surface melt water, the rapid deglaciation of the WAIS could be initiated. *Mercer* (1978) gives no values at all on how much time these processes would take. However, with time and repetition the likely threat of a rapid collapse of the WAIS became a paradigm (*Vaughan*, 2008).

The following increased interest in the potential instability of the WAIS led to much fieldwork throughout the 1980s and 1990s. The fieldwork was focused on the Filchner-Ronne Ice Shelf and its hinterland, the Ross Ice Shelf and the Siple Coast. Due to bad accessibility, the Amundsen Sea Embayment Area remained largely unvisited (*Vaughan*, 2008). These surveys did not produce any strong evidence that those parts of the WAIS were in danger of collapse. In the Third Assessment Report of the IPCC the contribution of the Antarctic Ice Sheet to sea level rise was described as being very small ( $1.04 \pm 1.06 \text{ mm a}^{-1}$ ) or even negative ( $-0.5 \text{ mm a}^{-1}$ ) (*IPCC-AR3*, 2001). The first new hint of a

transient behaviour was given by a study from *Wingham et al.* (1998), in which elevation change over about 50 % of the continental area was calculated. This was only possible due to satellite altimeter measurements. *Wingham et al.* (1998) found, in the period from 1992 to 1996, no significant elevation change over most parts of the EAIS. But in the ASEA they found an indication of surface lowering of as much as  $10 \text{ cm a}^{-1}$ . Due to very high rates of snowfall in this area, *Wingham et al.* (1998) were not sure if the surface lowering was due to a dynamic change. But in combination with another study by *Rignot* (1998), that showed a grounding line retreat at Pine Island Glacier of almost  $1 \text{ km a}^{-1}$  over the period 1992-1996, the signal for an ongoing dynamic change became clearer.

The observations in the ASEA, and especially at Pine Island Glacier, continued and revealed a variety of further indications for change. These findings will be further discussed in Section 1.3. Following the observations of change in the ASEA, an additional focus was set on modelling the transition zone between the grounded and floating ice, the grounding line, described in Section 1.2.3.

### 1.1.3 Basal properties

For the dynamics of an ice sheet, the basal properties below the ice sheet are important. The ice can exhibit very different basal motion over for example hard rock, till or marine sediments. The availability of liquid water also has a major influence on the basal motion of the ice sheet. In Antarctica the bed rock is a mosaic of hard rock and soft sediments, above which the fast ice streams flow (*Benn and Evans, 2010*).

It poses a big challenge to derive information on different basal conditions under ice sheets. Bore holes are one possibility to obtain information on basal properties. However, only very few boreholes in the WAIS exist (e.g. *Engelhardt et al., 1990; Engelhardt and Kamb, 1998*), as their retrieval is time consuming and expensive. Additionally, they give only a random sample at one point in time. This might be important to consider in areas with fast changing basal conditions, but is not of major concern in slow changing areas.

To derive a spatially more complete picture of the basal properties geophysical techniques and modelling are applied (*Bingham et al., 2010*). The geophysical techniques include RAdio Detection And Ranging (RADAR), seismic and gravity techniques. The radar systems applied today are mainly airborne and facilitate comprehensive coverage. Cold ice is transparent to electromagnetic waves in the high to very high frequency bands. Thus the Ice-Penetrating Radar (IPR, also called Radio-Echo Sounding (RES)) can detect the ice surface, internal layers and the ice-bed interface.

The bed-echo strength, also called bed reflectivity, is influenced by the presence of water, subglacial geology and roughness of the ice-bed interface. Brighter reflections can indicate wet, hard and smooth beds, while dimmer reflections indicate dry/frozen, soft/unconsolidated and rough beds (*Peters et al., 2005*). Thus also the possible existence of subglacial lakes can be inferred from bed reflectivity.

Apart from the bed reflectivity, which focuses on the amplitude of the returned signal, it is possible that also the length and phase of the returned signal can be related to basal properties (*Rippin et al., 2006; Bingham et al., 2010*).

From the basal topography itself the bed roughness can be derived, which is defined as the vertical variation of the bed with horizontal distance. Figure 1.3 shows the basal roughness distribution from *Bingham and Siegert (2009)*, for some regions below the Antarctic Ice Sheet. Also refer to Sections 4.4 and 5.5.1 for more details about the basal roughness

measure. There are a variety of algorithms for assessing bed roughness, but they all lead to similar regional-scale patterns (Bingham *et al.*, 2010). Here it has to be kept in mind, that high resolution data is only obtained along flight tracks and interpolation between tracks is applied. This is especially important to consider in data-sparse regions.

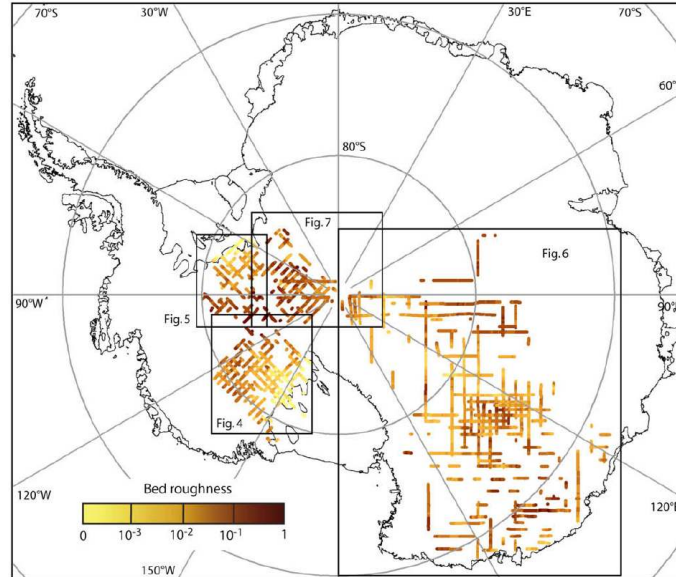


Figure 1.3: Bed roughness distribution below the Antarctic Ice Sheet. Figure taken from Bingham and Siegert (2009).

Seismic techniques are the oldest geophysical methods in glaciology and provided the first ice thickness measurements of the WAIS (Mothes, 1926; Bentley and Ostenso, 1961). Seismic techniques work with elastic waves, in contrast to electromagnetic waves, and can hence image sub-bed structures. It is thus possible to extract the porosity, composition and internal structure of subglacial sediments, which can play an important role for fast ice flow due to internal sediment deformation (Boulton and Hindmarsh, 1987; van der Meer *et al.*, 2003). Also the existence of a subglacial water layer is possible to detect with seismic methods (King *et al.*, 2004; Smith, 2007).

Inverse modelling techniques are applied with increasing frequency to infer basal properties, such as certain sliding parameters in sliding laws and basal drag (MacAyeal, 1992; Sergienko *et al.*, 2008; Joughin *et al.*, 2009; Pollard and DeConto, 2012). These techniques are usually based on measured surface velocity fields and use control methods to infer the basal fields. Modelling of ice flow dynamics is also an important tool to test hypotheses about subglacial bed properties (Bingham *et al.*, 2010).

From aerogravity measurements the crustal thickness can be inferred and thus a geothermal heat flux estimated (Jordan *et al.*, 2009). Geothermal heat flux is not directly considered a basal property, but can lead to enhanced subglacial melt water occurrence.

When modelling ice sheet dynamics, not only the type of bed rock can have a major influence, but also the resolution on which the data is available (Durand *et al.*, 2011).

## 1.2 Ice sheet models

For the formation of ice sheet models a variety of developments in different fields were necessary. There is the development of a physical description of glacier flow, and measurements that support the theories. Furthermore, the growing availability of computational resources fostered the field of numerical modelling. Here we will give a short overview of the different developments, followed by descriptions of some selected sub-items in glacier modelling. First we will have a look at different approximations used in glacier models (Section 1.2.1), followed by basal sliding (Section 1.2.2) and finally grounding line migration in numerical models (Section 1.2.3).

Observations of glacier flow, and attempts for a physical explanation, can already be found in the 18th century. David Forbes (1809-68) was perhaps the first to propose that glaciers flow like viscous fluids (*Clarke, 1987; Blatter et al., 2010*). Forbes' suggestion led to a heated controversy, due to the solid and brittle appearance of the ice (*Cuffey and Paterson, 2010*), but eventually prevailed. Laboratory experiments suggested a power-law for the deformation of ice (*Glen, 1952; Steinemann, 1954; Glen, 1955*), in more detail described in Section 2.2. *Nye (1953)* applied this power-law for the flow of ice, later called *Glen's flow law* or *Glen-Steinemann flow relation*, to field observations. It was eventually agreed on, that glacier flow is a problem within the field of fluid dynamics (*Blatter et al., 2010*). The fluid dynamical balance equations, together with a non-Newtonian rheology, can therefore describe the flow of glacier ice. Due to special properties of glacier ice, discussed in Section 2.1.2, the momentum balance becomes a force balance, given in components, such that

$$\operatorname{div}(\boldsymbol{\tau} - p\mathbf{I}) = -\rho_i\mathbf{g} \Rightarrow \begin{aligned} \frac{\partial}{\partial x}\boldsymbol{\tau}_{xx} + \frac{\partial}{\partial y}\boldsymbol{\tau}_{xy} + \frac{\partial}{\partial z}\boldsymbol{\tau}_{xz} &= \frac{\partial}{\partial x}p \\ \frac{\partial}{\partial x}\boldsymbol{\tau}_{yx} + \frac{\partial}{\partial y}\boldsymbol{\tau}_{yy} + \frac{\partial}{\partial z}\boldsymbol{\tau}_{yz} &= \frac{\partial}{\partial y}p \\ \frac{\partial}{\partial x}\boldsymbol{\tau}_{zx} + \frac{\partial}{\partial y}\boldsymbol{\tau}_{zy} + \frac{\partial}{\partial z}\boldsymbol{\tau}_{zz} &= \frac{\partial}{\partial z}p + \rho_i g, \end{aligned} \quad (1.1)$$

with  $\tau_{ij}$  being the different components of the deviatoric stress tensor  $\boldsymbol{\tau}$ ,  $p$  the pressure,  $\mathbf{I}$  the identity matrix,  $\rho_i$  the ice density and  $g$  the gravitational acceleration. For a derivation of the equations refer to Section 2.1.2. The colour indication will be used in Section 1.2.1 to describe the different approximations.

In a variety of scientific fields, numerical modelling has become a useful tool to expand understanding. Especially when *real* experiments and analytical theory reach their limits. This is among others the case for fluid dynamics. The equations of motion describing fluid flow are well known. But due to nonlinearities in many cases they can not be solved analytically. In Computational Fluid Dynamics the equations are solved numerically and this helps to understand the dynamics of fluid motion.

In the past decades the use of computer models in science has become increasingly popular. The experiments conducted with computer models are called *in-silico* experiments. This term is an analogue to *in-situ*, which is a Latin phrase meaning *in position*. *In-silico* refers to the material silicon, what most Central Processing Units (CPUs) are made of (*Gramelsberger, 2010*).

A glacier model is always a simplification of the reality, with several approximations and assumptions made. Continuum mechanics approximate the fluid motion by the Eulerian description, which assumes a continuous mass rather than discrete particles. To receive a numerical solution, the underlying system of equations needs to be discretized (refer to Section 2.5). The grid spacing hereby depends on the focus of the study. In general it

can be said that processes that take place on scales smaller than the grid spacing have to be parametrised, which is the aim to find a formulation for the larger scale impact of smaller scale processes. An example for this in glacier models is the sliding of a glacier over its bed. In reality it is influenced by numerous processes on a variety of scales. Sliding relations are introduced, that try to capture the main processes without becoming too complex to work with. Another example is given by the ice rheology, discussed in detail in Section 2.2.1. It describes the bulk creep behaviour of polycrystalline ice, instead of the deformation of every single ice crystal (*van der Veen, 2002; Benn and Evans, 2010*).

Another source of uncertainty can be given by the data used to calibrate the model. Measured data is also subject to assumptions and approximations made during the measurement process, and has to be handled with care.

Apart from these obvious shortcomings, computer experiments are a valuable tool to investigate systems that are not otherwise manageable for a real physical experiment, due to huge spatial or temporal scales, as is the case for glaciers. Still, when dealing with computer experiments, it is very important to remember the shortcomings of the tool. A common mistake is for example done by using the same data to validate a model, that was initially used to calibrate the system with (*van der Veen, 1999*).

### 1.2.1 Approximations

A glacier flow model consists of solving a coupled thermomechanical problem. This can be done for either a diagnostic or a prognostic problem. Diagnostic models usually focus on particular processes and their influence on the glacier system, while prognostic models usually simulate the evolution of glacier systems in time and their response to changing external conditions (*Benn and Evans, 2010*).

When solving the coupled thermomechanical problem, the computationally most expensive part is given by the mechanical part as shown in component form in Eq. (1.1). Solving for the full set of terms is the most exact solution that can be obtained and the models doing this are called *full-Stokes* (FS) models (*Alley et al., 2012*). As these models are computational expensive they are usually used diagnostically to study specific outlet glaciers (e.g. *Morlighem et al., 2010*). Increase in computational resources make it also possible to calculate the evolution of an ice sheet with a *full-Stokes* model over a certain period (e.g. *Seddik et al., 2012*).

Depending on the flow regime modelled, different terms in Eq. (1.1) can be shown to have minor influence and can therefore be neglected. The first three dimensional ice sheet models were based on the so called *Shallow Ice Approximation* (SIA) (*Hutter, 1983; Morland, 1984*). These models assume, that ice flow is dominated by internal shear deformation. This is true for large parts of the interior of an ice sheet, where the ice is frozen to the ground or the ice simply does not slide due to the high basal roughness. Also in the interior of an ice sheet typical horizontal extents are large compared to typical vertical extents. Therefore, longitudinal derivatives of stress, velocity and temperature are small compared to vertical derivatives and can be neglected (*Hooke, 2005*). This leaves only the black and red terms in Eq. (1.1), leading to a local balance of the stresses.

In ice shelves or fast flowing outlet glaciers vertical shear is negligible and horizontal velocity components therefore hardly vary with depth. The resulting flow is a so called plug-flow and described by the blue and black terms in Eq. (1.1). This approximation was first introduced by *Morland (1987)* for an unconfined ice shelf, and later on extended

by *MacAyeal* (1989) for ice stream flow over a viscous basal sediment. The approximation is called *Shelfy-Stream* or *Shallow Shelf Approximation* (SSA).

A *Higher Order Model* (HOM) was first introduced by *Blatter* (1995) and later on written in terms of velocities by *Pattyn* (2003). It incorporates longitudinal stress terms and only neglects part of the brown and red terms in Eq. (1.1).

Approximations always simplify the solution and if the requirements for its validity in certain applications are not considered, this can lead to errors. The SIA is for example not valid in key areas such as ice divides and grounding lines (*Baral et al.*, 2001; *Pattyn et al.*, 2012). In general the accuracy of the SIA decreases, as the contribution of basal slip increases (*Gudmundsson*, 2003).

### 1.2.2 Basal motion

The overall glacier motion consists of different components: internal creep deformation of the ice, sliding of ice over its bed and deformation of the bed itself. Basal motion or basal slip is the combined motion of sliding and bed deformation (*Cuffey and Paterson*, 2010). The strength, with which the components contribute to the total motion, strongly varies in different regions. In certain areas basal sliding can account for up to 90% of the glacier motion (*Schweizer*, 1989). It is agreed on, that basal slip can be a very important factor for ice dynamics, but still it is difficult to be precisely described in ice flow models, as it depends on many different and often locally unknown factors. A major drawback to the understanding of basal slip is the difficulty to observe it. Measurements have been conducted in subglacial cavities, tunnels and boreholes, but these are local measurements and can not necessarily be generalised to a wider area (*Cuffey and Paterson*, 2010). Although it might be impossible to know the basal conditions below a glacier well enough to accurately predict the rate of motion of the glacier over its bed, it is important to understand the processes, to place limits on the rate (*Hooke*, 2005). Theories were established to describe the slip mechanisms, with reasonable assumptions made where necessary, as a substitute for detailed data. For modelling glacier dynamics slip relations are necessary. These relations commonly connect basal velocity  $\mathbf{u}_b$ , basal shear stress  $\tau_b$  and bed characteristics. The bed characteristics can be the effective pressure  $N_b$ , the bed roughness and sediment properties (*Cuffey and Paterson*, 2010). When choosing a sliding relation for a glacier model, it is often a trade off between a realistic description and a workable formulation (*Benn and Evans*, 2010).

Following *Weertman* (1957), the sliding of a glacier over a hard bed is only possible for a temperate base, which is a base at pressure melting point, and due to a combination of regelation and enhanced creep. Regelation describes a process where the ice melts due to high pressure on one side of an obstacle and refreezes on the other side. Enhanced creep is due to a stress concentration on the upstream side of an obstacle. It was later found that sliding velocities exceeding  $20 \text{ m a}^{-1}$  on hard beds can only be explained with the existence of water filled cavities, stressing the importance of the effective pressure  $N_b$  (*Lliboutry*, 1968; *Bindschadler*, 1983). While the original sliding law by *Weertman* (1957), described in detail in Section 5.1.1, consisted mainly of physical parameters, it developed into a general sliding relation of a similar form, the so called *Weertman type sliding law*

$$\mathbf{u}_b \sim \tau_b^p N_b^{-q}. \quad (1.2)$$

The constants  $p$  and  $q$  are usually empirically determined. The effective pressure  $N_b$  has

to be either explicitly modelled as a subglacial hydraulic system (e.g. *Flowers et al.*, 2003) or a simple parametrisation is used (e.g. *Huybrechts and de Wolde*, 1999). The *Weertman type sliding law* in Eq. (1.2) is often extended with a temperature function  $f(T)$ , to control sliding for regions with temperatures below pressure melting point (e.g. *Fowler*, 1986; *Budd and Jenssen*, 1987).

One shortcoming of the above formulation is, that it results in infinite basal velocities  $\mathbf{u}_b \rightarrow \infty$ , if  $N_b = 0$  and  $\tau_b > 0$ . This would not happen in reality, as part of the driving stress is supported by lateral drag and longitudinal stress gradients, so called global controls (*Benn and Evans*, 2010). Looking at this from another side, for increasing basal velocities  $\mathbf{u}_b \uparrow$  and increasing effective pressure  $N_b \uparrow$ , there is no upper bound for the basal shear stress  $\tau_b$ , such that  $\tau_b < \tau_{b,max}$ . In reality though, cavities form as a result of increasing water pressure in the lee side of bedrock obstacles, putting an upper bound on  $\tau_b$ , determined by the slope of the bed (*Iken*, 1981; *Schoof*, 2005). Relations of the form shown in Eq. (1.2), that express the basal velocity  $\mathbf{u}_b$  explicitly as a function of basal shear stress  $\tau_b$  and effective pressure  $N_b$ , are called *sliding laws* and implemented as a Dirichlet boundary condition. Laws with an upper bound for  $\tau_b$ , that describe a relationship between the different terms, are called *friction laws* and implemented as a Robin boundary condition (*Gagliardini et al.*, 2007). These friction laws can be multi-valued, meaning a given basal velocity may be associated with more than one value of basal drag (*Benn and Evans*, 2010).

The above described *sliding* and *friction laws* only deal with hard bed sliding. On deformable substrates, hereafter generally referred to as till, high basal velocities can also be present (*Cuffey and Paterson*, 2010). Subglacial till can consist of glacial deposits or marine sediments. It can be modelled separately to derive the internal temperature dependent deformation (e.g. *Bougamont et al.*, 2003; *Christoffersen and Tulaczyk*, 2003). These models are based on a Coulomb-plastic yield criterion, which specifies the maximum basal shear stress  $\tau_b$  that can be supported by the till (*Benn and Evans*, 2010).

In reality many regions are dominated by a mixture of hard (bedrock) and soft or weak (till) beds. Simple parametrisations can be used to capture this by applying a law of the form  $\tau_b \sim \mathbf{u}_b^{1/m}$ , where  $m = 1$  should mimic linear-viscous till deformation (*MacAyeal*, 1992),  $m \rightarrow \infty$  plastic till behaviour or fast flow over hard bed (*Joughin et al.*, 2004) and  $m = 3$  slow flow over hard bed (*Cuffey and Paterson*, 2010).

### 1.2.3 Grounding line migration

The dynamics of marine ice sheets are sensitive to grounding line position and migration. Thus grounding line motion is an important factor for numerical investigation of the WAIS (*Katz and Worster*, 2010). Many current ice-sheet models do not yet include rapid ice loss due to grounding line migration, as most of the complex processes are poorly understood (*Docquier et al.*, 2011).

The different stress approximations in ice sheet models (Section 1.2.1) lead to different implementations of grounding line motion. For grounding line motion it is also of high importance what kind of mesh is applied. In Fixed Grid (FG) models the grounding line position always falls in between grid points. Moving Grid (MG) models explicitly model the position and follow it continuously. Adaptive Mesh (AM) models are a trade-off between fixed and moving grids, and refine the mesh near the grounding line (*Docquier et al.*, 2011).

Some *full-stokes* models solve a contact problem between the ice and a rigid bedrock (Durand et al., 2009). To determine the location of the grounding line two conditions have to apply, the floating condition and a stress condition, comparing the water pressure to the ice overburden pressure (Schoof, 2005; Gagliardini et al., 2007; Durand et al., 2009). Another way is to determine the grounding line position by solving for the ice thickness and apply the floating condition, hereby neglecting bridging effects (Pattyn et al., 2013).

Several studies show, that it is necessary to consider all stress terms in the transition zone from shear flow to plug flow across the grounding line (e.g. Lestringant, 1994; Pattyn, 2000; Pattyn and Durand, 2013). For large scale ice sheet models, this is not possible, due to computational costs. Schoof (2007a) developed a semi-analytical solution for the ice flux across the grounding line for shallow models, which Pollard and DeConto (2009) incorporated into a numerical ice sheet model at coarse grid resolution by applying a heuristic rule.

Mesh resolution around the grounding line is also a crucial issue (Viel and Payne, 2005). High mesh resolution is needed in the vicinity of the grounding line in order to generate consistent results (Durand et al., 2009; Gladstone et al., 2012). To save computational cost, ice sheet models with adaptive mesh refinements are of high interest and increasingly developed (e.g. Gladstone et al., 2010; Cornford et al., 2012).

For the hypothesis of marine ice sheet instability, the existence of steady state grounding line positions on reverse bed slopes is discussed. There are studies that suggest neutral equilibrium on a reversed bed slope (e.g. Hindmarsh, 1993, 1996) and others, that do not (e.g. Schoof, 2007a; Durand et al., 2009; Katz and Worster, 2010). The Marine Ice Sheet Model Intercomparison Project (MISMIP) shows common agreement on the hysteresis across an overdeepened bed for 2D flow-line models (Pattyn et al., 2012). Newer 3D model studies, however, stress the importance of lateral drag and are able to produce steady grounding line positions on a reversed bed slope (Gudmundsson et al., 2012; Jamieson et al., 2012).

A new Marine Ice Sheet Model Intercomparison Project for 3D models (MISMIP 3D) was conducted, which focuses on the reversibility of grounding line positions and not on reversed bed slopes though (Pattyn et al., 2013). These model intercomparisons are valuable to estimate the influence of model physics, approximations, grid resolutions and other factors onto the results of grounding line positions.

## 1.3 Pine Island Glacier

Pine Island Glacier is a fast flowing outlet glacier, draining a large part of the WAIS. In the past decades the glacier has shown acceleration, thinning and a significant grounding line retreat (Rignot, 2008; Wingham et al., 2009; Rignot, 1998). These ongoing processes are coinciding with a concentrated mass loss in the area around Pine Island Glacier, the Amundsen Sea Embayment (Horwath and Dietrich, 2009).

While the Weddell and Ross Sea sectors drain through  $\sim 500$  km wide ice shelves, the Amundsen Sea sector holds only narrow ice shelves, that provide less buffering against collapse. Due to this special setting, Mercer (1978) identified the Amundsen Sea sector as the most vulnerable to collapse.

In the following we will give an overview of the observed changes on Pine Island Glacier (Section 1.3.1) and the conducted model studies for this area (Section 1.3.2).

### 1.3.1 Observations

Observations on Pine Island Glacier became denser in the 1970s with increasing satellite observations. Earlier observations were sparse due to the remoteness of the glacier and an extensive sea ice cover in Pine Island Bay (Vaughan, 2008).

Pine Island Glacier drains an area of  $\sim 1.75 \times 10^6 \text{ km}^2$  (Vaughan *et al.*, 2006), which is about 9% of the WAIS. From the total potential of the WAIS to raise eustatic sea level by 3.3 m (Bamber *et al.*, 2009), 0.52 m can be accounted to Pine Island Glacier (Vaughan *et al.*, 2006). In case of a collapse of the WAIS, only 0.24 m from those 0.52 m of ice equivalent would really be lost to the ocean, as the drainage basin is subdivided into a northern and southern basin by a bed high (Vaughan *et al.*, 2006).

Under Pine Island Glacier sediment basins are suspected. Their existence is inferred from basal roughness distributions (Rippin *et al.*, 2011), aerogravity measurements (Jordan *et al.*, 2009) and seismics (Smith *et al.*, 2013). Subglacial geology influences the spatial pattern of ice flow (Smith *et al.*, 2013). In some areas, subglacial erosion rates of  $\sim 1 \text{ m a}^{-1}$  have been derived (Smith *et al.*, 2012), suggesting a possible change over time of the subglacial environment, and thus possibly the ice flow patterns.

The fast flowing ( $|\mathbf{u}_s| > 100 \text{ m a}^{-1}$ ) main trunk of the glacier is about 325 km long, while the total length from the ice divide to the calving front is about 400 km. The main trunk lies in a 500 m deep trough, which suggests a constrained and long-lived ice stream (Vaughan *et al.*, 2006).

The ice flows from the interior to the West, into the Amundsen Sea, where it forms a small ice shelf. The shape of the ice shelf is defined by a variety of ice rises, pinning the ice shelf. The areal extent of the ice shelf has not shown major changes since observations started in 1947, only the slow flowing northern shelf showed a slight ongoing retreat. The calving front undulates with calving events periodically about every 6 years (1995/96, 2001, 2007, 2013) (Rignot, 2002, pers. observation). At these calving events, big icebergs, several km long and 10 – 20 km wide, are calved off into the Amundsen Sea. The iceberg size for the last big calving event in 2013 was  $\sim 700 \text{ km}^2$  (pers. observation).

Beneath the ice shelf a ridge is located in the sea bed, perpendicular to the flow direction. The position of the ridge is suggested to be an earlier location of the grounding line (Jenkins *et al.*, 2010). In the past decades, the grounding line position strongly retreated further by  $1.2 \pm 0.3 \text{ km}$  between 1992 and 1996 (Rignot, 1998), and up to 20 km between 1996 and 2009 (Joughin *et al.*, 2010). For a further description also refer to Section 3.1.2. This recent retreat took place across a so called ice plain, an only slightly grounded area, which facilitated the ungrounding (Corr *et al.*, 2001). The grounding line position in 2009 includes a lightly-grounded island like area forward of the main grounding line (Joughin *et al.*, 2010). Park *et al.* (2013) infer from 1992 to 2011 a constant retreat rate of  $0.95 \pm 0.09 \text{ km a}^{-1}$ , which is accompanied by an accelerated rate of terminus thinning of  $0.53 \pm 0.15 \text{ m a}^{-2}$ . Figure 1.4, taken from Joughin *et al.* (2010), shows the surface velocity field at Pine Island Glacier, together with the grounding line positions from 1996 and 2009.

Acceleration of the entire glacier flow speed has been observed since the 1970s. The ice shelf, which is only the part of the glacier floating on the ocean, accelerated hereby from  $\sim 2300 \text{ m a}^{-1}$  in 1974 to  $\sim 4000 \text{ m a}^{-1}$  in 2007. The entire glacier, including grounded and floating ice, accelerated by 42% between 1996 and 2007 and by 73% between 1974 and 2007 (Rignot, 2008).

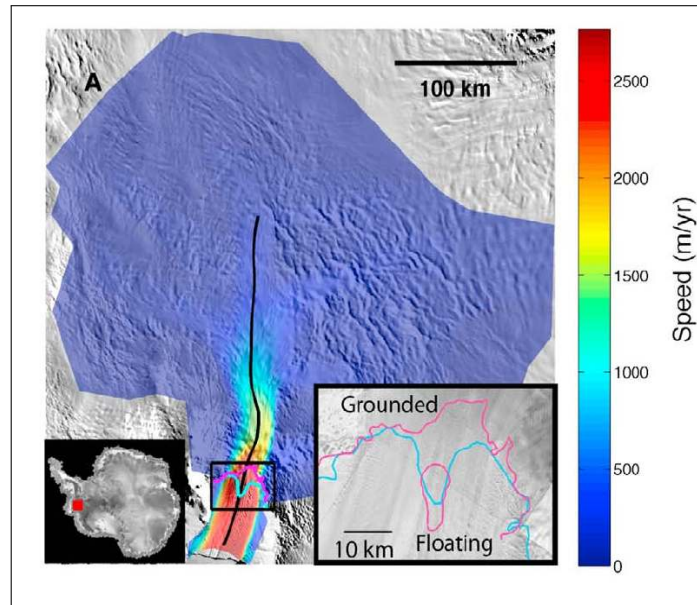


Figure 1.4: Surface velocity and grounding line positions 1996 (cyan) and 2009 (magenta). Figure taken from *Joughin et al.* (2010).

This acceleration is accompanied by an increased thinning near the grounding line from  $3 \text{ m a}^{-1}$  in 1995 to  $10 \text{ m a}^{-1}$  in 2006. In 1995, the thinning was limited to the main trunk of the glacier, with thinning rates over  $1 \text{ m a}^{-1}$  confined to the ice plain area. By 2006 the thinning was found in all the tributaries with rates over  $1 \text{ m a}^{-1}$  extending up to 100 km inland from the grounding line (*Wingham et al.*, 2009).

Warm ocean waters are suspected to be a major driver for these ongoing observed changes (*Payne et al.*, 2004; *Jacobs et al.*, 2011; *Pritchard et al.*, 2012). Different approaches have all come to the conclusion, that the melt rates beneath the Pine Island Ice Shelf are exceptionally high ( $24 \pm 4 \text{ m a}^{-1}$  (*Rignot*, 2006),  $15 \pm 2 \text{ m a}^{-1}$  (*Shepherd et al.*, 2004),  $10 - 12 \text{ m a}^{-1}$  (*Jacobs et al.*, 1996)).

Pine Island Glacier is undergoing drastic changes. Whether these changes are only the beginning of an ongoing retreat of the glacier, or if it will eventually stabilise again, are questions yet to be answered. Modelling studies are carried out to investigate this question and will be described in the next Section.

### 1.3.2 Model studies

Model studies on Pine Island Glacier address questions focusing on how sensitive the glacier is to changes in external conditions (ice shelf buttressing, basal conditions) (e.g. *Schmeltz et al.*, 2002) and how much the future contribution to sea level rise will be (e.g. *Joughin et al.*, 2010). The overarching question is though, if the system will stabilise again in the near future, or if retreat might even accelerate (e.g. *Katz and Worster*, 2010; *Gladstone et al.*, 2012).

A variety of models have been applied to the glacier, with different degrees of approximations and horizontal dimensions. There are basin wide SSA models (e.g. *Joughin et al.*, 2009, 2010), SSA models covering a smaller area fraction (e.g. *Schmeltz et al.*, 2002), SSA

flow-line models (*Gladstone et al.*, 2012) or a full-Stokes model (*Morlighem et al.*, 2010).

Some model studies explicitly deal with questions concerning the glacier, while others use Pine Island Glacier as an application example for newly developed tools (e.g. *Larour et al.*, 2012; *Cornford et al.*, 2012).

*Schmeltz et al.* (2002) investigated the sensitivity of Pine Island Glacier to ice shelf buttressing and basal conditions with a SSA model. They assume linear-viscous till deformation ( $m=1$ , refer to Section 1.2.2) and conclude, that the removal of the entire ice shelf, although not likely to happen soon, would lead to a speed up  $> 70\%$ . The glacier is less sensitive to softening of glacier shear margins and reduction in basal shear stress. They assume a constant temperature, and are thus not solving for the thermo-mechanically coupled problem.

*Joughin et al.* (2009) infer basal properties below Pine Island Glacier from a model constraint with surface velocities. They find mixed bed conditions, with areas of strong bed and areas of weak till. They used different basal sliding laws. Another study was carried out by *Joughin et al.* (2010), to test the time dependent response to grounding line retreat with the different sliding parametrisations. They find, that the mixed bed assumption delivers the most plausible results. Additionally, they estimate an upper bound of  $0.27 \text{ mm a}^{-1}$  to eustatic sea level rise from Pine Island Glacier, which is considerably smaller than previous estimates ( $0.4 - 1.5 \text{ mm a}^{-1}$  (*Pfeffer et al.*, 2008; *Joughin et al.*, 2010)). The present day ice mass loss of the entire ASEA, consisting of Pine Island and Thwaites Glacier, is equivalent to  $0.27 \text{ mm a}^{-1}$  (*Groh et al.*, 2012). They also conclude, that the rate of grounding-line retreat should diminish soon, suggesting a stabilisation of the system. *Joughin et al.* (2009) and *Joughin et al.* (2010) solve for the temperature, but not in a coupled manner.

*Gladstone et al.* (2012) couple a 2D flow-line model with a box model for cavity circulation and follow a more statistical approach. They carry out ensemble simulations over a 200 year period (1900 – 2100) and compare the results to recent observations. Thus they make a calibrated prediction in the form of a 95% confidence set that monotonic grounding line retreat will prevail.

*Morlighem et al.* (2010) diagnostically modelled the flow of Pine Island Glacier using three different degrees of approximation (SSA,HOM,FS) and inferred basal shear stress. They find that SSA and HOM overestimate drag near the grounding line due to neglected bridging effects, therefore arguing for the use of FS models near the grounding line. These findings are partly contrary to results from *Joughin et al.* (2009).

## 1.4 Objectives and structure of this study

The major aim of this study is to advance our knowledge about the internal dynamics, basal motion and thermal structure of Pine Island Glacier. The significant observed changes taking place at Pine Island Glacier are related to changes of the glacier dynamics. The interplay of external forcing and internal feedback are crucial for the future dynamics of the glacier. Among the biggest challenges today for simulating the dynamics of real glaciers and ice sheets, is the formulation of basal sliding, as the basal conditions are difficult to access.

We investigate the dynamics of Pine Island Glacier with use of a thermo-mechanically coupled 3D finite element full-Stokes flow model. To do this, the coupled flow model is set

up for the glacier and a variety of diagnostic numerical experiments are performed. Since we use a full-Stokes model, which is computationally expensive and therefore appropriate for diagnostic process studies in high resolution, rather than time dependent evolution of the glacier, we focus on local flow mechanisms and basal sliding. The simulated scenarios are developed to derive for one the locally dominant mechanisms driving the complex surface flow structure of the glacier. Based on these results the second part focuses on basal sliding and associated bed conditions. The aim is to step away from a commonly conducted empirical fit of basal sliding parameters with control methods to observed surface velocities, and move towards inclusion of measured basal properties to constrain basal sliding.

This introductory chapter is followed by a theory chapter, Chapter 2, in which the underlying equations of the coupled flow model, the boundary conditions and the finite element method are introduced. A large portion of the study is dedicated to the advancement, implementation and validation of the coupled flow model, which is described in Chapter 3. The coupled flow model is implemented in the commercial finite element method software COMSOL Multiphysics<sup>®</sup>. The used prismatic finite element mesh allows for easy refinement around the grounding line, where high resolution is necessary to resolve the dynamics accurately.

In Chapter 4 the focus lies on the identification of the dominant local mechanisms, driving the flow of the different tributaries. A variety of numerical experiments, with varying boundary conditions, are conducted. Also a reference simulation is conducted with a similar but simplified approach, as the above describe control methods.

In Chapter 5, we explicitly focus on basal sliding. By using information about the basal roughness distribution beneath the glacier, we constrain basal sliding by this additional physical information. A range for a locally varying basal sliding parameter is identified with the simplified inversion. This range is matched onto the normalised roughness distribution and applied in the basal sliding formulation of the forward coupled flow model. The results are analysed and discussed. Additionally, a theory by *Li et al.* (2010) is tested for its applicability to Pine Island Glacier, which connects the roughness measure to the original sliding assumptions made by *Weertman* (1957). The main findings are summarised and the final conclusions drawn in Chapter 6.



# Chapter 2

## Theory

In this chapter, the theoretical foundations of the model are described. At the length and time scales considered in this study, glacier ice is seen as a continuum and behaves like a fluid. Therefore, the flow of glacier ice can be described with the governing equations of fluid mechanics, a field of continuum mechanics. The governing equations are the balance equations for mass (Section 2.1.1), momentum (Section 2.1.2) and energy (Section 2.1.3). Additionally, a constitutive equation (Section 2.2) is needed to complete the system.

The field quantities we are interested in are the velocity field  $\mathbf{u}$ , the pressure  $p$  and the temperature  $T$ . The evolution of these quantities can not be calculated directly, as they are not conserved quantities, but can instead be derived from the balance equations for mass, momentum and energy.

The balance equations in local form (as described in Section 2.1) are only valid if the fields are sufficiently smooth. This is not the case at the outer boundaries of the glacier and therefore special conditions for these cases have to be formulated, which is done in Section 2.4.

In order to solve the resulting partial differential equations numerically, the finite element method is applied. The basic concepts of this method are described in Section 2.5.

### 2.1 Balance equations

The balance equations can be expressed in two different ways, the *Eulerian* and the *Lagrangian description*. The *Eulerian description*, also called *spatial description*, considers all matter passing through a fixed spatial location. The *Lagrangian description*, also called *material description*, focuses on a set of fixed material particles, irrespective of their spatial location (*Hutter and Jöhnk, 2004*). For the study of fluid flow and convective heat transfer, the *Eulerian description* is more convenient and will be used here.

The general balance equation describes the balance of a physical quantity  $G(\omega, t)$  (mass, momentum or energy) within a distinct volume  $\omega$  at time  $t$ . For this quantity the additivity assumption must hold, which states that the value of a physical variable of a body is given by the summation of its values over the parts of the body (*Hutter and Jöhnk, 2004*). These quantities are mass, momentum or energy and not velocity, pressure and temperature. It is assumed that the change of  $G$  with time may be due to three different processes:

1. flux  $\Phi(\partial\omega, t)$  of  $G$  across the boundary  $\partial\omega$ .
2. production  $P(\omega, t)$  of  $G$  within the volume.
3. supply  $S(\omega, t)$  of  $G$  within the volume.

The production  $P$  results from processes within the volume, while the supply  $S$  is acting from outside the volume, such that the whole volume becomes directly influenced (*Hutter and Jöhnk*, 2004). Conserved quantities are characterised by a vanishing production. Thus energy is conserved, while temperature is not. The balance of  $dG/dt$  within a volume  $\omega$  can be written as

$$\frac{d}{dt}G(\omega, t) = -\Phi(\partial\omega, t) + P(\omega, t) + S(\omega, t), \quad (2.1)$$

with positive fluxes defined as outflows from the volume (*Greve and Blatter*, 2009).

In order to reformulate Eq. (2.1) into its local form (Eulerian description), as we are interested in the local change of the quantity  $G$  over time, we express the quantity  $G$ , the production  $P$  and the supply  $S$  as volume integrals of corresponding densities  $g$ ,  $p$  and  $s$  respectively, such that

$$G(\omega, t) = \int_{\omega} g(\mathbf{x}, t) dv, \quad P(\omega, t) = \int_{\omega} p(\mathbf{x}, t) dv \quad \text{and} \quad S(\omega, t) = \int_{\omega} s(\mathbf{x}, t) dv,$$

with the position vector  $\mathbf{x} = (x, y, z)$ . The flux  $\Phi$  can be written as the surface integral of a flux density  $\phi$ , such that

$$\Phi(\partial\omega, t) = \oint_{\partial\omega} \phi(\mathbf{x}, t) \cdot \mathbf{n} da,$$

where  $\mathbf{n}$  is the unit normal vector of the surface and  $da$  is a scalar surface element. Inserting the integral expressions of the densities into Eq. (2.1) leads to the *general balance equation in integral form*. With the assumption that all fields are sufficiently smooth, the application of *Reynolds' transport theorem* (Eq. (A.1)) and the application of the *divergence theorem* (Eq. (A.2)), the *general balance equation in local form* can be written as

$$\frac{\partial g}{\partial t} + \text{div}(g\mathbf{u}) = -\text{div}(\phi) + p + s, \quad (2.2)$$

with the advective flux density  $g\mathbf{u}$ , given by the product of the quantity density  $g$  and the velocity field  $\mathbf{u}$ .

As stated above, Eq. (2.2) is only valid for parts of the volume where the fields are sufficiently smooth. This is usually not the case for the outer boundaries of the volume. For these outer boundaries special conditions apply, which are specified in Section 2.4.

In the following sections, the balance equations for mass, momentum and energy are derived. The derivation will be first conducted in a general form and then specified for the application to a thermomechanical glacier model. This is done as detailed as considered necessary for the given application. For further details refer to *Greve and Blatter* (2009) and *Hutter and Jöhnk* (2004).

### 2.1.1 Mass balance - Continuity equation

The balance equation for mass, the so called continuity equation, can be derived by letting the mass  $M$  be the arbitrary physical quantity  $G$ . The according mass density is  $\rho$ . The mass of a material volume can by definition not change. Therefore, there is no flux, production and supply of mass. With respect to the general balance equation (Eq. (2.2)), we thus find that  $g = \rho$ ,  $\phi = 0$ ,  $p = 0$ ,  $s = 0$ . With these densities the local balance equation for mass is given by

$$\frac{\partial \rho}{\partial t} + \text{div}(\rho\mathbf{u}) = 0 \quad (2.3)$$

The density of glacier ice  $\rho_i$  is dependent on the temperature  $T$  and the pressure  $p$  of the ice. Pure ice with no air or water inclusions has a density of  $\rho_i = 917 \text{ kg m}^{-3}$  at temperatures near  $0^\circ\text{C}$ . The densest polar ice with about  $\rho_i = 923 \text{ kg m}^{-3}$  can be found in mid-range depths where low temperatures and moderately high pressures prevail (*Cuffey and Paterson, 2010*). The highest value of  $\rho_i = 923 \text{ kg m}^{-3}$  presents only a 0.6% deviation from the lowest value of  $\rho_i = 917 \text{ kg m}^{-3}$ . Therefore it is an acceptable assumption to consider the ice as incompressible ( $\rho = \text{const.}$ ) and thus Eq. (2.3) becomes

$$\text{div}(\mathbf{u}) = 0, \quad (2.4)$$

which states that the velocity field  $\mathbf{u}$  is free of divergence.

### 2.1.2 Momentum balance - Momentum equation

The momentum balance equation can be derived from *Newton's second law*. The arbitrary physical quantity  $G$  is now the total momentum  $\mathbf{P}$ . The momentum is defined as the product of mass and velocity. The total momentum  $\mathbf{P}$  can be written as  $\mathbf{P}(\omega, t) = \int_{\omega} \rho \mathbf{u} dv$ , with the momentum density  $\rho \mathbf{u}$ . After *Newton's second law* the temporal change of the momentum  $\mathbf{P}$  is given by the sum of all forces  $\mathbf{F}$  acting on the volume  $\omega$ . These forces can be either external volume forces  $\mathbf{f}$  (such as gravitation or Coriolis force) acting on the volume element  $\omega$ , or surface forces (such as pressure, normal- or shear stresses)  $\boldsymbol{\sigma}_n$  acting on the element boundary  $\partial\omega$ . The surface force  $\boldsymbol{\sigma}_n$  depends on the orientation of the surface and must be a linear function of the normal vector  $\mathbf{n}$ , such that  $\boldsymbol{\sigma}_n = \boldsymbol{\sigma} \cdot \mathbf{n}$ , where  $\boldsymbol{\sigma}$  is a second-order tensor, the so called *Cauchy stress tensor*.

When comparing these terms to the general local balance equation (Eq. (2.2)), we find that  $g = \rho \mathbf{u}$ ,  $\phi = -\boldsymbol{\sigma}$ ,  $p = 0$ ,  $s = \mathbf{f}$  and thus for the momentum balance

$$\frac{\partial(\rho \mathbf{u})}{\partial t} + \text{div}(\rho \mathbf{u} \otimes \mathbf{u}) = \text{div}(\boldsymbol{\sigma}) + \mathbf{f}. \quad (2.5)$$

The ratio of inertial forces to viscous forces for given flow conditions can be expressed with the dimensionless Reynolds number  $Re$ . For slow flowing glacier ice with a high viscosity the Reynolds number has values of about  $Re \approx 10^{-10}$  (*Lliboutry, 1987*). The inertial forces, which are the terms on the left side of Eq. (2.5), can therefore be neglected and Eq. (2.5) simplifies to

$$\text{div}(\boldsymbol{\sigma}) + \mathbf{f} = 0. \quad (2.6)$$

In fluid dynamics it is common to split the *Cauchy stress tensor*  $\boldsymbol{\sigma}$  into a velocity dependent part, the deviatoric or viscous stress tensor  $\boldsymbol{\tau}$ , and a pressure dependent or hydrostatic part  $p\mathbf{I}$ , such that

$$\boldsymbol{\sigma} = \boldsymbol{\tau} - p\mathbf{I},$$

with the pressure  $p$  and the identity matrix  $\mathbf{I}$ . In incompressible materials, such as ice, only the deviatoric stress, the deviation of stress from the mean pressure acting in all directions, can result in strains. Thus, the deviatoric stress tensor  $\boldsymbol{\tau}$ , instead of the full stress tensor  $\boldsymbol{\sigma}$ , is related to strain rates, and thus the velocity field  $\mathbf{u}$ , via a constitutive relation, which is described in Section 2.2 (*Cuffey and Paterson, 2010*).

The volume force  $\mathbf{f}$  contains the force of gravity  $\mathbf{g}$ . Since the rotating Earth is a non-inertial system, the volume force  $\mathbf{f}$  also contains the centrifugal force and the Coriolis force. However, due to the very slow flow velocities of glacier ice the effect of the inertial

forces is very small, as shown above. Therefore, the Coriolis force can be neglected. The centrifugal and actual force of gravity can be combined to form the effective force of gravity  $\rho\mathbf{g}$ . The gravitational acceleration  $\mathbf{g}$  is a vector of the form  $\mathbf{g} = (0, 0, -g)$  with  $g = 9.81 \text{ m s}^{-2}$ .

The resulting equation is the Stokes equation

$$\text{div}(\boldsymbol{\tau} - p\mathbf{I}) = -\rho\mathbf{g} \quad (2.7)$$

and the flow it describes is called Stokes flow.

### Angular momentum balance

The angular momentum  $\mathbf{L}$  is defined as the cross product of the position vector  $\mathbf{x}$  and the momentum  $\mathbf{P}$ , such that  $\mathbf{L} = \mathbf{x} \times \mathbf{P}$ . When inserting this into the general balance equation Eq. (2.2) and evaluating (for more details refer to *Greve and Blatter (2009)*), the balance of angular momentum reduces to the statement that the Cauchy stress tensor  $\boldsymbol{\sigma}$  is symmetric, such that

$$\boldsymbol{\sigma} = \boldsymbol{\sigma}^T. \quad (2.8)$$

Boundary conditions for the angular momentum do not need to be imposed explicitly as they are the same as for momentum (see Section 2.4).

### 2.1.3 Energy balance - Heat transfer equation

The total relevant energy of the system consists of kinetic (mechanical) and internal (thermal) energy. The *first law of thermodynamics* states, that these energies are conserved together and not individually. Furthermore it states that the change of the total energy with time is given by the sum of the rate of work done by applied forces and the change of heat content per unit time. For an incompressible slow fluid flow, as glacier flow, the kinetic energy is not significant and therefore an internal energy equation is more appropriate (*Reddy and Gartling, 2010*). It has to be noted that the internal energy is not a conserved quantity as the production does not vanish (*Greve and Blatter, 2009*), only kinetic and internal energy together are conserved. The production term  $\psi$  is given by heat production due to internal friction and is thus related to the kinetic energy.

The internal energy  $E$  can be written as a volume integral, with the internal energy density  $\rho e$  as the product of density  $\rho$  and the specific internal energy  $e$ , such that  $E = \int_{\omega} \rho e \, dv$ . The flux density across the boundary is given by a heat flux  $\mathbf{q}$  and a supply is given by radiation  $\rho r$ .

When comparing now to the general local balance equation (Eq. (2.2)) we find that  $g = \rho e$ ,  $\boldsymbol{\phi} = \mathbf{q}$ ,  $p = \psi$ ,  $s = \rho r$ .

The local change of the internal energy  $E$  with time can thus be expressed as

$$\frac{\partial \rho e}{\partial t} + \text{div}(\rho e \mathbf{u}) = -\text{div}(\mathbf{q}) + \psi + \rho r \quad (2.9)$$

with the advective flux  $\rho e \mathbf{u}$  and the diffusive flux  $\mathbf{q}$ , the internal production  $\psi$  and the supply  $\rho r$ . In glacier ice the radiative heat supply  $\rho r$  can be neglected as it only reaches the uppermost centimetres (*Cuffey and Paterson, 2010*).

For an incompressible fluid the specific internal energy  $e$  is the product of the specific heat capacity  $c_p(T)$  (refer to Eq. (2.15)) and the temperature  $T$  (*Cuffey and Paterson, 2010*), such that

$$\frac{d\rho e}{dt} = \rho c_p(T) \frac{dT}{dt}. \quad (2.10)$$

The Fourier heat conduction law describes the diffusive flux  $\mathbf{q}$  as

$$\mathbf{q} = -\kappa(T) \text{grad } T \quad (2.11)$$

with the thermal conductivity  $\kappa(T)$  (refer to Eq. (2.14)). Now the heat transfer equation can be formulated such that

$$\rho c_p(T) \left( \frac{\partial T}{\partial t} + \mathbf{u} \text{grad } T \right) = \text{div}(\kappa(T) \text{grad } T) + \psi. \quad (2.12)$$

The internal heat source term  $\psi$  can consist of heat produced by ice deformation, firn compaction and freezing of water (*Cuffey and Paterson, 2010*). Since firn compaction and freezing of water occur mainly near the surface and we do not incorporate a firn model neither simulate temperature in an annual cycle, those two components are neglected and we only consider deformational heat. The deformational heat arises from the work done to accomplish the strain. It is defined by *Greve and Blatter (2009)* as

$$\psi = 4\mu\dot{\epsilon}_e^2 \quad (2.13)$$

with the viscosity  $\mu$  (refer to Eq. (2.24)) and the effective strain rate  $\dot{\epsilon}_e$  (refer to Eq. (2.21)).

### Thermal properties - Thermal conductivity $\kappa(T)$ and heat capacity $c_p(T)$

The thermal conductivity  $\kappa(T)$  for pure ice is temperature dependent and can be described with

$$\kappa(T) = 9.828 [\text{W m}^{-1} \text{K}^{-1}] e^{(-5.7 \times 10^{-3} T [\text{K}^{-1}])}. \quad (2.14)$$

Since glacier ice is mostly pure, this formula can be adapted. The thermal conductivity  $\kappa(T)$  increases with decreasing temperature (*Cuffey and Paterson, 2010*). For  $T = 273.15 \text{ K} = 0^\circ\text{C}$  this gives a value of  $\kappa = 2.07 \text{ W m}^{-1} \text{K}^{-1}$ .

The specific heat capacity  $c_p(T)$  does not depend on density and following *Cuffey and Paterson (2010)* is for glacier ice assumed to be

$$c_p(T) = 152.5 [\text{J kg}^{-1} \text{K}^{-1}] + 7.122 T [\text{J kg}^{-1} \text{K}^{-2}]. \quad (2.15)$$

Typical temperatures within the Antarctic Ice Sheet can range from about  $223.15 \text{ K} = -50^\circ\text{C}$  to  $273.15 \text{ K} = 0^\circ\text{C}$  and thus  $c_p(T)$  can vary about 17% (*Cuffey and Paterson, 2010*).

### Pressure melting point $T_{\text{pmp}}$ and homologous temperature $T'$

The melting temperature of ice is pressure dependent and therefore referred to as the pressure melting point  $T_{\text{pmp}}$ . For typical pressures in ice sheets ( $p \lesssim 50$  MPa) it is described by a linear relation

$$T_{\text{pmp}} = T_0 - \beta_c p, \quad (2.16)$$

with the melting point for low pressures ( $p \lesssim 100$  kPa)  $T_0 = 273.15$  K =  $0^\circ\text{C}$ , the Clausius-Clapeyron constant  $\beta_c$  and the pressure  $p$ . The Clausius-Clapeyron constant has a value of  $\beta_c = 9.8 \times 10^{-8}$  K Pa $^{-1}$  for air-saturated ice (*Hooke, 2005*). Thus under hydrostatic conditions the melting point is reduced by 0.87 K per km of ice thickness (*Greve and Blatter, 2009*).

The homologous temperature  $T'$  is defined as the temperature relative to the pressure melting point, such that

$$T' = T - T_{\text{pmp}} + T_0 = T + \beta_c p. \quad (2.17)$$

The homologous temperature  $T'$  for ice at the pressure melting point is thus always  $T' = 273.15$  K =  $0^\circ\text{C}$  (*Greve and Blatter, 2009*).

## 2.2 Constitutive relation - Rheology of ice

The constitutive relation describes the material behaviour of the body and is dependent on the material, while the balance equations are universally valid. The constitutive relation is usually set up from a combination of theory, laboratory experiments and field data (*Alley, 1992*). Depending on the strength and time scale of the applied stress ice responds with either creep (as a fluid, fluid mechanics) or fracture/elastically (as a solid body, fracture/solid mechanics). The constitutive relation for glacier ice thus depends on the focus of the study. In this study we focus on the flow dynamics and are hence only interested in the viscous creep behaviour of ice. Laboratory experiments with glacier ice led to creep curves that relate shear angles with time. For an applied stress this curve shows an initial instantaneous elastic deformation, followed by primary creep, where the shear rate decreases due to increasing geometric incompatibilities of the crystals. The next phase, the secondary creep, is characterised by a constant shear rate. In case of high temperatures and/or high stresses a tertiary creep phase can be seen, with a higher constant shear rate due to dynamic recrystallisation and therefore favourable deformation in the creep direction (*Greve and Blatter, 2009*). We describe in this section the bulk creep behaviour of isotropic polycrystalline ice, which is ice that consists of single ice crystals with varying size and orientation and has no preferred direction of deformation (*Cuffey and Paterson, 2010*), and is therefore characterised by the secondary creep phase described above.

### 2.2.1 Glen's flow law

The constitutive relation for a fluid is called rheology and acts as a closure relation to the balance equations above. It relates the deviatoric stresses to strain rates and for an isotropic fluid it can be written as

$$\boldsymbol{\tau} = 2\mu\dot{\boldsymbol{\epsilon}} \quad (2.18)$$

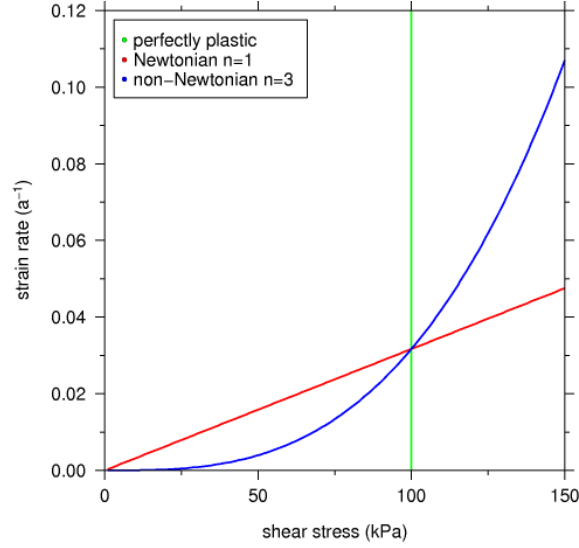


Figure 2.1: Stress-strain relationships. Figure modified from *Cuffey and Paterson* (2010).

with the viscosity  $\mu$  and the strain rate tensor  $\dot{\epsilon}$  in components

$$\dot{\epsilon}_{ij} = \frac{1}{2} \left( \frac{\partial u_i}{\partial x_j} + \frac{\partial u_j}{\partial x_i} \right)$$

in relation to Cartesian basis vectors.

If the viscosity  $\mu$  is a constant, such that the strain linearly depends on the stress, Eq. (2.18) describes a Newtonian fluid. For isotropic materials, as we assume glacier ice to be,  $\mu$  is a scalar, but not necessarily constant. For anisotropic materials  $\mu$  would be a fourth-order tensor.

For glacier ice, laboratory experiments have shown that under stresses important in normal glacier flow (50 to 150 kPa) strain is related to the dominant shear stress via a power law (*Glen*, 1955), such that

$$\dot{\epsilon} = \lambda \tau^n, \quad (2.19)$$

with the stress exponent  $n$ . This law is usually called *Glen's flow law*, as it was first suggested by *Glen* (1955). The value for  $n$  has a plausible range of 2 to 4 and is most commonly applied with  $n = 3$  (*Cuffey and Paterson*, 2010). For  $n = 1$  the ice would behave as a Newtonian fluid and for  $n \rightarrow \infty$  like a perfectly plastic material (*Nye*, 1957). Figure 2.1 shows stress-strain relations for perfectly plastic, Newtonian and non-Newtonian materials.

This flow law is commonly applied in the generalised form from *Nye* (1957)

$$\dot{\epsilon} = E A(T') \tau_e^{n-1} \tau, \quad (2.20)$$

with the enhancement factor  $E$  (detailed description in Section 2.2.3), the rate factor  $A(T')$  (detailed description in Section 2.2.2) and the effective stress  $\tau_e = \sqrt{\frac{1}{2} \text{tr}(\tau^2)}$ , the second invariant of the deviatoric stress tensor  $\tau$ .

To derive the inverse form of Eq. (2.20) the effective strain rate

$$\dot{\epsilon}_e = \sqrt{\frac{1}{2} \text{tr}(\dot{\epsilon}^2)} \quad (2.21)$$

is introduced, which is a scalar invariant of the strain rate tensor  $\dot{\epsilon}$ . By inserting Eq. (2.20) into Eq. (2.21), we derive

$$\dot{\epsilon}_e = E A(T') \tau_e^{n-1} \tau_e \Leftrightarrow \tau_e = [E A(T')]^{-1/n} \dot{\epsilon}_e^{1/n}. \quad (2.22)$$

If we consider now again Eq. (2.18) and (2.20), the viscosity  $\mu$  becomes

$$\mu = \frac{1}{2} \tau \dot{\epsilon}^{-1} = \frac{1}{2} \tau \tau^{-1} [E A(T')]^{-1} \tau_e^{1-n} \quad (2.23)$$

and can with Eq. (2.22) be written as

$$\mu(T', \dot{\epsilon}_e) = \frac{1}{2} [E A(T')]^{-1/n} \dot{\epsilon}_e^{\frac{1-n}{n}}. \quad (2.24)$$

Glacier ice has a high viscosity ( $\mu_{\text{ice}} \sim 1 \times 10^{13}$  Pa s at  $T' = 0^\circ\text{C}$  and  $\tau_e = 100$  kPa) compared to motor oil ( $\mu_{\text{oil}} = 0.1$  Pa s) and a low viscosity compared to the mantle of the Earth ( $\mu_{\text{earth}} \sim 1 \times 10^{21}$  Pa s) (*Greve and Blatter, 2009*).

### 2.2.2 Rate factor

The rate factor  $A$  parametrises the influence of the temperature and the pressure on the viscosity and therefore the flow behaviour. The rate factor  $A$  increases exponentially with ice temperature and the ice deforms much easier as it warms towards the pressure melting point  $T_{\text{pmp}}$ . The higher deformation rate with increasing temperatures is mainly due to the fact that creep processes are most effective when melting occurs at grain boundaries (*Benn and Evans, 2010*).

The rate factor can be described by the Arrhenius law (*Cuffey and Paterson, 2010*)

$$A(T, p) = A_0 e^{-(Q+pV)/RT} \quad (2.25)$$

with a pre-exponential constant  $A_0$ , an activation energy for creep  $Q$ , the pressure  $p$ , an activation volume  $V$ , the universal gas constant  $R = 8.314 \text{ J mol}^{-1} \text{ K}^{-1}$  and the temperature  $T$ .

For temperatures found in terrestrial ice, the value of  $A$  varies by a factor of  $10^3$  (*Cuffey and Paterson, 2010*). For the pressure dependence of  $A$ , measurements have shown that the effect on the rate factor  $A$  is accounted for satisfactorily if the absolute temperature  $T$  is replaced by the homologous temperature  $T'$  (refer to Eq. (2.17)) (*Greve and Blatter, 2009*). The rate factor  $A$  can now be written as

$$A(T, p) = A(T') = A_0 e^{-Q/RT'}. \quad (2.26)$$

*Paterson (1994)* finds that for temperatures  $T < 263.15 \text{ K} = -10^\circ\text{C}$  the temperature dependence of  $A$  is well described with constant values for  $A_0$  and  $Q$ . For temperatures above  $-10^\circ\text{C}$ , the ice softens more than would be predicted by the same values for  $A_0$  and  $Q$ . This might be due to grain-boundary sliding and the presence of liquid water on

the boundaries (*Barnes et al.*, 1971). To achieve a continuous function for  $A$  with a stress exponent  $n = 3$ , the suggested values for  $A_0$  and  $Q$  are

$$\begin{aligned} A_0 &= 3.985 \times 10^{-13} \text{ s}^{-1} \text{ Pa}^{-3}, & Q &= 60 \text{ kJ mol}^{-1} & \text{for } T' \leq 263.15 \text{ K} = -10^\circ\text{C}; \\ A_0 &= 1.916 \times 10^3 \text{ s}^{-1} \text{ Pa}^{-3}, & Q &= 139 \text{ kJ mol}^{-1} & \text{for } T' > 263.15 \text{ K} = -10^\circ\text{C}. \end{aligned}$$

An alternative description for the temperature dependence of  $A$  often used in ice flow modelling is given by *Hooke* (1981). For this study, we use the rate factor as suggested by *Paterson* (1994), because a comparison study shows that the parametrisation by *Hooke* (1981) can lead to unrealistic viscosity near the base (*Payne and Baldwin*, 2000).

The above stated relation has been established for ice below the pressure melting point, so called *cold ice*. *Temperate ice* is ice that is at pressure melting point  $T_{\text{pmp}}$ , and is in local equilibrium with its liquid phase (*Lliboutry*, 1971). *Duval* (1977) conducted creep experiments with ice samples at pressure melting for a maximal water content of 0.8%, and found a linear relation, the strain rate tripled when the water content passes from less than 0.01 to 0.8%. These findings lay the basis for the introduction of a water content dependent rate factor  $A_t$ . Following *Lliboutry and Duval* (1985), it can be chosen as

$$A_t(T, p, W) = A(T, p) \times (1 + 1.8125 W[\%]), \quad (2.27)$$

with  $W$  being the water content, valid for  $W < 1\%$ , being the rounded maximal value for the Duval relation ( $W < 0.8\%$ ). The water content can be explicitly calculated by solving for the inner energy instead as for the temperature  $T$  (*Aschwanden et al.*, 2012). Or the effect of the water content is approximated by assuming a water content of 1%, if the the temperature reaches the pressure melting point (e.g. *Kleiner and Humbert*, 2014). For temperatures  $< T_{\text{pmp}}$ , the rate factor for temperate ice  $A_t$  (Eq. 2.27) equals the rate factor for cold ice  $A(T, p)$  (Eq. (2.26)). If used this way in the ice flow model, the maximal impact of the water content onto the rate factor is simulated. A study of *Pettersson et al.* (2004) shows that the microscopic water content is generally  $< 3\%$ .

### 2.2.3 Enhancement factor

There are a variety of factors that can influence the creep rate of glacier ice and which are not captured by the rate factor  $A$  for cold ice. The creep rate can be influenced by the size and orientation of crystals, the so called *ice crystal fabric*, inclusions of impurities, surface rifts or crevasses and water content (*Budd and Jacka*, 1989).

The crystal c-axis orientation can lead to anisotropic behaviour, which is a preferred direction of deformation (e.g. *Gagliardini et al.*, 2009). On large scales the ice would appear softer in certain deformation directions. It is attempted to capture this effect by adjustment of the enhancement factor  $E$ . However, the introduction of  $E$  is somehow an admission to the failure of the isotropy assumption used to formulate Glen's flow law in the first place. So far no real empirical relation was established between temperature, strain rate, cumulative strain and the enhancement factor  $E$  (*Hooke*, 2005). A variety of laboratory experiments attempted to estimate values of  $E$  (e.g. *Jacka and Budd*, 1989; *Dierckx and Tison*, 2013), and result in a possible range  $E = [1, 10]$ . In general it can be said, the higher the value for  $E$ , the softer the ice. Since there are other factors possibly softening the ice, attempts were made to link these to a value for  $E$ . *Greve* (1997), for example, introduces an age dependent enhancement factor  $E$ , which parametrises the softening due to anisotropy and/or dust content. Also the large scale softening effect of

surface rifts and crevasses can be parametrised by variation of  $E$  (Pralong, 2005; Humbert, 2006).

The enhancement factor  $E$  thus can account for all factors influencing the rheology of the ice, that are not captured by the rate factor  $A$ . Cuffey and Paterson (2010) give a definition of  $E$  such that

$$E = \frac{\dot{\epsilon}_m}{\dot{\epsilon}}, \quad (2.28)$$

with a measured strain rate  $\dot{\epsilon}_m$  and a calculated strain rate  $\dot{\epsilon}$  (Eq. (2.20)).

The enhancement factor  $E$  can be seen in its origin as a somewhat physical parameter, but is often used more as a tuning parameter, as its influence on the ice rheology can be attributed to a variety of factors. Most commonly a value of  $E = 1$  is applied, but there are several studies in which it increases by a factor of up to  $10^3$  (e.g. Echelmeyer, 1987). Such high values obtained in field studies might be due to errors in stress and temperature estimates (Cuffey and Paterson, 2010). For shear margins in West Antarctic ice streams, a value as high as  $E = 12$  has been inferred (Echelmeyer et al., 1994).

## 2.3 Overview of equations

The formulation of the balance equations for mass, momentum and energy in addition with the constitutive relation give us a set of five equations to solve for the field quantities  $\mathbf{u}, p, T$  of our interest (Reddy and Gartling, 2010). Here, for a better overview, we explicitly list the equations solved for again.

### Continuity equation

$$\text{div}(\mathbf{u}) = 0,$$

### Momentum equation

$$\text{div}(2\mu\dot{\epsilon} - p\mathbf{I}) = -\rho\mathbf{g}$$

with

$$\mu = \frac{1}{2}[EA(T')^{-1/n}\dot{\epsilon}_e^{\frac{1-n}{n}}].$$

### Heat transfer equation

$$\rho c_p \left( \frac{\partial T}{\partial t} + \mathbf{u} \text{ grad } T \right) = \text{div}(\kappa \text{ grad } T) + 4\mu\dot{\epsilon}_e^2$$

## 2.4 Boundary conditions

The balance equations are defined under the assumption that the thermodynamic fields are sufficiently smooth, thus continuously differentiable. If this is not the case and a physical quantity experiences a discontinuity across a surface, it is called a *singular surface* (Hutter and Jöhnk, 2004). The boundaries of the glacier are singular surfaces and therefore additional jump conditions, also called boundary conditions, have to be formulated. A boundary condition can prescribe the derivative of the field quantity on the boundary and is then called a Neumann condition. If the value of the field quantity is known on the

boundary it can be prescribed directly and the according condition is called a Dirichlet condition. A so called Robin condition, also called *third type* condition, prescribes a linear combination of the field quantity value and its derivative. Boundary conditions are needed for the balance of mass, momentum and energy and are called kinematic, dynamic and thermodynamic boundary conditions, respectively. For a detailed derivation of the conditions refer to *Hutter and Jöhnk* (2004) and *Greve and Blatter* (2009). In the following description of the boundary conditions, we will show the position of the surfaces on a simplified geometry, which is used in the validation part (refer to Section 3.3.2). The surface described is highlighted in red.

### 2.4.1 Ice surface

The ice surface, highlighted in red in Figure 2.2, is a singular surface between the ice body and the atmosphere that can, in implicit form, be described by  $F_s(\mathbf{x}, t) = z - z_s = z - h(x, y, t) = 0$ . Since this also has to be valid with evolution in time, the time derivative can be written as

$$\frac{dF_s}{dt} = \frac{\partial F_s}{\partial t} + \mathbf{w} \cdot \text{grad} F_s. \quad (2.29)$$

The velocity vector  $\mathbf{w}$  hereby corresponds to the velocity of the singular surface, the so called displacement velocity. For the displacement of the surface only the normal components of the velocity are physically relevant (*Hutter and Jöhnk*, 2004). The surface mass balance  $a_s^\perp$  is defined as the difference of the displacement velocity  $\mathbf{w}$  and the ice velocity  $\mathbf{u}$  in normal direction to the surface

$$a_s^\perp = (\mathbf{w} - \mathbf{u}) \cdot \mathbf{n}. \quad (2.30)$$

With the unit normal vector of the surface defined as the normalised gradient  $\mathbf{n} = \text{grad} F_s / \|\text{grad} F_s\|$ , which points into the atmosphere, Eq. (2.29) can be written as

$$\frac{\partial F_s}{\partial t} + \mathbf{u} \cdot \text{grad} F_s = -a_s^\perp \|\text{grad} F_s\| = -a_s, \quad (2.31)$$

where  $a_s \geq 0$  means accumulation, while  $a_s < 0$  ablation. When inserting  $F_s(\mathbf{x}, t) = z - z_s$  into Eq. (2.31), the **kinematic boundary condition** for the ice surface can be written in Cartesian components as

$$\frac{\partial z_s}{\partial t} + u \frac{\partial z_s}{\partial x} + v \frac{\partial z_s}{\partial y} - w = a_s. \quad (2.32)$$

For the stationary case, when the surface does not evolve in time, Eq. (2.32) simplifies to

$$\mathbf{u} \cdot \mathbf{n} = -a_s^\perp. \quad (2.33)$$

The **dynamic boundary condition** for the surface can be derived by assuming that wind stress and atmospheric pressure are negligible compared to the typical stresses in the ice sheet. The surface can therefore be assumed to be traction free such that

$$\boldsymbol{\sigma} \cdot \mathbf{n} = 0. \quad (2.34)$$

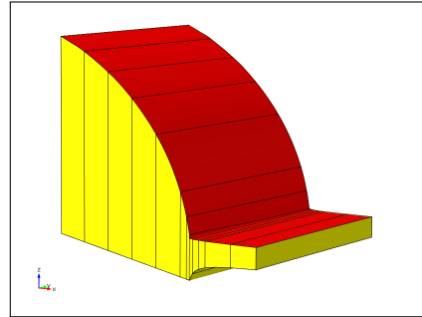


Figure 2.2: Ice surface

The **thermodynamic boundary condition** for the surface is given by a Dirichlet condition in prescribing the average annual surface temperature  $T_s(x, y, t)$ , such that

$$T = T_s(x, y, t). \quad (2.35)$$

### 2.4.2 Ice base

The **kinematic boundary condition** for the ice base singular surface  $F_b(\mathbf{x}, t) = z_b - b = b(x, y, t) - z = 0$  can be derived analogous to the surface kinematic boundary condition and leads to

$$\frac{\partial z_b}{\partial t} + u \frac{\partial z_b}{\partial x} + v \frac{\partial z_b}{\partial y} - w = a_b, \quad (2.36)$$

whereby the unit normal vector  $\mathbf{n}$  again points outwards from the ice, here into the bedrock or the sea water. To specify the rest of the boundary conditions for the base of the ice, it has to be distinguished between ice shelf areas, where the ice is freely floating on ocean water, highlighted in red in Figure 2.3, and grounded areas, where the ice is in contact with the bedrock below, highlighted in red in Figure 2.4.

#### Floating ice

For an ice shelf the basal mass balance  $a_b$  in the **kinematic boundary condition** can express melting ( $a_b \geq 0$ ) or freezing ( $a_b < 0$ ) processes.

The **dynamic boundary condition** for the base of ice shelf areas is based on the assumption that the shear stress induced by circulating sea water can be neglected (*Weis et al.*, 1999) and the only stress onto the ice is exerted by the water. As the shelf floats it is assumed to fulfil the floating condition and the stress applied equals the stress of the displaced water column (*Greve and Blatter*, 2009) such that

$$\boldsymbol{\sigma} \cdot \mathbf{n} = -\rho_{sw} g (z_{sl} - z_b) \cdot \mathbf{n} \quad (2.37)$$

with the density of sea water  $\rho_{sw}$  and the mean sea level  $z_{sl}$ . The density of sea water  $\rho_{sw}$  is temperature and salinity dependent and an average value of  $\rho_{sw} = 1028 \text{ kg m}^{-3}$  is chosen here.

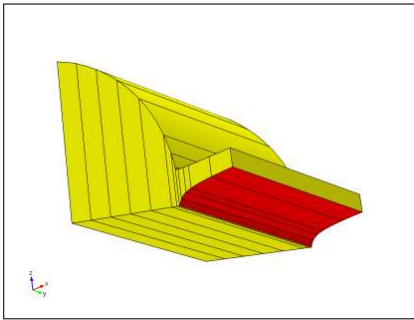


Figure 2.3: Ice base - floating

The **thermodynamic boundary condition** is given by either a Dirichlet condition in prescribing the freezing temperature of seawater  $T_{sw}$  or a Neumann condition by prescribing the oceanic heat flux  $q_{oc}$ . The freezing temperature of seawater  $T_{sw}$  is given by a weakly nonlinear function of salinity and a linear function of pressure (*Millero*, 1978) and for typical salinity and pressure values  $T_{sw} \approx 271.15 \text{ K} = -2^\circ\text{C}$ . The Dirichlet condition is given by

$$T = T_{sw}. \quad (2.38)$$

The oceanic heat flux  $q_{oc}$  is prescribed following *Holland and Jenkins* (1999) by

$$\text{grad } T \cdot \mathbf{n} \approx -\frac{\partial T}{\partial z} = \frac{\rho_{sw} c_p(T) \gamma (T - T_{pmp})}{\kappa(T)} \quad (2.39)$$

with the thermal exchange velocity  $\gamma \approx 10^{-4} \text{ m s}^{-1}$ .

### Grounded ice

In the grounded ice area, we assume that the ice base can not move into the bedrock and melting or refreezing is neglected. Therefore, the **kinematic boundary condition** with no ablation or accumulation becomes

$$\mathbf{u} \cdot \mathbf{n} = 0. \quad (2.40)$$

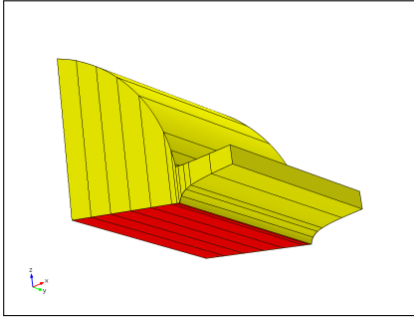


Figure 2.4: Ice base - grounded

For the **dynamic boundary condition** of the grounded ice, it is assumed that the stress vector  $\boldsymbol{\sigma} \cdot \mathbf{n}$  is continuous across the interface such that

$$\boldsymbol{\sigma} \cdot \mathbf{n} = \boldsymbol{\sigma}_{\text{lith}} \cdot \mathbf{n} \quad (2.41)$$

with the Cauchy stress tensor of the lithosphere  $\boldsymbol{\sigma}_{\text{lith}}$ . Since this tensor is not known, the condition is approximated by a *sliding law*. At this point only the basic idea of a sliding law is introduced. For further in depth discussion refer to Chapter 5. A commonly used sliding law, the so called *Weertman-type sliding law*, relates the basal sliding velocity  $\mathbf{u}_b$  to the basal drag  $\boldsymbol{\tau}_b$  and the basal normal stress  $N_b$

via a power law (refer to Section 1.2.2). The basal sliding velocity  $\mathbf{u}_b$  is defined as the horizontal velocity vector at the base, defined by

$$\mathbf{u}_b = \begin{pmatrix} u_b \\ v_b \end{pmatrix} = \begin{pmatrix} \mathbf{u} \cdot \mathbf{t}_x \\ \mathbf{u} \cdot \mathbf{t}_y \end{pmatrix} = \begin{pmatrix} u \cdot t_{x,x} + v \cdot t_{x,y} + w \cdot t_{x,z} \\ u \cdot t_{y,x} + v \cdot t_{y,y} + w \cdot t_{y,z} \end{pmatrix}$$

with the unit tangential vectors  $\mathbf{t}_x = (t_{x,x}, t_{x,y}, t_{x,z})$  in the xz-plane and  $\mathbf{t}_y = (t_{y,x}, t_{y,y}, t_{y,z})$  in the yz-plane. Together with the unit normal vector  $\mathbf{n}$ , the unit tangential vectors  $\mathbf{t}_x$  and  $\mathbf{t}_y$  form an orthonormal basis such that  $\mathbf{n} = \mathbf{t}_x \times \mathbf{t}_y$ . The basal drag vector  $\boldsymbol{\tau}_b$  is defined analogous to the basal sliding velocity vector  $\mathbf{u}_b$ , such that

$$\boldsymbol{\tau}_b = \begin{pmatrix} \tau_{b,x} \\ \tau_{b,y} \end{pmatrix} = \begin{pmatrix} (\boldsymbol{\sigma} \cdot \mathbf{n}) \cdot \mathbf{t}_x \\ (\boldsymbol{\sigma} \cdot \mathbf{n}) \cdot \mathbf{t}_y \end{pmatrix} = \begin{pmatrix} (\boldsymbol{\sigma} \cdot \mathbf{n})_x \cdot t_{x,x} + (\boldsymbol{\sigma} \cdot \mathbf{n})_y \cdot t_{x,y} + (\boldsymbol{\sigma} \cdot \mathbf{n})_z \cdot t_{x,z} \\ (\boldsymbol{\sigma} \cdot \mathbf{n})_x \cdot t_{y,x} + (\boldsymbol{\sigma} \cdot \mathbf{n})_y \cdot t_{y,y} + (\boldsymbol{\sigma} \cdot \mathbf{n})_z \cdot t_{y,z} \end{pmatrix}.$$

Now, a sliding law can be formulated (for a detailed derivation refer to Section 5.1), such that

$$\mathbf{u}_b = C_b |\boldsymbol{\tau}_b|^{p-1} N_b^{-q} f(T) \boldsymbol{\tau}_b, \quad (2.42)$$

whereby  $C_b$  is originally seen as a roughness parameter,  $p$  and  $q$  are basal sliding exponents,  $N_b$  is related to the basal normal stress, defined in Eq. (2.45), and  $f(T)$  a temperature function (refer to Eq. (2.46)) that determines if the ice is allowed to slide at all or if it is frozen to the ground. To simplify the inversion of Eq. (2.42), we define  $F_b = C_b |\boldsymbol{\tau}_b|^{p-1} N_b^{-q} f(T)$ . Thus Eq. (2.42) can be written as

$$\boldsymbol{\tau}_b = F_b^{-1} \mathbf{u}_b. \quad (2.43)$$

To connect the sliding law with the stress vector  $\boldsymbol{\sigma} \cdot \mathbf{n}$ , it needs to be separated into its normal and tangential components, such that

$$(\boldsymbol{\sigma} \cdot \mathbf{n}) \cdot \mathbf{t}_x = F_b^{-1} u_b, \quad (2.44a)$$

$$(\boldsymbol{\sigma} \cdot \mathbf{n}) \cdot \mathbf{t}_y = F_b^{-1} v_b, \quad (2.44b)$$

$$(\boldsymbol{\sigma} \cdot \mathbf{n}) \cdot \mathbf{n} = -N_b. \quad (2.44c)$$

The basal normal stress  $N_b$  is a vector of the form  $N_b = -N_b \mathbf{n}$  with

$$N_b = \begin{cases} \rho_i g H & \text{for } z_b \geq 0 \text{ m} \\ \rho_i g H + \rho_{sw} g z_b & \text{for } z_b < 0 \text{ m.} \end{cases} \quad (2.45)$$

Sliding can occur at temperatures below the pressure melting point, as found by *Fowler* (1986). Therefore, we chose a temperature function  $f(T)$  that reflects this mechanism. *Budd and Jenssen* (1987) suggest an exponential function for the temperature dependence of sliding by

$$f(T) = e^{\nu(T-T_{\text{pmp}})}, \quad (2.46)$$

with a tuning parameter  $\nu$  that was applied before with  $\nu = 0.1$  (more sliding for  $T < T_{\text{pmp}}$  (*Budd and Jenssen*, 1987)) and  $\nu = 1$  (less sliding for  $T < T_{\text{pmp}}$  (*Greve*, 2005)).

At the base of the grounded ice, the temperature is usually not available. Therefore, the **thermodynamic boundary condition** has to be formulated as a Neumann condition and the vertical temperature gradient is prescribed as

$$\text{grad } T \cdot \mathbf{n} \approx -\frac{\partial T}{\partial z} = \frac{q_{\text{geo}} + \mathbf{u}_b \cdot \boldsymbol{\tau}_b}{\kappa(T)} = \frac{q_{\text{geo}} + \sqrt{(u_b^2 + v_b^2)}(\tau_{b,x}^2 + \tau_{b,y}^2)}{\kappa(T)} \quad (2.47)$$

with the geothermal heat flux  $q_{\text{geo}}$  and the friction heating term  $\mathbf{u}_b \cdot \boldsymbol{\tau}_b$  *Pattyn* (2003). This condition is only valid as long as  $T \leq T_{\text{pmp}}$ . If the basal temperature  $T$  reaches the pressure melting point  $T_{\text{pmp}}$ , it has to be switched to a Dirichlet condition with

$$T = T_{\text{pmp}}. \quad (2.48)$$

### 2.4.3 Lateral boundaries - Ice divide, calving front and inflow

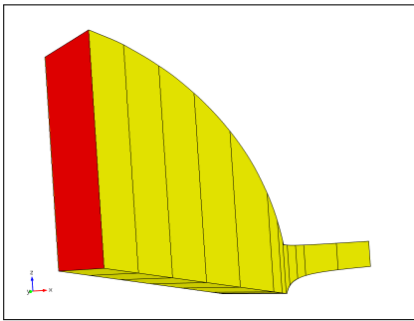


Figure 2.5: Ice divide

The model domain for Pine Island Glacier is chosen in a way that ice divides, a calving front and an inflow area are encountered lateral boundaries. Shear margins and outflow regions are further possible lateral boundaries. Here, we restrict our description to ice divides, the calving front and inflow.

The lateral boundaries of our model domain are fixed in space and thus there is no need to specify **kinematic boundary conditions** for them.

#### Ice divide

Ice divides are defined by a location that separates opposing flow directions of the ice. The surface slope and thus the driving stress vanishes. The ice divide can be seen as a mirror point where the direction of the driving stress and flow on one side of the divide opposes that of the

other side (*Cuffey and Paterson, 2010*). The lateral boundary coinciding with an ice divide is highlighted in red in Figure 2.5.

The **dynamic boundary condition** for the ice divide is given by

$$(\boldsymbol{\sigma} \cdot \mathbf{n}) \cdot \mathbf{t}_x = 0 \quad \text{and} \quad (\boldsymbol{\sigma} \cdot \mathbf{n}) \cdot \mathbf{t}_y = 0 \quad (2.49)$$

such that the tangential stresses vanish.

The **thermodynamic boundary condition** for the ice divide is based on the assumption that there is no temperature gradient across the divide. It can thus be written in form of a thermal insulation

$$(\kappa(T) \text{grad } T) \cdot \mathbf{n} = 0. \quad (2.50)$$

### Calving front

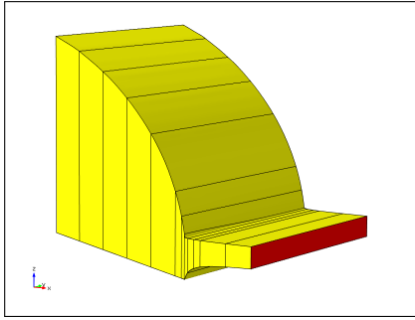


Figure 2.6: Calving front

The lateral boundary coinciding with the calving front is highlighted in red in Figure 2.6. The **dynamic boundary condition** can be derived similar to the one for the ice shelf base, such that

$$\boldsymbol{\sigma} \cdot \mathbf{n} = -p_{\text{sw}} \mathbf{n} \quad (2.51)$$

with the only difference, that the pressure from the water  $p_{\text{sw}}$  varies with depth and is defined as

$$p_{\text{sw}} = \begin{cases} 0 & \text{for } z \geq z_{\text{sl}} \\ \rho_{\text{sw}} g (z_{\text{sl}} - z) & \text{for } z < z_{\text{sl}} \end{cases} \quad (2.52)$$

The **thermodynamic boundary condition** for the calving front is given by thermal insulation as in Eq. (2.50).

### Inflow

The **dynamic boundary condition** is given as a Dirichlet condition by an inflow velocity field  $\mathbf{u}_{\text{SIA}} = (u_{\text{SIA}}, v_{\text{SIA}}, w_{\text{SIA}})$  defined with the *Shallow Ice Approximation* SIA (refer to Section 1.2.1). The horizontal velocity components  $u_{\text{SIA}}$  and  $v_{\text{SIA}}$  are given by

$$\begin{aligned} u_{\text{SIA}}(z) &= u_{\text{b,SIA}} - 2(\rho g)^n |\text{grad } z_{\text{s}}|^{n-1} \left( \frac{\partial z_{\text{s}}}{\partial x} \right) \int_{z_{\text{b}}}^z A(z_{\text{s}} - z)^n dz, \\ v_{\text{SIA}}(z) &= v_{\text{b,SIA}} - 2(\rho g)^n |\text{grad } z_{\text{s}}|^{n-1} \left( \frac{\partial z_{\text{s}}}{\partial y} \right) \int_{z_{\text{b}}}^z A(z_{\text{s}} - z)^n dz, \end{aligned} \quad (2.53)$$

with

$$|\text{grad } z_{\text{s}}| = \sqrt{\left( \frac{\partial z_{\text{s}}}{\partial x} \right)^2 + \left( \frac{\partial z_{\text{s}}}{\partial y} \right)^2}$$

and

$$\int_{z_{\text{b}}}^z A(z_{\text{s}} - z)^n dz = \frac{A}{n+1} ((z_{\text{s}} - z_{\text{b}})^{n+1} - (z_{\text{s}} - z)^{n+1}).$$

The basal velocity components  $u_{\text{b,SIA}}$  and  $v_{\text{b,SIA}}$  are assumed to be zero, as is the vertical velocity component  $w_{\text{SIA}}$ . The rate factor  $A$  is here taken as a constant value  $A = \text{const.} =$

1e – 25, which corresponds to a constant temperature  $T \sim -25^\circ \text{C}$  (Greve and Blatter, 2009).

The **thermodynamic boundary condition** for the inflow is given by a linear temperature profile

$$T_{\text{lin}} = \frac{T_{\text{pmp}} - T_{\text{s}}}{z_{\text{s}} - z_{\text{b}}}(z_{\text{s}} - z) + T_{\text{s}}. \quad (2.54)$$

## 2.5 Finite element method - FEM

The Finite Element Method (FEM) is a numerical method for finding approximate solutions to Partial Differential Equations (PDE). Numerical methods are for example needed when it is not possible to find an analytical solution to a problem, which is the case for the Navier-Stokes equations. Another commonly applied numerical method is the Finite Difference Method (FDM). Here we introduce the FEM, and when helpful for the understanding, highlight the difference to the FDM.

We introduce the FEM along a simple 1D problem, the 1D Poisson equation, which is an elliptic second-order PDE. The description in this section is based on Hughes (2000), Reddy and Gartling (2010) and Johnson (2009). We attempt to find a balance between mathematical elaboration and comprehensive description.

The 1D Poisson equation, defined on the domain  $\Omega = [0, 1]$  with the boundaries  $\partial\Omega = \{0, 1\}$ , is given by

$$f(x) = -\frac{\partial^2 u}{\partial x^2} \quad \text{on } \Omega, \quad (2.55)$$

with uniform Dirichlet boundary conditions

$$u = 0 \quad \text{on } \partial\Omega, \quad (2.56)$$

for which we aim to find a solution  $u$ .

Solving a PDE numerically requires partitioning of the domain  $\Omega$  into small units of a simple shape, the *mesh elements*. The process is called *discretization* or *meshing* of the domain, and is described in Section 2.5.1. On these *mesh elements* the physical field, in our example  $u$ , is approximated by simpler functions, the *approximation* or *basis functions*, described in Section 2.5.2. While the FDM is based on the original PDE, the FEM is based on a *weighted-integral form* of the PDE, which is introduced in Section 2.5.3. This is an important feature, giving the FEM higher flexibility in problem application. In Section 2.5.4 a few remarks about boundary conditions are made. The approximated fields need to be assembled into a global system of algebraic equations for the entire domain  $\Omega$ , described in Section 2.5.5. And finally, to obtain a solution, the assembled matrix, the so called *coefficient matrix*, needs to be solved, described in Section 2.5.6.

### 2.5.1 Meshing

Most numerical methods have in common, that the domain  $\Omega$ , on which the PDE is aimed to be solved, needs to be divided into small units of a simple shape, the so called *mesh elements*  $\Omega^e$ , with the element boundaries  $\partial\Omega^e$ . The entire mesh  $\Omega^h$  consists of the non-overlapping sum of all elements, such that

$$\Omega^h = \cup \Omega^e. \quad (2.57)$$

For complex geometries the mesh  $\Omega^h$  may not exactly equal the total domain  $\Omega$ .

In the FEM the *mesh elements*  $\Omega^e$  are not required to be equal sized and thus non-uniform meshes can be used. Additionally a variety of geometric shapes can be chosen. However, the choice of element shape is subject to certain conditions. For conforming elements, which are described here, neighbouring elements for example are required to share nodes. And the *approximation functions*, described in the next section, are required to be uniquely derivable for the elements. Still, a FEM mesh can conveniently be applied to complex geometries and refined in regions of interest, which could be regions with large gradients in the solution. An example of a FEM mesh is shown in Figure 2.7.

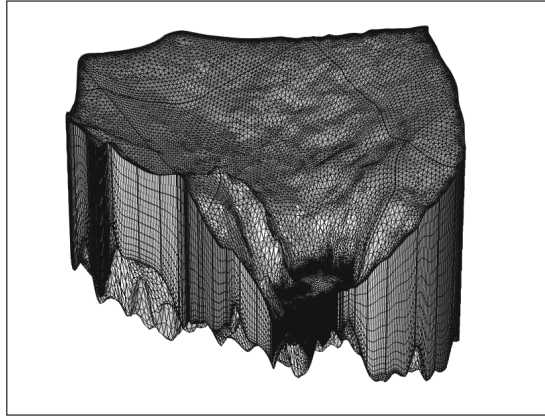


Figure 2.7: Example of a non-uniform FEM mesh on a complex geometry

In our 1D example we divide our domain  $\Omega = [0, 1]$  into two equal sized elements, which are described as mesh intervals  $0 < x < 0.5$  and  $0.5 < x < 1$ . The element or mesh nodes  $x_j$  are in this 1D example the boundaries of the elements, such that  $x_1 = 0$ ,  $x_2 = 0.5$  and  $x_3 = 1$ .

### 2.5.2 Approximation functions - Basis functions

To approach the solution  $u$  by an approximate solution  $\tilde{u}$  on the domain  $\Omega$ , we define *approximation functions*  $N_j$ , such that

$$u(x) \approx \tilde{u}(x) = \sum_{j=1}^n N_j(x) u^e(x_j), \quad (2.58)$$

where  $N_j$  are linearly independent functions, and  $u_j^e = u^e(x_j)$  the still unknown values of  $u$  at the mesh nodes  $x_j$ , which are discrete points in the domain. This is a so called *Galerkin approximation*.

The *approximation functions*  $N_j$  are also known as *basis functions*. When these functions are defined only over a reference element, and described in terms of element coordinates, which are local coordinates related to a uniform element shape, they are also called *shape functions*, because they assume one of a few basic shapes. In the subsequent description we will refer to the  $N_j$  as *basis functions*.

All *basis functions* are defined over the entire domain. The most common type are called *Lagrange basis functions* and required to be  $N_j = 1$  at node  $x_j$  and zero on all

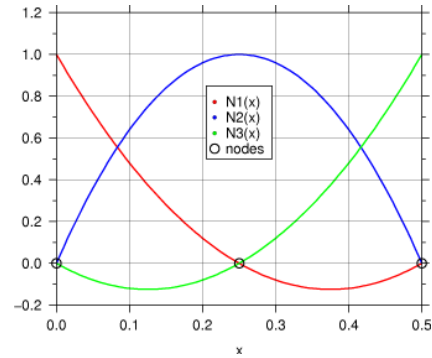
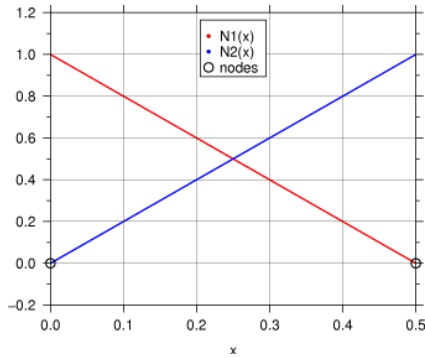


Figure 2.8: Linear basis functions  $N_1$  and  $N_2$  Figure 2.9: Quadratic basis functions  $N_1$ ,  $N_2$  and  $N_3$

other nodes. The quality of the solution depends on how well the *basis functions*  $N_j$  can approximate the solution of the PDE. The simplest conforming *basis functions* are linear and can be seen in Figure 2.8 over the first element  $0 < x < 0.5$ . Quadratic *basis functions* require another node in the middle of the 1D element and are shown in Figure 2.9 over the same element. The accuracy of the solution depends on the resolution of the underlying mesh and the choice of *basis functions*. A finer mesh results in more nodes on which the approximate solutions are found, while a higher order *basis function* leads to better approximation between the nodal values. It can be proven in a general form that the approximation error  $|u - \tilde{u}| \leq Ch^q$ , where  $u$  is the exact solution,  $\tilde{u}$  the discrete approximate solution,  $C$  a problem dependent constant,  $h$  the mesh size and  $q$  the polynomial order of the *Lagrange basis function*.

The phrase *finite element* refers to the geometry of the element plus the *shape functions* on the element. The mesh items alone are referred to as *mesh elements* or *cells*. Different choices of *shape functions* can define different types of *finite elements*. One type of *finite elements* are Lagrange elements, which are described here. Other *finite elements* are Bubble elements, Curl elements or Discontinuous elements, which are not described here in more detail.

### 2.5.3 Weighted-integral form

The method is based on a *weighted-integral form* of the PDE to be solved, given in Eq. (2.55). A *weighted-integral form* of a PDE can be obtained with the *variational formulation*. The resulting *weighted-integral statement* is equivalent to the governing PDE and sometimes referred to as the *global weak form*, which is different to the *weak form* of the *weighted-integral statement* and will be made clear below. The existence and uniqueness of the solution of the *weak form* can be shown with the Lax-Milgram theorem, but will not be further discussed here.

A *weight function*  $w_i$  is chosen, with which the original PDE (Eq. (2.55)) is multiplied on both sides, and integrated over the domain  $\Omega$ , such that for every choice of  $w_i$

$$\int_{\Omega} f w_i dx = \int_{\Omega} \left( -\frac{\partial^2 u}{\partial x^2} \right) w_i dx. \quad (2.59)$$

The *weight functions*  $w_i$  are also called *trial* or *test functions*.

Instead of the exact solution  $u$ , we now insert the approximate solution  $\tilde{u}$  into Eq. (2.59). The *basis functions*  $N_j$  need to be differentiable as many times as the solution  $u$ , that is twice in this example. This requires  $N_j$  to be a quadratic or higher-order polynomial. To reduce this continuity requirement, part of the differentiation can be moved from  $\tilde{u}$  to the *weight functions*  $w_i$ . This is done by applying integration by parts (Green-Gauss theorem, refer to Eq. A.3), together with the divergence theorem (Eq. A.2), such that

$$\int_{\Omega} f w_i dx = \int_{\Omega} \left( -\frac{\partial^2 \tilde{u}}{\partial x^2} w_i \right) dx = \int_{\Omega} \left( \frac{\partial w_i}{\partial x} \frac{\partial \tilde{u}}{\partial x} \right) dx - \oint_{\partial\Omega} w_i \frac{\partial \tilde{u}}{\partial n} da. \quad (2.60)$$

The result is the *weak form* of the *weighted-integral statement*, shown in *strong form* in Eq. (2.59). It is called *weak form* because the continuity requirement for the *basis functions*  $N_j$  is weakened. The *weighted-integral statement* can be constructed for any differential equation, while the *weak form* exists for any second- and higher-order equation.

With formulation of the *weighted-integral statement* the difference between the FEM and the FDM becomes relevant. The FDM is based on the original PDE. This requires a solution that satisfies the PDE point wise. The *weighted-integral form*, which the FEM is based on, requires a solution that satisfies the PDE in an integral sense and thus removes some of the high smoothness requirements.

A variety of different finite element methods exist. The *Galerkin finite element method* generally describes the procedure of discretising the domain, formulating *basis functions*, deriving a *weighted-integral statement* and solving for the fields. When additionally the *weak form* is derived, it is referred to as the *weak-form Galerkin finite element method*. Another distinction is made by the choice of the *weight functions*  $w_i$ . If  $w_i(x) = N_i(x)$  the solution method is referred to as the *Bubnov-Galerkin method*. If  $w_i(x) \neq N_i(x)$  the solution method is referred to as the *Petrov-Galerkin method*.

#### 2.5.4 Boundary conditions

The boundary integral in Eq. (2.60) is looked at here. The nodal unknowns  $u_j^e$  need to satisfy the Dirichlet boundary conditions, while the *weight functions*  $w_i$  need to be zero where Dirichlet boundary conditions are imposed. If we consider our 1D example, the boundary integral vanishes, since we have Dirichlet conditions on both boundaries and thus  $w_i = 0$  on  $\partial\Omega$ . It follows that Eq. (2.60) simplifies to

$$\int_{\Omega} f w_i dx = \int_{\Omega} \left( \frac{\partial w_i}{\partial x} \frac{\partial \tilde{u}}{\partial x} \right) dx. \quad (2.61)$$

A Dirichlet boundary condition, when the value of the solution  $u$  is prescribed directly, is also called *essential boundary condition*, while a Neumann condition is also called *natural boundary condition*.

#### 2.5.5 Assembly

With the approximate solution  $\tilde{u}$  in the *weak form* given in Eq. (2.61) we get

$$\int_{\Omega} \left( \frac{\partial w_i}{\partial x} \left( \sum_{j=1}^n u_j^e \frac{\partial N_j}{\partial x} \right) \right) = \int_{\Omega} f w_i dx. \quad (2.62)$$

Every choice of the *weight functions*  $w_i$  gives an algebraic relation between the nodal unknowns  $u_j$ . Thus  $m$  linearly independent choices of  $w_i$  lead to  $m$  linearly independent algebraic equations. Here we describe the *Bubnov-Galerkin method* with  $w_i(x) = N_i(x)$  and can therefore write

$$\sum_{j=1}^n \int_{\Omega} \left( \frac{\partial N_i}{\partial x} \frac{\partial N_j}{\partial x} \right) u_j^e = \int_{\Omega} f N_i \, dx. \quad (2.63)$$

Eq. (2.63) represents a system of  $n$  equations for  $n$  unknowns and can be written in matrix form. To do so we define

$$\sum_{j=1}^n K_{i,j} u_j^e = F_i \quad (2.64)$$

with

$$K_{i,j} = \int_{\Omega} \frac{\partial N_i}{\partial x} \frac{\partial N_j}{\partial x} \, dx \quad (2.65)$$

and

$$F_i = \int_{\Omega} f N_i \, dx \quad (2.66)$$

$K_{i,j}$  are the single entries of the *coefficient matrix*  $\mathbf{K}$  and  $F_i$  the single entries of the *force vector*  $\mathbf{F}$ . With the elements  $u_j^e$  of the *solution vector*  $\mathbf{u}$ , the matrix form can be written as

$$\mathbf{K}\mathbf{u} = \mathbf{F}. \quad (2.67)$$

The nodal unknowns  $u_j^e$  and the Dirichlet boundary conditions are the entries in the *solution vector*  $\mathbf{u}$ , while the Neumann boundary conditions are included in the *force vector*  $\mathbf{F}$ .

When assembling the *coefficient matrix*  $\mathbf{K}$ , continuity of the nodal unknowns  $u_j^e$  and balance of the derivatives on neighbouring elements have to be considered.

The number of entries  $n$  in the *solution vector*  $\mathbf{u}$  are the so called *Degrees Of Freedom* (DOF).

### 2.5.6 Solution

This system of linear algebraic equations given in Eq. (2.67) now needs to be solved for  $\mathbf{u}$ , such that

$$\mathbf{u} = \mathbf{K}^{-1}\mathbf{F}. \quad (2.68)$$

Most of the entries in the *coefficient matrix*  $K_{i,j}$  are zero, as the *basis* and *weight functions*  $N_i$  are defined to only be  $\neq 0$  on single nodes and its surroundings, as shown in Section 2.5.2. Thus, depending on the choice of  $N_i$ , the *coefficient matrix*  $\mathbf{K}$  can be a sparse matrix, whose non-zero entries are confined to the main diagonal, or some more diagonals on either side.

The *coefficient matrix*  $\mathbf{K}$  may be either symmetric, as in this example, or unsymmetric, depending on the underlying PDE. When considering bigger matrices that have to be solved computationally, the above mentioned characteristics of the *coefficient matrix*  $\mathbf{K}$  are very important for choosing an appropriate matrix solution procedure. The solution can be found by either a direct or iterative method. Direct methods, based on the Gauss

elimination technique, provide the solution after a fixed number of steps and are less sensitive to the conditioning of the *coefficient matrix*  $\mathbf{K}$ , but they are not practical for large numbers of DOFs due to high computational cost. Iterative methods do not need to form the global matrix as in the direct method and are therefore computationally cheaper and can more easily be parallelized, but they are more difficult to apply if the system is not well-conditioned.



## Chapter 3

# The 3D full-Stokes model for Pine Island Glacier

In this chapter the 3D full-Stokes model for Pine Island Glacier is introduced. This is begun with a data description in Section 3.1. The model implementation in the FEM software COMSOL Multiphysics<sup>©</sup> is described in Section 3.2. The verification and validation of the model is shown in Section 3.3.

In the following chapters all plots of the model region of Pine Island Glacier are according to the red box in Figure 3.1, which shows the location on Antarctica.

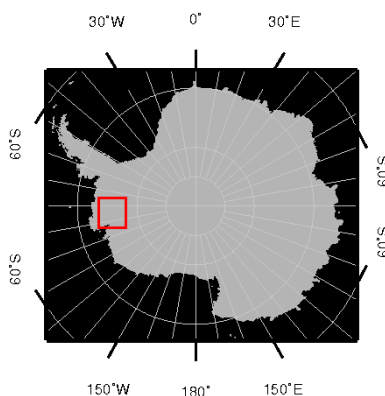


Figure 3.1: Location of following plots on Antarctica

### 3.1 Data

The geometric data to build the model, the forcing data and the evaluation data are shown in this section. All the data sets are shown in polar stereographic projections, with the outer boundary of the model domain, as shown in Figure 3.2. The outer boundary in the grounded area is defined by the ice divide and an inflow area, marked in blue and green in Figure 3.2, respectively. The outer boundary in the floating area is defined by the calving front, marked in yellow in Figure 3.2. The grounding line location, marked in red, will be discussed in more detail in Section 3.1.2.

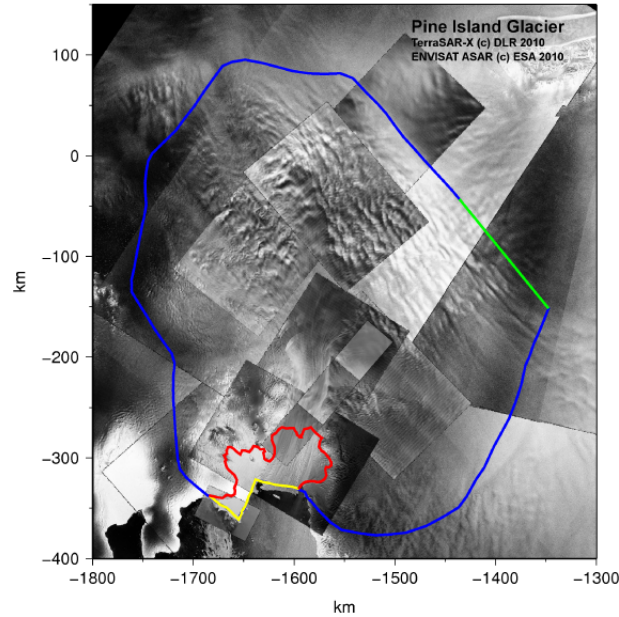


Figure 3.2: Model domain of Pine Island Glacier on a mosaic of satellite images

### 3.1.1 Ice geometry

The surface elevation data is taken from *Bamber et al. (2009)* and combines satellite radar and laser measurements. It is provided on a 1 km grid. The ice thickness data is from *Vaughan et al. (2006)*. Radio Echo Sounding (RES) measurements for the ice thickness were carried out in the austral summer 2004/05, but for the 5 km gridded data set older measurements were included as well. For the bathymetry outside the ice shelf area the data from *Nitsche et al. (2007)* is used. The bathymetry under the ice shelf was measured with the Autonomous Underwater Vehicle (AUV) Autosub3 in late January 2009 and is described in *Jenkins et al. (2010)*. They discovered a ridge below the ice shelf, which was incorporated into a bathymetric data set by *Timmermann et al. (2010)*.

Based on the above described data sets Anne Le Brocq created a new consistent set of surface elevation, ice thickness and bed topography on a 1 km grid, which was kindly provided by her for this work. The surface elevation together with the model domain is shown in Figure 3.3, and the bed topography with the model domain in Figure 3.4. For consistency the floatation condition is exactly fulfilled at the grounding line. The grounding line position is described in Section 3.1.2.

To create this data set Le Brocq calculated the thickness of the ice shelf with the surface Digital Elevation Model (DEM) and the floatation condition by assuming an ice density  $\rho_i$  of  $918 \text{ kg m}^{-3}$ , an ocean density  $\rho_{sw}$  of  $1028 \text{ kg m}^{-3}$  and a firm correction of 15.2 m. The so calculated ice shelf thickness and the grounded ice thickness do not match across the grounding line and were therefore interpolated within a certain margin in the shelf and finally smoothed on the grounded part. The ice thickness data of the grounded ice was solely interpolated onto a 1 km grid and therefore does not provide a better representation of the field than the original 5 km grid.

For the bed topography under the grounded ice Le Brocq used the surface DEM and subtracted the modified ice thickness. Under the ice shelf the area around the ridge is

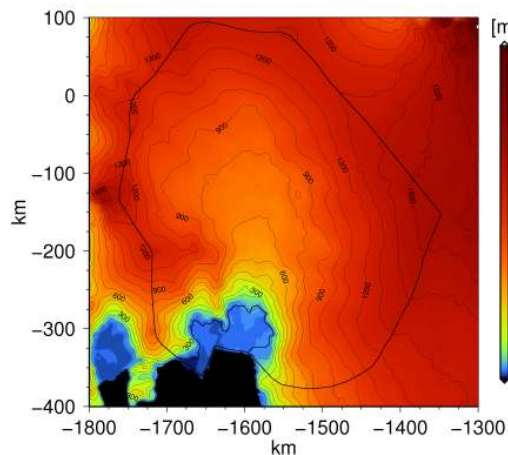


Figure 3.3: Surface elevation

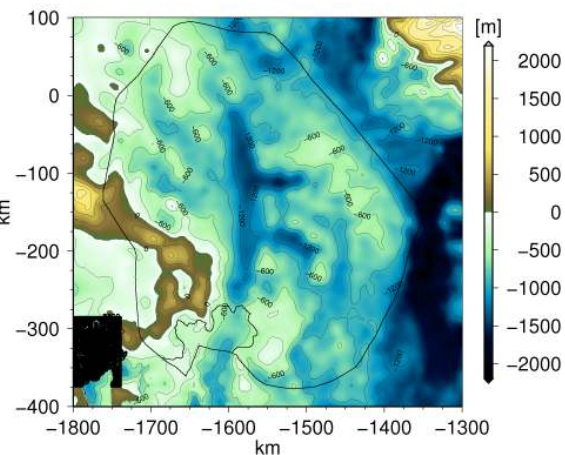


Figure 3.4: Bed topography

incorporated from *Timmermann et al.* (2010) and the rest is interpolated, but still making sure no unrealistic shallow areas develop where the ice shelf would ground.

This data set finally represents the thickness distribution of Pine Island Glacier for the year 2005 and earlier. A lot of new thickness measurements have been conducted in the area during the Ice Bridge Campaign in the years 2009, 2010 and 2011. This thickness data is not yet incorporated.

### 3.1.2 Grounding line position

The GROUNDING LINE (GRL) position used in the diagnostic model is given by a combination of the positions in the MODIS (MODerate-resolution Imaging Spectroradiometer) Mosaic Of Antarctica (MOA) (*Bohlander and Scambos*, 2007) (corresponding to the years 2003/2004), the position in *Rignot* (1998) (corresponding to 1996) and the position that gives the smoothest ice thickness join of the procedure described above, all shown in Figure 3.5. This combination was chosen because there is no single source to describe the location best. Though the MOA grounding line position corresponds to the years 2003/2004, it shows unrealistic retreat in the central trough area, as shown in red in Figure 3.5. For the central trough area grounding line location estimates exist for the years 1992, 1994, 1996 (yellow in Figure 3.5) (all *Rignot*, 1998), 2000 (*Rignot*, 2002), 2003/2004 (red in Figure 3.5) (*Bohlander and Scambos*, 2007), 2007 (*Rignot*, 2008) and 2009 (blue in Figure 3.5) (*Joughin et al.*, 2010). The procedures to derive these positions differ in their accuracy.

The 1992 and 1994 positions were determined with InSAR (Interferometric Synthetic Aperture Radar) from the ERS-1 (European Remote Sensing) Satellite. The repeat periods between the acquisitions for 1992 and 1994 are 6 and 3 days respectively (*Rignot*, 1998). The 1996 and 2000 positions were determined with InSAR using the ERS tandem acquisitions, with a repeat period of 1 day. The ERS tandem mission ended in 2000 and with this for the time being the ability to measure grounding-line positions on Pine Island Glacier in high accuracy, as the repeat periods of other radar satellites were much too large. A too large repeat period ( $\gg 1$  day) produces interferometric phases that are too

aliased to measure tidal flexing, and thus grounding line position (*Joughin et al.*, 2010, Auxiliary Material). The 2003/2004 positions were hand-digitised from the MODIS Mosaic of Antarctica (MOA) image map (*Bohlander and Scambos*, 2007). For 2007 *Rignot* (2008) also used MODIS images to infer an approximate location, which was not confirmed with InSAR. Those image based locations are subject to considerable ambiguity and thus should be considered with care. The 2009 position was derived by *Joughin et al.* (2010) with speckle-tracked range offsets from TerraSAR-X images in 0.9 m resolution (*Joughin et al.*, 2010, Auxiliary Material).

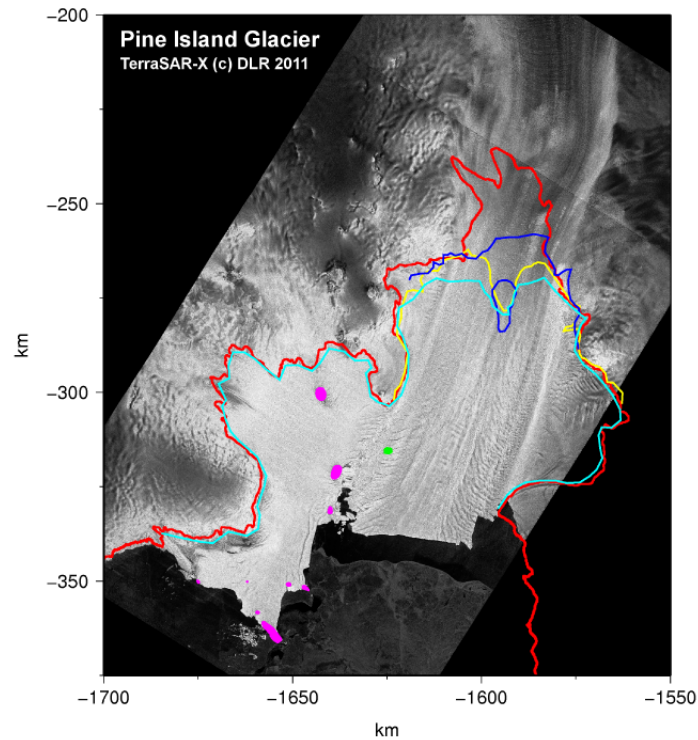


Figure 3.5: Grounding line positions for the years 1996 (yellow), 2003/2004 (red), 2009 (blue), as used in the model (cyan) and ice rise locations, of ones that still exist (purple) and already ungrounded (green).

### 3.1.3 Ice rises

The shape of the ice shelf of Pine Island Glacier is defined by the location of ice rises pinning the shelf. Due to ice shelf thinning it lost contact to a few ice rises over the past years. The location of the ice rises pinning the ice shelf at present are detected from a TerraSAR-X image from 2011, with assistance of interferograms from *Rignot* (2002). The locations are shown in purple in Figure 3.5. The location of an ice rise that disappeared sometime after 2004, shown in green in Figure 3.5, was detected from the MODIS MOA (<http://nsidc.org/data/nsidc-0280.html>). The images for MOA in the Pine Island Glacier region were collected around February 2004.

The onset of a rifted area downstream of the ice rise was associated with the location of this ice rise as early as 1973 (*Bindschadler*, 2002). Sometime between 1991 and 1997 the rifting started also upstream of the ice rise, associated with the grounding line location.

The two rifted regions eventually merged and the ice shelf was not grounded on the ice rise any longer.

### 3.1.4 Surface temperature

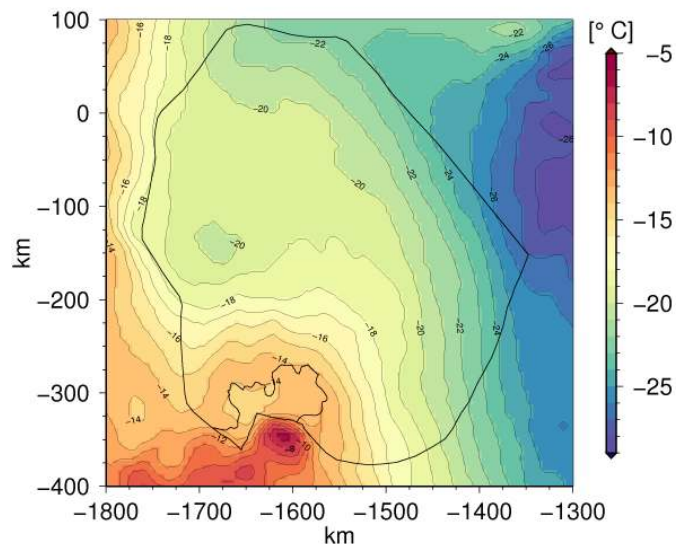


Figure 3.6: Surface temperature  $T_{s,obs}$

The data set used here is on a 5 km grid compiled by *Le Brocq et al.* (2010) (ALBMAP v1), based on the temperature data described in *Comiso* (2000). The surface temperature is estimated from Advanced Very High Resolution Radiometer (AVHRR) infrared data. Annual mean temperatures from 1982 to 2004 were averaged for the temperature field shown in Figure 3.6 (*Le Brocq et al.*, 2010). The annual mean temperature shows no temperatures near the melting point, but in the annual cycle surface melting is occasionally present in the lower regions and on the ice shelf. The lowest temperatures are found on the highest elevated surface and increase towards the shelf, where the high heat capacity of the ocean water lead to the lowest annual temperatures.

### 3.1.5 Geothermal heat flux

The geothermal heat flux  $q_{geo}$  varies spatially because it depends on local geologic conditions such as the tectonic history of the crust, heat production within the crust due to decay of radioactive isotopes and the mantle heat flux. The global average heat flux is estimated to be about  $0.06 \text{ W m}^{-2}$  and is enough to melt 6 mm of ice at its pressure melting point each year (*Cuffey and Paterson*, 2010). Due to the distinct geologic history of West and East Antarctica (refer to Section 1.1.1), the geothermal heat flux in West Antarctica is expected to be nearly three times higher than in East Antarctica and much more variable (*Shapiro and Ritzwoller*, 2004). Therefore especially in West Antarctica the geothermal heat flux is an important component when modelling ice dynamics. The

distribution of the field can have a significant influence on where fast flowing areas will be located, as high heat flux can cause subglacial melting and thus lubrication of the base. Studies have shown that the geothermal heat flux can vary strongly on scales smaller than 100 km (*Dahl-Jensen et al., 2003*). Direct measurements of geothermal heat flux in ice-covered areas are hard to obtain, as they require drilling to the bedrock. Another complication is the possible existence of other heat sources such as deformational heat, frictional heat at the base, advected heat or latent heat from melting processes. The measured values have thus to be carefully analysed and measurement locations with small or no basal velocities are preferable (*Kleiner, 2010; Cuffey and Paterson, 2010*). So far only a few direct measurements under ice sheets have been conducted (e.g. *Engelhardt (2004)* in Antarctica).

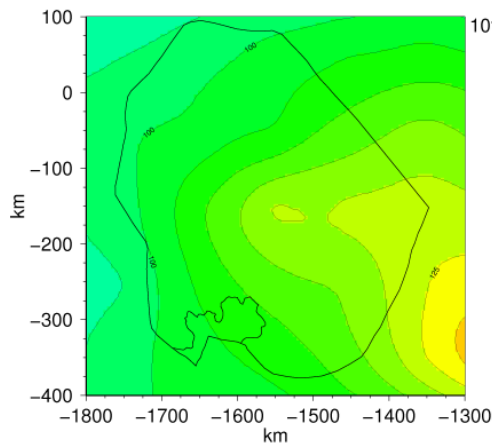


Figure 3.7:  $q_{geo}$  Shapiro 2004

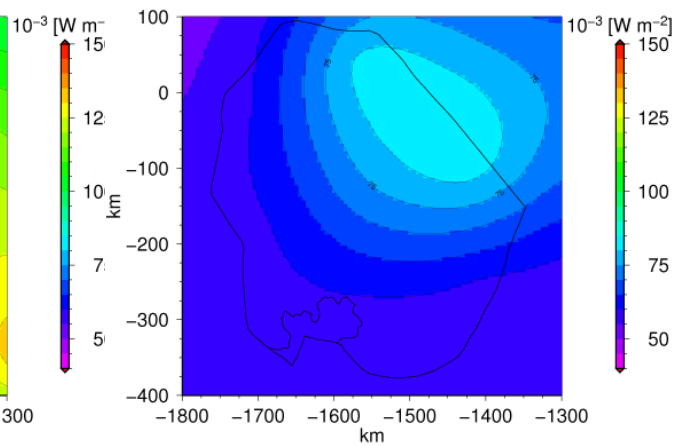


Figure 3.8:  $q_{geo}$  Fox Maule 2005

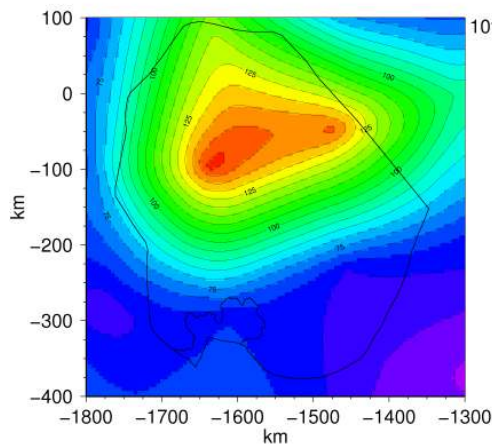


Figure 3.9:  $q_{geo}$  Purucker 2012

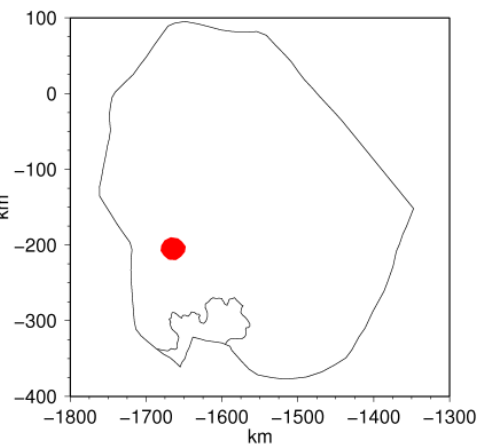


Figure 3.10: Location of volcanic center

Because the geothermal heat flux in ice-covered regions is difficult to measure directly, extrapolation techniques have been developed. The method from *Shapiro and Ritzwoller* (2004) uses a global seismic model of the crust and upper mantle to find structural similarities. This is possible because the vertical seismic velocity gradient is related to the temperature gradient and thus the heat flux. The resulting similarities are used to extrapolate the directly measured heat flux values (*Pollack et al.*, 1993) to regions with no direct measurements, for example below the Antarctic Ice Sheet. The resulting distribution for the field around Pine Island Glacier is shown in Figure 3.7.

A different method, developed by *Fox Maule et al.* (2005), uses the Earth’s magnetic field to extrapolate measured values. This is possible because the magnetic properties of rocks are temperature dependent up to the Curie temperature  $T_C$ , above which materials lose their ability to sustain a magnetic field. The Curie temperature  $T_C$  is about 580 °C for low-Ti magnetite, which is believed to be the dominant source of crustal magnetic anomalies (*Langel and Hinze*, 1998). *Fox Maule et al.* (2005) use Satellite Magnetic Data in combination with a thermal model of the crust to derive geothermal heat flux values for the Antarctic continent. Figure 3.8 shows  $q_{geo}$  around Pine Island Glacier from the original study from 2005 (*Fox Maule et al.*, 2005). Figure 3.9 shows the values from an updated version of the same method from 2012 (updated version of *Fox Maule et al.*, 2005), later referred to as Purucker 2012. The differences in the data sets are clearly visible and emphasise the difficulty to derive a good estimate for the geothermal heat flux below the Antarctic Ice Sheet.

Another important point when considering the geothermal heat flux in the Pine Island area is the existence of a subglacial volcano very close to its fast streaming central trough area (*Corr and Vaughan*, 2008), that is likely to have erupted at  $207\text{BC} \pm 240\text{a}$ . The approximate location of its eruptive center is shown in Figure 3.10. *Corr and Vaughan* (2008) called this volcano the Hudson Mountains Subglacial Volcano (HMSV). They state the possibility that high geothermal heat flux may exist above HMSV today, delivering subglacial water to Pine Island Glacier. It is thus possible that volcanic activity in the area contributed to recent velocity changes at Pine Island Glacier. None of the above shown data sets includes an elevated heat flux around the location of the volcano. The elevated heat fluxes on volcanic centres have been estimated to be as high as  $7\text{ W m}^{-2}$  on Mount Wrangell, Alaska (*Clarke et al.*, 1989), and as high as  $50\text{ W m}^{-2}$  on Vatnajökull, Iceland (*Björnsson*, 1988). Elevated heat fluxes can cause surface depressions in the ice (*Blankenship et al.*, 1993), which is not observed over HMSV. This might be due to the fact that HMSV is located beneath an ice divide and can not be taken as evidence that no high geothermal heat flux exists here (*Corr and Vaughan*, 2008).

### 3.1.6 Surface velocity

The surface velocity vector field  $\mathbf{u}_{\text{obs}}$  consists of the two horizontal velocity components  $u_{\text{obs}}$  and  $v_{\text{obs}}$ , such that  $\mathbf{u}_{\text{obs}} = (u_{\text{obs}}, v_{\text{obs}})$ . Only the horizontal velocity components can be measured with InSAR data, which is the technique used for the velocity field by *Rignot et al.* (2011), which is used throughout this work to validate the model with. The surface velocity data set from *Rignot et al.* (2011) can be seen in Figure 3.11.

The surface velocity field of Pine Island Glacier is characterised by several tributaries feeding the central ice stream. A non-uniform colour scale is chosen to show the whole range of velocities adequately. The data is derived from InSAR data acquired during the

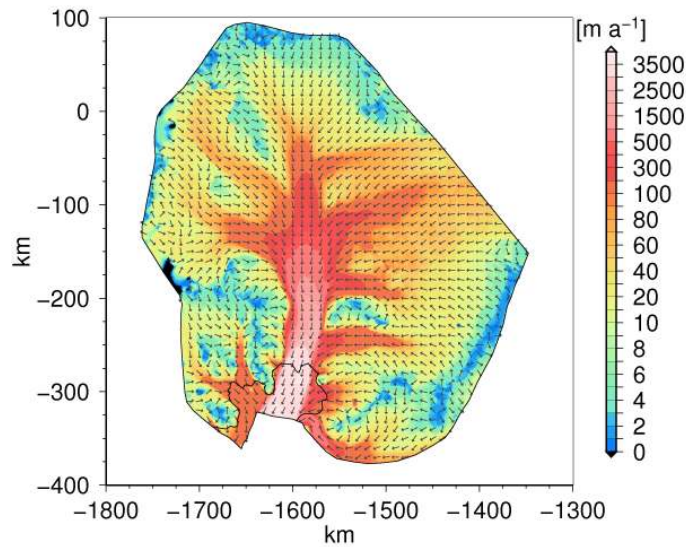


Figure 3.11: Surface Velocity  $|\mathbf{u}_{\text{obs}}|$  with normed vector field  $\mathbf{u}_{\text{obs}}$

years 2007 to 2009. The area, where the outer boundary does not coincide with the ice divide but an inflow, can be seen.

The main flow direction in the central trough is towards the west, where the ice shelf is located. To the north of the ice shelf two smaller ice streams, and to the south one small and fast stream, can be seen.

## 3.2 Implementation

The 3D full-Stokes model for the flow of Pine Island Glacier is set up with the commercial Finite Element Method software COMSOL Multiphysics<sup>©</sup>. The FEM is a numerical technique (for details refer to Section 2.5) for finding approximate solutions to partial differential equations, which form the basis for most physical laws. COMSOL provides an environment where complex 3D FEM models can be created without the need for an in-depth knowledge of mathematics or numerical analysis. On the other hand, because it is a commercial software, it is not possible to access the actual source code.

The application of COMSOL Multiphysics<sup>©</sup> for ice dynamic simulations will be referred to as the model *COMice* in the subsequent description.

To set up a model with COMSOL a Graphical User Interface (GUI) is provided, a screenshot of which is shown in Figure 3.12. This is very convenient to start of with and try new settings, but not needed any longer once the model is set up and running. Additionally, with the so called COMSOL LiveLink for MATLAB, it is possible to use script programming in Java (COMSOL API (Application Programming Interface) Java) or the MATLAB language, to set up and modify a model. To solve the model COMSOL internally compiles a set of equations representing the entire model.

The following GUI description is based on COMSOL version 4.3a. The COMSOL GUI consists primarily of the *Model Builder*, *Node Settings*, and *Graphics* windows. The *Model*

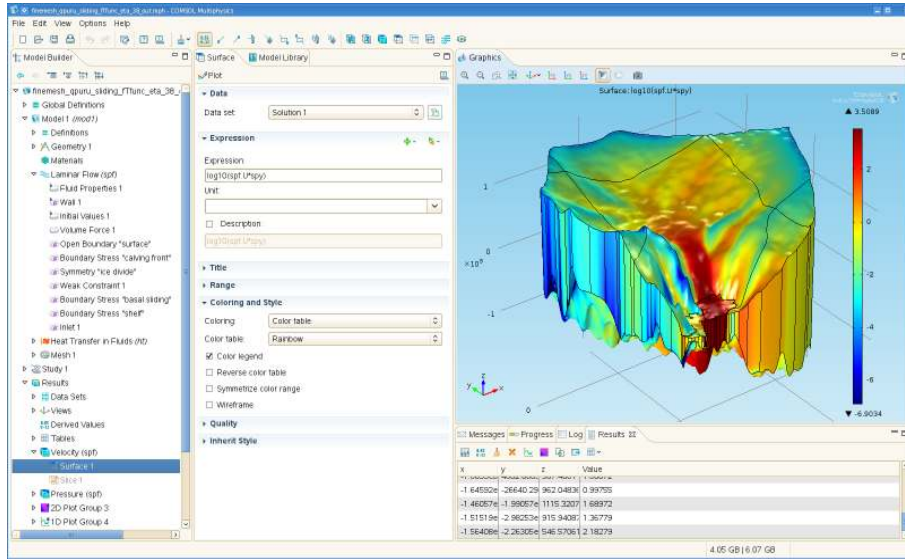


Figure 3.12: Screenshot of the COMSOL GUI

*Builder* shows the so called *Model Builder Tree* with different branches. The branches contain by default *Global Definitions*, *Model*, *Study* and *Result* nodes. The *Global Definitions* are used to define parameters that can be used everywhere in the *Model Builder Tree*, like *Parameters* (listed in Table 3.1) and imported data fields (*Interpolation*, in the following written in the form  $\text{data}(\mathbf{x}, \mathbf{y})$ ). The *Model* node is subdivided into several smaller branches and is the main feature to build the actual model. Here the *Local Definitions*, *Geometry*, *Material*, *Physics* and *Mesh* are defined. The *Local Definitions* branch exists, because several *Model* nodes can separately be defined in one multiphysics file (COMSOL file format: file.mph). Under *Local Definitions* the variables listed in Table 3.2 and 3.3 are inserted.

Table 3.1: Parameters

name	expression	unit	description
$\rho_{hoi}$	918	$\text{kg} \cdot \text{m}^{-3}$	ice density
$\rho_{hosw}$	1028	$\text{kg} \cdot \text{m}^{-3}$	density of seawater
$g$	9.81	$\text{m} \cdot \text{s}^{-2}$	acceleration of gravity
$E$	1		enhancement factor
$n$	3		stress exponent
$R$	8.314	$\text{J} \cdot \text{mol}^{-1}$	gas constant
$\beta$	$9.8 \cdot 10^{-8}$	$\text{K} \cdot \text{Pa}^{-1}$	Clausius-Clapeyron constant

COMSOL provides the possibility to implement the equations to be solved directly via the PDE mode. Or a variety of so called *Physics* modes can be selected. These *Physics* modes provide interfaces that are preset for several typical physical questions. They have preset the most commonly used kinds of boundary conditions, but also leave the option to insert other kinds of boundary conditions. The chosen *Physics* branches appear under

*Physics* in the *Model Builder Tree*. To simulate the Stokes flow the *Physics* mode *Laminar Flow* is selected, which provides the Navier-Stokes equation. The temperature is solved for with the *Physics* mode *Heat Transfer in Fluids*, which provides the heat transport equation. How the boundary conditions are implemented in the *Physics* modes will be described below.

In the following sections it is explained how the geometry is built (Section 3.2.1), how the *Laminar Flow* (Section 3.2.2) and *Heat Transfer in Fluids* (Section 3.2.3) modes with appropriate boundary conditions are applied, how the mesh is created (Section 3.2.4) and which solvers are selected (Section 3.2.5). This is done by describing the path to follow in *italic* characters. The actual input that needs to be done is written in **typewrite** characters and further specifications if needed can be found in Tables 3.1, 3.2 and 3.3.

### 3.2.1 Model geometry

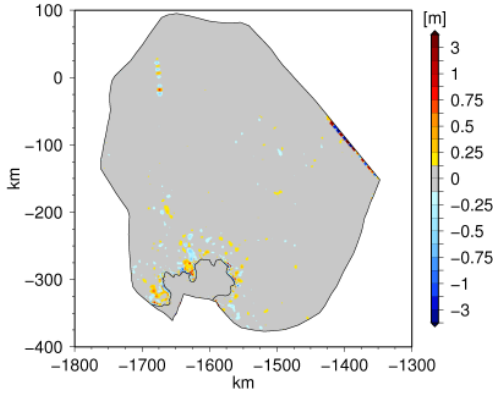
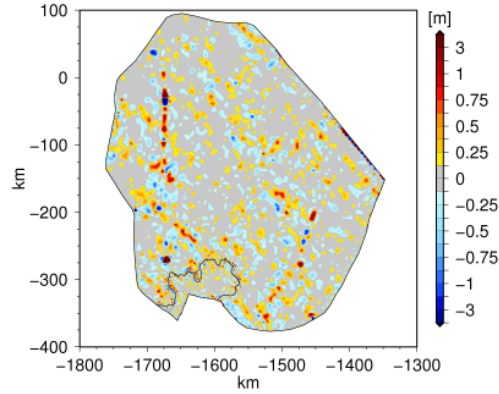
The geometry in a COMSOL model is the central object. For a glacier model it has to be created as a solid, the so called *Model Domain*. This main *Model Domain* can be divided into a variety of *Model Subdomains*, which will become important for defining different boundary conditions or mesh resolutions.

The basic idea to create a realistic model geometry based on topographic data is to first create the horizontal domain boundary, possibly including horizontal subdomains. For Pine Island Glacier the outer domain boundaries are described in Section 3.1 and shown in Figure 3.2. The ice shelf area represents hereby a subdomain, separated by the grounding line position from the grounded ice. This flat xy-plane is next extruded in z-direction to create a 3D object. The gridded topographic data of the upper and lower surfaces have to be converted into solid interpolated 3D COMSOL surfaces. To receive the final 3D object, the extruded 3D object has to be cut with the two surfaces.

COMSOL version 4.3a provides in theory functionalities to conduct the above described steps. The interpolated 3D COMSOL surfaces are created with the function *parametric surface*. Unfortunately this functionality seems to be only practical for smaller geometries, where deviations (due to smoothing) from the input data do not matter greatly. The topographic input data for Pine Island Glacier is in high resolution and consists for the upper and lower surfaces of a 1 km mesh for an area roughly 1000 x 500 km<sup>2</sup>. The surfaces have to be represented as exact as possible, since otherwise for example the position of the grounding line might change. When the geometry is set up completely in version 4.3a, the resulting COMSOL file becomes huge and impractical to work with.

Therefore, the model geometry was built with the help of version 3.5a and the COMSOL LiveLink for MATLAB. In version 3.5a the COMSOL function *geomsurf* is available, which creates solid interpolated 3D COMSOL surfaces. The so created surfaces use a lot less memory and are thus more practical to work with. Unfortunately this function is not available in later versions. A quadratic interpolation is used to create a surface with *parametric surface* (COMSOL, 2012a, p.707), while *geomsurf* uses a piecewise quadratic interpolation on a triangular mesh (COMSOL, 2008, p.275).

The geometry is built in MATLAB with COMSOL version 3.5a, saved as a geometry object and imported into COMSOL version 4.3a. To represent and work with complex 3D geometries, like the Pine Island Glacier geometry, the *CAD Import* module for COMSOL 4.3a is required. This module has its own geometry kernel (Parasolid). With this module arbitrary lines can be cut through the 3D geometry and thus new subdomains can be

Figure 3.13:  $z_s(x,y) - z$  [m]Figure 3.14:  $z_b(x,y) - z$  [m]

created within the 4.3a environment. The finalised 3D geometry for Pine Island Glacier can be seen as part of the GUI in Figure 3.12.

Figure 3.13 shows the difference between the original topographic data at the surface  $z_s(x,y)$ , imported as interpolated field described for the *Initial Values* in the next section, and the surface  $z$  of the geometry object. Figure 3.14 shows the difference between the original topographic data at the base  $z_b(x,y)$ , also imported and described in next section, and the base  $z$  of the geometry object. The deviations are small and in most areas  $< 1$  m. They are shown here, because the  $z$ -coordinates of the real geometric surfaces are not easily accessible within COMSOL and for further use the imported data sets are used, e.g. for the ice thickness  $H$  in Table 3.2.

### 3.2.2 Ice flow model

The variables needed for the ice flow model, inserted under *Local Definitions* as mentioned above, are given in Table 3.2. The Stokes flow is simulated with the help of the *Physics* mode *Laminar Flow*. The dependent variables are  $u, v, w$  and  $p$ . To simulate ice as an incompressible fluid the setting (*Laminar Flow*  $\rightarrow$  *Physical Model*  $\rightarrow$  *Compressibility: Incompressible flow*) has to be made. The Babuska-Brezzi condition states, that for numerical stability the basis functions (refer to Section 2.5) for the pressure must be of lower order than the basis functions for the velocity, for example linear elements for the pressure (P1) and quadratic elements for the velocity (P2). If the basis functions are of the same order, a stabilisation technique has to be applied, like the streamline diffusion (Galerkin Least Square (GLS)) (COMSOL, 2008, p.714). For the discretisation the following setting has to be made: (*Laminar Flow*  $\rightarrow$  *Discretization*  $\rightarrow$  *Discretization of fluids: P2 + P1*). Under (*Laminar Flow*  $\rightarrow$  *Fluid Properties*) the value for the density (*Laminar Flow*  $\rightarrow$  *Fluid Properties*  $\rightarrow$  *Density (User defined): rho\_i*) and for the viscosity (*Laminar Flow*  $\rightarrow$  *Fluid Properties*  $\rightarrow$  *Dynamic Viscosity (User defined): eta*) have to be filled in.

The viscosity term  $\eta$  is defined in Table 3.2 (Eq. (2.24)). The effective strain rate  $\dot{\epsilon}_e$  (Eq. 2.21) is here termed  $\mathbf{de}$  and a small value of  $10^{-30}$  is added to keep the term non-zero. Model experiments have shown, that this does not affect the overall results (Pattyn, 2003; Cornford et al., 2012).

To implement the gravity force a node *Volume Force* has to be added to *Laminar Flow*.

Under this node it has to be chosen (*Domain Selection* → *Selection: All domains*) and the force term  $-\rho_i g$  has to be inserted (*Volume Force* → *Volume Force:  $F = (0, 0, -\rho_{hoi} * g)$* ).

Under the *Initial Values* node the initial values can be inserted. This can be done by either directly prescribing values or functions for the fields, by prescribing imported interpolated data sets (*Global Definitions* → *Functions* → *Interpolation* → *Data source: File*) or by using the fields of a previous solution as the initial values (*Study* → *Solver* → *Dependent Variables* → *Initial Values of Variables Solved For*).

Table 3.2: Laminar Flow Variables

name	expression	description
nu	0.1	parameter for fT
H	zs(x,y)-zb(x,y)	ice thickness
Nb	rhoi*g*H+(rhosw*g*zb(x,y)*(zb(x,y)<0))	effective pressure
ub	u*t2x+v*t2y+w*t2z	basal velocity xz-plane
vb	u*t1x+v*t1y+w*t1z	basal velocity yz-plane
fT	exp(nu*(Tr-Tpmp))	temperature function (Tr, Tpmp in Table 3.3)
de	sqrt((ux^2)+(vy^2)+(ux*vy)+((1/4)*(uy+vx)^2)+((1/4)*(uz+wx)^2)+((1/4)*(vz+wy)^2))+1e-30	effective strain rate
A0	3.985e-13*(Th<=263.15)+1.916e3*(Th>263.15)	pre-exponential constant (Th in Table 3.3)
Q	60e3*(Th<=263.15)+139e3*(Th>263.15)	activation energy
A	A0*exp(-Q/(R*Th))	rate factor
eta	(1/2)*(E*A)^(-1/n)*de^((1-n)/n)	viscosity
source	4*eta*de^2	heat source term
tbx	-sign(ub)*(abs(ub)*Nb^q/(C*fT))^(1/p)	basal stress xz-plane
tby	-sign(vb)*(abs(vb)*Nb^q/(C*fT))^(1/p)	basal stress yz-plane

### Boundary conditions

The default boundary condition is *Wall*, which is a no slip condition  $\mathbf{u} = 0$ . To overwrite this default condition different boundary conditions have to be selected and the corresponding surfaces assigned to it. To do this it is useful to group the different surfaces into selections to which certain boundary conditions apply. This is done via (*Definitions* → *Selections* → *Explicit*). The *Selections* can be renamed, to clarify for which purpose they were selected. For assigning boundary conditions the following selections have been made and renamed: **Surface**, **Bottom**, **Bottom Shelf**, **Bottom Grounded**, **Ice Divide**, **Inflow** and **Calving Front**. Selections can also be used for the mesh creation (Section 3.2.4).

Since in this case we refer to a diagnostic model and describe the Stokes flow (*Laminar Flow*), we refer to the **dynamic boundary conditions** described in Section 2.4.

### Ice surface

The ice surface, highlighted in yellow in Figure 3.15, is seen as a traction free surface (Eq. 2.34) and implemented as (*Laminar Flow*  $\rightarrow$  *Open Boundary*), which adds the boundary condition node to the *Model Builder Tree*. Under the *Open Boundary* node the surface has to be selected (*Boundary Selection*  $\rightarrow$  *Selection: Surface*). Additionally (*Boundary Condition*  $\rightarrow$  *Boundary Condition: Normal Stress*; *Normal Stress:  $f_0 = 0$* ) is set.

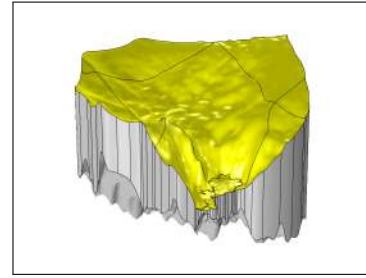


Figure 3.15: Ice surface

### Ice base

For the diagnostic model and the assumption that basal melt or freeze can be neglected, the **kinematic boundary condition** is given by Eq. (2.40). For the total ice base, consisting of the floating part, highlighted in blue in Figure 3.16, and the grounded part, highlighted in red in Figure 3.16, this condition is implemented via (*Laminar Flow*  $\rightarrow$  *Weak Constraint*). A weak constraint has to be chosen here, as otherwise no smooth velocity field across the grounding line can be achieved. Weak constraints apply boundary conditions in an integral sense and are therefore not as strict. They stand in contrast to pointwise constraints, which force the nodal value to the constraint and can thus lead to numerical instability.

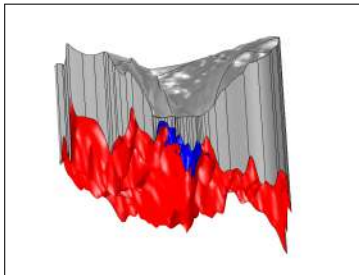


Figure 3.16: Ice base

The following settings have to be made: (*Boundary Selection*  $\rightarrow$  *Selection: Bottom*) and (*Weak Constraint*  $\rightarrow$  *Constraint type: Bidirectional, symmetric*; *Constraint expression:  $-(\mathbf{u} \cdot \mathbf{n}_x + \mathbf{v} \cdot \mathbf{n}_y + \mathbf{w} \cdot \mathbf{n}_z)$* ). Here it has been made use of the local boundary orthonormal base vector system that COMSOL provides. It consists of the normalised normal vector ( $\mathbf{n}=(n_x, n_y, n_z)$ ) and 2 normalised tangential vectors ( $\mathbf{t1}=(t1_x, t1_y, t1_z)$  and  $\mathbf{t2}=(t2_x, t2_y, t2_z)$ ). The normal vector  $\mathbf{n}$  always points to the exterior of the geometry object. The following directions for the tangential vectors are only valid for the Pine Island Glacier geometry and must be due to the particular creation process described above (Section

3.2.1). At the base of the geometry object  $\mathbf{t1}$  lies in the  $yz$ -plane and points in positive  $y$  direction, while  $\mathbf{t2}$  lies in the  $xz$ -plane and points in positive  $x$  direction. This base vector system is also used to implement the basal sliding law described below.

The *Constraint expression* is evaluated to be zero. The rest of the options is left at the default setting.

### Ice base - floating

The **dynamic boundary condition** for the floating ice is given in Eq. (2.37) and implemented as (*Laminar Flow*  $\rightarrow$  *Boundary Stress*), with the following settings: (*Boundary Selection*  $\rightarrow$  *Selection: Bottom Shelf*) and (*Boundary Condition*  $\rightarrow$  *Boundary Condition: Normal stress*; *Normal stress:  $f_0 = \rho_{\text{hgw}} \cdot \mathbf{g} \cdot (-z)$* ).

### Ice base - grounded

The boundary condition for the grounded part is given in Eq. (2.42) in form of a sliding law. To be implemented it has to be chosen in its inverse form (Eq. (2.43)). In Eq. (2.44a),(2.44b) and (2.44c) the tangential and normal components of the stress vector  $\boldsymbol{\sigma} \cdot \mathbf{n}$  are shown. The stress vector  $\boldsymbol{\sigma} \cdot \mathbf{n}$  can thus also be expressed as

$$\boldsymbol{\sigma} \cdot \mathbf{n} = F_b^{-1} u_b \mathbf{t}_x + F_b^{-1} v_b \mathbf{t}_y - N_b \mathbf{n}. \quad (3.1)$$

This is used to implement the boundary condition as (*Laminar Flow*  $\rightarrow$  *Boundary Stress*), with the settings: (*Boundary Selection*  $\rightarrow$  *Selection: Bottom Grounded*) and (*Boundary Condition*  $\rightarrow$  *Boundary Condition: General stress; Stress: F = (-Nb\*nx+tbx\*t2x+tby\*t1x,-Nb\*ny+tbx\*t2y+tby\*t1y,-Nb\*nz+tbx\*t2z+tby\*t1z)*).

### Ice divide

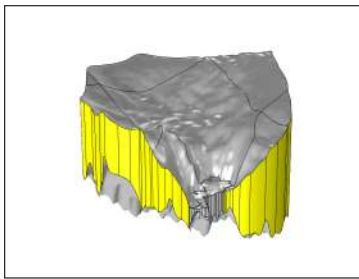


Figure 3.17: Ice divide

The boundary condition for the ice divide, highlighted in yellow in Figure 3.17, is given in Eq. (2.49) and implemented as (*Laminar Flow*  $\rightarrow$  *Symmetry*). Only the boundary selection (*Boundary Selection*  $\rightarrow$  *Selection: Ice Divide*) has to be made.

### Calving front

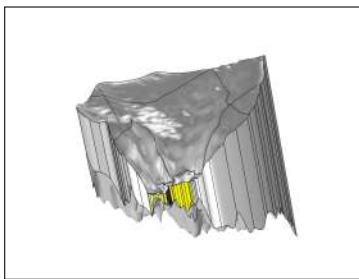
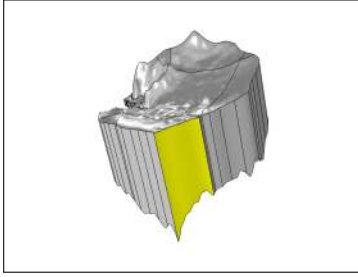


Figure 3.18: Calving front

The boundary condition for the calving front, highlighted in yellow in Figure 3.18, is given in Eq. (2.52) and implemented as (*Laminar Flow*  $\rightarrow$  *Boundary Stress*), with the following settings: (*Boundary Selection*  $\rightarrow$  *Selection: Calving Front*) and (*Boundary Condition*  $\rightarrow$  *Boundary Condition: Normal Stress; Normal Stress: f0 = rho\*g\*(-z)\*(z<0)*).

### Inflow



The boundary condition for the inflow area, highlighted in yellow in Figure 3.19, is given in Eq. (2.53) and implemented as (*Laminar Flow*  $\rightarrow$  *Inlet*). The following settings are made: (*Boundary Selection*  $\rightarrow$  *Selection: Inflow*), (*Boundary Condition*  $\rightarrow$  *Boundary Condition: Velocity*) and either (*Velocity*  $\rightarrow$  *Normal inflow velocity;  $U_0 = \text{sqrt}(uSIA^2+vSIA^2)$* ) or (*Velocity*  $\rightarrow$  *Velocity field;  $\mathbf{u}_0 = (uSIA, vSIA, 0)$* ).

Figure 3.19: Inflow

### Ice rises

Since the default boundary condition is *Wall*, it applies to all boundaries that have no other boundary condition assigned to them. The only undefined boundaries are at this point the ice rises, that are implemented as holes in the geometric object and thus have surfaces on the “inside“. The boundary condition for the ice rises is thus given by a no slip condition.

### 3.2.3 Thermal model

The variables needed for the thermal model, inserted under *Local Definitions* as mentioned above, are given in Table 3.3. The thermal model is implemented with the *Physics mode Heat Transfer in Fluids*. The dependent variable is  $T$ . The temperature is solved for with linear elements (*Heat Transfer in Fluids*  $\rightarrow$  *Discretization*  $\rightarrow$  *Temperature: Linear*). The first subnode is also named *Heat Transfer in Fluids* (*Heat Transfer in Fluids*  $\rightarrow$  *Heat Transfer in Fluids*) and here general entries have to be made (comparable to the *Fluid Properties* node under *Laminar Flow*). The following settings are made here:

(...  $\rightarrow$  *Model Inputs*  $\rightarrow$  *Absolute pressure:  $p = \text{Pressure (spf/fp1)}$* )  
 (...  $\rightarrow$  *Model Inputs*  $\rightarrow$  *Velocity field:  $\mathbf{u} = \text{Velocity field (spf/fp1)}$* )  
 (...  $\rightarrow$  *Heat Conduction*  $\rightarrow$  *Thermal conductivity:  $k$  (User defined) =  $kT$  (Isotropic)*)  
 (...  $\rightarrow$  *Thermodynamics*  $\rightarrow$  *Density:  $\rho$  (User defined) =  $\rho_{hoi}$* )  
 (...  $\rightarrow$  *Thermodynamics*  $\rightarrow$  *Heat capacity at constant pressure:  $c_p$  (User defined) =  $cpT$* )  
 (...  $\rightarrow$  *Thermodynamics*  $\rightarrow$  *Ratio of specific heats:  $\gamma$  (User defined) = 1).*

The first two settings, under (...  $\rightarrow$  *Model Inputs*), create the coupling between the ice flow and the thermal model, such that the calculated velocity and pressure fields serve as input for the heat advection.

Under the *Initial Values* node the initial values can be inserted as for the ice flow model in Section 3.2.2.

To include the internal heat source term (Eq. (2.13)) a *Heat Source* node has to be added (*Heat Transfer in Fluids*  $\rightarrow$  *Heat Source*). Under this node the following settings have to be made: (*Domain Selection*  $\rightarrow$  *Selection: All domains*) and (*Heat Source*  $\rightarrow$  *General source:  $Q$  (User defined) =  $\text{source}$* ).

Table 3.3: Heat Transfer Variables

name	expression	description
T0	273.15 [K]	low pressure melting point
Tsw	271.15 [K]	freezing temperature of seawater
Tpmp	$T_0 - (\beta * p)$ [K]	pressure melting point
Tr	$\text{if}(T > T_{\text{pmp}}, T_{\text{pmp}}, T)$ [K]	controlled temperature
Th	$T_r + (\beta * p)$ [K]	homologous temperature
kT	$9.828 * \exp(-5.7e-3 * T_r)$	thermal conductivity
cpT	$152.5 + (7.122 * T_r)$	heat capacity
qgeo	$q_{\text{puru}}(x, y)$	geothermal heat flux
taubx	$\text{spf}.T_{\text{stressx}} * t_2x + \text{spf}.T_{\text{stressy}} * t_2y + \text{spf}.T_{\text{stressz}} * t_2z$	
tauby	$\text{spf}.T_{\text{stressx}} * t_1x + \text{spf}.T_{\text{stressy}} * t_1y + \text{spf}.T_{\text{stressz}} * t_1z$	
qfric	$\text{sqrt}((ub+vb)^2 * (taubx+tauby)^2)$	friction heating
f	$((-z_b(x, y) * \rho_{\text{hosw}}) / ((H - 15.2) * \rho_{\text{hoi}})) > 1$	floatation mask
Qdot	$(q_{\text{geo}} + q_{\text{fric}}) + f$	basal heat flux
Tb	$T_{\text{pmp}} + f * (T_{\text{sw}} - T_{\text{pmp}})$	maximum basal temperature

### Boundary conditions

The default boundary condition is *Thermal Insulation* as shown in Eq. (2.50). As for the ice flow model, the corresponding surfaces have to be assigned to the different boundary conditions and will be described below. For Figures showing the different surfaces refer to Section 3.2.2. Since here we describe the thermal model we will refer to the **thermodynamic boundary conditions** described in Section 2.4.

### Ice surface

The boundary condition for the surface is shown in Eq. (2.35) and implemented with (*Heat Transfer in Fluids* → *Temperature*) with the settings (*Boundary Selection* → *Selection: Surface*) and (*Temperature* → *Temperature:  $T_0 = T_s(x, y)$* ). The surface temperature is described in Section 3.1.4 and shown in Figure 3.6. Furthermore all Dirichlet conditions for the thermal model have to be implemented as *Weak Constraints: (Constraint Setting* → *Classic constraints* → *Constraint type: Bidirectional, symmetric; Use weak constraints*).

### Ice base

The thermodynamic boundary condition for the base is implemented slightly different than suggested in Eq. (2.38), (2.39), (2.47) and (2.48), due to stability issues. The whole base receives a heat flux implemented with (*Heat Transfer in Fluids* → *Heat Flux*) and the selection of the basal surface (*Boundary Selection* → *Selection: Bottom*). The following settings have to be made: (*Heat Flux* → *General inward heat flux:  $q_0 = Q_{\text{dot}} * (f_{\text{lc2hs}}(T_b - T, 0.01))$* ). The term  $Q_{\text{dot}}$  is the basal heat flux (refer to Table

3.3, a combination of geothermal heat flux, described in Section 3.1.5, and frictional heat). The function `flc2hs` is a smoothed Heaviside function with a continuous second derivative and without overshoot. With the specifying parameters `x` and `scale`, `flc2hs(x,scale)` is a function that approximates the logical expression  $y = (x > 0)$  by smoothing the transition within the interval  $-\text{scale} < x < \text{scale}$ . The basal temperature `Tb` is a spatially variable field that defines the maximal basal temperature that can be reached and is  $Tb = T_{\text{pmp}}$  for grounded areas, and  $Tb = T_{\text{sw}}$  for floating areas. The whole expression  $Q_{\text{dot}} * (\text{flc2hs}(Tb - T, 0.01))$  thus prescribes a heat flux  $Q_{\text{dot}}$ , as long as  $T < (Tb - 0.01)$ . When  $T$  becomes  $T \geq (Tb - 0.01)$ ,  $Q_{\text{dot}}$  is gradually reduced and turns zero when  $T = (Tb + 0.01)$ . This procedure ensures a stable way to not let the basal heat flux increase the temperature above  $Tb + 0.01$ . The function is shown in Figure 3.20.

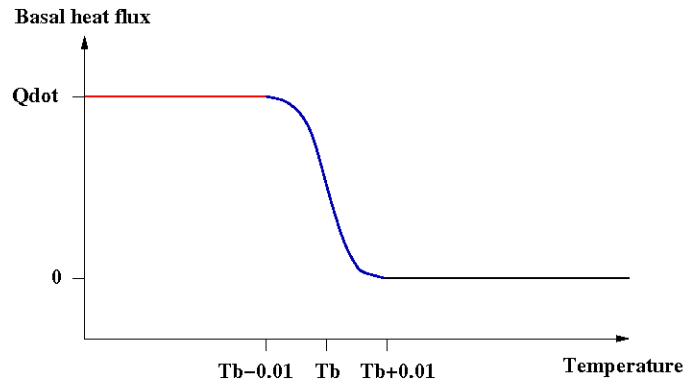


Figure 3.20:  $Q_{\text{dot}} * (\text{flc2hs}(Tb - T, 0.01))$

### Inflow

The boundary condition for the inflow is shown in Eq. (2.54) and implemented with a Dirichlet condition (*Heat Transfer in Fluids*  $\rightarrow$  *Temperature*) with the settings (*Boundary Selection*  $\rightarrow$  *Selection: Inflow*), (*Temperature*  $\rightarrow$  *Temperature:  $T_0 = (Tb - Ts(x, y)) / H * (zs(x, y) - z) + Ts(x, y)$* ) and (*Constraint Setting*  $\rightarrow$  *Classic constraints*  $\rightarrow$  *Constraint type: Bidirectional, symmetric; Use weak constraints*).

### Ice divide, calving front and ice rises

The boundary conditions for the remaining boundaries are given by the default condition *Thermal Insulation* as shown in Eq. (2.50).

### 3.2.4 Mesh

The mesh of the 3D model for Pine Island Glacier consists of unstructured prism elements and is shown in Figure 3.21. It is constructed in a number of substeps. This is necessary due to the very small aspect ratio of Pine Island Glacier, which is the ratio of vertical to horizontal extent  $\epsilon = H L^{-1}$ . For Pine Island Glacier the vertical extent, which is the average thickness, is about 3 km and the horizontal extent about 500 km, which leads to an aspect ratio of the order  $10^{-3}$ . In the main part of the modelling domain in the grounded ice, apart from the area adjacent to the grounding line, the biggest gradient of the variables

is present in the vertical direction. This is why the SIA can be applied in those areas. It is therefore important to have a decent resolution in the vertical. If we aim at a high mesh quality this would lead to an extremely fine horizontal resolution in the order of 100 m. Such a high resolution is not applicable due to limited computational resources. Therefore, an approach is chosen that results in high vertical and feasible horizontal resolution at the expense of mesh quality, described below and shown in Figure 3.22.

The areas with strong gradients and high resolution needed are meshed first. This is done by defining a maximum element size for the edges via (*Mesh* → *Edge* → *Size*). For the following boundaries the maximum element sizes are:

grounding line → 500 m  
 calving front → 500 m  
 inflow area → 1000 m  
 rest of outer boundary → 2000 m

Afterwards the surface of the modelling domain is meshed with a free triangular mesh (*Mesh* → *Free Triangular* → *Size*). The central trough area with the fast flowing stream and the shelf area get hereby a higher resolution (maximum element size 5000 m) than the rest of the domain (maximum element size 6000 m). The resulting surface mesh is shown in Figure 3.21. It is important to start meshing from the highest resolution as otherwise the interfaces will receive a lower resolution than wanted.

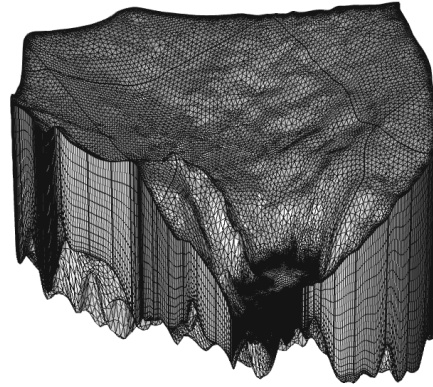


Figure 3.21: FEM mesh

The rest of the model domain is meshed by adding a swept mesh (*Mesh* → *Swept*). This option projects the surface mesh (*Mesh* → *Swept* → *Source Faces: Surface*) onto the bottom (*Mesh* → *Swept* → *Destination Faces: Bottom*) and creates a certain number of vertical layers (*Mesh* → *Swept* → *Distribution* → *Number of elements: 12*). The element ratio specifies the ratio in size between the last and first vertical element and is set under (*Mesh* → *Swept* → *Distribution* → *Element ratio: 0.01*), to receive a higher resolution near the base. The chosen values are derived from the vertical local element Peclet number (Durrant, 2010) given by

$$Pe = \frac{|w| dz c_p \rho_i}{\kappa}, \quad (3.2)$$

which is a nondimensional parameter describing the ratio of thermal advection to thermal

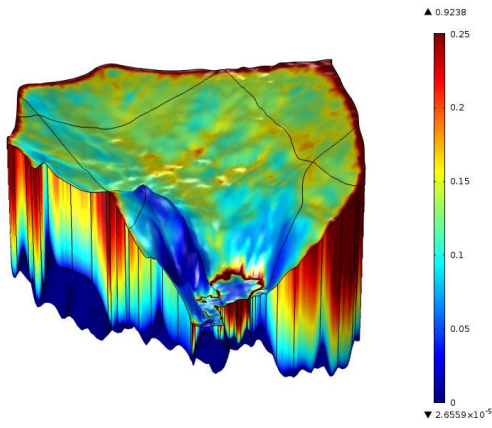


Figure 3.22: Mesh quality

diffusion. At the base of the glacier the stability requirement of  $Pe < 1$  is given almost everywhere with the above stated values. The final mesh consists of  $\sim 370\,000$  prism elements.

The mesh quality in COMSOL gives a measure of how evenly an element is formed. The aim is to have elements with the nodes on the surface of a sphere and even length edges. A 2D triangular element would have a mesh quality of 1 for an equilateral triangle and 0 if the triangle degenerated into a line. The mesh quality is important so the gradient of the variables solved for does not become too large over the element volume. For mesh quality dependent remeshing the default minimum mesh quality is 0.2 and an acceptable mesh quality has to be larger than 0.1 (COMSOL, 2012b). The mesh quality may become important when using an iterative linear system solver, as it requires a higher mesh quality than a direct solver.

### 3.2.5 Solver

COMSOL Multiphysics<sup>©</sup> provides a variety of solver choices for solving the FEM model equations. The solver options can be set under the (*Study*  $\rightarrow$  *Solver Configurations*) node of the *Model Builder Tree*. For computation of a diagnostic solution, a *Stationary Solver* is selected. The settings for the *Stationary Solver* are adjusted under (...  $\rightarrow$  *Solver Configurations*  $\rightarrow$  *Solver*  $\rightarrow$  *Stationary Solver*).

We chose a direct solver, which is uncommon for such a high number of DOF's, but seems to be the best choice in our case. Iterative solvers work not well due to the bad mesh quality described above. The *Direct Solver* node is added under the *Stationary Solver* node in the *Model Builder Tree*. Here one of three direct solvers, MUMPS, PARDISO or SPOOLES, can be selected.

The chosen *Direct Solver* can be combined with either a *Fully Coupled* or *Segregated* node. The *Fully Coupled* node makes the *Direct Solver* solve for all variables at once. The *Segregated* node can be applied such that groups of variables are solved for iteratively. For the glacier model this can be done by solving for the temperature  $T$  in the *Segregated Step 1* and for  $u, v, w$  and  $p$  in the *Segregated Step 2*. The variables not solved for in a step are held constant at the previous value of the solution. This way the working memory usage can be reduced. If sufficient working memory is available, the use of a *Fully Coupled* node is preferable as it converges faster.

Under either, the *Fully Coupled* or *Segregated* node, an appropriate setting for *Method and Termination* has to be chosen, where the *Nonlinear method* and the *Termination technique* are defined. Because the system of model equations is nonlinear, it has to be set (...  $\rightarrow$  *Method and Termination*  $\rightarrow$  *Nonlinear method: Automatic (Newton)/Automatic highly nonlinear (Newton)*).

Under the *Fully Coupled* node the following termination technique is selected: (...  $\rightarrow$  *Method and Termination*  $\rightarrow$  *Termination technique: Iterations or tolerance*). This terminates the solving process if either a maximum number of iterations is reached (...  $\rightarrow$  *Method and Termination*  $\rightarrow$  *Number of iterations: 25*), or the relative error (defined in Eq. (3.3)) is smaller than the relative tolerance value chosen, set under (...  $\rightarrow$  *Solver*  $\rightarrow$  *Stationary Solver*  $\rightarrow$  *Relative tolerance: 1e-6*) and (...  $\rightarrow$  *Method and Termination*  $\rightarrow$  *Tolerance factor: 1*). The *Tolerance factor* is only meaningful in combination with the *Segregated* node, because it can be used to modify the relative tolerance for different segregated steps.

Under the *Segregated* node the termination techniques to be selected are very similar. Here it has to be chosen for the main *Segregated* node, which can be seen as the outer loop, and additionally for the different *Segregated Steps*.

The relative error  $err$  is for a *Direct Solver* defined by the weighted Euclidean norm

$$err = \sqrt{\frac{1}{M}} \sqrt{\sum_{j=1}^M \frac{1}{N_j} \sum_{i=1}^{N_j} \left( \frac{|E_{i,j}|}{W_{i,j}} \right)^2}, \quad (3.3)$$

with  $M$  being the number of fields (variables solved for),  $N$  the number of DOF's in field  $j$ ,  $W_{i,j} = \max(|U_{i,j}|, S_i)$  with  $U_{i,j}$  being the current approximation to the solution vector and  $S_i$  a pre-defined scale factor, and  $E_{i,j}$  the estimated error in this vector (COMSOL, 2012a, p.630).

### 3.3 Verification and validation

The results of a numerical model need to be verified and validated. The terms *verification* and *validation* are subject to many controversies, but used in the following sense here (Bueler, 2008). Verification describes the process of testing if the implementation and solution of the underlying equations is complete and bug free. Validation on the other hand can be carried out if the model has already been verified and its aim is to test whether or not the mathematical model is an appropriate representation of the real-world process it wants to simulate (Leng et al., 2013). A verification can be done by comparing the model output to an analytical solution. A validation can be achieved by comparing the model output to measured data. A model intercomparison can not be accounted clearly to either method (Bueler, 2008), but in the latter it will be accounted to the validation methods.

This model consists of different parts. There is the ice flow model, with ice-sheet and ice-shelf flow, and the thermal model. The ice sheet flow has been validated by M. Rückamp within the first Ice Sheet Model Intercomparison Project for Higher-Order and full-Stokes ice sheet Models (ISMIP-HOM) (Pattyn et al., 2008; Rückamp, 2011). The ice-shelf flow is verified with an analytical solution in Section 3.3.1. It has to be noted here, that the analytical solution is based on simplified assumptions, the Shallow Shelf Approximation (SSA), and is therefore not strictly an exact solution to the full-Stokes flow problem. The coupled ice sheet and ice shelf flow model is validated within the Marine Ice Sheet Intercomparison Project (MISMIP 3D) described in Section 3.3.2 (Pattyn et al., 2013). The temperature model is verified by M. Rückamp with an exact solution from Bueler et al. (2007) (Rückamp, 2011). The full thermo-mechanically coupled model is validated via an application to Pine Island Glacier and compared to measured surface velocities in the next chapter.

#### 3.3.1 Ice shelf ramp

In a first step we will verify the floating part of the model. This is done by comparing the model output to an analytical solution. This analytical solution is obtained for an idealised ice shelf ramp with the equations of the SSA (refer to Section 1.2.1). As the model solves the full-Stokes equation, it is thus not a strict verification but still used as an

indication for the right solution. Furthermore the 3D model is compared to the analytical solution for 2D flow in the  $xz$ -plane. Since the 3D model is axis-symmetric with no lateral drag, comparison to the 2D flow line solution is valid but does not create any further insight into the 3D behaviour (for this refer to Section 3.3.2).

We will show the analytical results for the velocity components  $u$  and  $w$  and the total mass balance  $a_s - a_b$ , and compare them to the model results. For a detailed derivation of the solutions refer to *Greve and Blatter (2009)*.

We consider an ice shelf that extends from the grounding line at  $x = 0$  to the calving front at  $x = L$ . The ice thickness  $H$  decreases linearly from the thickness at the grounding line  $H_{gl}$  to the thickness at the calving front  $H_{cf}$ , such that

$$H = H_{gl} - \frac{H_{gl} - H_{cf}}{L} x. \quad (3.4)$$

The mean sea level is located at  $z = 0$  and the inflow at the grounding line is given by  $\mathbf{u}_{gl} = (u_{gl}, 0, 0)$ . Furthermore steady state conditions and constant rate factor  $A(T') = A = \text{const.}$  are assumed. Table 3.4 gives an overview of the parameter values used in this section.

Table 3.4: Overview of parameters for the ice shelf ramp

name	value	description
$H_{gl}$	400 m	ice thickness at grounding line
$H_{cf}$	200 m	ice thickness at calving front
$L$	200 km	calving front position
$B$	10 km	extent in y-direction
$u_{gl}$	100 m a <sup>-1</sup>	inflow velocity at grounding line
$n$	3	stress exponent
$A$	4.9e-25 s <sup>-1</sup> Pa <sup>-3</sup>	rate factor (for $T' = -10^\circ\text{C}$ )
$\rho_i$	910 kg m <sup>-3</sup>	ice density
$\rho_{sw}$	1028 kg m <sup>-3</sup>	sea water density
$g$	9.81 m s <sup>-2</sup>	acceleration of gravity

In Figure 3.23 the model geometry is shown. The velocity field is indicated by the black arrows. The red line indicates the sea level and is also the line on which the horizontal velocity component  $u$  is evaluated. The blue line lies at  $x = L/2$  and  $y = B/2$  and is the line where the vertical velocity component  $w$  is evaluated.

Since the model consists of an idealised ice shelf, it is not necessary to apply *Weak Constraints* to the ice base as shown in Section 3.2.2 (Boundary conditions - Ice base). Instead it is sufficient to apply a Symmetry condition as for the Ice Divide (Section 3.2.2 - Boundary conditions - Ice divide).

The model is run for different mesh resolutions as listed in Table 3.5. The first column "Identifier" gives a name the simulation is referred to hereafter. Columns "horizontal" and "layers" give information about the horizontal and vertical mesh resolution, respectively. Under "elements" the total number of prism elements and under "DOF's" the degrees of freedom, for the different simulations, are listed. The time needed to find a solution, given

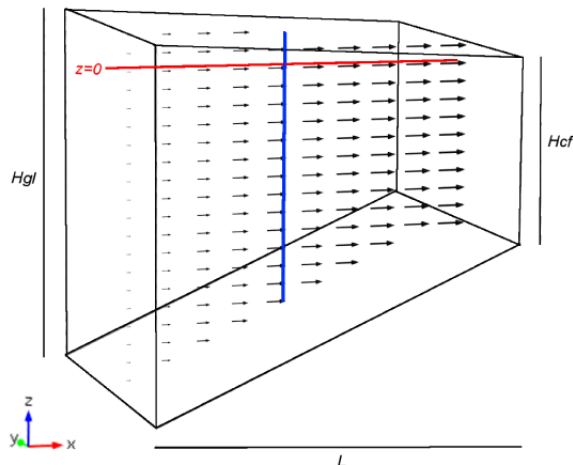


Figure 3.23: 3D ice shelf ramp with flow field

in column "solution time", applies to a parallel job on 4 cores, conducted on a compute server with 32 cores (8 Quad-Core AMD Opteron 8356, 2.3 GHz) and 128 GB RAM, located at the University of Hamburg.

The different resolutions, listed in Table 3.5, are used to demonstrate the effect onto the solution. The number of vertical layers is always chosen to be 5, as ice shelf flow is a plug flow and the vertical gradient in the horizontal velocity components  $u$  and  $v$  is very small. Mesh 1 has a coarse even horizontal resolution, mesh 2 has a much finer but also even horizontal resolution and mesh 3 has a horizontal resolution with refinements around the in- and outflow edges.

As described in Section 3.2.5, different termination techniques can be selected. For the *ice shelf ramp* we chose the termination technique *Tolerance*, such that the solving process is terminated, once the relative error, as given in Eq. (3.3), is smaller than  $err = 1e-6$ .

Table 3.5: Mesh specifications for the ice shelf ramp

identifier	horizontal [km]	layers	elements	DOF's	solution time [s]
mesh 1	2.5	5	4 030	61 701	128
mesh 2	0.5	5	92 210	1 302 777	6 071
mesh 3	0.05/1.5	5	30 070	441 573	1 224

The horizontal velocity for the ice shelf ramp in Shallow Shelf Approximation is given by

$$u(x) = u_{gl} + \left( \frac{\varrho g}{4A^{-1/n}} \right)^n O(x) \quad (3.5)$$

with  $B = A^{-1/n}$  and

$$\varrho = \frac{\rho_i}{\rho_{sw}} (\rho_{sw} - \rho_i) \quad (3.6)$$

and

$$O(x) = \frac{L}{(n+1)(H_{\text{gl}} - H_{\text{cf}})} H_{\text{gl}}^{n+1} \left[ 1 - \left( 1 - \frac{H_{\text{gl}} - H_{\text{cf}}}{LH_{\text{gl}}} x \right)^{n+1} \right]. \quad (3.7)$$

Figure 3.24 shows the analytical horizontal velocity  $u(x)$  (Eq. (3.5)) and the simulated horizontal velocities, evaluated at  $z = 0$  (red line in Figure 3.23) in the middle of the shelf at  $y = 5$  km. The maximal horizontal velocities  $u_{\text{max}}$  are listed in Table 3.6.

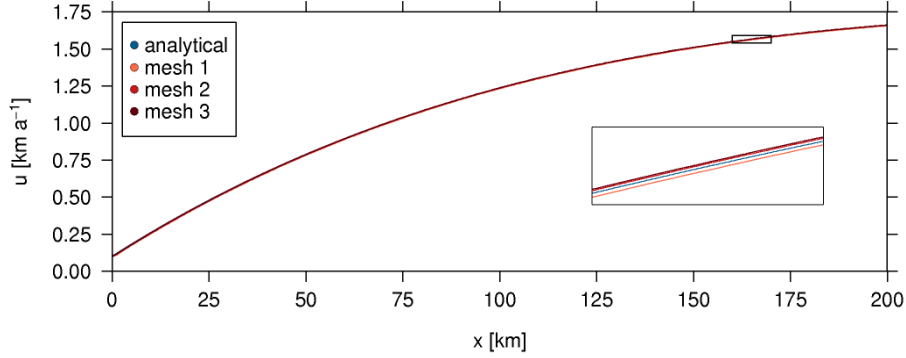


Figure 3.24: horizontal velocity  $u(x)$ , with enlarged region

In general all mesh resolutions manage to reproduce the horizontal velocity component  $u$  very well.

The analytical vertical velocity component  $w(z)$  in SSA is given by

$$w(z) = w(z = 0) - \left( \frac{\rho g H}{4B} \right)^n z. \quad (3.8)$$

To determine the vertical velocity at sea level  $w(z = 0)$  the distributions of the surface and basal mass balance  $a_s$  and  $a_b$  need to be known. To plot the analytical solution anyway  $w(z = 0)$  is assumed to be zero. The analytical solution together with the simulated solution at  $x = 100$  km and  $y = 5$  km (blue line in Figure 3.23) is shown in Figure 3.25. To compare the results the gradient of function  $w(z) = az + b$  is looked at and listed in Table 3.6. All the simulated gradients of the vertical velocity component  $w$  agree well with the

Table 3.6: Velocity results for the ice shelf ramp

identifier	$u_{\text{max}}$ [m a <sup>-1</sup> ]	$w_{\text{max}}$ [m a <sup>-1</sup> ] at $x = 100$ km	$w_{\text{min}}$ [m a <sup>-1</sup> ] at $x = 100$ km	a [a <sup>-1</sup> ]	b [m a <sup>-1</sup> ]
mesh 1	1658.168	1.09179	-1.02211	-0.0070463	-0.77946
mesh 2	1662.675	1.09556	-1.01836	-0.0070464	-0.77571
mesh 3	1663.790	1.09631	-1.01762	-0.0070464	-0.77497
analyt.	1658.73	1.86275	-0.24154	-0.0070143	0
analyt.(m3-b)	1658.73	1.08778	-1.01651	-0.0070143	-0.77497

analytical value.

The total mass balance at the upper and lower interface  $a_s - a_b$  at steady state is given by

$$a_s - a_b = \frac{d(Hu)}{dx}. \quad (3.9)$$

The analytical solution for total mass balance can be derived such that

$$a_s - a_b = H \left( \frac{\rho g H}{4B} \right)^n + \frac{dH}{dx} \left[ u_{gl} + \left( \frac{\rho g}{4B} \right)^n O(x) \right] \quad (3.10)$$

and is shown for the parameters from Table 3.4 in Figure 3.26. The simulated mass balance can also be derived from the stationary kinematic boundary condition (for the surface given in Eq. (2.33)). Because we apply a *no penetration* condition  $\mathbf{u} \cdot \mathbf{n} = 0$  at the base of the ice sheet, it is  $a_b = 0$  and therefore  $a_s - a_b = -\mathbf{u} \cdot \mathbf{n}$ , which is shown in Figure 3.26 for the different meshes evaluated on the surface in the center of the ice shelf at  $y = 5$  km.

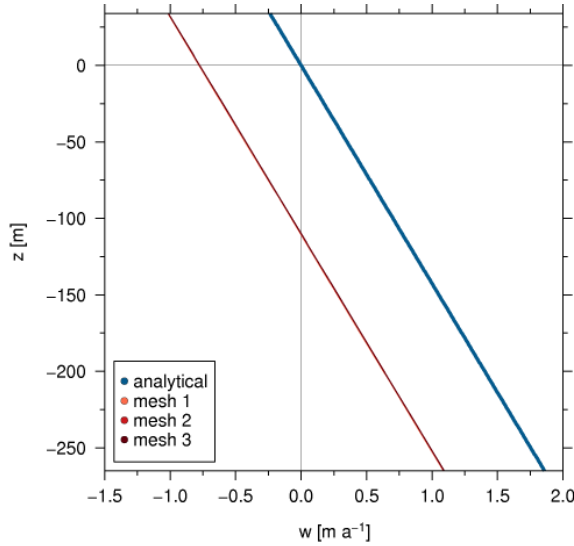


Figure 3.25: vertical velocity  $w(z)$

The minimum and maximum values of the mass balance of the analytical solution and the different simulations are shown in Table 3.7. In Figure 3.26 the importance of the vertical mesh resolution becomes apparent. In a 2D flow line model it is possible to strongly refine horizontally and still result in a manageable amount of DOF's. In a 3D model it has to be carefully balanced between horizontal and vertical resolution and solving time. Here the local mesh refinement becomes important. The overshoot is due to the inflow boundary condition with  $\mathbf{u} = (u_{gl}, 0, 0)$ . The vertical velocity component has to adjust and results in oscillation. For finer horizontal resolutions the overshoot becomes smaller.

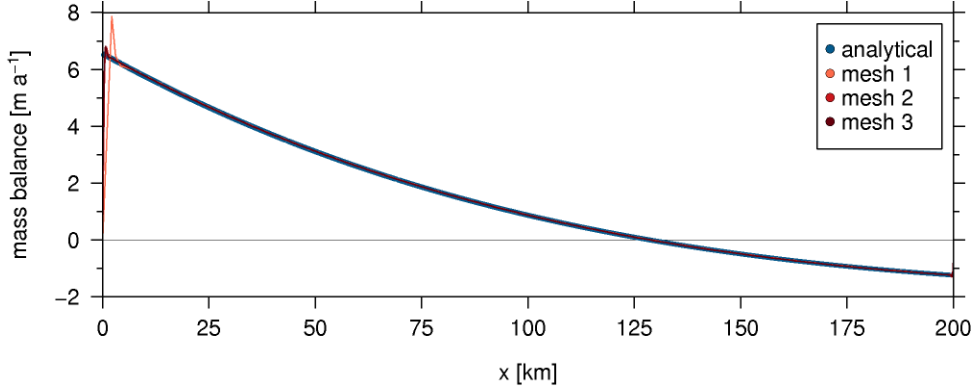


Figure 3.26: mass balance

Table 3.7: Mass balance results for the ice shelf ramp

identifier	$(a_s - a_b)_{\max}$ [ $\text{m a}^{-1}$ ]	$(a_s - a_b)_{\min}$ [ $\text{m a}^{-1}$ ]
mesh 1	7.8853	-1.2273
mesh 2	6.7969	-1.2859
mesh 3	6.8254	-1.2988
analyt.	6.5506	-1.2431

### 3.3.2 MISMIP 3D

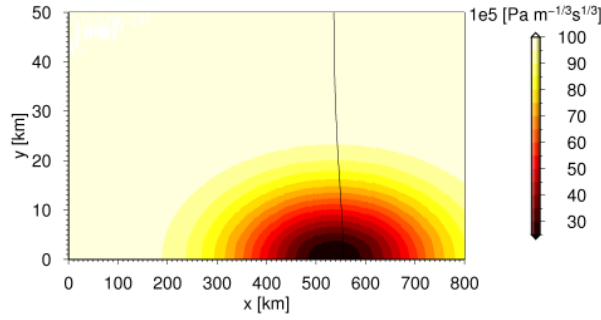
The coupled ice sheet-ice shelf flow is validated along the Marine Ice Sheet Intercomparison Project (MISMIP 3D) (*Pattyn et al., 2013*). The models compared are isothermal, incompressible and non-linear viscous. The intercomparison is focused on prognostic 3D grounding line motion, but also diagnostic experiments are conducted. Our model only took part in the diagnostic experiments and the results will be shown here. For an overview about modelling grounding line motion refer to Section 1.2.3.

The development of models being able to simulate grounding line motion is increasing. This includes full-Stokes models and models coupled to ocean dynamics. These developments also increase the need for adequate validation and verification methods. The processes surrounding grounding line motion are complex and it is difficult to separate effects due to feedback mechanisms. Additionally a lack of direct observations of grounding line motion complicate the direct validation of models with observations.

The verification with an approximate analytical solution based on boundary layer theory (*Schoof, 2007a*) is only possible for simplified geometrical configurations with no lateral variations and no buttressing effects from lateral drag. This verification was conducted for 2D flow line models by *Pattyn et al. (2012)*.

In the present intercomparison project a perturbation in the basal sliding parameter is introduced which causes a curved grounding line. This is done to achieve a real 3D effect and not just a 3D extrusion of a 2D flow line model. The curved grounding line invalidates the analytical solution due to generated buttressing effects. Therefore, for the curved grounding line only the intercomparison remains as a validation method.

In total 17 distinct models participated with 33 different realisations, meaning varying


 Figure 3.27: Perturbed friction parameter  $C^*$ 

resolution or time step. As our model too, not all models participated in the prognostic and diagnostic experiments though.

The prognostic experiment starts from a steady state solution for the ice sheet, referred to as the standard experiment. This steady state solution is obtained by growing an ice sheet, with constant parameters described in detail in *Pattyn et al. (2013)*, on a plane bedrock with a constant downward slope in  $x$  and no variation in  $y$  direction. The model domain spans from 0 to 800 km in  $x$  and from 0 to 50 km in  $y$ . The domain is bounded by an ice divide at  $x = 0$  and a calving front at  $x = 800$  km. The lateral boundaries at  $y = 0$  and  $y = 50$  km are symmetry axis, while the surface is an stress free surface. The grounded ice is subject to a non-linear sliding law and the floating ice experiences the water pressure. For implementation of the boundary condition refer to Section 3.2.2.

The standard experiment can be started from either a 10 m thick slab of ice or an extruded version of the converged 2D flow line case. The bedrock position is hereby defined as

$$b(x, y) = -100 - \left(\frac{x}{1000}\right). \quad (3.11)$$

The non-linear sliding law at the base of the ice is given by

$$\boldsymbol{\tau}_b = -C|\mathbf{u}_b|^{m-1}\mathbf{u}_b \quad (3.12)$$

with the constant bed friction parameter  $C = 10^7 \text{ Pa m}^{-1/3} \text{ s}^{1/3}$  and the bed friction exponent  $m = 1/3$ . The resulting 3D marine ice sheet has no lateral variations and can be therefore compared to the analytical solution by *Schoof (2007a)*.

To achieve a curved grounding line the bed friction parameter  $C$  is locally perturbed resulting in a new bed friction parameter  $C^*$ . This results in faster sliding ice at the side of the perturbation. The perturbation is centred at the grounding line of the standard experiment and has the form of a Gaussian bump given by

$$C^* = C \left[ 1 - a \exp \left( -\frac{(x - x_b)^2}{2x_c^2} - \frac{(y - y_b)^2}{2y_c^2} \right) \right] \quad (3.13)$$

with the precise position of the initial steady state grounding line  $x_b$  at  $y = 0$ . The parameters  $y_b = 0$  km,  $x_c = 150$  km and  $y_c = 10$  km define the spatial extent of the perturbation. The amplitude of the perturbation has a maximum of 75% and is defined

by the value  $a = 0.75$ . The distribution of  $C^*$  can be seen in Figure 3.27, together with the resulting curved grounding line from the participating full-Stokes model Elmer/Ice (Favier *et al.*, 2012).

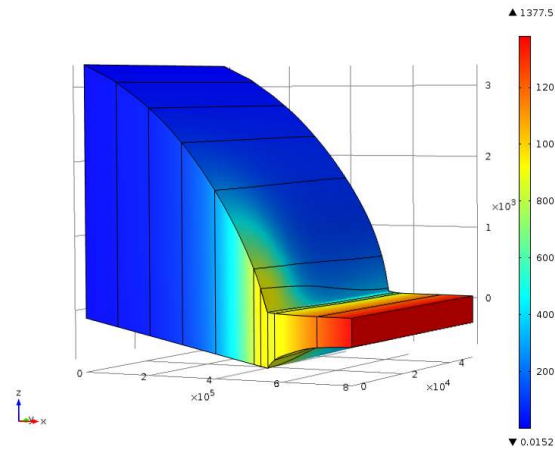


Figure 3.28: MISMIP 3D geometry with velocity  $|\mathbf{u}|$

The prognostic experiment starts from the steady state solution of the standard experiment with the constant  $C$ . The perturbed bed friction parameter  $C^*$  is inserted and the models are run forward for 100 years. This results in a new solution with a curved grounding line. The constant  $C$  is inserted again and the model is run until it reaches again a steady state solution. The final steady state should be more or less the same as the initial standard experiment steady state solution, based on reversibility postulated by Schoof (2007b).

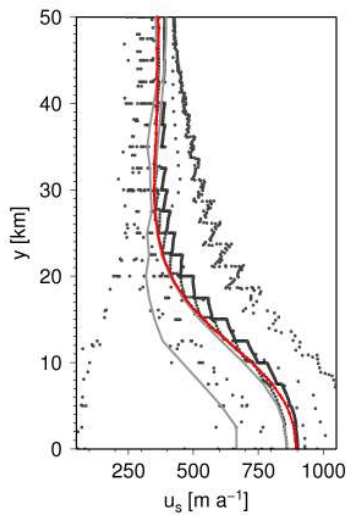


Figure 3.29:  $u_s$  at grounding line

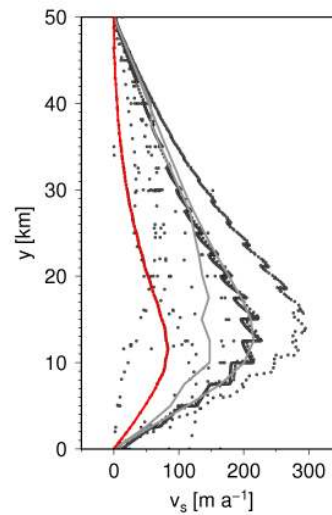


Figure 3.30:  $v_s$  at grounding line

The results of the prognostic experiment are not discussed further here, for details refer to Pattyn *et al.* (2013). The experimental set up for the prognostic experiment is

described though because the diagnostic experiment is based on the perturbed solution. The geometry for the diagnostic experiment is provided by the full-Stokes Elmer/Ice model (Favier *et al.*, 2012). This geometry can be downloaded from the MISMIP 3D website (<http://homepages.ulb.ac.be/~fpattyn/mismip3d>), and is shown in Figure 3.28. The aim is to test the performance of the different approximations to the Stokes equations and detect possible inconsistencies within the model set up by reproducing the 3D flow field.

The surface flow component perpendicular to the grounding line is compared for the different models. Most models reach a maximum flow speed between 700 and 1000  $\text{m a}^{-1}$  on the symmetry axis at  $y = 0 \text{ km}$  and a flow speed between 250 and 500  $\text{m a}^{-1}$  at  $y = 50 \text{ km}$ . A few models show significantly higher or lower flow speeds, which might be due to the way the Elmer/Ice geometry was interpolated. Our model results lie well within the range described above. Figures 3.29 and 3.30 show the surface horizontal velocity components  $u_s$  and  $v_s$  at the grounding line. The results from our model are shown in red, the two other participating full-Stokes models are marked in light grey while all other models are marked in dark grey. The horizontal velocity  $u_s$  from our model lies in the middle of all other results, while the horizontal velocity  $v_s$  is somewhat slower than most other results. The model differences might be partly due to the detected location of the grounding line. In

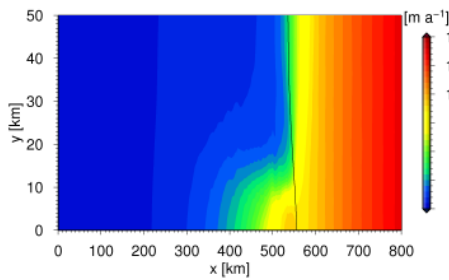


Figure 3.31:  $u$  at surface

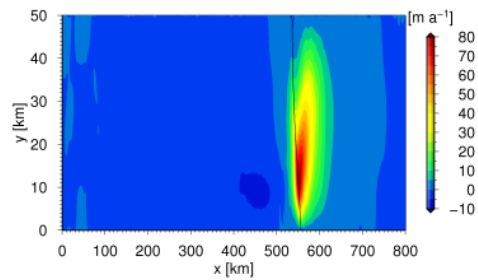


Figure 3.32:  $v$  at surface

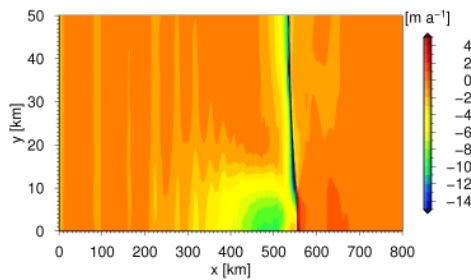


Figure 3.33:  $w$  at surface

Figures 3.31, 3.32 and 3.33 the velocity components  $u, v$  and  $w$  of our model at the surface are shown. In the vertical component  $w$  the original mesh structure of the Elmer/Ice geometry is visible.

## Chapter 4

# Identification of dominant local flow mechanisms

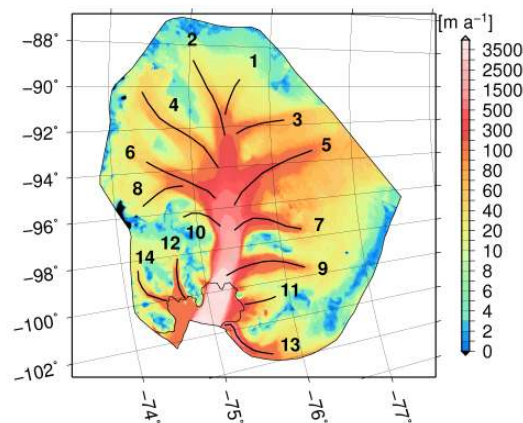


Figure 4.1: Numbered tributaries on  $|\mathbf{u}_{\text{obs}}|$

The total glacier motion is made up of different components, which are internal deformation, basal sliding of the ice over the bedrock and internal deformation of the bed itself. The contributions of the different components to the overall motion can locally vary strongly. In this chapter the question is discussed, which flow mechanisms dominate in which regions driving the flow of Pine Island Glacier.

To facilitate the distinction of the different regions, the tributaries entering the central flow area are numbered. Figure 4.1 shows the observed surface velocity field  $|\mathbf{u}_{\text{obs}}|$  from *Rignot et al.* (2011) together with the numbered tributaries, entering the central main ice stream. The numbering of the tributaries for tributaries 1-10 is based on *Stenoien and Bentley* (2000). The numbering used in *Vaughan et al.* (2006), *Karlsson et al.* (2009) and *Rippin et al.* (2011) is the same for the even numbers, but shifted by 1 for the odd numbers, as they missed tributary 1 from the numbering by *Stenoien and Bentley* (2000). We extended the numbering from *Stenoien and Bentley* (2000) to the tributaries 11-14, which are entering the ice shelf.

To distinguish the different flow mechanisms, the numerical glacier model is used as a tool to qualitatively identify the contributions by separation. The internal deformation of the bed itself can not be inferred with this method, since the bed is not modelled explicitly, but the availability of water, the hydraulic potential and the basal roughness might hint the existence of water saturated till.

In a first step, in Section 4.1, a number of no-slip simulations are conducted, where the ice is not allowed to slide over the bed. Even though it is an unrealistic setting for the flow of Pine Island Glacier, where large areas are dominated by strong basal sliding, the simulations give some insight to the interplay of mechanisms. Along these simulations the effect of the driving stress is discussed in Section 4.1.1. The basal temperature distribution solely due to heat conduction is looked at in Section 4.1.2, followed by a discussion about the effect of internal strain heating in Section 4.1.3. The contribution of the internal deformation to the surface velocity is discussed in Section 4.1.4.

Some findings from the no-slip simulations are subsequently used in Section 4.2 for reference simulations. The technique for these reference simulations, a “quasi-inversion” of a basal sliding parameter, is introduced in Section 4.2.1. The single reference run, which will be referred to as a reference for later simulations, is analysed in Section 4.2.2. The temperature distribution from the reference run shows a small layer of temperate ice, and is discussed in Section 4.2.3. The effect of considering the water content in the viscosity is discussed in Section 4.2.4, followed by a discussion of the relative contributions of full-Stokes versus SIA terms in Section 4.2.5. Additionally, the reference simulation is used to investigate the sensitivity to geothermal heat flux in Section 4.2.6.

Available water at the base of an ice sheet moves along the hydraulic potential. The hydraulic potential for Pine Island Glacier, which is with a simplified approach solely dependent on geometrical considerations, is looked at in Section 4.3. Additionally the distribution of the basal roughness is considered in Section 4.4.6, and used as an indication for the presence of sediments below the ice sheet, supported by findings from *Smith et al.* (2013).

In the last section, Section 4.5, the results are combined for an overall discussion of the flow pattern and the dominant mechanisms in the different tributaries.

All simulations in this and the following chapter are conducted on a high-performance computing system at the Alfred-Wegener-Institute, Bremerhaven. The computing system is composed of one node, consisting of 28 blades with SGI NL5 interconnect, 448 cores (56 Intel Xeon E7-8837, 8 cores, 2.66GHz), 3.5 TB RAM (8GB/core) and 140 TB disk space. All following simulations are conducted as parallel jobs on 32 cores.

## 4.1 No-slip simulations

In Table 4.1 an overview is given of the simulations conducted in this section. Each simulation has an identifier in the first column, which will be used in the subsequent text to refer to the according simulation. In column “ $q_{\text{geo}}$ ” the data set for the geothermal heat flux is listed, where *Purucker* stands for the data by Purucker 2012 (updated version of *Fox Maule et al.*, 2005), *Fox* for the data from (*Fox Maule et al.*, 2005) and *Shapiro* for the data from *Shapiro and Ritzwoller* (2004), all described in Section 3.1.5. Further it is listed in column “source” if the source term for internal heat production (refer to Eq. 2.13 and Section 4.1.3) is applied. This is only relevant, if both, the flow model and the thermal model is solved. In column “ $u, p$ ” it is listed if the ice flow model is used (refer to Section 3.2.2) and in column “ $T$ ” if the thermal model is used (refer to Section 3.2.3). If the thermal model is not used, either a constant temperature (e.g. T\_const (-10°C)) or a constant temperature field (e.g. T\_field (qp-ref1)), where in brackets, the run from which the temperature field is taken, is listed (refer to Section 4.2). The

column "convergence" contains the minimum error (Eq. (3.3)) reached for the according simulation. All simulations are conducted with a *Fully Coupled Solver* described in Section 3.2.5.

Table 4.1: Overview of simulations conducted for Section "No-slip simulations"

identifier	$q_{\text{geo}}$	source	$\mathbf{u}, p$	$T$	convergence
qp_s	<i>Purucker</i>	yes	yes	yes	3.1e-05
qp_ns	<i>Purucker</i>	no	yes	yes	1.2e-03
qp_T	<i>Purucker</i>	no	no	yes	2.7e-10
qc_up	-	-	yes	T_const (-10°C)	3.9e-07
qp_up	<i>Purucker</i>	-	yes	T_field (qp_ref1)	5.8e-07
qf_up	<i>Fox</i>	-	yes	T_field (qf_ref1)	6.7e-07
qs_up	<i>Shapiro</i>	-	yes	T_field (qs_ref1)	4e-08

#### 4.1.1 Driving stress

When describing glacier flow inertial forces are negligible (refer to Section 2.1.2). Even though the ice is in motion, a glacier is effectively in static equilibrium. This gives rise to a force balance analysis, assuming the sum of all forces to be zero (*Cuffey and Paterson, 2010*). The driving stress is balanced by resistive stresses. The driving stress  $\tau_d$  is given by the gradients of forces exerted by the ice and the resistive stresses are the basal drag  $\tau_b$ , the lateral or wall drag  $\tau_w$  and the longitudinal drag  $\tau_l$ , also called internal drag, described by the ice viscosity  $\mu$  (*Benn and Evans, 2010*), such that

$$\tau_d = \tau_b + \tau_w + \tau_l. \quad (4.1)$$

The driving stress can be interpreted as the action which drives the flow of the ice. A change in the velocity field can thus be due to a change in either of the components in the above equation. Thus the flow velocities of a glacier can be influenced by either a change in the driving stress  $\tau_d$  due to surface steepening, shown to happen on Pine Island Glacier by *Scott et al. (2009)*, or by a change in the resistive stresses  $\tau_b$ ,  $\tau_w$  or  $\tau_l$  (*Joughin et al., 2003*). The wall drag  $\tau_w$  can for example change due to rifts in shear margins (*MacGregor et al., 2012*), the longitudinal drag  $\tau_l$  due to changes of the ice temperature and the basal drag  $\tau_b$  for example due to varying availability of sediment or/and water (*Smith et al., 2012, 2013*).

In most cases the basal drag  $\tau_b$  is the most dominant of the resistive stresses (*Cuffey and Paterson, 2010*). Following *Greve and Blatter (2009)* the driving stress can be constructed for the SIA and is given by

$$\tau_{d,\text{SIA}} = -\tau_{b,\text{SIA}} = -\rho_i g H \begin{pmatrix} \frac{\partial z_s}{\partial x} \\ \frac{\partial z_s}{\partial y} \end{pmatrix}, \quad (4.2)$$

The SIA driving stress  $\tau_{d,\text{SIA}}$  corresponds to the negative of the SIA basal shear stress  $\tau_{b,\text{SIA}}$ . This shows, that the forces are balanced locally at the base of the ice.

The concept of the force balance is though not only applicable to the SIA. In the full-Stokes problem the forces are not balanced locally, and so called *bridging effects* have to be considered, leading to  $|\tau_d| = f' |\tau_b|$ , whereby  $f'$  usually is within the range 0.5 to 1.5 (Cuffey and Paterson, 2010). The forces still balance on average over the total ice sheet (Greve and Blatter, 2009).

For the geometry of Pine Island Glacier the norm of the SIA basal drag  $|\tau_{b,SIA}|$  (Eq. 4.2) is shown in Figure 4.2. The norm of the simulated basal drag  $|\tau_{b,qp,s}|$  from simulation qp\_s is shown, together with the numbered tributaries, in Figure 4.3.

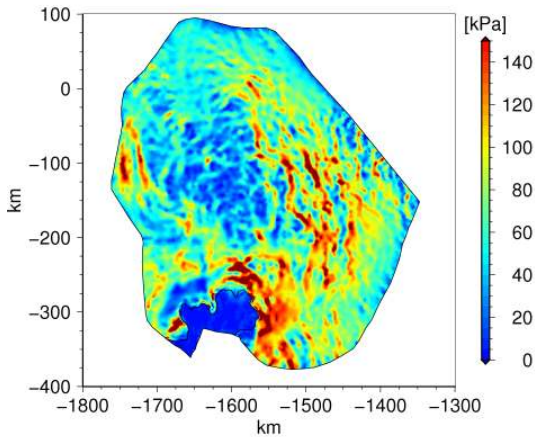


Figure 4.2: SIA basal drag  $|\tau_{b,SIA}|$

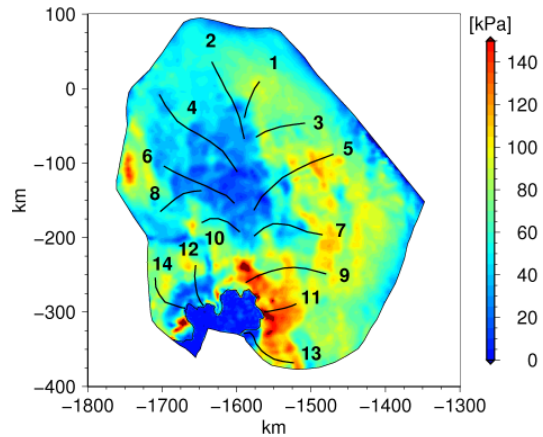


Figure 4.3: Sim. basal drag  $|\tau_{b,qp,s}|$

In the SIA basal drag  $|\tau_{b,SIA}|$ , in Figure 4.2, small scale features are visible, because the surface gradient is taken to represent the local surface slope. These small scale features should not effect the flow of the ice, as the surface slope should be interpreted as the average value over distances of several times the ice thickness (Cuffey and Paterson, 2010).

The simulated full-Stokes basal drag  $|\tau_{b,qp,s}|$ , in Figure 4.3, shows a much smoother field but the overall structure of low and high drag areas is similar. Important to note is though the high basal drag in the central trunk near the grounding line, which is not present in the SIA basal drag  $|\tau_{b,SIA}|$ . It is likely to be caused by the drastic change of boundary conditions across the grounding line, from no-slip to free slip conditions.

The overall distribution of basal drag  $\tau_b$  agrees also with simulations from Joughin *et al.* (2009) and Morlighem *et al.* (2010). Morlighem *et al.* (2010) compare the basal drag patterns for Pine Island Glacier simulated by a FS-, a SSA- and a HOM-model, which include different degrees of approximations to the Stokes equations (refer to Section 1.2.1). They find the basal drag near the grounding line to be lower for the FS-model, and argue that the SSA- and HOM-model overestimate the basal drag due to neglect of bridging effects. This argument contradicts the results of Joughin *et al.* (2009), who find low basal drag near the grounding line despite the use of a SSA-model. Joughin *et al.* (2010) suspect the difference to be caused by the different inversion procedures applied in the two studies (Joughin *et al.*, 2010, Auxiliary material).

### 4.1.2 Heat conduction

In this section we are analysing the effect of heat conduction alone, thus not considering any advection of heat, onto the basal temperature  $T_b$ . For this we investigate the results from simulation qp-T (refer to Table 4.1), which is solved for heat conduction alone.

The effect of heat conduction can also be estimated with a simplified approach. For this we need a basal heat flux  $q_{\text{geo}}$ , which is described as a temperature gradient normal to a surface. By neglecting the slope of the basal surface under the ice and assuming a constant thermal conductivity  $\kappa$ , we can write

$$\text{grad } T \cdot \mathbf{n} \approx -\frac{\partial T}{\partial z} = \frac{q_{\text{geo}}}{\kappa}. \quad (4.3)$$

Without advection and in equilibrium the gradient can be written such that

$$\frac{\partial T}{\partial z} = \frac{T_s - T_b}{z_s - z_b} = \frac{T_s - T_b}{H} = -\frac{q_{\text{geo}}}{\kappa} \Rightarrow T_b = \frac{q_{\text{geo}} H}{\kappa} + T_s. \quad (4.4)$$

The result of simulation qp-T for the homologous basal temperature  $T'_{b,\text{qp-T}}$ , the temperature relative to the pressure melting point  $T_{\text{pmp}}$ , is shown in Figure 4.4. The temperatures are only shown for the grounded areas, as the shelf is not subject to the geothermal heat flux  $q_{\text{geo}}$ .

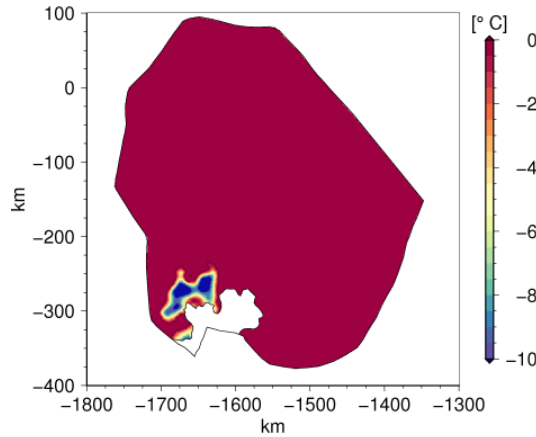


Figure 4.4:  $T'_{b,\text{qp-T}}$

The simulated basal temperature  $T_{b,\text{qp-T}}$  reaches temperatures above  $T_{\text{pmp}}$ , which is not physical. For ice the temperature can not be higher than the pressure melting point  $T_{\text{pmp}}$ , as it would start to melt. Here we are interested in the effect of the geothermal heat flux and the ice thickness and therefore ignore for the moment the physically unrealistic setting. With this setting areas can be identified where the ice would be at pressure melting point  $T_{\text{pmp}}$  solely due to its thickness and the geothermal heat flux. In Figure 4.4 it can be seen, that with the geothermal heat flux from *Purucker* and heat conduction alone, almost the entire ice sheet would be at pressure melting point with  $T'_{b,\text{qp-T}} \geq 0$ . Only a small area near the grounding line is colder, which is due to the relatively thin ice of 10 m to 300 m in that area.

When comparing the simulated field of  $T_{b,qp\_T}$  to the field of  $T_b$  calculated with the simplified formula given in Eq. 4.4, a maximal difference in the warmest part of  $7^\circ\text{C}$  is found. The difference is due to the neglected slope and a constant thermal conductivity  $\kappa = 2.2 \text{ W (m K)}^{-1}$ , in the simplified formula. For the simulation qp\_T the temperature used to calculate the thermal conductivity  $\kappa(T)$  (refer to Eq. (2.14)) is held at pressure melting point  $T_{pmp}$  for temperatures higher than  $T_{pmp}$ , as it is not defined for those.

### 4.1.3 Strain heating

In this section we focus on the effect of internal strain heating along the simulations qp\_ns and qp\_s (refer to Table 4.1).

The no-slip simulations are a highly artificial set up. The ice is fixed at the base, which would imply that the ice is frozen to the bed. But at the same time we solve for the temperature which leads to temperatures at pressure melting point  $T_{pmp}$  in most areas at the base. The way the thermal basal boundary condition is implemented (refer to Section 3.2.3) it does prevent the temperatures from rising much higher than  $T_{pmp}$  by reducing the geothermal heat flux. There is no upper limit though for the heat produced by internal strain heating. The amount of internal strain heating is defined by the source term  $\psi$ , which connects the kinetic energy and the internal energy (refer to Section 2.1.3) and is defined as (e.g. *Greve and Blatter, 2009*)

$$\psi = 4\mu\dot{\varepsilon}_e^2, \quad (4.5)$$

with the viscosity  $\mu$  and the effective strain rate  $\dot{\varepsilon}_e$ . In a next step the available extra energy could be used to calculate the amount of ice that would melt. This in turn would have an impact on the ice geometry. Since the set up is artificial anyway we neglect the unphysical result for now and use this experiment to investigate the effect of the source term and to identify areas mostly effected by it.

To do so we consider the simulations qp\_ns, which does not include the source term in the heat transfer equation (Eq. (2.12)), and simulation qp\_s, which does include the source term. By doing this we identify the contribution of strain heating onto the overall temperature distribution.

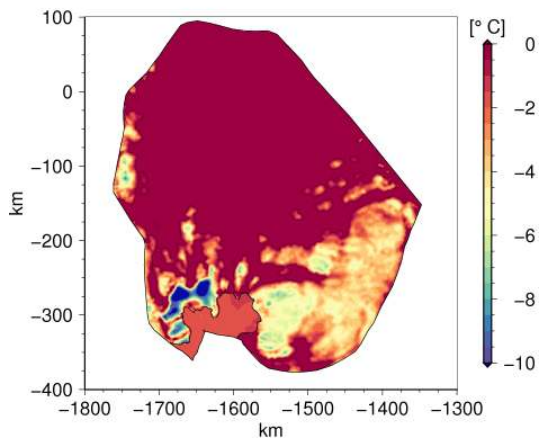


Figure 4.5:  $T'_{b,qp\_ns}$

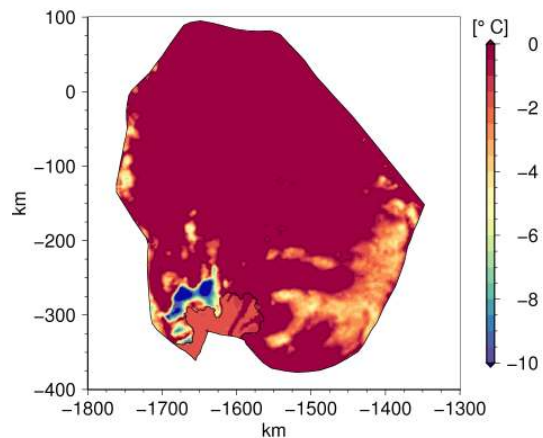


Figure 4.6:  $T'_{b,qp\_s}$

The results of the simulation qp\_ns are shown in Figure 4.5 for the homologous basal temperature  $T'_{b,qp\_ns}$ . The results of the simulation qp\_s are shown in Figure 4.6 for the homologous basal temperature  $T'_{b,qp\_s}$ .

For simulation qp\_s some areas show very high temperatures of  $T > 2^\circ\text{C}$ , which also advect into the shelf. The total area being at pressure melting point  $T_{pmp}$  is bigger for simulation qp\_s than for qp\_ns, as can be seen by comparing Figure 4.5 and Figure 4.6. When comparing the temperate area fraction of simulation qp\_ns (Figure 4.5) and qp\_s (Figure 4.6) now to that of the simulation with only heat conduction considered qp\_T (Figure 4.4), it is apparent that introducing advection does cool the ice at the base. This is caused by cold ice from the surface being advected down and out towards the shelf.

Since the ice is warmer in simulation qp\_s than in simulation qp\_ns, it would be expected to flow faster. That this is really the case is shown in the next section, in Figures 4.18 and 4.16, which show the surface velocity fields for simulations qp\_s and qp\_ns respectively.

Introducing advection by trend cools the base of the ice. Warmer ice temperatures lead to higher deformational velocities, which would by trend cool the base of the ice further. At the same time simulation qp\_s shows a bigger temperate ice area fraction than simulation qp\_ns. We conclude that even though faster ice would by trend cool the ice, the source term dominates to warm the ice at the base.

To investigate the cause for the pattern of the basal temperature due to the source term in Figure 4.6, in a next step we will look at the single components contributing to the heating. The source term  $\psi$  is composed of the viscosity  $\mu$  and the squared effective strain rate  $\dot{\epsilon}_e^2$  (refer to Eq. (4.5)). Figure 4.7 shows the spatial distribution of the source term  $\psi$  at the base of the ice, Figure 4.8 shows the spatial distribution of the viscosity  $\mu$  at the base and Figure 4.9 of  $\dot{\epsilon}_e^2$ , also at the base, all for the simulation qp\_s.

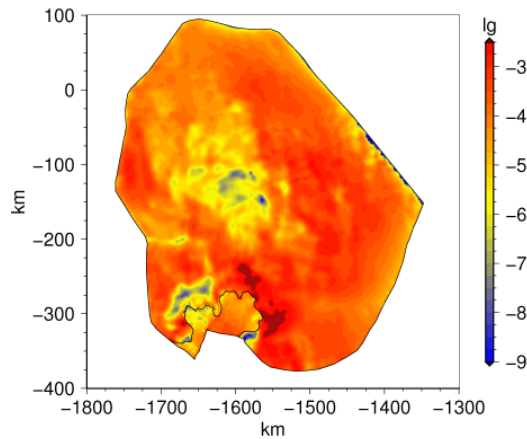
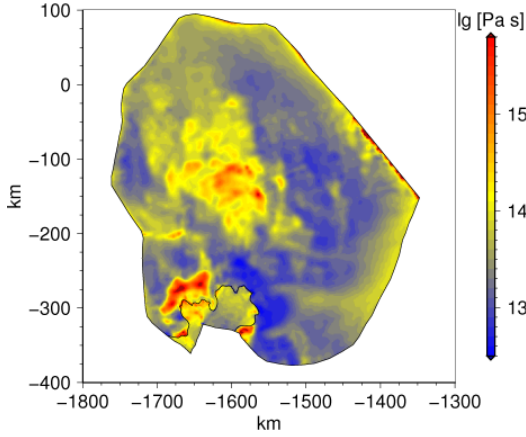
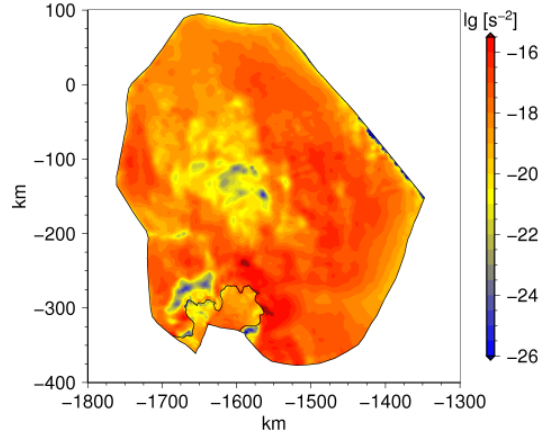


Figure 4.7: Basal source term  $\psi$

The areas with the highest source term (Figure 4.7) partly coincide with the warmest areas in simulation qp\_s (not shown here), which is not surprising. It is also apparent, that the effective strain rate  $\dot{\epsilon}_e$  alone controls the pattern of  $\psi$ , while the viscosity  $\mu$  (Figure 4.8) slightly dampens the effect, with lower values for higher temperatures.

To investigate which terms in the effective strain rate  $\dot{\epsilon}_e$  are the most dominant, we untangle the term further. Following *Greve and Blatter (2009)* the effective strain rate  $\dot{\epsilon}_e$


 Figure 4.8: Basal viscosity  $\mu$ 

 Figure 4.9: Basal effective strain rate  $\varepsilon_e^2$ 

is given by

$$\begin{aligned} \varepsilon_e = \sqrt{\varepsilon_{11}^2 + \varepsilon_{22}^2 + \varepsilon_{11}\varepsilon_{22} + \varepsilon_{12}^2 + \varepsilon_{13}^2 + \varepsilon_{23}^2} = & \left\{ \left( \frac{\partial u}{\partial x} \right)^2 + \left( \frac{\partial v}{\partial y} \right)^2 + \frac{\partial u}{\partial x} \frac{\partial v}{\partial y} \right. \\ & \left. + \frac{1}{4} \left( \frac{\partial u}{\partial y} + \frac{\partial v}{\partial x} \right)^2 + \frac{1}{4} \left( \frac{\partial u}{\partial z} + \frac{\partial w}{\partial x} \right)^2 + \frac{1}{4} \left( \frac{\partial v}{\partial z} + \frac{\partial w}{\partial y} \right)^2 \right\}^{1/2}. \end{aligned} \quad (4.6)$$

We now look at the different terms and their contribution to the source term  $\psi$ . Therefore we define

$$\begin{aligned} D1 &= \sqrt{\left( \frac{\partial u}{\partial x} \right)^2}; & D2 &= \sqrt{\left( \frac{\partial v}{\partial y} \right)^2}; & D3 &= \sqrt{\left( \frac{\partial u}{\partial x} \frac{\partial v}{\partial y} \right)} \\ D4 &= \sqrt{\frac{1}{4} \left( \frac{\partial u}{\partial y} + \frac{\partial v}{\partial x} \right)^2}; & D5 &= \sqrt{\frac{1}{4} \left( \frac{\partial u}{\partial z} + \frac{\partial w}{\partial x} \right)^2}; & D6 &= \sqrt{\frac{1}{4} \left( \frac{\partial v}{\partial z} + \frac{\partial w}{\partial y} \right)^2} \end{aligned}$$

The spatial patterns at the base of the ice of the different terms D1-D6 are shown in Figures 4.10-4.15, respectively. Figure 4.10 is displayed in latitude and longitude, to facilitate the pattern description in terms of cardinal directions, while Figures 4.10-4.15 are displayed in Polarstereographic coordinates, as done before.

The term D1 (Figure 4.10), which is  $\frac{\partial u}{\partial x}$ , has the highest values of  $10^{-7.7}$  to the South of the ice shelf, near the grounding line, and on the northern side of the curvature of the grounding line in the central flow area. This displays the effect of the ice flowing from the South into the ice shelf, thus in positive x-direction.

The term D2 (Figure 4.11) has by far the highest values in the grounded part in flow direction just before the grounding line. This is not surprising as the term is basically  $\frac{\partial v}{\partial y}$ , the main flow direction is in negative y-direction and at the grounding line the basal condition changes from no-slip to free slip. The values are as high as  $10^{-6.2}$  in that area.

The terms D3 (Figure 4.12) and D4 (Figure 4.13) have similar moderate patterns with the maximal values of  $10^{-8.1}$  and  $10^{-8.0}$ , respectively, near the grounding line.

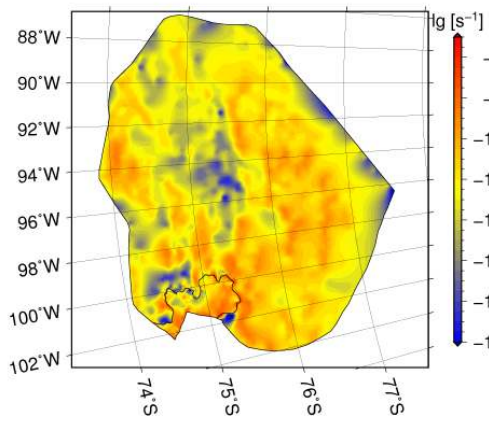


Figure 4.10: D1

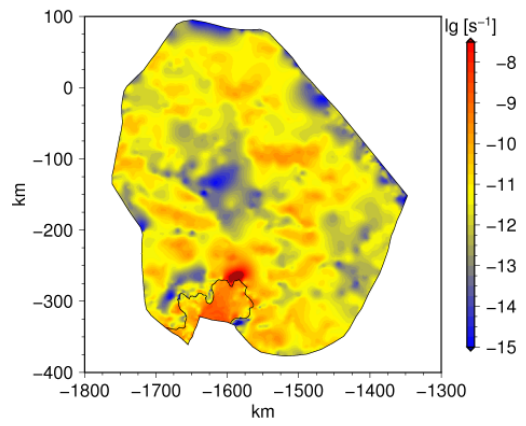


Figure 4.11: D2

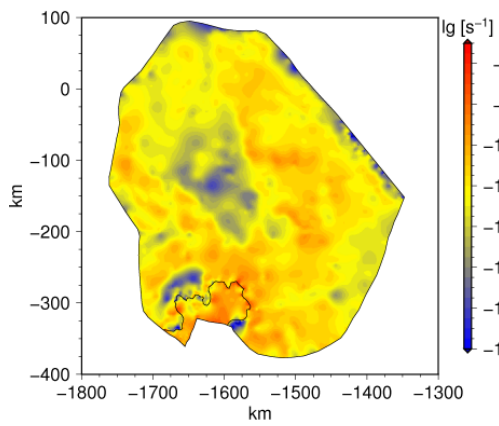


Figure 4.12: D3

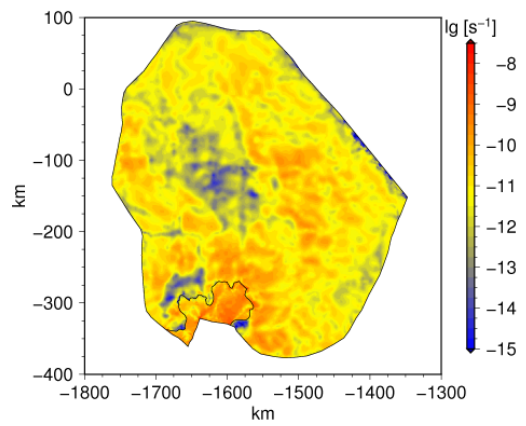


Figure 4.13: D4

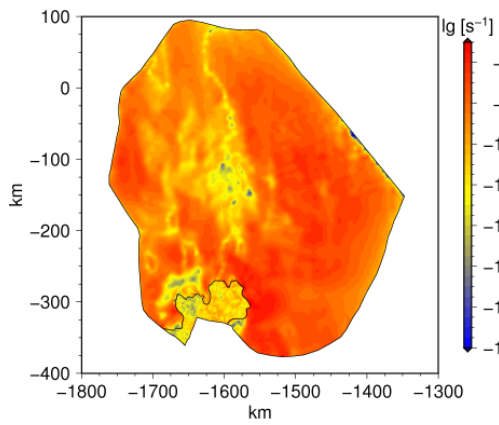


Figure 4.14: D5

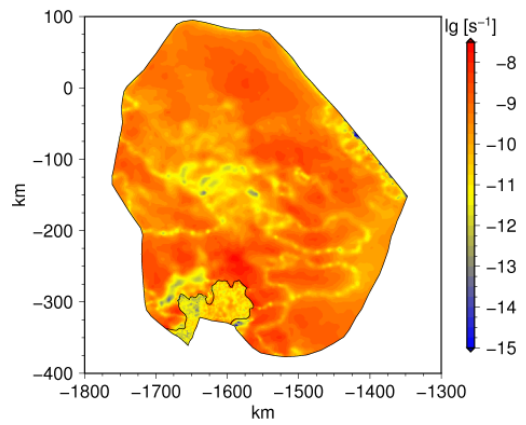


Figure 4.15: D6

The terms D5 (Figure 4.14) and D6 (Figure 4.15) have on average much higher values than D1-D4. The maximal value of D5 and D6 is  $10^{-7.1}$ . The term D5 has higher values to the South of the ice shelf, again reflecting the flow from the side in positive x-direction into the ice shelf, while the term D6 has higher values near the grounding line in the central flow trough, reflecting the flow in negative y-direction.

All terms reflect the pattern of the driving stress (Figure 4.2-4.3), with the highest shear terms in the areas with largest driving stress.

#### 4.1.4 Internal deformation

Since the ice is fixed at the base, the simulated surface velocity is solely due to internal deformation. The strain rate  $\dot{\epsilon}$  is strongly influenced by the temperature distribution within the ice (refer to Section 2.2.2). By comparing the different simulated surface velocity fields to the measured surface velocity field  $|\mathbf{u}_{\text{obs}}|$ , shown in Figure 4.1 and introduced in Section 3.1.6, we aim to infer some further insight into likely and unlikely temperature distributions. A much higher simulated than measured surface velocity could for example indicate, that the ice temperature is too high, which leads to softer ice and higher strain rates.

The surface velocity vector fields  $\mathbf{u}_s$ , compared in this section, consist of the two horizontal velocity components  $u_s$  and  $v_s$ , such that  $\mathbf{u}_s = (u_s, v_s)$ . The simulated surface velocities from the no-slip simulations are named  $\mathbf{u}_{s,\text{nosl}}$ , with *nosl* being the according simulation identifier from Table 4.1.

The error in measured surface velocity magnitude  $|\mathbf{u}_{\text{obs}}|$  in the Pine Island Glacier region is  $2.5 - 5.5 \text{ m a}^{-1}$  (Rignot *et al.*, 2011, Supporting Online Material). Thus the relative error for lower velocities is higher and therefore our method has to be considered with care.

The first simulation considered here is the no-slip simulation qc\_up, with a constant temperature of  $-10^\circ\text{C}$ . The temperature  $-10^\circ\text{C}$  is chosen, as it was used in previous studies to estimate the internal deformation (e.g. Stenoien and Bentley, 2000).

The other three simulations considered here are the no-slip simulations qp\_up, qf\_up and qs\_up. The flow fields are simulated with constant temperature fields, which correspond to a realistic flow field and the heat fluxes from Purucker, Fox and Shapiro (refer to Section 3.1.5), respectively.

To receive a realistic temperature field within the ice, the velocity patterns need to be reproduced. This is achieved with a method introduced in the next section, Section 4.2. The procedure described in Section 4.2 is conducted for the different geothermal heat fluxes, with use of results from simulation qp\_s. These simulations, qp\_ref1, qf\_ref1 and qs\_ref1, show temperature distributions dependent on the flow field and corresponding geothermal heat fluxes. These temperature fields are used for simulations qp\_up, qf\_up and qs\_up, respectively, as a constant input field.

In the following we show the surface velocity fields  $|\mathbf{u}_{s,\text{nosl}}|$ , and the differences between the simulated and measured surface velocity fields  $|\mathbf{u}_{\text{obs}}| - |\mathbf{u}_{s,\text{nosl}}|$ , in the grounded areas for the four simulations. The surface velocity fields are shown in Figures 4.16, 4.18, 4.20 and 4.22 for simulations qc\_up, qp\_up, qf\_up and qs\_up, respectively. The differences between the simulated and measured surface velocity fields are shown in Figures 4.17, 4.19, 4.21 and 4.23 for simulations qc\_up, qp\_up, qf\_up and qs\_up, respectively.

The differences  $|\mathbf{u}_{\text{obs}}| - |\mathbf{u}_{s,\text{nosl}}|$  are shown from  $-40$  to  $65 \text{ m a}^{-1}$ . Negative values indicate hereby that the simulated surface velocity is too large compared to the measured surface

velocity. Positive areas are seen as dominated by basal sliding, as this mechanism is not considered in the no-slip simulations.

All four simulations have in common, that the highest surface velocities are coinciding

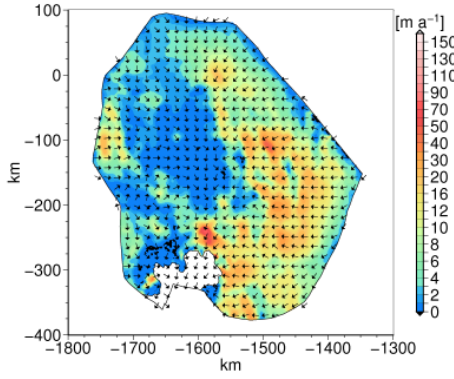


Figure 4.16:  $|u_{s,qc-up}|$

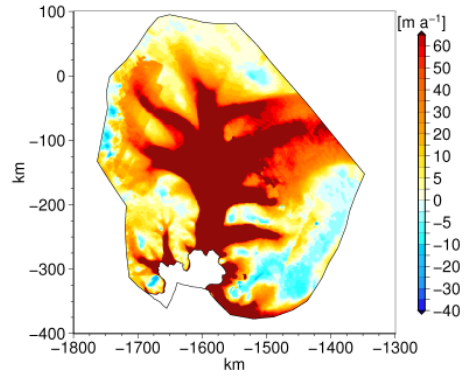


Figure 4.17:  $|u_{obs}| - |u_{s,qc-up}|$

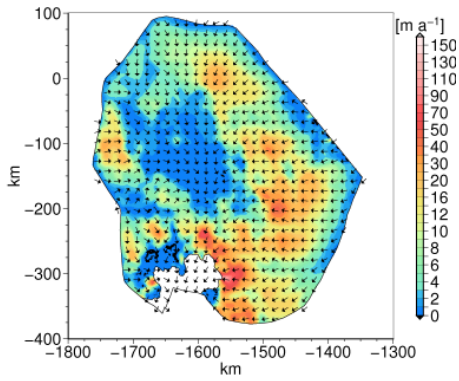


Figure 4.18:  $|u_{s,qp-up}|$

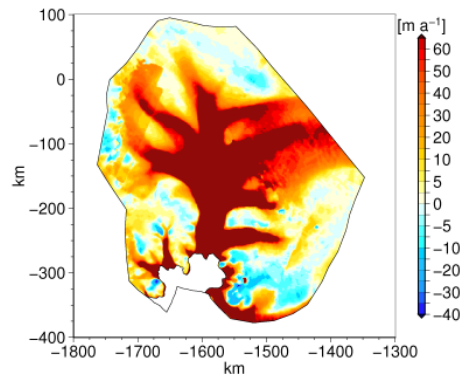


Figure 4.19:  $|u_{obs}| - |u_{s,qp-up}|$

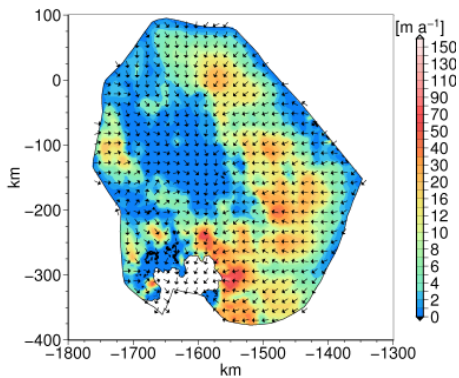


Figure 4.20:  $|u_{s,qf-up}|$

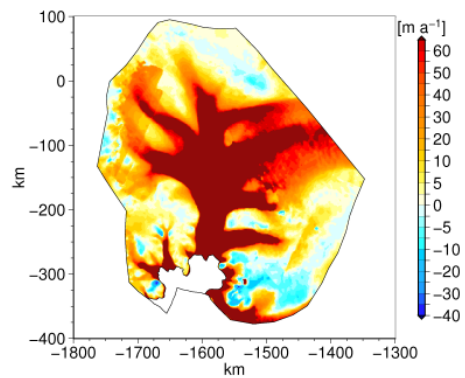
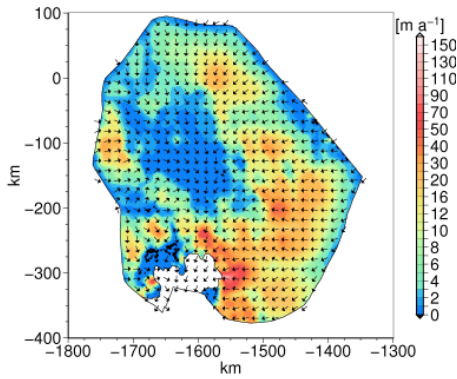
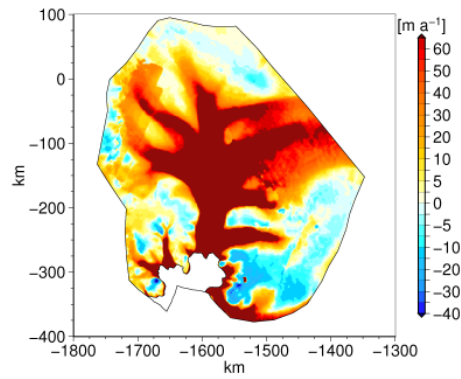


Figure 4.21:  $|u_{obs}| - |u_{s,qf-up}|$

Figure 4.22:  $|\mathbf{u}_{s,qs-up}|$ Figure 4.23:  $|\mathbf{u}_{obs}| - |\mathbf{u}_{s,qs-up}|$ 

with areas of higher driving stress. This is not a surprising result, as the driving stress initiates internal deformation, which is reflected in the surface velocity field. As the main trunk of the ice stream partly coincides with an area of very low driving stress, it is reflected in low deformational velocities in those areas. Other factors must thus be driving the flow in this area. The flow structure is likely dominated by shelf like flow, with small vertical variations in the horizontal velocity components. High basal sliding velocities must be present, where the simulated deformational velocity is much smaller than the measured surface velocity. This is visible in the Figures showing the difference  $|\mathbf{u}_{s,nosl}|$  (Figures 4.17, 4.19, 4.21 and 4.23), where areas with  $|\mathbf{u}_{s,nosl}| > 65 \text{ m a}^{-1}$  are shown in dark red and interpreted as being dominated by basal sliding. The value of  $65 \text{ m a}^{-1}$  is chosen somewhat arbitrarily, and just serves as an indicator.

All simulations show areas, where the simulated velocity is higher than the observed one, indicated by negative values. Most of these areas differ by a maximum of  $10 \text{ m a}^{-1}$ , which is about the magnitude of the measurement error. Simulation qc\_up, with a constant temperature of  $-10^\circ\text{C}$  suggests, that most parts are dominated by basal sliding, shown in Figure 4.17.

The simulation qs\_up shows the biggest areal extent of negative values, shown in Figure 4.23, and overestimates the surface velocities in parts by as much as  $619 \text{ m a}^{-1}$ . The other simulations qc\_up, qp\_up and qf\_up overestimate maximal with  $681 \text{ m a}^{-1}$ ,  $615 \text{ m a}^{-1}$  and  $606 \text{ m a}^{-1}$ , respectively.

## 4.2 Reference simulations

Pine Island Glacier has a distinct surface flow pattern (Figure 4.1), which can not be explained solely by internal deformation (refer to Section 4.1.4). In large areas basal sliding must be present. To capture this in a flow model, assumptions about the base have to be made, which is widely unknown. In Section 4.2.1 we introduce a method to get around the difficulty of making appropriate assumption about the ground, and still produce a somewhat realistic surface velocity field. This simulation, discussed in Section 4.2.2, will in the subsequent work be used as a reference simulation. It is necessary to have such a reference simulation, which is validated against observed surface velocities, to

distinguish effects from the model itself to effects due to the experimental set up.

In Section 4.2.4 we estimate the effect of parameterising the microscopic water content in the viscosity onto the flow field. In Section 4.2.5 the importance of using a full-Stokes model for Pine Island Glacier is demonstrated on the basis of the reference simulation. And finally, in Section 4.2.6 the sensitivity of the basal temperature distribution on different geothermal heat fluxes is shown.

Table 4.2 gives an overview of all simulations conducted for this section. The first column again contains the simulation identifier. The geothermal heat flux, listed in column "q<sub>geo</sub>", is for *Purucker* from Purucker 2012 (updated version of *Fox Maule et al.*, 2005), for *Fox* from (*Fox Maule et al.*, 2005) and for *Shapiro* from *Shapiro and Ritzwoller* (2004) (all described in Section 3.1.5), for  $q_{\text{geo,const}}$  as constant value of  $0.06 \text{ W m}^{-2}$  and for  $q_{\text{geo,art}}$  an artificial data set, described in detail in Section 4.2.6, is used. The columns "fric.heat", " $\mathbf{u}, p$ " and " $T$ " describe the insertion of the friction heating term, the use of the ice flow model and the use of the thermal model, respectively. All simulations are carried out with a *Segregated Solver* described in Section 3.2.5, as for the *Fully Coupled Solver* the temperature field does not converge. Therefore, the convergence for the velocity field and the temperature is stated separately in columns "conv. $\mathbf{u}, p$ " and "conv. $T$ ", respectively. Column " $\beta^2$ " contains the simulation identifier on which the inversion technique is based and will be further explained in the subsequent sections. Column " $A$ " lists, if the simulation is conducted with the rate factor for cold or temperate ice (refer to Section 2.2.2).

Table 4.2: Overview of simulations conducted for Section "Reference simulations"

identifier	$q_{\text{geo}}$	fric.heat	$\mathbf{u}, p$	$T$	conv. $\mathbf{u}, p$	conv. $T$	$\beta^2$	$A$
qp_ref1	<i>Purucker</i>	yes	yes	yes	1.7e-08	2e-06	qp_s	$A(T, p)$
qp_ref2	<i>Purucker</i>	yes	yes	yes	1.7e-08	1.6e-06	qp_up	$A(T, p)$
qp_ref3	<i>Purucker</i>	yes	yes	yes	7.6e-05	3e-04	qp_up	$A_t(T, p, W)$
qp_ref4	<i>Purucker</i>	yes	yes	yes	3.9e-06	2.7e-05	qp_up	$A_t(T, p, W = 1\%)$
qf_ref1	<i>Fox</i>	yes	yes	yes	4.9e-08	2e-05	qp_s	$A(T, p)$
qf_ref2	<i>Fox</i>	yes	yes	yes	3.9e-06	4.9e-06	qf_up	$A(T, p)$
qs_ref1	<i>Shapiro</i>	yes	yes	yes	9.6e-09	3.7e-06	qp_s	$A(T, p)$
qs_ref2	<i>Shapiro</i>	yes	yes	yes	7.1e-07	1.6e-05	qs_up	$A(T, p)$
qc_ref1	$q_{\text{geo,const}}$	yes	yes	yes	1.5e-07	2.8e-06	qp_up	$A(T, p)$
qc_ref2	$q_{\text{geo,const}}$	no	yes	yes	3.3e-05	1.4e-04	qp_up	$A(T, p)$
qc_ref3	$q_{\text{geo,const}}$	no + ns	yes	yes	6.7e-03	1.5e-02	qp_up	$A(T, p)$
qv_ref1	$q_{\text{geo,art}}$	yes	yes	yes	1.5e-07	3.5e-06	qp_up	$A(T, p)$

### 4.2.1 Quasi-inversion technique

Many ice modelling studies use a constant set of basal sliding parameters to reproduce somewhat realistic surface velocity fields (e.g. *Kleiner*, 2010; *Rückamp*, 2011). This approach can not be adopted for Pine Island Glacier (refer to Section 5.3). From the observed

flow pattern of Pine Island Glacier it is apparent, that locally varying basal conditions must be present. To capture these, spatial varying assumptions have to be made about basal sliding parameters. A common approach to avoid this problem is to infer the basal sliding parameter from control methods (e.g. *MacAyeal, 1992; Joughin et al., 2009; Morlighem et al., 2010*). We will briefly introduce this approach, although it is not used here, to then explain our simplified method.

The control method approach is prepared by rewriting Eq. (2.43) with

$$F_b^{-1} = C_b^{-1} |\tau_b|^{1-p} N_b^q f(T)^{-1} = \beta^2, \quad (4.7)$$

such that

$$\tau_b = \beta^2 \mathbf{u}_b \quad (4.8)$$

with  $\beta^2$  being the basal sliding parameter to be inferred. It is squared to ensure that the basal drag represents a sink to the mechanical energy at all points (*MacAyeal, 1992*).

The explicit problem can be written as

$$\mathbf{u} = G(\beta) \quad (4.9)$$

with the velocity field  $\mathbf{u} \in U$ , the sliding parameter  $\beta \in B$  and an operator  $G : B \rightarrow U$  representing the model equations. If a set of surface velocity measurements  $\mathbf{u}_{\text{obs}}$  is available, an inverse problem formulation can be made to receive a set of  $\beta \in B$ , such that

$$\beta = G^{-1}(\mathbf{u}_{\text{obs}}) \quad (4.10)$$

is fulfilled. For ice sheet modelling there is usually no explicit formulation of  $G^{-1}$ . And the problem is often either over-determined, such that a solution does not exist, or under-determined, such that the solution is not unique. Therefore a minimisation problem is introduced, to ensure the model output is as close as possible to the observations

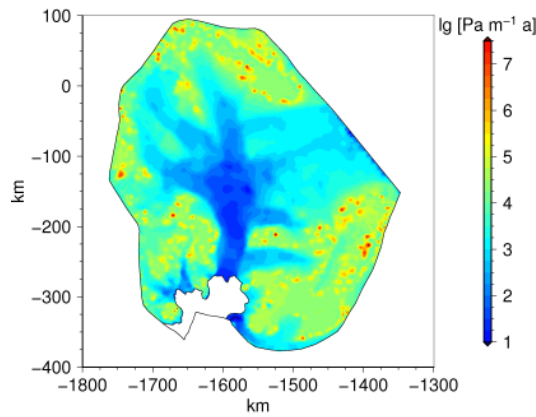
$$\min \|G(\beta) - \mathbf{u}_{\text{obs}}\|. \quad (4.11)$$

For further details refer to *Morlighem (2011)*.

We chose a different simplified approach. Our aim is to produce a realistic flow field to validate the model on a realistic case, and furthermore to initialise the temperature field. We call the approach “quasi-inversion” for  $\beta^2$  (cf. *Schmeltz et al., 2002*). Instead of minimising the misfit between observed and simulated surface velocities, the following assumptions are made: the basal drag  $\tau_b$  is very similar if no sliding is allowed and the basal sliding velocity  $\mathbf{u}_b$  can be approximated by subtracting the surface velocity due to internal deformation  $\mathbf{u}_{\text{s,nosl}}$  from the measured surface velocity field  $\mathbf{u}_{\text{obs}}$ . The basal sliding parameter  $\beta^2$  is then defined as

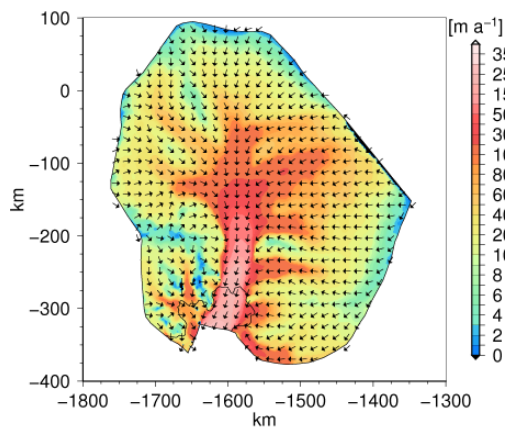
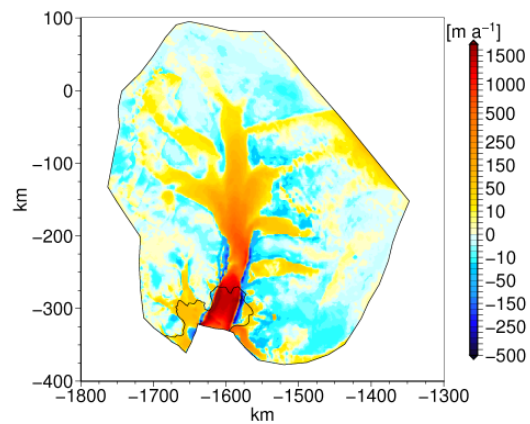
$$\beta^2 = |\tau_{\text{b,nosl}}| (|\mathbf{u}_{\text{obs}}| - |\mathbf{u}_{\text{s,nosl}}|)^{-1}. \quad (4.12)$$

The column “ $\beta^2$ ” in Table 4.2 indicates from which no-slip simulation the values for Eq. (4.12) are taken. Figure 4.24 shows the spatial distribution of  $\beta^2$  for the reference simulation qp\_ref2, described in the next section.

Figure 4.24: Spatial distribution of  $\beta^2$ 

### 4.2.2 Reference simulation

In this section we discuss the reference simulation qp\_ref2. The simulation qp\_ref2, with the geothermal heat flux from Purucker 2012 (updated version of *Fox Maule et al., 2005*), is chosen as a reference, as the heat flux is identified as the most realistic (refer to Section 4.1.4). Simulation qp\_ref1 is already described in Section 4.1.4 and only needed to receive a realistic temperature field for simulation qp\_up. For simulation qp\_ref2 the basal drag  $\tau_{b, \text{nosl}}$  and the surface velocity due to internal deformation  $\mathbf{u}_{s, \text{nosl}}$  are taken from simulation qp\_up, as it includes the most realistic internal temperature distribution. The inferred basal sliding velocity  $|\mathbf{u}_b| = |\mathbf{u}_{\text{obs}}| - |\mathbf{u}_{s, \text{qp-up}}|$  is shown in Figure 4.23, but with negative values clipped as the norm of the sliding velocity can not be negative, such that  $|\mathbf{u}_b| = \min\{|\mathbf{u}_{\text{obs}}| - |\mathbf{u}_{s, \text{qp-up}}|, 0\}$ .

Figure 4.25:  $|\mathbf{u}_{s, \text{qp-ref2}}|$ Figure 4.26:  $|\mathbf{u}_{\text{obs}}| - |\mathbf{u}_{s, \text{qp-ref2}}|$ 

The resulting surface velocity field is shown in Figure 4.25. The main flow pattern with the different tributaries are captured (compare to the observed surface velocity field shown

in Figure 4.1). The difference between the observed and modelled surface velocity is shown in Figure 4.26. Positive values imply here that the simulated velocity field is slower than the observed one, while negative values imply that the simulated velocity field is faster.

The slower flowing areas differ by a maximum of  $\pm 50 \text{ m a}^{-1}$ . The highest differences can be seen in the ice shelf, where the simulated velocities are much smaller than the observed ones. These differences might be partly related to a slow inflow from the grounded areas.

The simulated velocity is about  $1 \text{ km a}^{-1}$  slower than the observed surface velocity just before the grounding line in flow direction. This might be due to the position of the grounding line in our model. The grounding line position in our model is further downstream than the location in 2009 (see Figure 3.5), to which the observed surface velocity field belongs (2007-2009, refer to Section 3.1.6). Or it might be caused by the inversion technique with an increased  $\tau_b$  just before the grounding line (see to Figure 4.3).

Along both sides of the central stream, for grounded and floating ice, blue bands are visible in Figure 4.26, where the simulated velocity is slower than the observed one. In satellite images (refer to Figures 3.2 and 3.5) can be seen, that these areas roughly coincide with the location of rifted shear margins. These shear margins have been shown to be rheologically softer than undamaged ice (e.g. *Humbert et al.*, 2009). In reality the shear margins partly uncouple the fast flowing central part from the surrounding ice. In our model they are not included and we treat the shear margins rheologically equal to undamaged ice. This leads to an overestimation of the flow outside the central stream, and an underestimation within the central stream in the main trunk. The softening due to shear margins could be included in the model with an increase of the enhancement factor  $E$  (refer to Section 2.2.3). *Joughin et al.* (2010) rather adjust the rate factor (refer to Section 2.2.2) in their study (*Joughin et al.*, 2010, Auxiliary material), leading to the same effect.

The observed  $|\mathbf{u}_{\text{obs}}|$  and simulated surface velocity norms  $|\mathbf{u}_{\text{s,qp-ref2}}|$  are interpolated onto a structured 5 km grid and compared point wise as shown in Figure 4.27. The colour of the circles shows the velocity magnitude of the observed field  $|\mathbf{u}_{\text{obs}}|$ . If the simulated and observed velocity fields are identical at a grid point, the according circle lies on the diagonal black line.

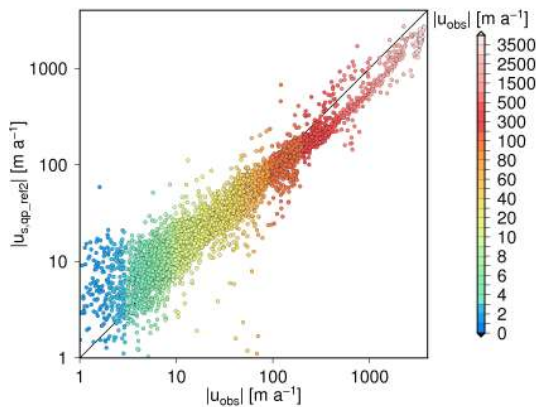


Figure 4.27:  $|\mathbf{u}_{\text{obs}}|$  versus  $|\mathbf{u}_{\text{s,qp-ref2}}|$

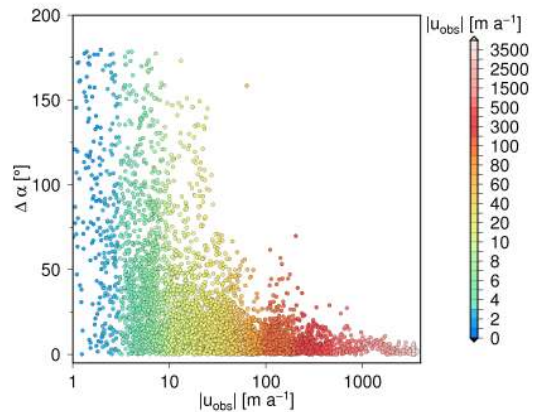


Figure 4.28:  $|\mathbf{u}_{\text{obs}}|$  versus  $\Delta\alpha$

To compare the angles of the velocity vectors on a structured 5 km grid, the difference between the angles  $\Delta\alpha$  is plotted against the observed surface velocity magnitude  $|\mathbf{u}_{\text{obs}}|$ , shown in Figure 4.28. The colour of the circles again shows the velocity magnitude of the observed field  $|\mathbf{u}_{\text{obs}}|$ .

For the velocity magnitudes in Figure 4.27 it can again be seen, that for higher velocities the simulated velocity field  $|\mathbf{u}_{\text{s,qp-ref2}}|$  is slower than the observed field  $|\mathbf{u}_{\text{obs}}|$ . The spread around the diagonal for lower velocities appears bigger, which is mainly due to the logarithmic axes chosen. The angles agree better for higher velocities, as shown in Figure 4.28. At the same time the measurement error is bigger for slower velocities.

The distribution of the homologous basal temperature  $T'_{\text{b,qp-ref2}}$  is shown in Figure 4.29. Since sliding is included in this simulation the basal temperatures are lower than in the no-slip simulations (compare to Section 4.1.3). The shear heating term is less dominant near the grounding line as there is no drastic change from no-slip to free-slip conditions. Due to the basal sliding the friction heating term  $\mathbf{u}_{\text{b}} \cdot \boldsymbol{\tau}_{\text{b}}$  (compare to Eq. 2.47) becomes important.

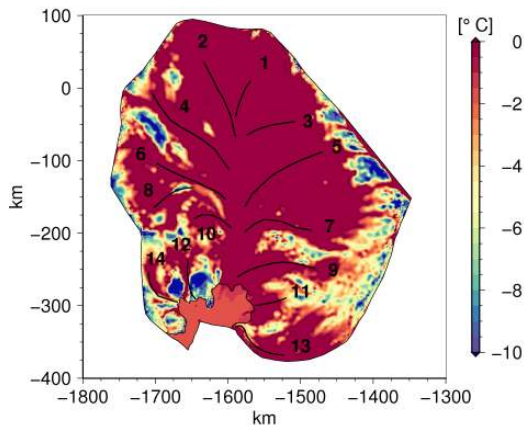


Figure 4.29:  $T'_{\text{b,qp-ref2}}$

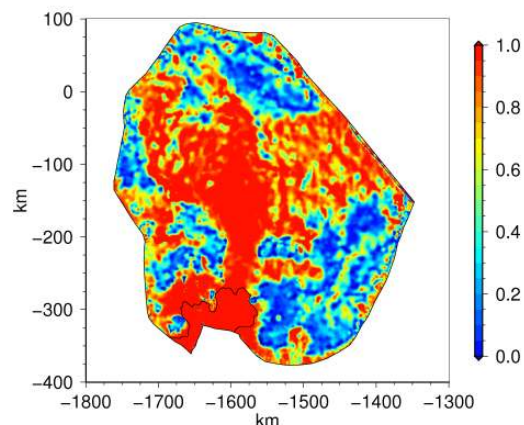


Figure 4.30:  $|\mathbf{u}_{\text{b,qp-ref2}}|/|\mathbf{u}_{\text{s,qp-ref2}}|$

To the North of the ice shelf, the area described earlier with a cold base due to thin ice, is now separated by two strings with a temperate base. They correlate with two smaller ice streams (12 and 14 in Figure 4.1). The ice is probably warmed in this area due to friction heating and the effect will be discussed further in the Section about basal roughness (Section 4.4).

In general the overall flow pattern is reflected in the basal temperature, with still the biggest part being at pressure melting point. At least in the main trough this is supported by findings with ice-penetrating radar (RES) data by *Vaughan et al.* (2001).

Figure 4.30 shows the ratio of the basal to surface velocity  $|\mathbf{u}_{\text{b,qp-ref2}}|/|\mathbf{u}_{\text{s,qp-ref2}}|$ . In the fast flowing areas the basal velocity  $|\mathbf{u}_{\text{b,qp-ref2}}|$  serves for almost the entire speed. In Figure 4.30 some areas show a ratio of one, even though the basal temperature is well below pressure melting  $T_{\text{pmp}}$ , as shown in Figure 4.29. This is for example the case near the lateral inflow region, indicated in Figure 3.2. The effect is due to our “quasi-inversion” technique, which does not couple basal sliding to the basal temperature. That the simulated surface velocity near the inflow boundary is still slower than the observed

velocity, as seen in Figure 4.26, although basal sliding is present, must thus be due to an underestimation of the inflow velocity (refer to Section 2.4 and 3.2.2).

### 4.2.3 Temperate layer

Here the temperate layer thickness ( $TLT$ ) is analysed along the reference simulation qp\_ref2. Ice is called temperate, if its temperature is at pressure melting point  $T_{\text{pmp}}$ . The ice can warm due to the pressure effect, internal strain heating or basal friction heating. Usually, and also the case for Pine Island Glacier, the annual mean surface temperature is well below  $T_{\text{pmp}}$ . The geothermal heat flux at the base prescribes a vertical temperature gradient. Without advection this gradient alone can cause parts of the ice to be at  $T_{\text{pmp}}$ , refer to Section 4.1.2. If advection is included, colder ice is transported down from the surface, by trend cooling the ice. At the same time the motion of the ice can induce internal strain heating and basal friction heating, by trend warming the ice. The internal temperature structure is given by a combination of all these effects. The homologous temperature  $T'$  from the reference simulation qp\_ref2 is shown on the 3D model for Pine Island Glacier in Figure 4.31. Cold ice is transported down from the surface, and enters the shelf ice in form of a cold core.

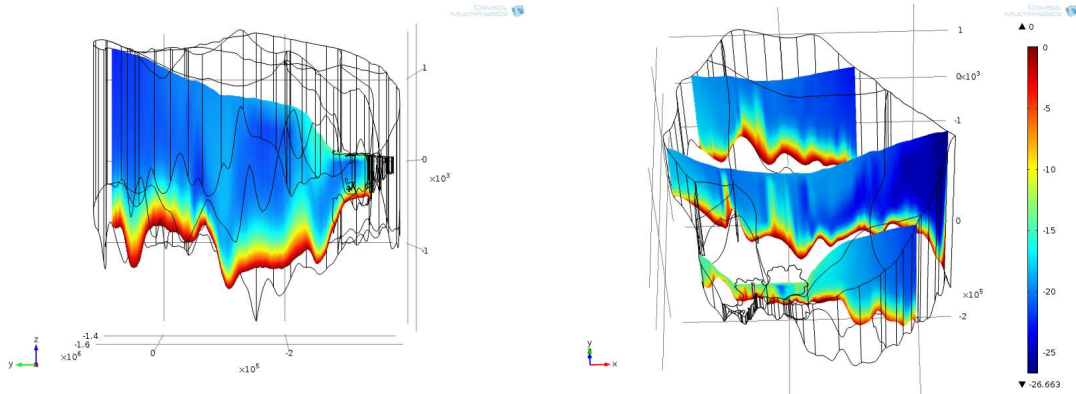
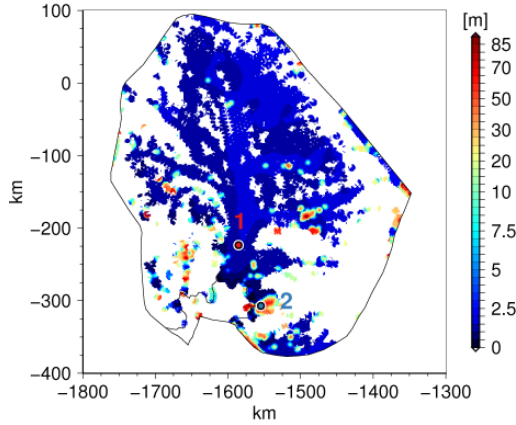
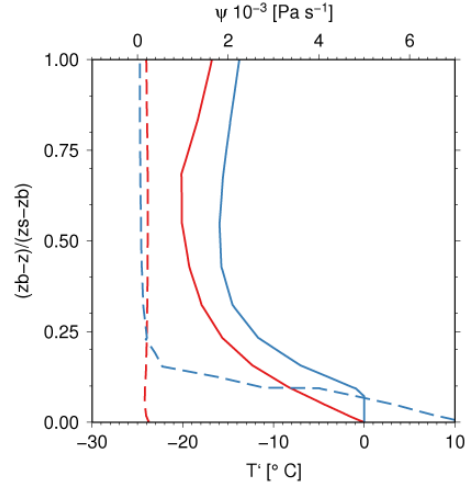


Figure 4.31:  $T'_{\text{qp\_ref2}}$

The transition from cold to temperate ice is given by a cold-temperate transition surface (CTS) (*Blatter and Hutter, 1991*). Pine Island Glacier is an Antarctic glacier, where, due to the cold conditions at the surface, the CTS is located at or near the base. As shown in Figure 4.29, large areas of the base are at  $T_{\text{pmp}}$  ( $T' = 0$ ). In Figure 4.32 it is shown, how far the temperate layer reaches into the ice from the base, thus the temperate layer thickness  $TLT$ . The  $TLT$  in most regions is thin with  $TLT < 10$  m, and only a few locations reach a thickness of  $TLT > 50$  m.

*Blatter and Hutter (1991)* conclude that strain heating is the necessary or dominant mechanism to produce a temperate ice layer. To test their finding along our results we look at the homologous temperature  $T'$  and the strain heating source term  $\psi$  (Section 2.1.3 and Eq. 4.5), on two vertical profiles numbered 1 and 2. The locations of the vertical profiles are indicated in Figure 4.32. Profile 1 lies within a region of very thin  $TLT$ , while profile 2 lies in one of the few locations with a thicker  $TLT$ . In Figure 4.33 the homologous temperature  $T'$  and the strain heating source term  $\psi$  of those two profiles are plotted against the normed local ice thickness, where the dashed lines indicate the

Figure 4.32:  $TLT_{qp\_ref2}$ Figure 4.33: Normed thickness vs.  $T'$ ,  $\psi$ 

source term  $\psi$  and the solid line the homologous temperature  $T'$ . Our results agree well with the findings of *Blatter and Hutter (1991)*. A significant temperate layer is found where strain heating is large. This is not the case for most areas of Pine Island Glacier. If basal sliding is strong and responsible for almost the entire speed measured at the surface, internal deformation must be small, and hence strain heating. Figure 4.30 shows the ratio of basal to surface velocities  $|\mathbf{u}_{b,qp\_ref2}|/|\mathbf{u}_{s,qp\_ref2}|$ . Where the ratio is one, thus  $|\mathbf{u}_{b,qp\_ref2}| = |\mathbf{u}_{s,qp\_ref2}|$ , no internal strain heating is expected.

Our results could in a next step be compared to radar profiles across Pine Island Glacier, and maybe thus validated. The water lenses in temperate ice scatter the radar signal. During the IceBridge Campaigns in 2002, 2004, 2009 and 2010 the glacier was surveyed extensively (<http://gf2.ucs.indiana.edu/Antarctica.html>), and the results could be used to infer the occurrence of temperate ice.

#### 4.2.4 Water content

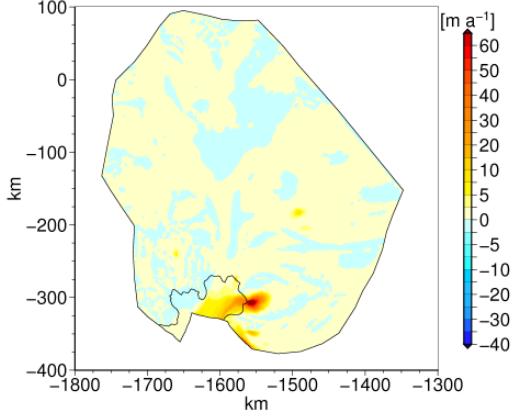
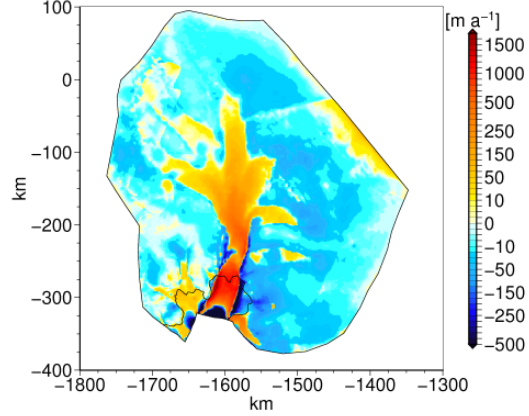
In Section 2.2.2 the rate factor, for cold ice being dependent on temperature and pressure (Eq. (2.26)), is discussed. For temperate ice, which is at pressure melting point and contains liquid water, the rate factor can be expressed with an additional dependence on water content (Eq. (2.27)). In this Section we test the effect of the water content onto the flow field. For this the simulations qp\_ref3 and qp\_ref4 are analysed.

In simulation qp\_ref3 the rate factor for temperate ice is applied (Eq. (2.27)) and the water content is set to 1%, if the temperature reaches pressure melting point ( $T' = 0$ ). Assuming a water content of 1% leads to nearly a triplication of the rate factor  $A$  and reduces the viscosity by about one third (assuming the stress effect to be constant). Thus including the water content can influence the flow field significantly.

In Figure 4.34 the difference in surface velocities between simulation qp\_ref2 (no water content) and simulation qp\_ref3 ( $W = 1\%$  if  $T' = 0$ ) is shown. The differences are relatively small and only really visible where a significant temperate layer is present (refer to Figure 4.32).

To test the maximal effect the inclusion of the water content can have, we assumed a

water content of 1 % everywhere, not dependent on the temperature, in simulation qp\_ref4. Practically speaking we nearly tripled the rate factor  $A$  everywhere. The result can be seen in Figure 4.35, where we show the difference between the observed surface velocity  $|\mathbf{u}_{\text{obs}}|$  and the simulated one,  $|\mathbf{u}_{\text{s,qp\_ref4}}|$ . It is apparent, that the simulated velocity is much higher than the observed one, outside the main central stream. Inside the central stream the simulated velocity is still too slow. This finding underlines the presumptions, that the difference in speeds must be due to other factors. Surface rifting might be one of these.


 Figure 4.34:  $|\mathbf{u}_{\text{s,qp\_ref3}}| - |\mathbf{u}_{\text{s,qp\_ref2}}|$ 

 Figure 4.35:  $|\mathbf{u}_{\text{obs}}| - |\mathbf{u}_{\text{s,qp\_ref4}}|$ 

#### 4.2.5 Full-Stokes vs. SIA

To derive the Shallow Ice Approximation (SIA) (refer to Section 1.2.1 and *Greve and Blatter (2009)*) one assumption made is that horizontal derivatives of the vertical velocities  $\partial w/\partial x$  and  $\partial w/\partial y$  are small compared to the vertical derivatives of the horizontal velocities  $\partial u/\partial z$  and  $\partial v/\partial z$ , and can therefore be neglected. This is shown along a scale analysis (e.g. in *Greve and Blatter, 2009*), for which typical values for horizontal extents  $L = 1000$  km, vertical extents  $H = 1$  km, horizontal velocities  $U = 100$  m a<sup>-1</sup> and vertical velocities  $W = 0.1$  m a<sup>-1</sup> are introduced and which leads to

$$\frac{U}{H} = 10^{-8} \text{ s}^{-1} \sim \frac{\partial u}{\partial z} \sim \frac{\partial v}{\partial z}, \quad (4.13)$$

and

$$\frac{W}{L} = 10^{-14} \text{ s}^{-1} \sim \frac{\partial w}{\partial x} \sim \frac{\partial w}{\partial y}. \quad (4.14)$$

To estimate the importance of using a full-Stokes model for the simulation of the flow field of Pine Island Glacier, we compare the above shown expected typical values for grounded ice to results from simulation qp\_ref2. The velocity derivatives are shown along vertical profiles on distinct locations along the central flow line and in two other regions, in and between tributaries, indicated in Figure 4.36.

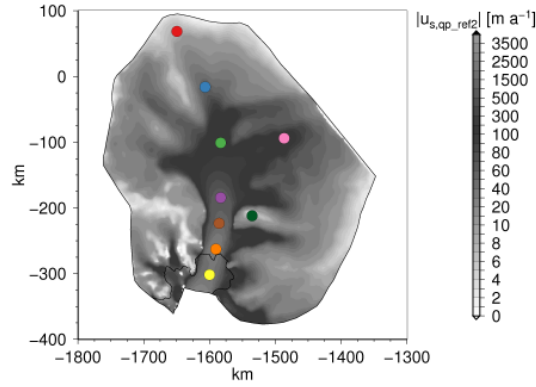


Figure 4.36: Location of extracted profiles on surface velocity  $|\mathbf{u}_{s,qp\_ref2}|$

Figure 4.37 shows the vertical profiles of the velocity derivatives, normed to the local ice thickness. The colours of the different lines correspond to the locations indicated in Figure 4.36.

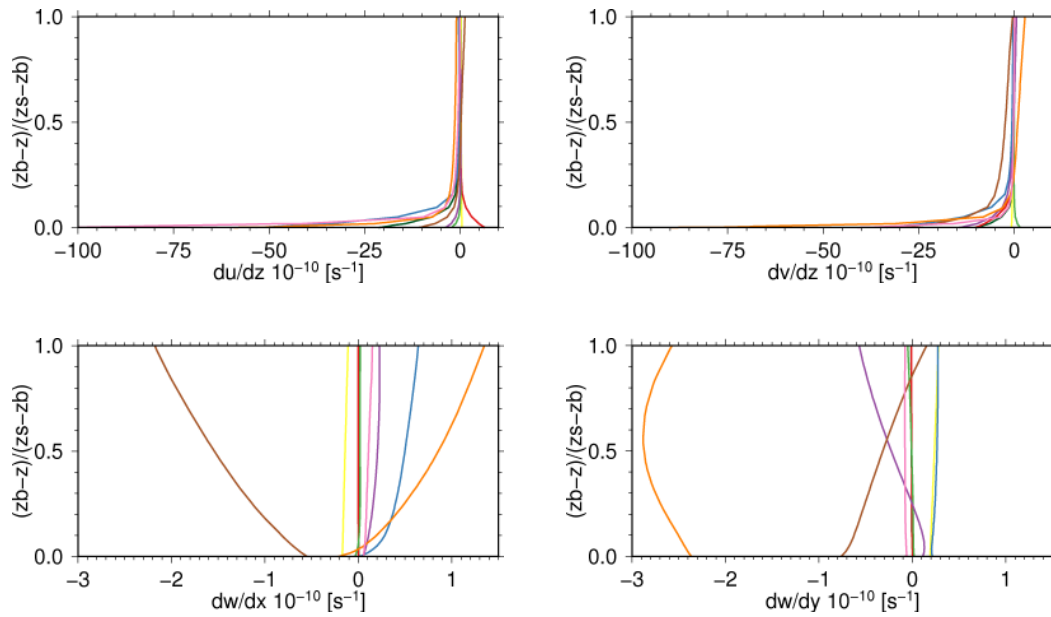


Figure 4.37: horizontal and vertical derivatives

The vertical derivatives of the horizontal velocity components  $\partial u/\partial z$  and  $\partial v/\partial z$ , shown in the upper two plots in Figure 4.37, are with values between  $10^{-10} \text{ s}^{-1}$  and  $10^{-8} \text{ s}^{-1}$  of a comparable magnitude, or smaller than, the estimated value of  $10^{-8} \text{ s}^{-1}$  given in Eq. (4.13).

The horizontal derivatives of the vertical velocity components  $\partial w/\partial x$  and  $\partial w/\partial y$ , shown in the lower two plots Figure 4.37, are with values between  $10^{-14} \text{ s}^{-1}$  and  $10^{-10} \text{ s}^{-1}$  up to 4 magnitudes larger than the estimated value of  $10^{-14} \text{ s}^{-1}$  given in Eq. (4.14). The highest values of  $\partial w/\partial x$  and  $\partial w/\partial y$  are present in the locations marked with brown and orange and

which are closest to the grounding line. The smallest values are with  $\sim 10^{-14} \text{ s}^{-1}$  present at the location marked with a dark green point, an area with slow surface velocities. The dark green lines are not visible in the lower two plots in Figure 4.37, as they lie behind the others.

The magnitudes of  $\partial w/\partial x$  and  $\partial w/\partial y$ , the so called non-SIA components, especially near the grounding line, emphasise the usefulness of a full-Stokes model.

#### 4.2.6 Sensitivity to geothermal heat flux

In this section we test the effect of the different geothermal heat flux data sets onto the basal temperature field. The runs analysed in this section are `qf_ref2`, `qs_ref2`, `qc_ref1`, `qc_ref2` and `qv_ref1`, all listed in Table 4.2. The set up is identical to simulation `qp_ref2`, with just the data for the geothermal heat flux varied. The different geothermal heat flux data sets are from *Fox Maule et al.* (2005) (shown in Section 3.1.5, Figure 3.8) for run `qf_ref2`, from *Shapiro and Ritzwoller* (2004) (also shown in Section 3.1.5, Figure 3.7) for `qs_ref2` and a constant value of  $q_{\text{geo, const}} = 0.06 \text{ W m}^{-2}$ , which is the global average geothermal heat flux (*Cuffey and Paterson*, 2010), is chosen for `qc_ref1` and `qc_ref2`. For run `qv_ref1` an artificial data set  $q_{\text{geo, art}}$  is created, to estimate the effect of an elevated heat flux in the area around the subglacial volcano described in Section 3.1.5. The data set is described below.

Because we chose the "quasi-inversion" technique described in Section 4.2, the geothermal heat flux has no direct effect onto the basal sliding behaviour, as the temperature effect is completely included in the term  $\beta^2$  (refer to Eq. (4.7)). This way we make sure that the general flow pattern is preserved and the influence of the geothermal heat flux onto the temperature field is somehow separated.

The artificial data set for run `qv_ref1` is created with an assumed background value of  $0.06 \text{ W m}^{-2}$ , a peak value of  $0.15 \text{ W m}^{-2}$  at the inferred location of the volcanic center (refer to Figure 3.10) and a Gaussian bump with a 50 km radius given by

$$q_{\text{geo, art}} = 0.06 \left[ 1 + 1.5 \exp \left( -\frac{(x - x_v)^2}{2x_r^2} - \frac{(y - y_v)^2}{2y_r^2} \right) \right], \quad (4.15)$$

with  $x_v = -1665 \text{ km}$  and  $y_v = -205 \text{ km}$  being the approximate location of the volcanic center (*Corr and Vaughan*, 2008) and  $x_r$  and  $y_r$  being the radius of 50 km.

The homologous basal temperatures  $T'_b$  are shown for simulations `qf_ref2`, `qs_ref2`, `qc_ref1`, `qc_ref2` and `qv_ref1` in Figures 4.38-4.43, respectively.

The five different results for the homologous basal temperature strongly resemble each other. The overall structure of temperate areas at the base is dominated by the flow structure. The lowest geothermal heat flux with  $0.06 \text{ W m}^{-2}$  is given for simulation `qc_ref1`, with  $T'_{b, \text{qc\_ref1}}$  shown in Figure 4.40. The complete main trunk is at pressure melting point. North of the main trunk the mark of the tributaries in the temperature is more delicate. The friction heating term ( $\mathbf{u}_b \cdot \boldsymbol{\tau}_b$ ) (compare to Eq. 2.47) is here the dominant factor due to the high sliding velocities, delivering up to  $20 \text{ W m}^{-2}$  extra for basal warming. This can also be seen by comparing Figure 4.40,  $q_{\text{geo}} = 0.06 \text{ W m}^{-2}$  and friction heating included, to Figure 4.41,  $q_{\text{geo}} = 0.06 \text{ W m}^{-2}$  and friction heating not included. Especially the tributaries 3 and 5 and parts of the main trunk are strongly affected by friction heating. Additionally to the friction heating term, the strain heating term is excluded in simulation

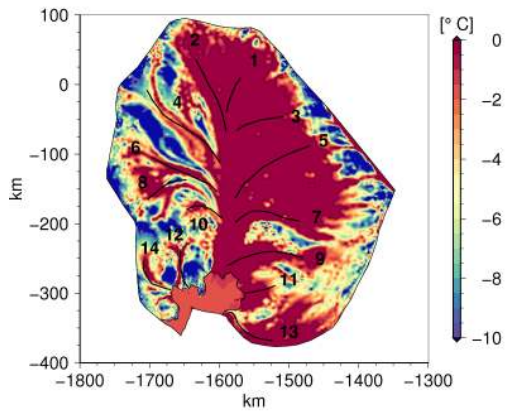


Figure 4.38:  $T'_{b,qf\_ref2}$

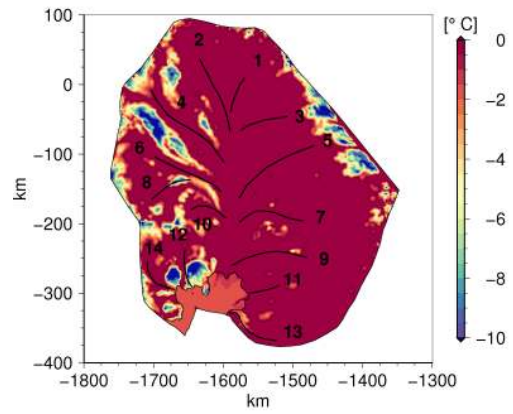


Figure 4.39:  $T'_{b,qs\_ref2}$

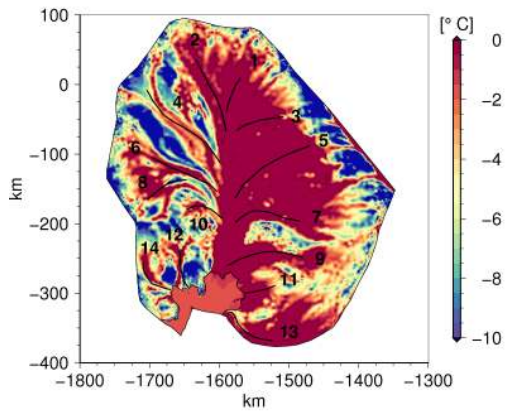


Figure 4.40:  $T'_{b,qc\_ref1}$

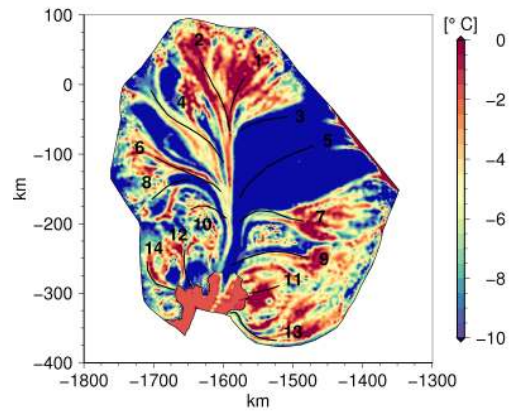


Figure 4.41:  $T'_{b,qc\_ref2}$

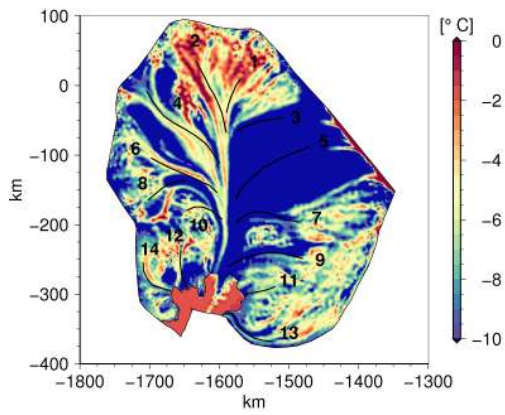


Figure 4.42:  $T'_{b,qc\_ref3}$

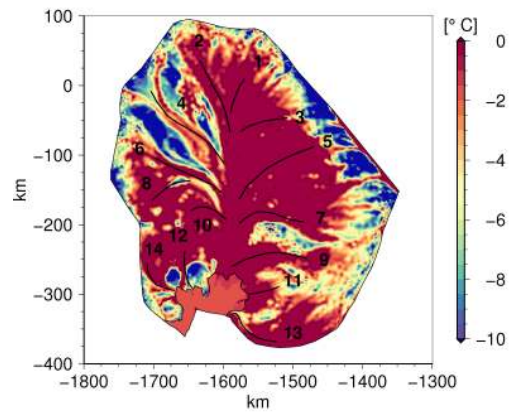


Figure 4.43:  $T'_{b,qv\_ref1}$

qc\_ref3. The result  $T'_{b,qc\_ref3}$  is shown in Figure 4.42. It can be seen that tributaries 7, 9, 11, 13 are partly warmed by strain heating.

Figure 4.43 shows  $T'_{b,qv\_ref1}$  for the simulation qv\_ref1, with the artificial high heat flux around the volcanic center. Now also areas not affected by strong frictional heat to the North of the ice shelf reach pressure melting point  $T_{pmp}$ . This is related to the higher geothermal heat fluxes of  $q_{geo} \geq 0.1 \text{ W m}^{-2}$ , as is also the case in simulation qs\_ref2, shown in Figure 4.39.

### 4.3 Hydraulic potential

In the previous section we have shown, that large areas at the base of Pine Island Glacier are likely to be at the pressure melting point  $T_{pmp}$ . This finding is supported by a study from *Smith et al.* (2013). If this potentially available water is likely to accumulate in certain areas, or take distinct routes below the ice sheet, can be investigated by looking at the hydraulic potential and its gradient. This is done in this section and considered an additional information about the structure at the glacier bed, supporting or counteracting basal sliding.

Water at the glacier base does not simply flow downhill following the basal topography, but down the gradient of a hydraulic potential  $\phi_h$ , given by *Shreve* (1972) as

$$\phi_h = p_w + \rho_w g z_b, \quad (4.16)$$

with  $p_w$  being the water pressure. Following *Cuffey and Paterson* (2010) the water pressure  $p_w$  can be approximated with the assumption that it equals the pressure of the overlying ice and thus

$$p_w = \rho_i g (z_s - z_b). \quad (4.17)$$

The hydraulic potential  $\phi_h$  equals the basal normal stress  $N_b$  for areas that lie below sea level (refer to Eq. 2.45). The field of the hydraulic potential  $\phi_h$  with the approximations made thus only depends on the geometry of the ice and is shown in Figure 4.44.

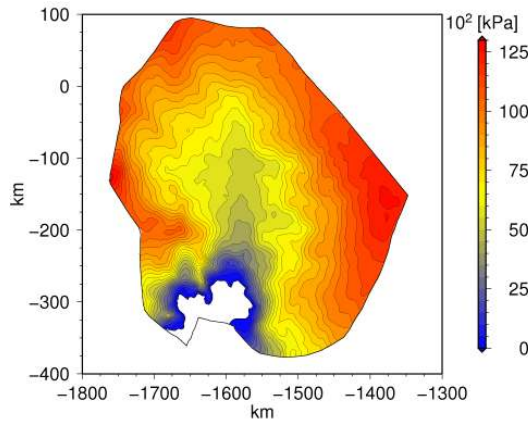


Figure 4.44: Hydraulic potential  $\phi_h$

The potential gradient, which determines the opposite direction of flow, is given with  $p_w$  from Eq. (4.17) as

$$\text{grad } \phi_h = \text{grad } p_w + \rho_w g \text{ grad } z_b = \rho_i g \text{ grad } z_s + (\rho_w - \rho_i) g \text{ grad } z_b. \quad (4.18)$$

The contribution of the ice surface gradient  $\text{grad } z_s$  to the potential gradient  $\text{grad } \phi_h$ , and thus to the water flow path, is  $\sim 10$  times higher than the contribution of the gradient of the basal topography  $\text{grad } z_b$  (Cuffey and Paterson, 2010).

The field of the potential gradient norm  $|\text{grad } \phi_h|$  together with the normalised vector field  $-\text{grad } \phi_h$ , indicating the direction of flow, is shown in Figure 4.45.

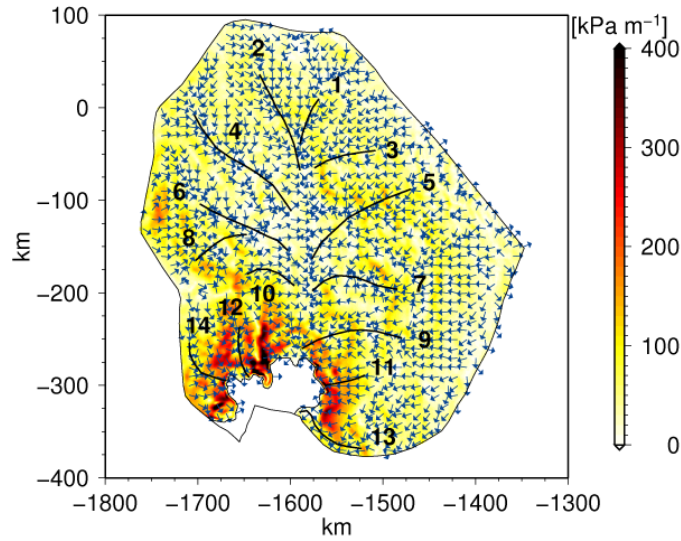


Figure 4.45: Potential gradient  $-\text{grad } \phi_h$

The water flows from high to low potential and thus mainly into the basal trough in which the central fast flowing trunk of the glacier is located, as shown in Figure 4.44. The lowest potential is situated all along the grounding line. The strength and direction of the water path can be seen in Figure 4.45, where the potential gradient is shown. Some tributaries show a higher tendency to accumulate water than others, with actual flow patterns depending also on water availability, and will be further discussed in Section 4.5.

## 4.4 Basal roughness

The basal roughness measure itself simply classifies the roughness of the bed. For an introduction to basal properties below ice sheets refer to Section 1.1.3. For a more detailed description of the derivation process of basal roughness, explicitly of the single and two-parameter roughness index, refer to Section 5.5.1. *Rippin et al.* (2011) assess the single parameter basal roughness index beneath Pine Island Glacier from a RES data set. The basal roughness distribution in the Pine Island area is shown in Figure 4.46. The roughness measure  $\xi$  is shown with a logarithmic scale, such that the most negative values represent

the smoothest bed. *Rippin et al.* (2011) interpret the smoother areas as marine sediment basins beneath Pine Island Glacier, deposited after disappearance of the West Antarctic Ice Sheet in the Pliocene (5.3 – 2.6 Ma ago) or Pleistocene (2.6 – 0.01 Ma ago) (*Walker and Geissman*, 2009). For an overview of the geologic history and the marine ice sheet instability refer to Section 1.1.1 and 1.1.2, respectively.

By combining the basal roughness distribution with information about potential water availability and the bed strength, indicated by the basal shear stress discussed in Section 4.1.1, we aim at further distinguishing the basal properties below Pine Island Glacier.

## 4.5 Discussion

Figure 4.1 shows the observed surface velocity field  $|\mathbf{u}_{\text{obs}}|$  from *Rignot et al.* (2011) together with the numbered tributaries, entering the central main flow field. The basal topography, for a detailed description refer to Section 3.1.1, is shown in Figure 4.47, together with the numbered tributaries.

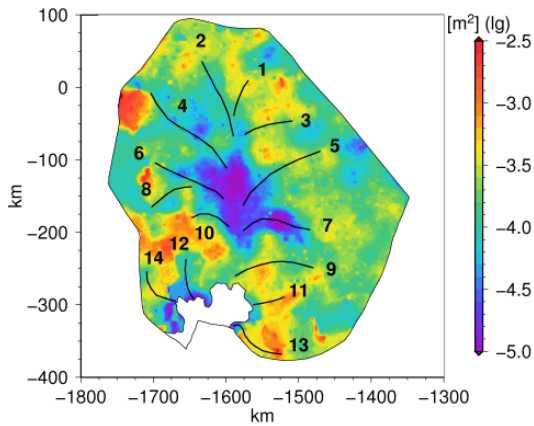


Figure 4.46: Single parameter roughness  $\xi$

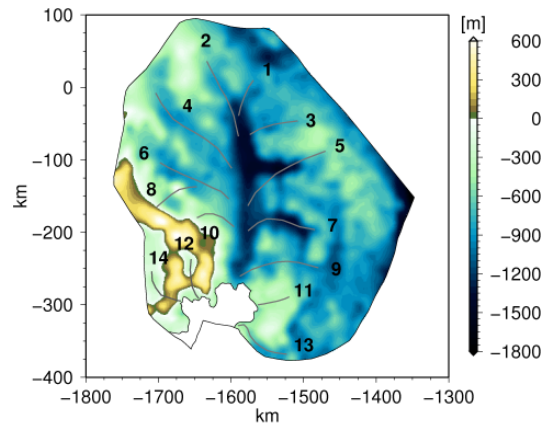


Figure 4.47: Bed topography  $z_b$

In Table 4.3 a classification of the relative importance of different factors influencing the flow field for the single tributaries is listed. For this a variety of fields are considered. In the first column the tributary number is listed. In column “basal topography” is listed, if the location of the tributary coincides with a depression in the basal topography, thus is directed by it. In column “ $\tau_d$ ” is listed, if a high driving stress coincides with the path of the tributary. Column “ $T_{\text{pmp}}$ ” lists, if the base below the tributary is at pressure melting point. For this all geothermal heat flux data sets are considered. To estimate the importance of the friction heating to the temperate base, another run is conducted where the friction heating term is not included. In column “friction heating dominant for  $T_{\text{pmp}}$ ” is listed, if the friction heating term is crucial for the ice base to be at pressure melting point  $T_{\text{pmp}}$ . Column “hydraulic sink” lists if the tributary coincides with a hydraulic sink. And in column “roughness” is listed, if the tributary is underlain by a smooth bed, and thus maybe sediment.

To distinguish the relative strength of the signal, a V stands for a strong signal, a v for an intermediate signal, a x for a signal that is not present and a X for an exclusion of the

signal.

Table 4.3: Strength of signal. V: strong signal, v: intermediate signal, x: no clear signal, X: clearly no signal.

tributary	basal topography	$\tau_d$	$T_{\text{pmp}}$	friction heating dominant for $T_{\text{pmp}}$	hydraulic sink	low $\xi$
1	v	v	V	x	v	x
2	v	x	V	x	v	v
3	v	v	V	V	v	x
4	v	X	v	v	x	V
5	x	v	V	V	V	x
6	v	X	V	x	x	V
7	V	x	V	v	V	V
8	x	X	v	v	v	v
9	v	V	V	V	v	X
10	x	v	v	v	v	v
11	X	V	V	x	V	X
12	v	v	v	x	V	V
13	v	v	v	v	v	X
14	v	v	v	x	V	x

Tributary 1 is a small tributary entering the main ice stream from the South-East. It has a small signal in the basal topography. The driving stress seems to initiate the tributary, which flows at a intermediate speed of  $50 - 100 \text{ m a}^{-1}$ . The basal temperature is in all simulations at pressure melting point, independent of friction heating. The hydraulic gradient suggests a water flow in ice flow direction with an intermediate strength. The base below the tributary is relatively rough. We thus suggest tributary 1 to be initiated by the driving stress, and sustained due the trough in the basal topography, which channels the basal melt water, as the base is at pressure melting.

Tributary 2 can also be seen as the most distant end of the main stream from the grounding line. The tributary enters the main stream from the North-East at similar speed as tributary 1. It also shows a small signal in the basal topography. The basal temperature is also, independent of friction heating, at pressure melting point. In contrast to tributary 1, the driving stress at tributary 2 is very small. Instead the basal roughness is low below the tributary. It is no major hydraulic sink, but a small signal is noticeable, also following the ice flow direction. The tributary seems to be driven by the low basal roughness, suggesting a long existence of the tributary, and a temperate base, while the direction is guided by a basal trough.

Tributary 3 enters the main ice stream from the South. It shows a small signal in the basal topography and the driving stress. The base is temperate, although mainly due to friction heating. The base below the tributary is relatively rough and a small signal in the hydraulic gradient is visible. We suggest that the tributary sustains itself by lubrication of the base due to friction heating.

A seismic survey by *Smith et al.* (2013) across tributary 4 and the main stream, where

tributaries 1 to 3 have already entered, suggests a geological boundary towards the South, separating sedimentary strata from basement rocks. They suggest, that the geological boundary coincides with a change from a thick sediment layer to a much thinner sediment layer, towards tributary 3. This thinner layer could be increasingly eroded, possibly leading to a change in basal drag and subsequently a change in flow speed.

Tributary 4 is characterised by a very low driving stress and low basal roughness. It enters the main stream from the North-East and has a small signal in the basal topography. The basal temperature below the tributary is partly at pressure melting point, and even less so if friction heating is not considered. The hydraulic gradient has no clear signal below tributary 4. *Smith et al.* (2013) find evidence for a relatively thick sedimentary basin below tributary 4, coinciding with the low roughness. We suggest tributary 4 to be mainly driven by the basal sediments, which can not sustain the basal drag.

Tributary 5 enters the main stream from the South-East. The flow direction crosses a deep trough in the basal topography, not directly being guided by it. The flow is initiated by the driving stress, while the base is temperate, mainly caused by friction heating. Below the tributary a hydraulic sink is present. The base is at the onset of the tributary relatively rough, becoming smoother were it meets the main stream.

Tributary 6 enters from North-East. The driving stress is very low, and so is the basal roughness. An intermediate signal in the basal topography is present below the glacier. The central part of tributary 6 is at  $T_{\text{pmp}}$ , not strongly dependent on friction heating. The hydraulic gradient has no strong signal.

Tributary 7 enters the main stream from the South and is clearly steered by the basal topography. It is characterised by a small driving stress and a low basal roughness. The water, if available, would flow right below the tributary, with a strong signal in the hydraulic gradient. The base is temperate, in the onset region not due to friction heating.

Tributary 8 flows into tributary 6 from the North-West. It is not topographically steered and the driving stress is very small. The base is only partly at  $T_{\text{pmp}}$ , and friction heating is partly responsible for the heating. The water below the tributary would possibly accumulate in a topographic low, but not necessarily follow the flow path of the ice. The base is characterised by low roughness.

Tributary 9 enters the main stream from the South, relatively close to the grounding line. The signal in the basal topography is small, but present. The driving stress is high, especially near the grounding line, coinciding with a rough base. The base is temperate, mainly due to friction heating. The base below the tributary is no clear hydraulic sink, but the water flow direction agrees with the ice flow direction. We suggest the main factor for the flow of this tributary to be the driving stress, whose existence is supported by a rough base.

Tributary 10 flows with velocities around  $20 - 40 \text{ m a}^{-1}$  relatively slow from the North into the main stream. It has no signal in the basal topography. In the onset the driving stress is high, but reduces rapidly in flow direction. The basal temperature is largely at  $T_{\text{pmp}}$ , partly depending on friction heating. The base becomes smoother towards the main stream. The hydraulic gradient supports the flow direction.

Tributary 11 flows from the South into the ice shelf. It is not steered by the basal topography, but instead by a high driving stress. The base below the tributary is relatively rough. It has a temperate base, independent of friction heating. And the hydraulic gradient is strong, with the water flowing towards the grounding line.

Tributary 13 is the furthest west and enters the Amundsen sea from the South-West. It

does not directly flow into the ice shelf of Pine Island Glacier. A small signal in the basal topography is present, combined with a relatively high driving stress, slightly to the East of the tributary. The base is temperate, largely due to friction heating. The hydraulic gradient strongly supports the flow direction and the base is rough, becoming smoother towards the ice shelf.

Tributaries 12 and 14 enter the ice shelf from the East and North-East, respectively. They have both a small signal in the basal topography. The driving stress for both is higher in the onset region, reducing towards the grounding line. They have a temperate base, which is not necessarily due to friction heating. Both tributaries are strong hydraulic sinks, steering the water in ice flow direction towards the grounding line. The main difference between the two tributaries is the basal roughness. While tributary 12 has a relatively smooth bed, tributary 14 flows over a rougher base.

Additionally to the above classification of different mechanisms being important for the flow pattern of the single tributaries, we have shown, in Section 4.1.4, that the geothermal heat flux from *Shapiro and Ritzwoller (2004)* leads in our simulations to ice temperatures which in turn lead to velocities higher than the measured surface velocities. We therefore infer that the geothermal heat flux from *Shapiro and Ritzwoller (2004)* is unrealistically high in the Pine Island area. For further simulations we thus use the geothermal heat flux from *Purucker 2012 (updated version of Fox Maule et al., 2005)*, as it gives similar results to, and is an updated version from *Fox Maule et al. (2005)*.

We also show, that the “quasi-inversion” technique, introduced in Section 4.2.1, leads to good results in reproducing the flow field for Pine Island Glacier, shown in Section 4.2.2. We analyse the basal temperate layer in Section 4.2.3. The mismatch between simulated and observed surface velocities is not due to the use of the rate factor  $A$  for cold ice, which is shown in Section 4.2.4. The importance of using a full-Stokes model for our simulations is shown in Section 4.2.5.



# Chapter 5

## Basal sliding

In this chapter we are analysing the impact of different sliding and slip assumptions onto the modelled flow field of Pine Island Glacier. In the previous chapter we avoided the challenge to find an appropriate formulation for basal sliding, by introducing the “quasi-inversion” technique described in Section 4.2.1. In this chapter we address basal sliding and its difficulties and implications, which are already briefly introduced in Section 1.2.2. To do so we will first give an overview of existing theories dealing with basal sliding in Section 5.1, and thereafter test their applicability for Pine Island Glacier with the ice flow model, in Section 5.3.

In the last two Sections we will use some measured, and therefore afore known, information about the bed, which is the basal roughness, already briefly introduced in Section 1.1.3 and 4.4, and include this in different ways into the sliding law. In Section 5.4 we combine the spatial structure of the basal roughness to the sliding law. And finally, in Section 5.5, we test the applicability of an existing theory by *Li et al.* (2010), which also connects the measured basal roughness to basal sliding, for Pine Island Glacier.

### 5.1 Theory - Basal sliding

In the theories about basal motion generally two different mechanisms are considered, which are for one sliding over a hard bed, described in Section 5.1.1, and secondly, sliding over or with a deformable bed, described in Section 5.1.2. These mechanisms are arbitrarily complex, but need to be broken down into their main components, to formulate a relation that can be applied as a boundary condition for the modelling of ice dynamics.

To establish a basal sliding relation for an individual glacier, usually an empirical approach is taken and the relations are calibrated for the specific glacier (*Cuffey and Paterson*, 2010). This was done for Pine Island Glacier in a variety of studies (e.g. *Joughin et al.*, 2009, 2010; *Morlighem et al.*, 2010), and also here in Section 4.2. Still we aim at finding some physical framework to base the sliding relation on and not having to arbitrarily chose parameters.

Rapid sliding over hard beds only occurs if basal temperatures are at pressure melting point  $T_{\text{pmp}}$ , while the underlying till or sediment layer only deforms rapidly if it is saturated with water at pressure close to the weight of the overlying ice (*Cuffey and Paterson*, 2010).

In the following we will give a short introduction to the original ideas, on which the commonly applied sliding relations are based, as they are of importance in the subsequent sections of this chapter.

### 5.1.1 Hard beds

First we consider a hard bed to be rigid and rough. The sliding of glaciers over hard beds is dominated by two mechanisms, that make the ice flow past obstacles in the bedrock, as already briefly introduced in Section 1.2.2. These two mechanisms are *regelation* and *enhanced creep* (Deeley and Parr, 1914; Weertman, 1957). Both are initiated by a pressure difference between the up- and downstream sides of an obstacle.

*Regelation* means refreezing. The upstream side of an obstacle provides the highest resistance to flow and therefore experiences the highest pressure. The higher pressure reduces the pressure melting point  $T_{\text{pmp}}$ , as can be seen in Eq. (2.16). The resulting melt water migrates to the downstream side of the obstacle, where a lower pressure prevails, and thus refreezes. The latent heat produced by refreezing can be conducted through the obstacle to assist melting at the upstream side. Therefore *regelation* is most effective for smaller obstacles (Benn and Evans, 2010). *Regelation* can be demonstrated by drawing a thin metal wire through a block of ice. The block remains intact and there is no net heat source nor melt water production (Clarke, 2005).

For the mechanism of *enhanced creep* the nonlinear connection of stress and strain rates in ice is important (refer to Section 2.2.1). Stress concentration on the upstream side of an obstacle results in locally high strain rates, allowing the ice to deform around and, to a lesser extent, over the bump (Benn and Evans, 2010). The two mechanisms of *regelation* and *enhanced creep* can be strongly interrelated (Lliboutry, 1993).

Weertman (1957) developed a mathematical description for these mechanisms, often taken as the basis for modern sliding laws. We discuss the theoretical basis here in considerable detail, as it will be of importance in the subsequent sections.

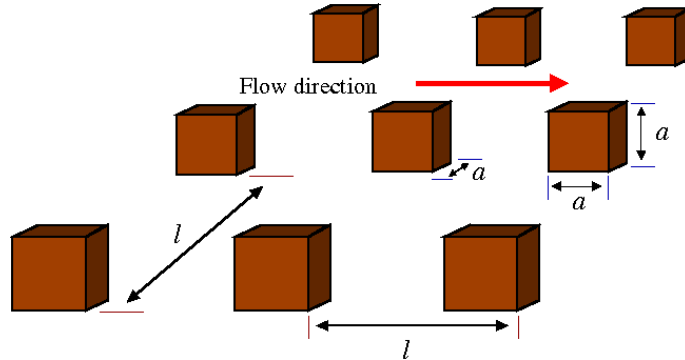


Figure 5.1: Obstacle size  $a$  and spacing  $l$  (Figure modified from Weertman (1957)).

For the mathematical description, an array of cubical obstacles of dimension  $a$  at a distance  $l$  apart is considered, as shown in Figure 5.1. The flow direction is orthogonal to the face of the obstacles. The average shear stress at the bed is  $\tau_b$ . Because there is exactly one obstacle in each area  $l^2$ , the average drag on each obstacle is  $\tau_b l^2$ . The drag causes a pressure increase of about  $\tau_b l^2 / 2a^2$  on the upstream side of the obstacle, and the pressure difference across the obstacle is  $\tau_b l^2 / a^2$ . This causes a temperature difference  $dT$  of

$$dT = \frac{\beta_c \tau_b l^2}{3 a^2}, \quad (5.1)$$

with the Clausius-Clapeyron constant  $\beta_c = 9.8 \times 10^{-8} \text{ K Pa}^{-1}$ , for air-saturated ice (Hooke, 2005). If  $\mathbf{u}_R$  is the ice velocity due to regelation,  $\mathbf{u}_R a^2$  is the regulative water flux. The latent heat released when refreezing this water is  $\rho_i L \mathbf{u}_R a^2$ , with the density of ice  $\rho_i = 918 \text{ kg m}^{-3}$ , and the latent heat of fusion  $L = 334 \text{ kJ kg}^{-1}$ . This heat is conducted through the obstacle at a rate of  $\kappa_b dT a$ , where  $\kappa_b = 5 \text{ W m}^{-1} \text{ K}^{-1}$  is an approximate value for the thermal conductivity of the bedrock. It follows that  $\rho_i L \mathbf{u}_R a^2 = \kappa_b dT a$ , assuming that no heat is conducted through the surrounding ice. Replacing  $dT$  leads to

$$\mathbf{u}_R = C_R \frac{\tau_b}{a \nu^2}, \quad (5.2)$$

with  $\nu = a/l$  being a measure of the bed roughness, and  $C_R = \kappa_b \beta_c / 3 \rho_i L$ .

Figure 5.2 shows the expected basal velocity due to *regelation*  $|\mathbf{u}_R|$  for the range of obstacle dimensions  $a = [10^{-3}, 10^3]$  and obstacle spacings  $l = [10^{-3}, 10^3]$ , with the above stated values and an assumed average shear stress at the bed of  $|\tau_b| = 100 \text{ kPa}$ . This are only theoretical considerations, and it will be explained later, that sliding velocities due to *regelation* of  $\mathbf{u}_R > 20 \text{ m a}^{-1}$  are not likely.

Let  $\mathbf{u}_V$  now be the velocity due to *enhanced creep*, or viscous deformation, past the obstacle. With  $\nu$ , the pressure increase at the high stress side can be rewritten as  $\tau_b / 2\nu^2$ . With Glen's flow law, which relates the deviatoric stresses  $\boldsymbol{\tau}$  to the strain rates  $\dot{\boldsymbol{\epsilon}}$ , such that  $\dot{\boldsymbol{\epsilon}} = \lambda \boldsymbol{\tau}^n$  (for details refer to Section 2.2.1), the strain rate produced by the additional longitudinal stress is  $\approx \lambda (\tau_b / 2\nu^2)^n$ . If we assume that the length over which the additional stress acts is the length  $a$  of the object, we infer

$$\mathbf{u}_V = C_V a \left( \frac{\tau_b}{\nu^2} \right)^n, \quad (5.3)$$

with  $C_V = \lambda / 2^n$ .

The basal velocity due to *enhanced creep*  $|\mathbf{u}_V|$  is shown in Figure 5.3, with  $n = 3$  and  $\lambda = 5.0337 \times 10^{-24} \text{ s}^{-1} \text{ Pa}^{-n}$ , which is the value of  $A(T')$  at  $T = T_{\text{pmp}}$  (refer to Section 2.2.2, Eq. (2.26)). The same applies here, as stated above, that  $\mathbf{u}_V > 20 \text{ m a}^{-1}$  is not likely.

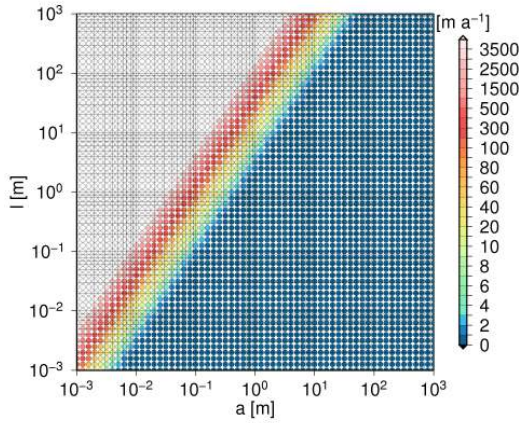
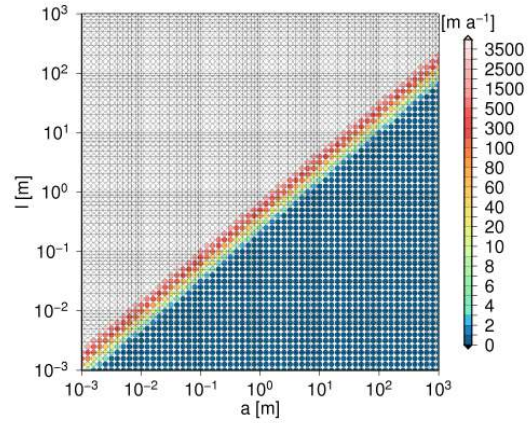
It is often argued, that *regelation* is more effective for small obstacles, while *enhanced creep* is more effective for larger objects (e.g. Weertman, 1957; Hooke, 2005; Cuffey and Paterson, 2010). This is only true, if the bed roughness  $\nu$  is seen as a constant value. Then  $\mathbf{u}_R$  decreases with increasing  $a$ , as  $\mathbf{u}_R \propto 1/a$  (Eq. (5.2)), and  $\mathbf{u}_V$  increases with increasing  $a$ , as  $\mathbf{u}_V \propto a$  (Eq. (5.3)). If otherwise the bed roughness  $\nu$  is still considered as the ratio between obstacle size and spacing  $\nu = a/l$ , the statement does not hold, as can be seen in Figures 5.2 and 5.3.

The total sliding speed is generally considered to be

$$\mathbf{u}_b = \mathbf{u}_R + \mathbf{u}_V. \quad (5.4)$$

A big variety of obstacle sizes is usually found at the bedrock. To find the one obstacle size that exerts the highest drag on the base of the ice, the so called *controlling obstacle size*  $a_c$ , the minimum of  $\mathbf{u}_b$  needs to be found. So  $d\mathbf{u}_b/da = 0$  is evaluated and leads to  $a_c = \sqrt{C_R/C_V} (\tau_b/\nu^2)^{(1-n)/2}$  and  $\mathbf{u}_R = \mathbf{u}_V$ . Reinserting this into Eq. (5.4) leads to

$$\mathbf{u}_b = C_W \left( \frac{\tau_b}{\nu^2} \right)^{\frac{1+n}{2}}, \quad (5.5)$$


 Figure 5.2:  $|\mathbf{u}_R|$  due to *regelation*

 Figure 5.3:  $|\mathbf{u}_V|$  due to *enhanced creep*

with  $C_W = 2C_V\sqrt{C_R/C_V}$ . This is valid for beds where all objects have the *controlling obstacle size*  $a_c$  (estimated to be  $a_c \approx 0.5$  m (Clarke, 2005);  $a_c \approx 0.01 - 0.1$  m (Cuffey and Paterson, 2010)), or for beds with a homogeneous distribution of roughness elements - so-called *white roughness*.

With  $n = 3$  the sliding velocity  $\mathbf{u}_b$  then varies with  $\tau_b^2$ , as shown in Eq. (5.5). When following the above made statement, where the bed roughness  $\nu$  is seen as a constant value, for absence of small obstacles  $< a_c$ , a smooth bedrock possibly caused by abrasion, sliding occurs mainly by *enhanced creep*, and thus varies with  $\tau_b^3$ , as seen in Eq. (5.3). On the other hand, if only obstacles  $< a_c$  are present, sliding is dominated by *regelation* and thus varies linearly with  $\tau_b$ , as shown in Eq. (5.2). In all cases sliding velocity also sensitively depends on the basal roughness  $\nu$ .

The bed structure assumed by Weertman (1957) is highly artificial. Nye (1969) and Kamb (1970) also analysed basal sliding by considering a more realistic bed structure consisting of superimposed sine waves. The mechanisms that let the ice flow past obstacles are also *regelation* and *enhanced flow*. For an exact solution of their approach they unfortunately had to assume a linear rheology ( $n = 1$ ) for the ice. For a nonlinear rheology, Kamb (1970) still obtained an approximate solution. Without going into detail of their theory, it can be noted that Nye (1969) and Kamb (1970) both conclude that  $\mathbf{u}_b \propto \tau_b/\nu^2$  for the linear rheology, which is also the case for the theory by Weertman (1957, Eq. (5.5 with  $n = 1$ )). Kamb's nonlinear theory leads to  $\mathbf{u}_b \propto \tau_b^2$ , at least for some roughness spectra (Hooke, 2005).

Measurements show an upper limit for basal velocities due to hard bed sliding (Cuffey and Paterson, 2010). This is not reflected in Figures 5.2 and 5.3, which show very high sliding velocities for some combinations of obstacle size and spacing. Faster basal sliding can for example occur due to underlying weak deformable substrate, discussed in the next section. Hard bed sliding velocities  $> 20$  m a<sup>-1</sup> are only possible if water filled cavities are considered (e.g. Lliboutry, 1968). Water filled cavities on the downstream side of an obstacle can form, when the water pressure  $p_w$  exceeds the compressive normal stress (Cuffey and Paterson, 2010). The dominant quantity is thus the effective pressure, or basal normal stress,  $N_b$  (refer to Eq. (2.45)). Cavities reduce the contact between the ice

and the bedrock, effectively reducing the roughness of the bed. Measurements have shown, that  $\mathbf{u}_b \propto N_b^{-1}$  (Iken, 1981). By introducing a bed-separation index  $\tau_b/N_b$ , Bindenschadler (1983) extended the Weertman-type sliding law, such that

$$\mathbf{u}_b = C_b \tau_b^p N_b^{-q}, \quad (5.6)$$

where  $C_b$  is now a value that depends on the thermal and mechanical properties at the ice bed rock interface, like for example the roughness. The positive values for  $p$  and  $q$ , within the common ranges  $p = [1; 3]$  and  $q = [0; 2]$ , are usually empirically determined.

Gudmundsson (2011) impressively demonstrates, that a non-linear sliding relation ( $p = 3$ ) is able to reproduce observed velocity changes induced by ocean tides and strengthens therewith the use of such a relation, at least for Rutford Ice Stream in West Antarctica.

### 5.1.2 Deformable beds

Glaciers are often underlain not only by hard beds, but also by deformable beds. These can consist of glacial deposits or marine sediments. In the following the word till is used for all forms of deformable beds. The presence of till can lead to high basal velocities due to deformation of the bed or sliding at its surface (Boulton and Jones, 1979; Cuffey and Paterson, 2010). The mechanical properties of till strongly depend on the basal effective pressure  $N_b$  (Kamb, 2001; Cuffey and Paterson, 2010). At low effective pressure  $N_b$ , the shear strength of till can be as low as a few kPa (Boulton and Dent, 1974; Kamb, 2001), which would produce no significant deformation within ice (Cuffey and Paterson, 2010). The presence of a deformable bed can thus explain high surface velocities, even if low driving stresses are present, as found at Pine Island Glacier (refer to Section 4.1.1).

A common method is to use Eq. (5.6) with the parameter values  $(p, q) = (1, 0)$  (Greve and Blatter, 2009). As the effective pressure  $N_b$  is usually not known in detail, its effect is moved into the coefficient  $C_b$  (Joughin et al., 2009), turning it more into a spatially varying parameter like  $1/\beta^2$  (refer to Section 4.2.1). The resulting sliding relation corresponds to a linear-viscous deforming bed model, which was used in previous modelling studies of Pine Island Glacier (e.g. Schmeltz et al., 2002; Payne et al., 2004). Most model studies using control methods, thus inversion for a basal sliding parameter, are also based on the linear-viscous assumption (e.g. Vieli and Payne, 2003; Morlighem et al., 2010, with  $(p, q) = (1, 1)$ ).

A shearing till can also show perfectly plastic behaviour and attain a yield stress  $\tau_*$ , which is essentially independent of the deformation rate (Tulaczyk et al., 2000). Higher velocities do not increase the stress after having reached the yield stress. Based on this, assuming the till is always in plastic failure, Joughin et al. (2004) suggest a slip relation for till of the form

$$\tau_b = \alpha^2 \frac{\mathbf{u}_b}{|\mathbf{u}_b|}, \quad (5.7)$$

where the direction is determined by the basal velocity  $\mathbf{u}_b$ , but the magnitude is independent from the velocity and determined by  $\alpha^2$ .

Sliding over hard beds, in combination with low effective pressure and high basal velocities, can show similar behaviour as the above described plastic beds, with a diminishing resistance with increasing speed, so called *velocity weakening* (Schoof, 2005).

## 5.2 Evaluation method of results

The results in the subsequent part of this chapter are all evaluated in a certain manner. Here we give an overview of the method used for evaluation of the results.

All simulations in this chapter are conducted with the geothermal heat flux from Purucker 2012 (updated version of *Fox Maule et al.*, 2005), if the temperature model is solved for. The results are here not compared against the measured surface velocity field, introduced in Section 3.1.6, but to the evaluated reference simulation qp\_ref2, described in Section 4.2.2. The reference simulation qp\_ref2 is also conducted with the geothermal heat flux from Purucker 2012 (updated version of *Fox Maule et al.*, 2005) (refer to Table 4.2). This is done to avoid wrong assumptions about the cause of the misfit. It is not necessarily only the choice of the sliding law causing differences to the observed field, as discussed in Section 4.2.2. In this chapter the identifier for the reference simulation qp\_ref2 is abbreviated to ref, for convenience. The norm of the surface velocity field of the reference simulation  $|\mathbf{u}_{s,\text{ref}}|$  and the homologous basal temperature of the reference simulation  $T'_{b,\text{ref}}$ , discussed in Section 4.2.2, are for easier orientation shown here again in Figures 5.4 and 5.5, respectively.

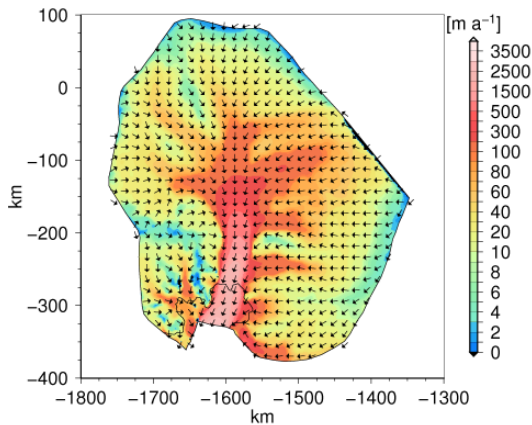


Figure 5.4:  $|\mathbf{u}_{s,\text{ref}}|$

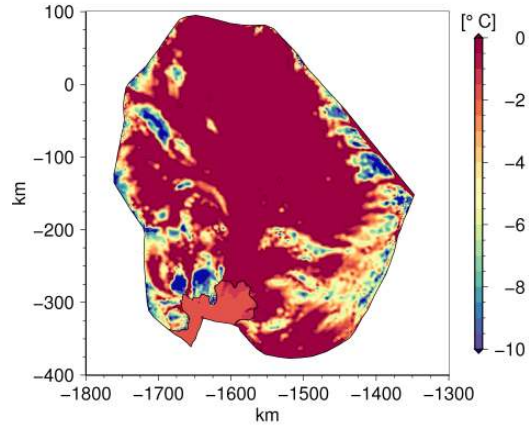


Figure 5.5:  $T'_{b,\text{ref}}$

To facilitate the evaluation of the results in this chapter, the flow field of Pine Island Glacier is partitioned into smaller regions, as shown in Figures 5.6(a) and (b). The partitioning enables a differentiated analysis of the results for regions, that are dominated by basal sliding, and those dominated by internal deformation. It is conducted along the grounding line and different contour lines of the measured surface velocity field  $\mathbf{u}_{\text{obs}}$  from *Rignot et al.* (2011) (Section 3.1.6), as shown in Figure 5.6(a). The according naming of the regions is shown in Figure 5.6(b). The ice shelf is a single region named “Shelf”. The central stream, named “CS”, is bordered to the West by the “Shelf” region, to the North by the  $200 \text{ m a}^{-1}$  contour line and to the South by the  $500 \text{ m a}^{-1}$  contour line and the adjacent tributaries. All tributary areas are named “T” with the according number. Tributaries 5, 7, 9, 11, 12, 13 and 14 are bordered by the  $100 \text{ m a}^{-1}$  contour line and the grounding line, the CS or neighbouring tributaries. Tributaries 6 and 8 are joined in a single region, named “T6.8”, and bordered by the  $50 \text{ m a}^{-1}$  contour line and the CS, as

is tributary 4. Tributary 3 is bordered by the  $75 \text{ m a}^{-1}$  contour line and the CS. Tributaries 1 and 2 are joined, named "T1\_2", and bordered by the  $20 \text{ m a}^{-1}$  contour line, the CS and neighbouring tributaries. The same applies to tributary 10. All tributaries, the central stream and ice shelf are further combined to the fast flowing region called "Fast", indicated in red in Figure 5.6(b). The slower flowing region outside the fast streams and the ice shelf is called "Slow", indicated in blue in Figure 5.6(b). The "Fast" and "Slow" regions together are combined to the region "All", which is bordered with a thick black line in Figure 5.6(b).

The partitioning is somewhat arbitrary, but facilitates nonetheless a differentiated discussion of the results.

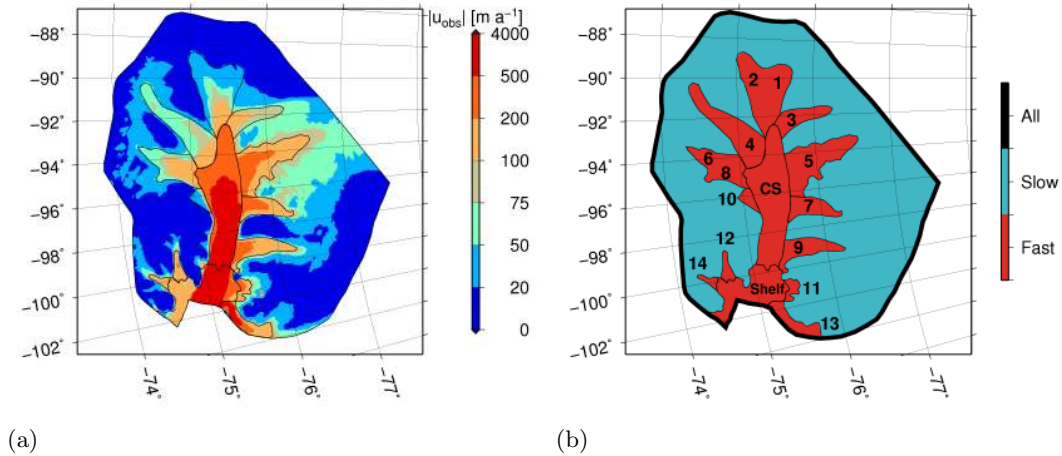


Figure 5.6: Partitioning of regions for evaluation

The results are evaluated on the one hand in a qualitative manner. On the other hand, we also evaluate the root-mean-square deviation  $\text{RMS}_{\mathbf{u}_s}$  (Eq. (5.8)) for the different regions. The difference calculated here is between the simulated and reference surface velocity fields, such that

$$\text{RMS}_{\mathbf{u}_s} = \sqrt{\frac{1}{m} \sum_{i=1}^m (|\mathbf{u}_{s,\text{sim}}|_i - |\mathbf{u}_{\text{ref}}|_i)^2}, \quad (5.8)$$

with  $m$  being the number of the discrete values. We evaluate the  $\text{RMS}_{\mathbf{u}_s}$  value on a regular grid with 1 km spacing.

The  $\text{RMS}_{\mathbf{u}_s}$  value enables a quantitative evaluation of the results. In the  $\text{RMS}_{\mathbf{u}_s}$  value, higher deviations are weighted stronger than in a calculated mean deviation. Furthermore, the  $\text{RMS}_{\mathbf{u}_s}$  value relates to the absolute deviation between the simulations and the reference. The relative misfit is not shown with this measure. In an overall slower flowing region therefore the  $\text{RMS}_{\mathbf{u}_s}$  value is naturally smaller, than in faster flowing regions, assuming the flow pattern is reproduced to some extent. We chose the  $\text{RMS}_{\mathbf{u}_s}$  deviation, instead of the mean deviation, as a quantitative measure, because it has been used in similar studies and thus enables comparison (e.g. *Joughin et al.*, 2009; *Rückamp*, 2011).

Our aim is to reproduce the surface flow field with all tributaries, by making appropriate

assumptions about the basal sliding behaviour. In the following three sections, different approaches are taken to achieve this.

### 5.3 Constant sets of sliding parameters $p$ , $q$ and $C_b$

A variety of studies simulating glacier flow have successfully been conducted with constant sets of parameters for  $p$ ,  $q$  and  $C_b$ , in a sliding law as shown in Eq. (5.6). Although we already stated, that a constant set of parameters is not likely to be applicable to Pine Island Glacier, we will here nonetheless test some combinations and analyse the implications. The results of the simulations are shown in Section 5.3.1 and discussed in Section 5.3.2.

#### 5.3.1 Simulations

A tabular overview of simulations conducted for this chapter is given in Table 5.1. The simulations are numbered, as listed in column "Nr.", and also received an identifier, as listed in column "identifier". The columns " $p$ ", " $q$ " and " $C_b$ " give the parameter values used. In column " $N_b$ " the form of the effective pressure  $N_b$ , as used in the sliding law, is listed. The water pressure  $p_w$  is here used in the form  $p_w = -\rho_{sw}gz_b$ , which implies that it is sea water lowering the effective pressure, rather than melt water. All simulations are carried out with a *Segregated Solver* described in Section 3.2.5. The convergence for the velocity field and the temperature is stated separately in columns "conv. $\mathbf{u}, p$ " and "conv. $T$ ", respectively.

Table 5.1: Overview of simulations with constant parameter sets

Nr.	identifier	$p$	$q$	$C_b$ [ $\text{Pa}^{(q-p)} \text{m a}^{-1}$ ]	$N_b$ [Pa]	conv. $\mathbf{u}, p$	conv. $T$
1	qp_p1q2	1	2	5e9	$\rho_i g H - p_w$	1e-04	8.1e-04
2	qp_p2q0	2	0	4e-9	-	1.4e-06	1.2e-06
3	qp_p3q1	3	1	2e-7	$\rho_i g H - p_w$	3.9e-05	1.3e-04
4	qp_p3q2	3	2	11.2	$\rho_i g H$	3e-05	3.8e-04
5	qp_p1q0	1	0	1e-2	-	2.7e-04	4.7e-04

The different sets of values for  $p$ ,  $q$  and  $C_b$  are for simulation qp\_p1q2 from *Budd and Jenssen* (1987), for simulation qp\_p2q0 from *Klauke* (2006), for simulation qp\_p3q1 from *Van der Veen* (1987), for simulation qp\_p3q2 from *Greve* (2005) and for simulation pq\_p1q0 from *MacAyeal* (1992). For simulation pq\_p1q0 though we chose a smaller value of  $C_b = 0.01 \text{ Pa m a}^{-1}$ , than the range given by *MacAyeal* (1992) of  $C_b = [0.03; 0.25] \text{ Pa m a}^{-1}$ , as those values produced extremely high sliding velocities in our model.

The obtained surface velocity fields for the different simulations are shown in Figures 5.7, 5.9, 5.11, 5.13 and 5.15, respectively. The difference of the surface velocity fields to the reference simulation, such that  $|\mathbf{u}_{s,\text{ref}}| - |\mathbf{u}_{s,\text{sim}}|$ , with "sim" being the according simulation identifier from Table 5.1 are shown in Figures 5.8, 5.10, 5.12, 5.14 and 5.16.

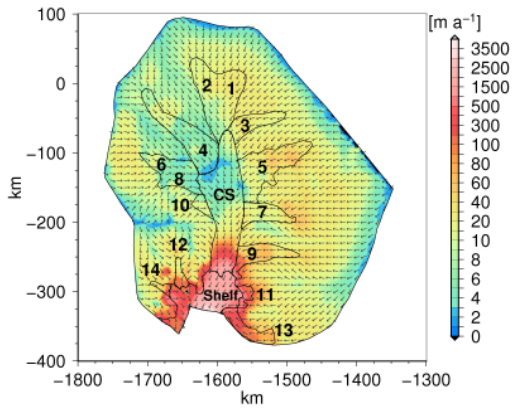


Figure 5.7:  $|u_{s,qp-p1q2}|$

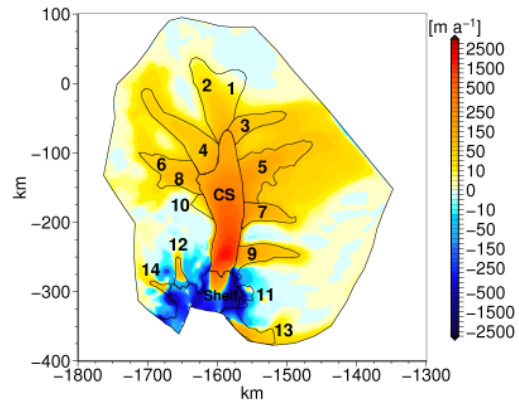


Figure 5.8:  $|u_{s,ref}| - |u_{s,qp-p1q2}|$

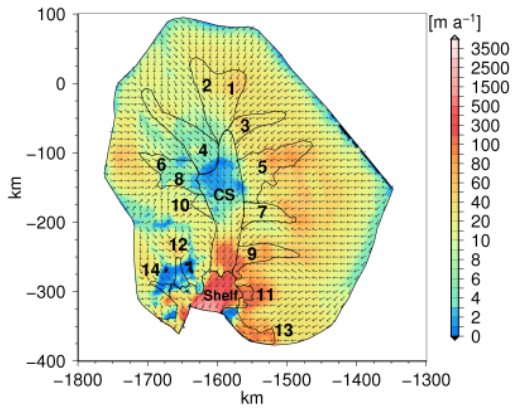


Figure 5.9:  $|u_{s,qp-p2q0}|$

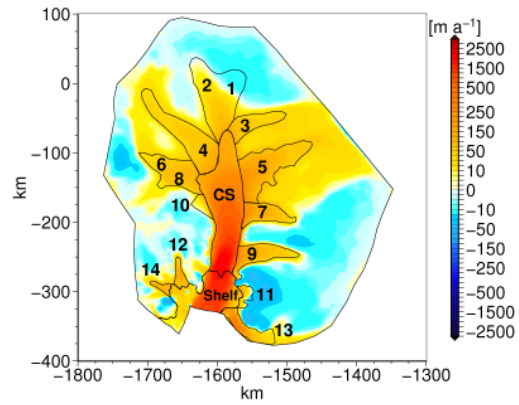


Figure 5.10:  $|u_{s,ref}| - |u_{s,qp-p2q0}|$

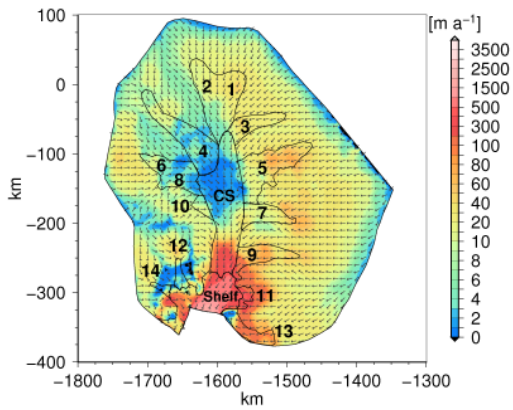


Figure 5.11:  $|u_{s,qp-p3q1}|$

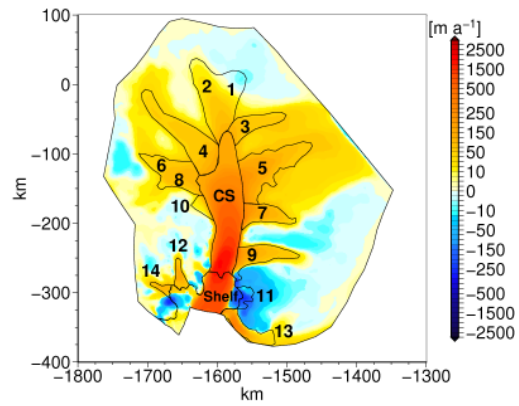


Figure 5.12:  $|u_{s,ref}| - |u_{s,qp-p3q1}|$

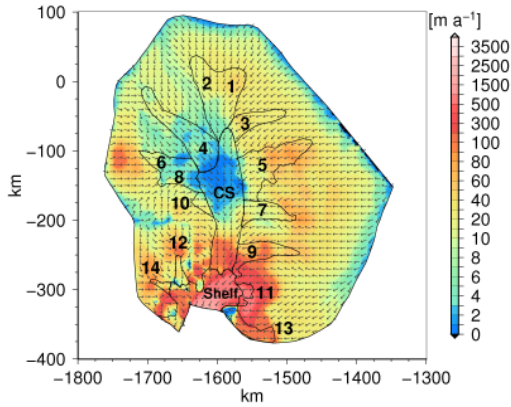


Figure 5.13:  $|u_{s,qp-p3q2}|$

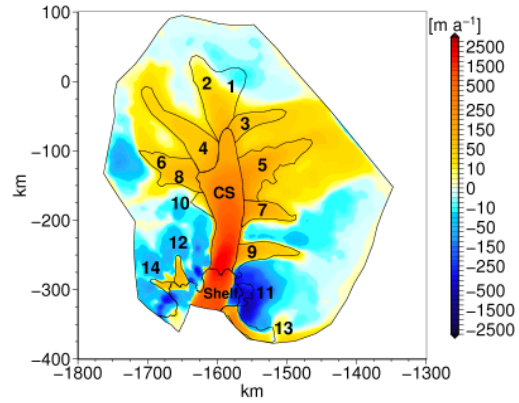


Figure 5.14:  $|u_{s,ref}| - |u_{s,qp-p3q2}|$

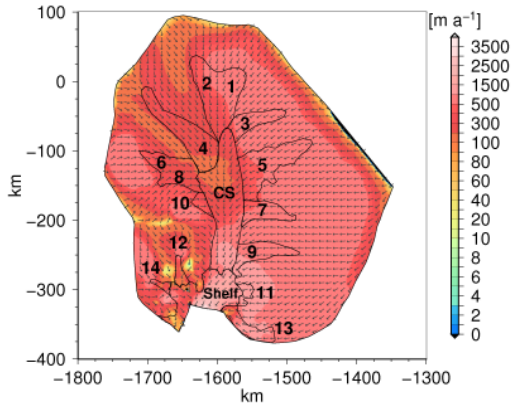


Figure 5.15:  $|u_{s,qp-p1q0}|$

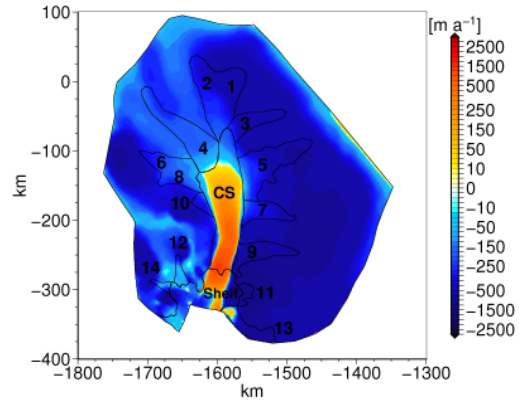
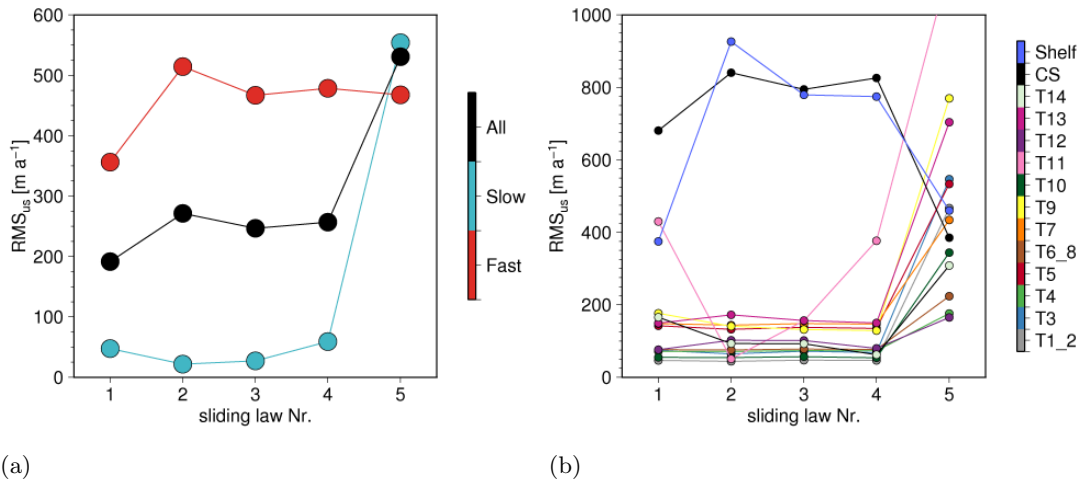


Figure 5.16:  $|u_{s,ref}| - |u_{s,qp-p1q0}|$

In Figures 5.17(a) and (b) the root-mean-square value  $RMS_{u_s}$  is plotted versus the sliding law number, as given in Table 5.1. As stated above in Section 5.2, the  $RMS_{u_s}$  value for the different simulations refers to the deviation to the reference simulation. In Figure 5.17(a) the  $RMS_{u_s}$  value is calculated for the different regions "All", "Slow" and "Fast", as shown in Figure 5.6(b). In Figure 5.17(b) the  $RMS_{u_s}$  value is calculated for the subdivided faster flowing regions, which are the single tributaries, the central stream and the ice shelf, as named in Figure 5.6(b).

The sliding law Nr.1, used in simulation qp-p1q2, has the smallest  $RMS_{u_s}$  value for the entire region "All", as well as for the fast flowing regions "Fast". When looking at the surface flow field structure in Figure 5.7, the entire central stream is not reproduced, but the inflow into the shelf is reasonably fast. This causes the  $RMS_{u_s}$  value for the ice shelf to be smallest, as its flow velocity crucially depends on the inflow from the grounded ice.

From all simulations in this section, sliding law Nr. 2, used in simulation qp-p2q0, produced the smallest  $RMS_{u_s}$  value for the slow flowing regions "Slow" and tributary 11. At the same time simulation qp-p2q0 has the largest  $RMS_{u_s}$  value for the fast flowing regions "Fast" and the ice shelf "Shelf". The qualitative structure of the central stream,

Figure 5.17:  $RMS_{u_s}$  vs. sliding law Nr.

as can be seen in Figure 5.9, reveals fast velocities in the lower part towards the ice shelf, but slowing down just before crossing the grounding line and entering the ice shelf. This structure leads to the high  $RMS_{u_s}$  value for the ice shelf in this simulation.

Sliding law Nr. 3, used in simulation qp\_p3q1, produces a similar flow field structure as sliding law Nr. 2, shown in Figure 5.11. However, the ice flow velocity does not slow down as much before crossing the grounding line, leading to a smaller  $RMS_{u_s}$  value for the ice shelf. At the same time, Tributary 11 is much faster than in the reference simulation, leading to a higher  $RMS_{u_s}$  value for this tributary.

The simulation qp\_p3q2, with sliding law Nr. 4, uses with  $N_b = \rho_i g H$  an effective pressure, that is not reduced for areas lying below sea level. The central stream, in this simulation, again slows down just before crossing the grounding line and entering the ice shelf, as can be seen in Figure 5.13, although not as much as in simulation qp\_p2q0. Tributary 11 is even faster than in simulation qp\_p3q1 and also much wider, influencing the  $RMS_{u_s}$  value for the slower flowing regions.

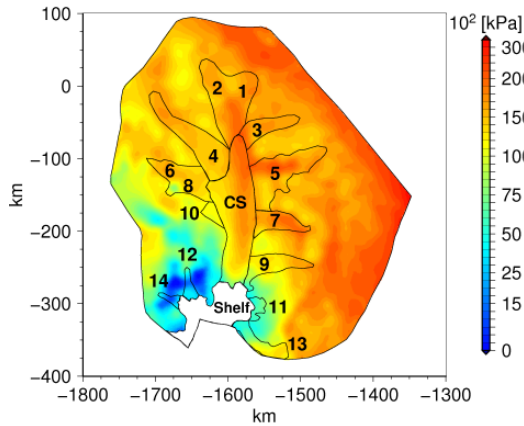
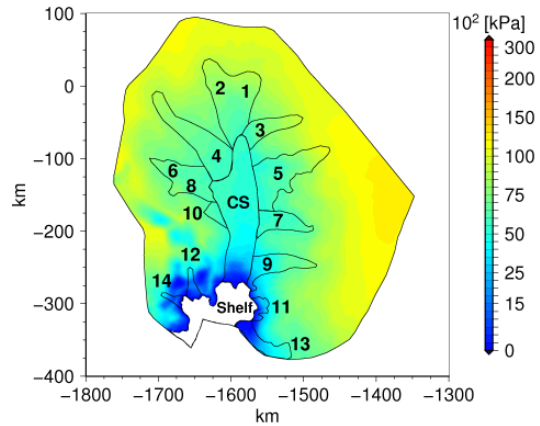
And finally, sliding law Nr. 5, used in simulation qp\_p1q0, produces a flow field that is fast everywhere, as seen in Figure 5.15. The  $RMS_{u_s}$  value for the central stream is smallest, compared to the other simulations in this section. Although the reduction in velocity just before the grounding line can also be seen here.

### 5.3.2 Discussion

It is obvious that none of the tested sliding laws serves for simulating the entire flow field of Pine Island Glacier in the form applied here. The location of tributaries 1, 5, 7, 9, 11 and 13 are in most simulations at least suggested. While tributaries 2, 4, 6 and 8 and, in particular, the central stream are not reproduced at all. Even though there was no parameter tuning involved, it can be suspected that a constant set of parameters for the entire region, as used here, does not lead to a surface flow field structure similar to that of Pine Island Glacier.

Still some conclusions can be drawn from the conducted simulations. We will first look

at the effect of the effective pressure  $N_b$ . The use of  $N_b$  in the Weertman-type sliding law (Eq. (5.6)) is in Section 5.1.1 reasoned with cavity formation. Thus assuming a constant ice thickness  $H$  and hence a constant ice overburden pressure  $\rho_i g H$ , the formation of water filled cavities, with an internal water pressure  $p_w$ , reduces the effective pressure  $N_b = \rho_i g H - p_w$  and therefore increases the basal sliding velocity  $u_b$ . The same effect can also be attributed to sea water penetrating below the grounded ice, which is possible near the grounding line. This process is more likely to happen, when the ice is only slightly grounded, thus close to floatation, and the bed rock is well below sea level, as is the case for Pine Island Glacier.


 Figure 5.18:  $N_b = \rho_i g H$ 

 Figure 5.19:  $N_b = \rho_i g H - p_w$ 

If the effective pressure  $N_b$  is applied in a form where it only represents the ice overburden pressure, such that  $N_b = \rho_i g H$ , it regulates the basal sliding velocity in the sense, that, not considering the effect of basal stress, there is less basal sliding for thicker ice (refer to Eq. (5.6)).

The effective pressure field  $N_b = \rho_i g H$  for Pine Island Glacier, representing the ice overburden pressure, is shown in Figure 5.18. The reduced effective pressure field  $N_b = \rho_i g H - p_w$  for Pine Island Glacier is shown in Figure 5.19. The reduced effective pressure has much lower values, especially in the area of the central stream and near the grounding line. Thus the effective pressure  $N_b = \rho_i g H - p_w$  is reduced in areas dominated by fast flow, making it the more plausible choice.

This finding, that the effective pressure in its reduced form  $N_b = \rho_i g H - p_w$ , seems to be important to be included in the sliding law, is supported by the results of the simulations. The two simulations qp\_p1q2 and qp\_p3q1, that produce an inflow of the central stream into the ice shelf, without speed reduction just before crossing the grounding line, both use the reduced effective pressure, as listed in Table 5.1.

Now coming back to the inability of all sliding laws tested here, with a constant parameter set, to reproduce the flow pattern of Pine Island Glacier. One of the obvious reasons, is the low in basal shear stress  $\tau_b$  in the middle of the central trough area, as can be seen in Figure 4.3. All the above applied sliding laws connect the basal sliding velocity  $u_b$  to some power of the basal shear stress  $\tau_b$ . This leads to low sliding velocities  $u_b$  for low basal stresses  $\tau_b$ . As shown in Section 4.1.4 (refer also to Figure 4.30), the basal sliding

velocity  $\mathbf{u}_b$  is an important component for the overall flow field of Pine Island Glacier.

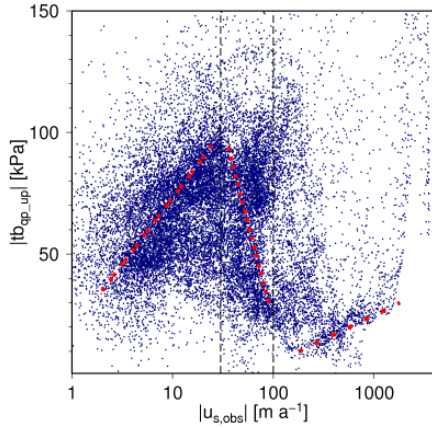


Figure 5.20:  $|\tau_{b,qp-up}|$  vs.  $|\mathbf{u}_{obs}|$

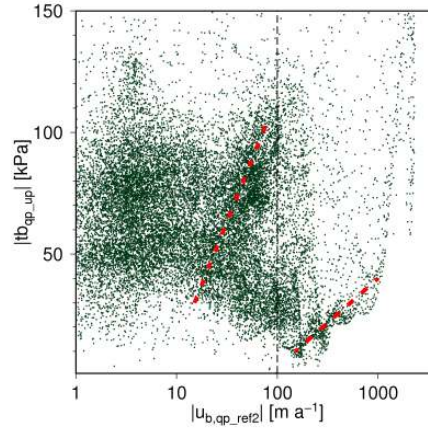


Figure 5.21:  $|\tau_{b,qp-up}|$  vs.  $|\mathbf{u}_{b,qp-ref2}|$

To demonstrate the relation between the basal sliding velocity  $\mathbf{u}_b$  and the basal shear stress  $\tau_b$ , we use some results from the previous chapter, and follow an approach by *MacAyeal* (1992). We take the basal shear stress from the no-slip simulation qp\_up (refer to Table 4.1),  $|\tau_{b,qp-up}|$ , as a proxy for the general basal shear stress. By plotting it separately, on a structured 2.5 km grid, against the observed surface velocity field  $|\mathbf{u}_{obs}|$ , shown in Figure 5.20, and the simulated basal velocity field from the reference simulation  $|\mathbf{u}_{b,ref}|$ , shown in Figure 5.21, we can estimate their relation.

For velocities  $\mathbf{u}_{obs} < 30 \text{ m a}^{-1}$ , the surface velocity increases with increasing basal shear stress, for a majority of the plotted grid points, as indicated with a red dashed line in Figure 5.20. For higher velocities this relation does not hold. For velocities  $30 \text{ m a}^{-1} < \mathbf{u}_{obs} < 100 \text{ m a}^{-1}$ , a slight opposing correlation between surface velocities and basal shear stress can be observed, showing increasing velocities with decreasing shear stress. Note that the trend appears small in Figure 5.20, as the velocities are plotted in logarithmic scale. A second part for increasing velocities with increasing basal shear stress is also visible for  $\mathbf{u}_{obs} > 100 \text{ m a}^{-1}$ , starting again from very low stresses.

For the simulated basal velocities  $|\mathbf{u}_{b,ref}|$  the picture is slightly different. We identified a region of increasing velocities with increasing basal shear stress for  $\mathbf{u}_{b,ref} < 100 \text{ m a}^{-1}$ , as indicated with a red dashed line in Figure 5.21. A second part of increasing velocities with increasing basal shear stress, similar to described above for the observed surface velocity field  $|\mathbf{u}_{obs}|$ , is visible for  $\mathbf{u}_{b,ref} > 100 \text{ m a}^{-1}$ , also shown in Figure 5.21.

The different identified sections of the relations between the basal shear stress  $|\tau_b|$  and the basal velocity  $|\mathbf{u}_b|$  suggest the presence of different bed conditions. As stated above in Section 5.1.2, high velocities that are present despite low basal stresses suggest the existence of weak bed regions below Pine Island Glacier.

In Section 4.2 a “quasi-inversion” for the basal sliding parameter  $\beta^2$  was conducted for the reference simulation. This sliding parameter is also referred to as a *drag factor*, and can be seen as a simple measure of lubrication or slipperiness at the bed (*Cuffey and Paterson*, 2010). The basal sliding parameter  $\beta^2$  corresponds to  $1/C_b$  for Eq. (5.6) with  $(p, q) = (1, 0)$ . The spatial distribution of the derived value  $C_b$  for the reference simulation

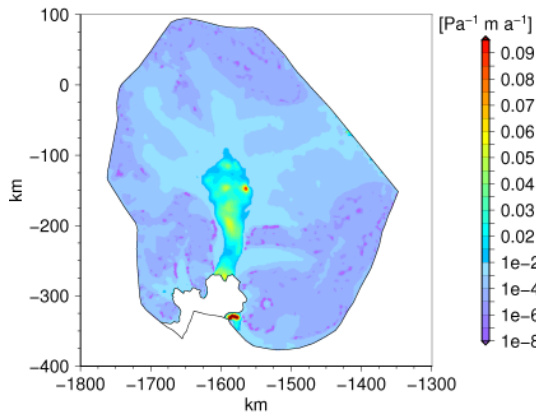
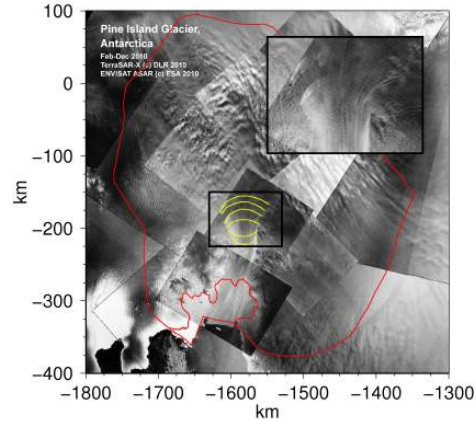

 Figure 5.22:  $1/\beta^2 = C_b$  for  $p = 1, q = 0$ 


Figure 5.23: Surface Crevasses

is shown in Figure 5.22. Higher values indicate stronger slipperiness. Coinciding with the region of highest slipperiness in the central stream, shown in Figure 5.22, is the onset region of bands of arcuate crevasses, stretching across the central stream. The crevasses are clearly visible in high-resolution TerraSAR-X images, shown in Figure 5.23. The positions of some crevasses are marked in yellow in Figure 5.23, and they are enlarged in the extra box. These crevasses suggest strong stretching as longitudinal stress gradients likely increase to compensate for the slippery bed (Joughin *et al.*, 2009). Thus the presence of the arcuate surface crevasses support the weak bed hypothesis.

## 5.4 Matching of roughness measure $\xi$ and sliding parameter $C_b$

The previous section illustrated, that different basal conditions are suspected to be present below Pine Island Glacier. To consider this in the basal boundary condition, a common approach is to assign different regions with different slip relations (e.g. Joughin *et al.*, 2009, 2010). A multitude of possibilities exist to separate the regions, and are still dependent on control methods. We aim to constrain basal sliding by physical parameters instead of being dependent on control methods.

The basal roughness measure  $\xi$  shown in Figure 4.46 is the physical parameter we consider. Therefore we will refer to the basal sliding parameter  $C_b$ , when it is related to the basal roughness measure  $\xi$  in this section as  $C_\xi$ . As shown above, in Section 5.1, the sliding parameter  $C_b$  in Eq. (5.6) depends on the basal roughness. The absolute values of the roughness measure  $\xi$  are dependent on parameters chosen for its derivation. At the same time the sliding parameter  $C_b$  depends not only on mechanical properties, such as basal roughness, but also thermal properties (refer to Section 5.1.1). Therefore the roughness measure  $\xi$ , as shown in Figure 4.46, can not directly be used as the sliding parameter  $C_\xi$ .

To use the roughness information anyhow, we select a range for the sliding parameter  $C_b$ , obtained via the “quasi-inversion” technique introduced in Section 4.2. The thus received logarithmic range is thereafter matched onto the normed and inverted distribution of the roughness measure  $\xi_n$ . It is inverted as lowest roughness correlates with highest basal

sliding and therefore highest values of  $C_\xi$ . This way we make sure to receive surface velocities within a realistic range.

The range for  $C_b$  is found (refer to Section 4.2.1) with

$$C_b = \frac{(|\mathbf{u}_{\text{obs}}| - |\mathbf{u}_{\text{s,qp-up}}|) N_b^q}{|\boldsymbol{\tau}_{\text{b,qp-up}}|^p}. \quad (5.9)$$

As discussed in Section 5.1.1, the sliding exponents  $p$  and  $q$  can be assigned with different values. Here we will keep  $p = 1$ , as an increase of the stress exponent will lead to a bigger error in the “quasi-inversion”, due to the assumptions made about the basal shear stress in that technique. On the other hand we consider a range of the effective pressure exponent  $q = [0; 2]$ . In the “quasi-inversion” technique, the choice of  $q$  does not alter the resulting surface velocity field. The effect of  $N_b^q$  is completely compensated for by the inferred basal sliding parameter  $C_b$ . This is due to the fact, that in our model the effective pressure  $N_b$  is a constant field, only influenced by the geometry. Altering the range of  $q$  is motivated by the structure of the spatial roughness distribution  $\xi$ , as will be made clear below. The reduced effective pressure  $N_b = \rho_i g H - p_w$  is used here (refer to Section 5.3.2).

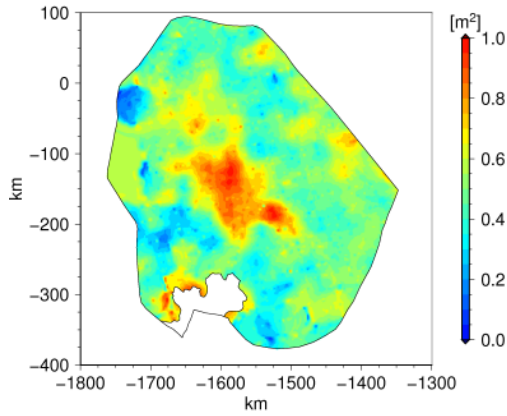


Figure 5.24: Normed and inverted  $\xi_n$

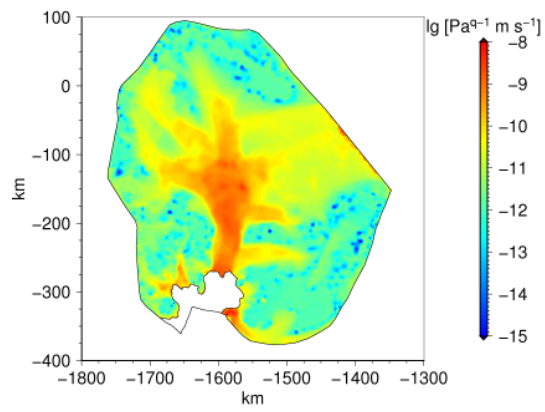


Figure 5.25:  $C_b$  for  $q = 0$

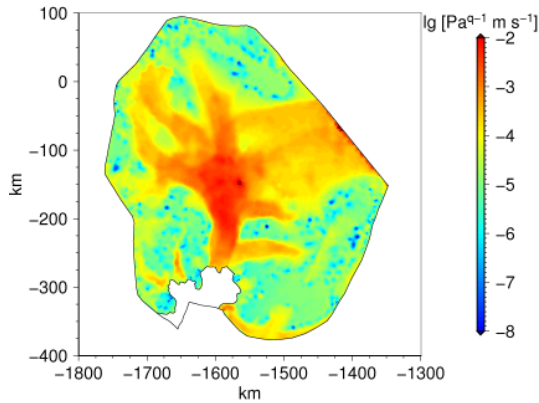


Figure 5.26:  $C_b$  for  $q = 1$

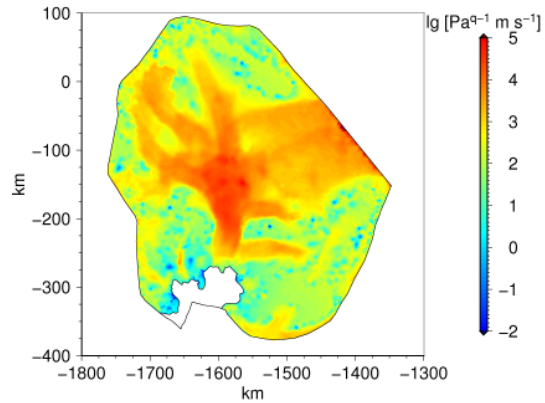


Figure 5.27:  $C_b$  for  $q = 2$

Figure 5.24 shows the distribution of the normed and inverted roughness measure  $\xi_n$ . In Figures 5.25-5.27 the inferred fields of the sliding parameter  $C_b$  for the different values of  $p = 1$  and  $q = 0$ ,  $q = 1$  and  $q = 2$  are shown in logarithmic scale, respectively. The logarithmic scales are matched onto the normed roughness, to create distributions of  $C_\xi$ .

The choice of  $q = 2$  reduces the value of  $C_b$  in the main stream just before the grounding line. The roughness measure  $\xi$  shows higher values in the same area, and the normed and inverted roughness measure  $\xi_n$ , as shown in Figure 5.24, accordingly lower values.

### 5.4.1 Simulations

Table 5.2: Overview of conducted simulations with  $C_\xi$

Nr.	identifier	$p$	$q$	$C_\xi$ range [Pa <sup>(<math>q-1</math>)</sup> m s <sup>-1</sup> ]	conv. $\mathbf{u}, p$	conv. $T$	solution time
1	p1q0_1	1	0	[1e-13;1e-8]	2.8e-04	4.9e-04	522646 s. ( $\sim$ 6 d)
2	p1q0_2	1	0	[1e-14;1e-8]	9.2e-04	6.4e-04	284519 s. ( $\sim$ 3.25 d)
3	p1q0_3	1	0	[1e-15;1e-8]	1.4e-03	1.1e-03	338716 s. ( $\sim$ 4 d)
4	p1q0_4	1	0	[1e-15;1e-9]	9e-03	3.5e-01	262000 s. ( $\sim$ 3 d)
5	p1q0_5	1	0	[1e-15;1e-10]	2.5e-02	6.4e-02	228452 s. ( $\sim$ 2.5 d)
6	p1q1_6	1	1	[1e-7;1e-2]	1.1e-03	1.9e-03	349398 s. ( $\sim$ 4 d)
7	p1q1_7	1	1	[1e-8;1e-2]	1.9e-03	4.4e-02	338333 s. ( $\sim$ 4 d)
8	p1q1_8	1	1	[1e-9;1e-2]	1.3e-02	3.4e-02	406324 s. ( $\sim$ 4.75 d)
9	p1q1_9	1	1	[1e-9;1e-3]	2.6e-02	1.8e-02	302137 s. ( $\sim$ 3.5 d)
10	p1q1_10	1	1	[1e-9;1e-4]	3e-02	5e-02	303634 s. ( $\sim$ 3.5 d)
11	p1q2_11	1	2	[1e-2;1e5]	3.7e-03	7.8e-02	719156 s. ( $\sim$ 8.25 d)
12	p1q2_12	1	2	[1e-3;1e5]	7.6e-04	5.2e-02	463512 s. ( $\sim$ 5.25 d)
13	p1q2_13	1	2	[1e-4;1e5]	1e-02	1.1e-02	253182 s. ( $\sim$ 3 d)
14	p1q2_14	1	2	[1e-4;1e4]	1.9e-02	7.9e-02	357307 s. ( $\sim$ 4 d)
15	p1q2_15	1	2	[1e-4;1e3]	6.3e-04	4e-02	525726 s. ( $\sim$ 6 d)

We conduct 15 simulations, where each parameter combination represents a potential subglacial setting. Table 5.2 gives an overview of the simulations, with the identifier for each simulation given in column “identifier“. 5 simulations are conducted with  $q = 0$ ,  $q = 1$  and  $q = 2$  each. The values for  $p$  and  $q$  are listed in the columns “ $p$ “ and “ $q$ “, respectively. The range for  $C_\xi$  is listed in column “ $C_\xi$  range“. For the different values of  $q$ , the range of  $C_\xi$  is varied. The widest range of  $C_\xi$  consists of the maximum values found by inversion for  $C_b$  (refer to Eq. (5.9)). The range is additionally narrowed from both sides, as the maximum values might represent outliers. Please note, that the values for  $C_\xi$  are here given in Pa<sup>( $q-p$ )</sup> m s<sup>-1</sup>, in contrast to the values used for the simulations with constant parameter sets (Section 5.3, Table 5.1), which are given in Pa<sup>( $q-p$ )</sup> m a<sup>-1</sup>. The value range  $C_\xi = [1e-15;1e-8]$  Pa<sup>-1</sup> m s<sup>-1</sup> for simulation Nr. 1, correspond to  $C_\xi \sim [3e-8;3e-1]$  Pa<sup>-1</sup> m a<sup>-1</sup>. The constant value given in Table 5.1 for  $(p, q) = (1, 0)$  falls with  $C_b = 1e-2$  Pa<sup>-1</sup> m a<sup>-1</sup> within this range. For  $(p, q) = (1, 1)$  no previously applied constant set of values was found, that could be referenced here. For  $(p, q) = (1, 2)$  the range for

simulation Nr. 11 of  $C_\xi = [1e-4; 1e5] \text{ Pa m s}^{-1}$  corresponds to  $C_b \sim [3e3; 3e12] \text{ Pa m a}^{-1}$ , which includes the constant value of  $C_b = 5e9 \text{ Pa m a}^{-1}$ .

The columns "conv. $\mathbf{u}$ , $p$ " and "conv. $T$ " again list the convergence, given as the smallest relative error achieved, as given in Eq. (3.3). The column "solution time" lists the real time needed for the solution process. The time needed crucially depends on the initial field. Dependent on the time when a simulation finished, it was either started with the solution from the reference simulation, or with a solution from another similar simulation in Table 5.2.

The  $RMS_{\mathbf{u}_s}$  deviation between the simulated surface velocity fields and the reference field for all simulations are shown in Figures 5.28(a) and (b). As done before, the total glacier region is divided into "All", "Slow" and "Fast" regions, as shown in Figure 5.6(b), for which the  $RMS_{\mathbf{u}_s}$  values are shown in Figure 5.28(a). The different tributaries are also separated as before, and the  $RMS_{\mathbf{u}_s}$  values for them are shown in Figure 5.28(b).

Figure 5.28(a) shows, that for  $q = 0$  and  $q = 1$ , smaller values of  $C_\xi$  lead to a smaller  $RMS_{\mathbf{u}_s}$  value for the "Slow" regions, and a higher  $RMS_{\mathbf{u}_s}$  value for the "Fast" regions. Also the  $RMS_{\mathbf{u}_s}$  value increases for the ice shelf "Shelf" and the central stream "CS", with smaller values of  $C_\xi$ , while the  $RMS_{\mathbf{u}_s}$  value for some tributaries decreases, as can be seen in Figure 5.28(b).

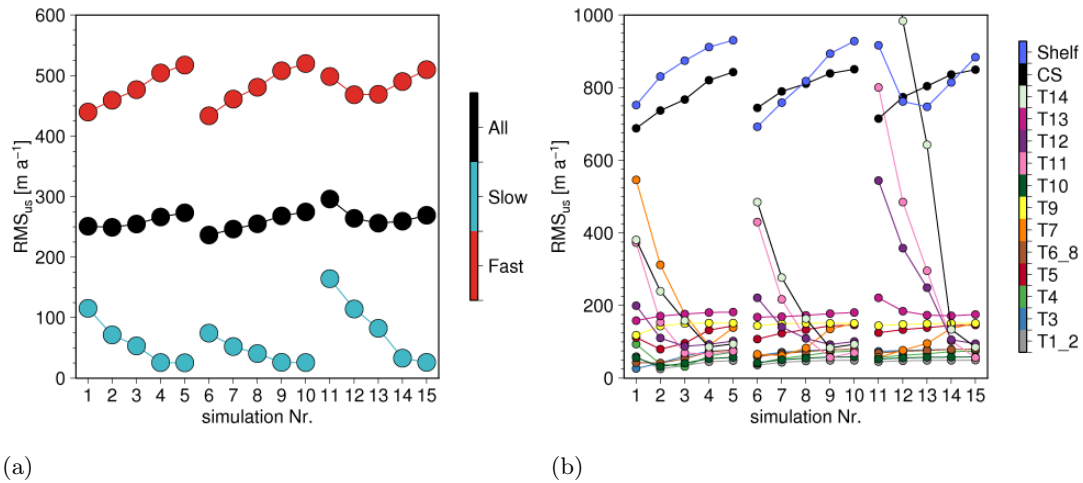


Figure 5.28:  $RMS_{\mathbf{u}_s}$  vs. simulation Nr.

For  $q = 2$  the behaviour is different. The  $RMS_{\mathbf{u}_s}$  value decreases for the "Slow" regions for smaller values of  $C_\xi$ , but first decreases and then increases for the "Fast" regions, shown in Figure 5.28(a). The same behaviour of first decreasing and then increasing  $RMS_{\mathbf{u}_s}$  values for smaller values of  $C_\xi$  is shown by the "Shelf", while the rest of the tributaries and the central stream by trend behave similar as for  $q = 0$  and  $q = 1$ , which can be seen in Figure 5.28(b).

The overall  $RMS_{\mathbf{u}_s}$  values are of a similar magnitude as for the simulations with constant sets of parameters (refer to Figures 5.17(a) and (b) in Section 5.3). Just looking at the  $RMS_{\mathbf{u}_s}$  values therefore does not imply a significant improvement of the structure of the surface flow field with the technique applied here. In the following we will therefore look at the qualitative structure of the surface flow field. To do so, we chose a few simulations,

which we will analyse in more detail. The ones chosen are not necessarily the ones with the smallest overall  $RMS_{u_s}$  value, but with interesting features.

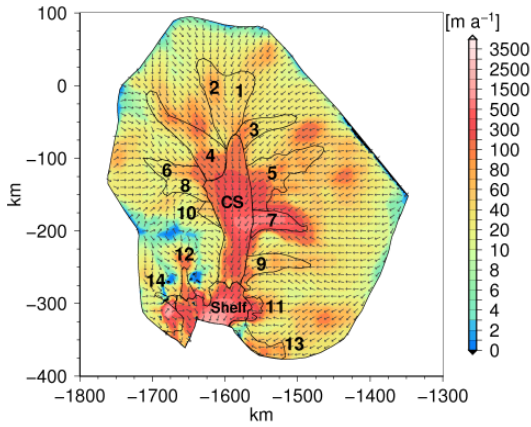


Figure 5.29:  $|\mathbf{u}_{s,p1q0.2}|$

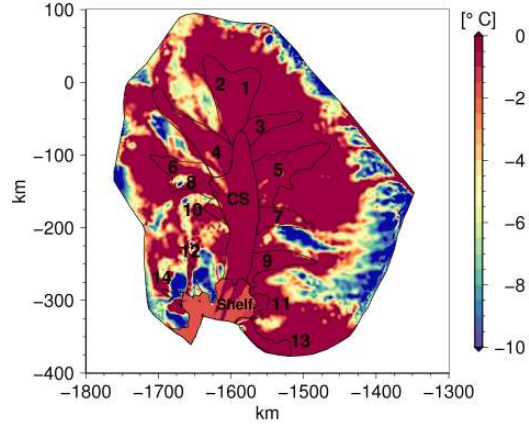
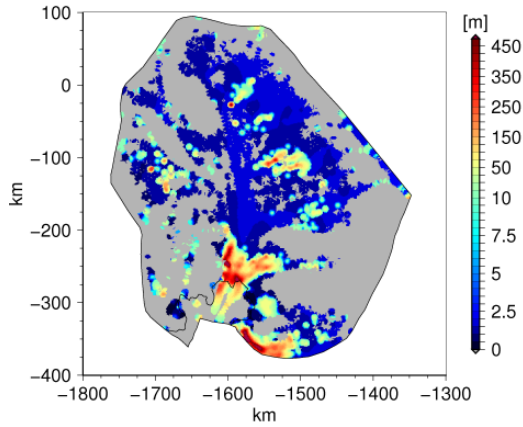
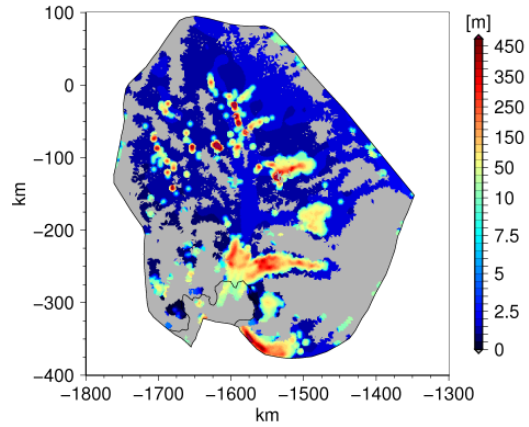


Figure 5.30:  $T'_{b,p1q0.2}$

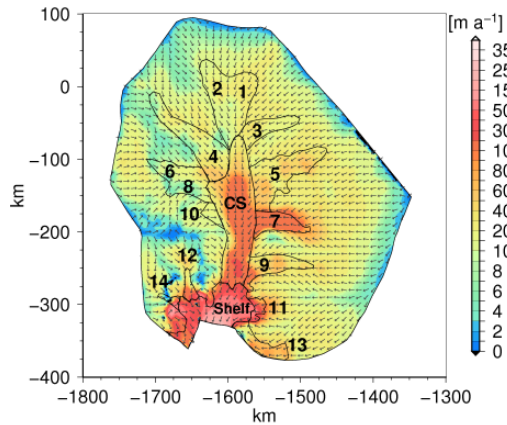
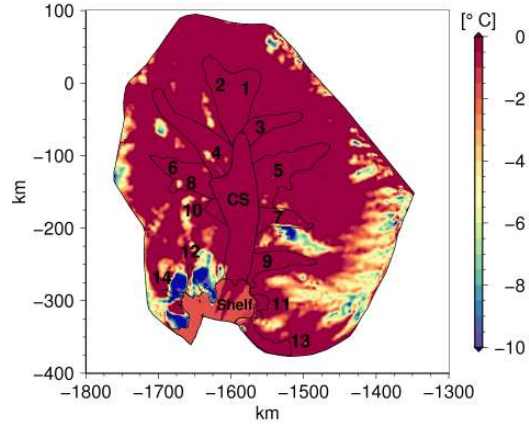
Figure 5.29 shows the surface velocity  $|\mathbf{u}_{s,p1q0.2}|$  and Figure 5.30 the homologous basal temperature  $T'_{b,p1q0.2}$  of simulation Nr. 2, with  $p, q = (1, 0)$  and  $C_b = [1e-14; 1e-8] \text{ Pa}^{-1} \text{ m s}^{-1}$ .

In the surface velocity field of simulation Nr. 2, the locations of tributaries 7, 11 and 12 are well reproduced. The locations of all other tributaries, apart from tributary 8 and 14, are also slightly visible in the surface flow field. In the vicinity of the observed location of tributary 14, the simulation shows an area of ice flowing with high velocities into the ice shelf. A striking feature is, that the velocities in tributary 7 are higher than in the central stream. The central stream itself flows reasonably fast, but slowing down just before the grounding line. This behaviour, as discussed in the last section, does not correlate with the observations. It leads to higher internal deformation in that region, and thus a high strain heating source term  $\psi$ . As already mentioned in the last chapter in Section 4.2.3, strain heating is the necessary or dominant mechanism to produce a temperate ice layer. The thickness of the temperate ice layer  $TLL$  is shown for simulation Nr. 2 in Figure 5.31. A thick temperate ice layer of  $\sim 300 \text{ m}$  is found in the central stream just before the grounding line and in the area of tributary 13. The warm ice from within the temperate layer in the central stream is transported into the shelf, leaving stripes of ice at  $T_{\text{pmp}}$  within the shelf (Figure 5.30). The homologous basal temperature  $T'_b$ , as shown in Figure 5.30, reflects the location of most tributaries with a temperate base, such that  $T'_b = 0^\circ \text{C}$ . Only tributary 14 is not found at its expected location, as already discussed for the surface velocity field, shown in Figure 5.29. Tributaries 4, 9, 11, 12 and 13 are, on the other hand, especially clearly separated from the surrounding colder ice by their temperate bases. This feature is even more dominant than in the homologous basal temperature of the reference simulation  $T'_{b,\text{ref}}$ , shown in Figure 5.5. This finding is especially interesting, as the tributary locations in the simulation Nr. 2 are not as clearly defined by the surface velocity field (Figure 5.29), as is the case for the reference simulation (Figure 5.4).

Figures 5.33 and 5.34 show the surface velocity field  $|\mathbf{u}_{s,p1q1.7}|$  and the homologous basal temperature  $T'_{b,p1q1.7}$ , respectively, for simulation Nr. 7, with  $(p, q) = (1, 1)$ . The slowing down of the main stream just before the grounding line is not as apparent in this


 Figure 5.31:  $TLL_{p1q0_2}$ 

 Figure 5.32:  $TLL_{p1q2_11}$ 

simulation, compared to simulation Nr. 2 (Figure 5.29). The locations of tributaries 7 and 11 are clearly visible, while they are not quite as clearly visible for tributaries 5, 9, 12 and 13. Tributaries 1, 2, 3, 4, 6, 8, 10 and 14 are not reproduced. Although this is not clearly visible in the  $RMS_{u_s}$  value (Figure 5.28(b)), due to the overall slower velocities in those tributaries if  $< 200 \text{ m a}^{-1}$ . Tributary 7 shows with a small  $RMS_{u_s}$  value a very good agreement with the reference simulation. The homologous basal temperature field  $T'_{b,p1q1-7}$  of simulation Nr. 7 (Figure 5.34) shows a much higher area fraction of temperate ice than simulation Nr. 2 (Figure 5.30). Thus the tributaries are not as clearly separated.


 Figure 5.33:  $|u_{s,p1q1-7}|$ 

 Figure 5.34:  $T'_{b,p1q1-7}$ 

Figures 5.35 and 5.36 show the surface velocity field  $|u_{s,p1q2_11}|$  and the homologous basal temperature  $T'_{b,p1q2_11}$ , respectively, for simulation Nr. 11, with  $(p, q) = (1, 2)$ . The feature observed already in the surface velocity of simulation Nr. 7 (Figure 5.33), that the main stream does not slow down before the grounding line as in simulation Nr. 2 (Figure

5.29), is even stronger visible in simulation Nr. 11 (Figure 5.35). The flow field in the main stream now resembles more the observed field, with increasing velocities towards the grounding line.

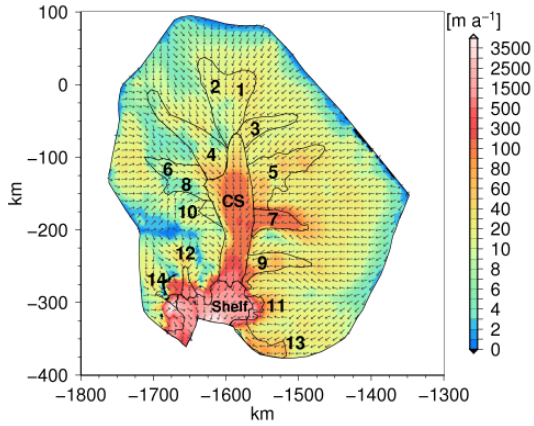


Figure 5.35:  $|\mathbf{u}_{s,p1q2.11}|$

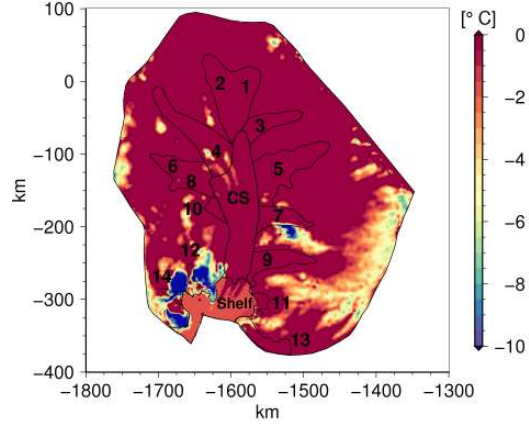


Figure 5.36:  $T'_{b,p1q2.11}$

The vicinity of the observed location of tributary 14 at the same time speeds up extremely, with an  $RMS_{u_s}$  value of  $1461 \text{ m a}^{-1}$  falling outside the plotted range in Figure 5.28(b). Since the location of tributary 14 in all simulations is not reproduced, and a wider area is effected with high flow velocities, the high speed also influences the  $RMS_{u_s}$  deviation for the "Slow" areas, as shown in Figure 5.28(a). Choosing a range for  $C_\xi$  with  $(p, q) = (1, 2)$  that best resembles the flow behaviour of the central stream unfortunately leads to exaggerated speed up of all other tributaries entering the ice shelf, namely tributaries 11, 12 and 14, as can be seen in Figure 5.28(b).

Also for simulation Nr. 11 the homologous basal temperature field  $T'_{b,p1q2.11}$  (Figure 5.36) shows a much higher area fraction of temperate ice than simulation Nr. 2 (Figure 5.30). The structure is similar to that of simulation Nr. 7, with the location of the tributaries not as clearly defined. The stripes of warmer ice at  $T_{pmp}$  within the ice shelf are shorter in simulation Nr. 11 (Figure 5.36), than in simulation Nr. 2 (Figure 5.30) and 7 (Figure 5.34). This is related to less internal deformation in front of the grounding line and therefore a thinner layer of temperate ice  $TLL_{p1q2.11}$ , as shown in Figure 5.32.

#### 5.4.2 Discussion

In this section we test the applicability of including actual measured roughness data in a sliding law, to reproduce the surface flow field structure of Pine Island Glacier. As a motivation we use the original ideas that motivated the Weertman-type sliding law, as shown in Eq. (5.6), and that relate the basal sliding parameter  $C_b$  to the basal roughness. We combine the spatial distribution of the basal roughness  $\xi$  with a plausible range of the basal sliding parameter  $C_b$ , to create a new basal sliding parameter  $C_\xi$ . This new parameter  $C_\xi$  is applied in the basal sliding law in different forms. On the one hand the range of values for  $C_\xi$ , on the other hand the influence of the effective pressure  $N_b$  in the sliding law is varied. The variation of the range for  $C_\xi$  is done to test the influence of the

extreme values onto the flow field. The increase of the influence of the effective pressure  $N_b$  in the sliding law is motivated by the results from Section 5.3, which find the reduced effective pressure to be important for the flow of Pine Island Glacier (refer to Section 5.3.2), as large areas of the base are below sea level.

With the approach presented here we were able to reproduce some of the complex features of the observed surface velocity field of Pine Island Glacier. This effect is not necessarily represented within the  $RMS_{u_s}$  values shown in Figures 5.28(a) and (b). The values do not differ strongly from the results of the previous section, where constant sets of basal sliding parameters were applied (Section 5.3). However, when looking at the results in a more qualitative manner, a much better representation of the flow field is apparent. Especially in the simulations Nr. 11-15, with  $(p, q) = (1, 2)$ , a much better representation of the central stream and the inflow into the ice shelf across the grounding line is found, than was achieved with a constant set of parameters. The influence of the reduced effective pressure  $N_b = \rho_i g H - p_w$  is thus emphasised again. At the same time the method, as applied here, does not lead to a full reproduction of the surface flow structure. This suggests that other processes, not considered here, are also important for the basal sliding behaviour. A possibility not tested yet due to computational constraints is the effect of the basal stress exponent  $p$ . Increasing it would possibly to some extent regulate the high velocities in some areas, due to low basal stresses (Figure 4.3).

Our results furthermore support our previous finding, that no significant temperate ice layer is suspected in the main stream. Strong basal sliding is necessary for the reproduction of the flow field, which leads to little strain heating, due to lack of internal deformation.

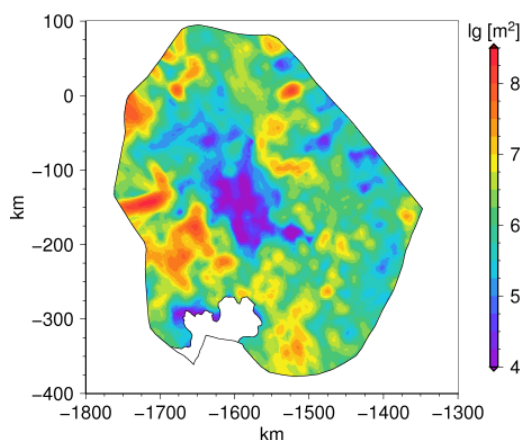
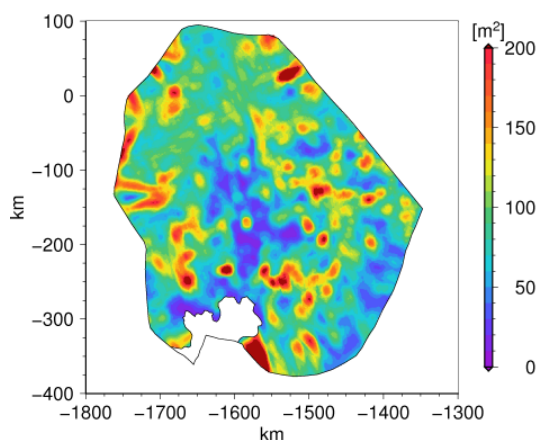
## 5.5 Li-sliding

The Weertman-type sliding law commonly used in ice flow models, and shown in Eq. (5.6), is based on the idea of *regelation* and *enhanced creep* (as shown in Section 5.1), but not really related to these mechanisms anymore. The more parametrised and tuned sliding assumptions were necessary due to complex unknown processes taking place, but also due to lack of knowledge about the physical composition of the bed itself. The increasing availability of RES profiles across Antarctica is changing the latter progressively. RES profiles can be analysed for the basal roughness (refer to Sections 1.1.3 and 4.4). The roughness of the base is becoming increasingly recognised as an important factor in glaciological research (e.g. *Rippin et al.*, 2006). *Li et al.* (2010) had the idea to bring the original principles of *regelation* and *enhanced creep* back into the formulation of the basal sliding law by considering the measured roughness of the bed below the ice.

In this chapter we test the ideas of *Li et al.* (2010) by application to Pine Island Glacier. In Section 5.5.1 the two-parameter roughness index from *Li et al.* (2010) is introduced and discussed on the example of Pine Island Glacier. In Section 5.5.2 it is shown how the original ideas by *Weertman* (1957) are connected to the ideas by *Li et al.* (2010), and the sliding relation, as applied in our model, is formulated. And finally, in Section 5.5.3, the simulations for Pine Island Glacier with the Li sliding assumption are shown and discussed.

### 5.5.1 The two parameter roughness index - $\xi_2$ and $\eta_2$

A key technique to derive basal roughness are Fourier transformations (FT). A FT can be used to transform any surface into a sum of several periodically undulated surfaces. This way the amplitude and spatial frequency of the undulations can be expressed. For theoretical dynamic studies characterising the roughness by FT works well. However, to show the spatial distribution of roughness, in a glaciological context, a single parameter index  $\xi$  was introduced (*Hubbard et al.*, 2000; *Taylor et al.*, 2004). The single parameter roughness index  $\xi$  is defined as the integral of the spectrum within a specified wavelength interval. This method represents the amplitude of the undulations, but information about the frequencies is lost. For Pine Island Glacier the single parameter roughness index  $\xi$  was calculated by *Rippin et al.* (2011) (Section 4.4) and already used in the previous section (Section 5.4).

Figure 5.37: roughness amplitude  $\xi_2$ Figure 5.38: roughness frequency  $\eta_2$ 

*Li et al.* (2010) introduce a two-parameter roughness index that represents the amplitude  $\xi_2$  and frequency  $\eta_2$  of the undulations. Because of the statistical meanings of  $\xi_2$  and  $\eta_2$ , they can be used as a proxy for the vertical and horizontal length scales present at the base. To do so the integration interval for  $\{\xi_2, \eta_2\}$  should be in the metre-scale waveband. In the example in *Li et al.* (2010) they use a moving window length of 1024 points ( $N = 10$ ,  $2^N = 1024$ ). The spatial resolution is 70 m and thus gives a moving window length of  $\sim 70$  km. David Rippin calculated the two-parameter roughness index for Pine Island Glacier and kindly provided it to us for this study. He first modified his programme so he could reproduce the values presented in *Li et al.* (2010) (personal communication, 2012). Still the spatial resolution of the underlain data for Pine Island is different to that of *Li et al.* (2010). It is calculated with ( $N = 5$ ,  $2^N = 32$ ), which is the minimum for  $N$  that should be used (e.g. *Taylor et al.*, 2004). With a spatial resolution of 34 m this leads to a moving window length of 1088 m, which is in the metre-scale waveband required by *Li et al.* (2010), to be able to apply the data in a sliding relation. Rippin applied the programme to Pine Island Glacier and received the fields for  $\xi_2$ , shown in Figure 5.37 in logarithmic scale, and for  $\eta_2$ , shown in Figure 5.38. The modification of the programme to reproduce the values of *Li et al.* (2010) leads to a difference in the total values between

$\xi$  as shown in Figure 4.46, and  $\xi_2$  as shown in Figure 5.37, although the pattern remains the same.

*Li et al.* (2010) introduce an interpretation how different basal topographies with their geomorphic implications can be distinguished from patterns of  $\xi$  and  $\eta$ , which is based on ideas by *Bingham and Siegert* (2009). According to this, a marine setting with intensive deposition and fast and warm ice flow, as proposed for the central part of Pine Island Glacier, is characterised by low values of  $\xi$  and high values of  $\eta$ , thus low-amplitude, low-frequency roughness. This is not necessarily the case for the central trunk area, as can be seen in Figures 5.37 and 5.38. Instead it seems to be more dominated by low-amplitude, high-frequency roughness, which can be, following *Li et al.* (2010), interpreted as a continental setting after intensive erosion, also with fast and warm ice flow. Still, this interpretation can not be seen as a contradiction to the earlier stated suspicion of the presence of marine sediments. We only considered the relative relation of high and low values. Absolute values can not be taken here, as they always depend on the spatial resolution of the underlain data, the moving window length and other details for the derivation process of the roughness index.

### 5.5.2 Assumptions - Controlling obstacle size - Constant $C_L$

To combine the two-parameter roughness index  $\{\xi_2, \eta_2\}$  with the basal sliding law from *Weertman* (1957), *Li et al.* (2010) state that  $\xi_2$  is proportional to the mean square of amplitudes such that Weertman's obstacle dimension  $a$  can be written as

$$a = c_1 \cdot \xi_2^{1/2}, \quad (5.10)$$

with a proportionality factor  $c_1$ . The same applies to  $\eta_2$ , so that Weertman's obstacle spacing  $l$  can be written as

$$l = c_2 \cdot \eta_2^{1/2}, \quad (5.11)$$

with a proportionality factor  $c_2$ .

By assuming, that the controlling obstacle size is dominating, as discussed in Section 5.1.1 (Eq. (5.5)), *Li et al.* (2010) build on the idea of *Weertman* (1957) and relate the two-parameter roughness index  $\{\xi_2, \eta_2\}$  to a basal sliding velocity, such that

$$\mathbf{u}_b = c \left( \frac{\eta_2}{\xi_2} \right)^{\frac{(n+1)}{2}}, \quad (5.12)$$

where  $c$  is a factor not depended on geometrical conditions, and  $n = 3$  is the stress exponent (refer Section 2.2.1).

To be able to apply the above stated relation as a sliding law, we relate the basal sliding velocity  $\mathbf{u}_b$  to the basal shear stress  $\tau_b$ , by considering the original approach by *Weertman* (1957), such that

$$\mathbf{u}_b = C_L \left( \tau_b \frac{\eta_2}{\xi_2} \right)^{\frac{(n+1)}{2}}, \quad (5.13)$$

with the constant  $C_L = C_W (c_2/c_1)^{1+n}$ . The value for  $C_W$  can be estimated, as shown in Section 5.1.1, and is in our example about  $C_W = 4.46 \times 10^{-29} \text{ m}^3 \text{ s}^3 \text{ kg}^{-2}$ . The proportionality factors  $c_1$  and  $c_2$  on the other hand are not further defined. Therefore we decided to take  $C_L$  as a single parameter to adjust.

To implement the sliding relation, as given in Eq. (5.13), in our model, we need to rewrite it in terms of the basal stress  $\tau_b$ , such that

$$\tau_b = \left( \frac{\mathbf{u}_b}{C_L} \right)^{\frac{2}{(n+1)}} \left( \frac{\xi_2}{\eta_2} \right). \quad (5.14)$$

We estimate a value for  $C_L$  by assuming, as introduced in Section 4.2.1, the following

$$C_L = (|\mathbf{u}_{\text{obs}}| - |\mathbf{u}_{\text{s,qp-up}}|) |\tau_{\text{b,qp-up}}|^{-\frac{(n+1)}{2}} \left( \frac{\xi_2}{\eta_2} \right)^{\frac{(n+1)}{2}}. \quad (5.15)$$

This method does not result in a single value for  $C_L$ , but in a distribution of values in the range of  $C_L = [6.8\text{e-}7; 4.3\text{e}4] \text{ Pa}^{-2} \text{ m a}^{-1}$ . The maximum and minimum values are hereby only outliers, while the majority of the values lie within  $C_L = [1\text{e-}9; 1\text{e-}6] \text{ Pa}^{-2} \text{ m s}^{-1} \sim [3\text{e-}2; 3\text{e}2] \text{ Pa}^{-2} \text{ m a}^{-1}$ . In the next section we show the simulations conducted with the values for  $C_L$  in the smaller range.

To put the sliding law applied here into context with the previous sections, it can be noted that, with  $n = 3$ , Eq. (5.13) represents a Weertman-type sliding law with  $p = 2$  and  $q = 0$  (Eq. (5.6)), as already discussed in Section 5.1.1 for the *controlling obstacle size*  $a_c$ .

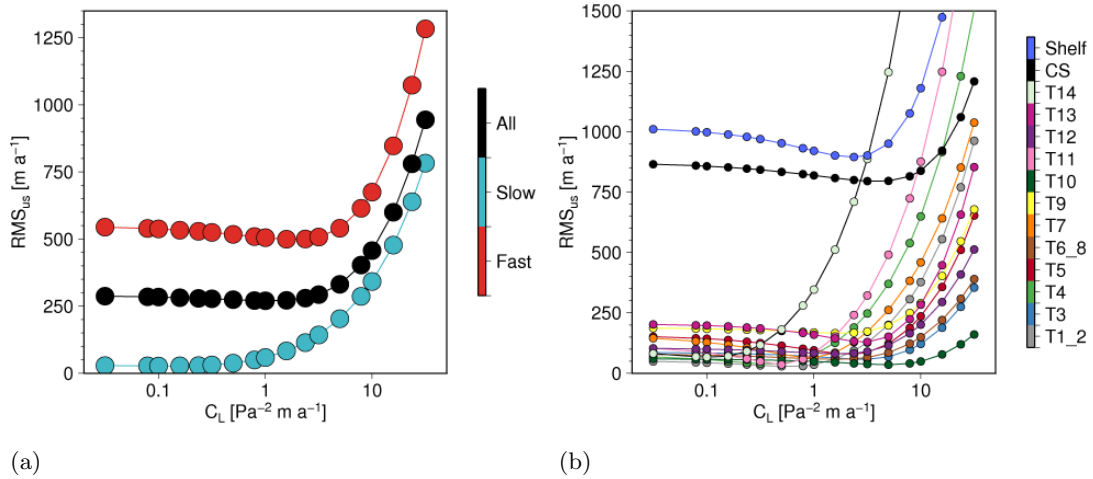
### 5.5.3 Simulations

For all simulations conducted in this section, only the ice flow model (refer to Section 3.2.2) is solved for. The temperature distribution within the ice is taken from the reference simulation (Section 4.2.2). The base below the fast flowing areas is thus temperate in all simulations, as can be seen in the distribution of the homologous basal temperature of the reference simulation, shown in Figure 5.5. The fully-coupled model is not suitable for a parameter study, due to time constraints. Use of the temperature field from the reference simulation gives the opportunity to connect the sliding behaviour to the basal temperature, thus only allowing ice to slide where  $T$  is close to  $T_{\text{pmp}}$ . This is achieved with the temperature function  $f(T)$  (refer to Eq. (2.46)), such that the basal boundary condition is now given as

$$\tau_b = \left( \frac{\mathbf{u}_b}{C_L f(T)} \right)^{\frac{2}{(n+1)}} \left( \frac{\xi_2}{\eta_2} \right). \quad (5.16)$$

The use of the temperature function  $f(T)$  slightly improves the results shown below, but does not change the overall picture.

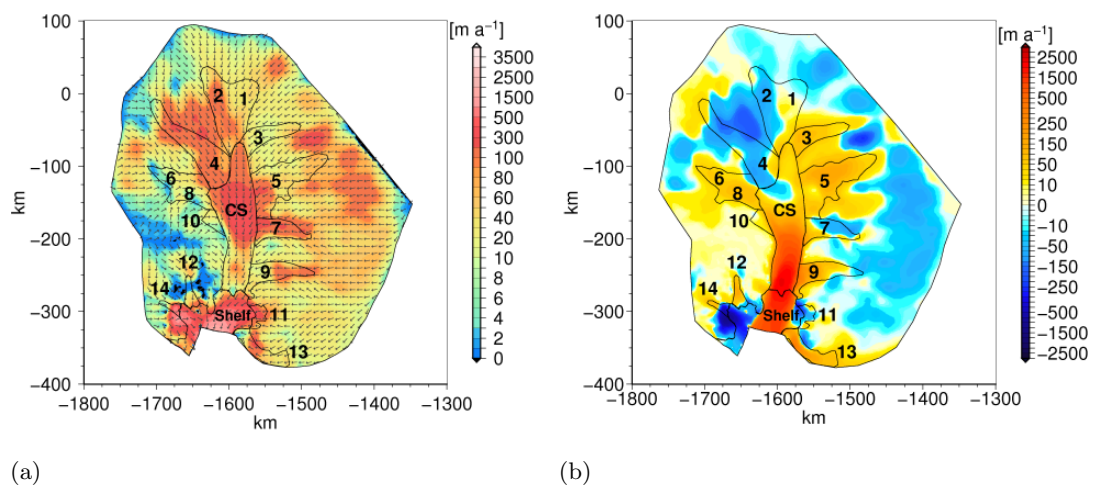
The simulations conducted vary over  $C_L$  in the range  $[1\text{e-}9; 1\text{e-}6] \text{ Pa}^{-2} \text{ m s}^{-1} \sim [3\text{e-}2; 3\text{e}2] \text{ Pa}^{-2} \text{ m a}^{-1}$ , as described above. The  $\text{RMS}_{\mathbf{u}_s}$  deviations between the reference and simulated results are shown for all simulations in Figures 5.39(a) and (b), and show a somewhat regular pattern. For the slower flowing areas, the  $\text{RMS}_{\mathbf{u}_s}$  value increases with increasing  $C_L$ , shown in Figure 5.39(a). For the faster flowing areas, the  $\text{RMS}_{\mathbf{u}_s}$  value first slightly decreases with increasing  $C_L$ , and, after reaching a minimum of  $\text{RMS}_{\mathbf{u}_s} = 499.7 \text{ m a}^{-1}$  for  $C_L = 1.58 \text{ Pa}^{-2} \text{ m a}^{-1}$ , increases with increasing  $C_L$ . Since we conduct simulations with discrete values for  $C_L$ , the value of  $\text{RMS}_{\mathbf{u}_s} = 499.7 \text{ m a}^{-1}$  represents the minimum value for the simulations conducted here, and not an absolute minimum. The  $\text{RMS}_{\mathbf{u}_s}$  value for the

Figure 5.39:  $RMS_{u_s}$  vs.  $C_L$  [Pa<sup>-2</sup> m a<sup>-1</sup>]

entire region "All", shows a similar behaviour of first decreasing and then increasing with increasing  $C_L$ , with a minimum  $RMS_{u_s}$  value of 270.6 m a<sup>-1</sup> for  $C_L = 1$  Pa<sup>-2</sup> m a<sup>-1</sup>. Some of the  $RMS_{u_s}$  values for the different tributaries show a similar pattern as the "Slow", and some as the "Fast" regions, as can be seen in Figure 5.39(b).

In the following we will look at two selected simulations in more detail. First the simulation with  $C_L = 1$  Pa<sup>-2</sup> m a<sup>-1</sup>, which has the smallest  $RMS_{u_s}$  value for the entire region "All", is looked at. Secondly, the simulation with  $C_L = 31.56$  Pa<sup>-2</sup> m a<sup>-1</sup>, which is the highest value of  $C_L$  simulated with, is considered.

The surface velocity field  $|\mathbf{u}_s|$  for  $C_L = 1$  Pa<sup>-2</sup> m a<sup>-1</sup>, is shown in Figure 5.40(a). The difference between the simulated ( $C_L = 1$  Pa<sup>-2</sup> m a<sup>-1</sup>) and the reference surface velocity field, thus  $|\mathbf{u}_{s,ref}| - |\mathbf{u}_s|$ , is shown in Figure 5.40(b).

Figure 5.40: (a)  $|\mathbf{u}_s|$  and (b)  $|\mathbf{u}_{s,ref}| - |\mathbf{u}_s|$  for  $C_L = 1$  Pa<sup>-2</sup> m a<sup>-1</sup>

Some features of the surface flow field are reproduced, as can be seen in Figure 5.40(a). High velocities are found in the upper part of the central stream. However, the central stream strongly reduces the speed towards the grounding line. This pattern is even more dominant than in the simulations discussed in the previous sections. Tributaries 2, 4, 5, 7, 9, 11 and 13 are reproduced to some extent in the surface flow field, while tributaries 1, 3, 6, 8, 10 and 12 are difficult to identify. The area around tributary 14 is, as also discussed in the previous section, dominated by very high velocities. These high velocities are also reflected in the difference  $|\mathbf{u}_{s,\text{ref}}| - |\mathbf{u}_s|$ , shown in Figure 5.40(b). The grounded area around tributary 14, as well as the adjacent ice shelf, are dominated by dark blue colours, representing much higher here simulated velocities, than present in the reference simulation. This can also be observed in the  $\text{RMS}_{\mathbf{u}_s}$  value for tributary 14 and  $C_L = 1 \text{ Pa}^{-2} \text{ m a}^{-1}$ , shown in Figure 5.39(b). The highest  $\text{RMS}_{\mathbf{u}_s}$  value for this simulation ( $C_L = 1 \text{ Pa}^{-2} \text{ m a}^{-1}$ ) is found for the ice shelf, which is characterised by strong over- and underestimation of the surface velocities, compared to the reference simulation (Figure 5.40(b)). The second highest  $\text{RMS}_{\mathbf{u}_s}$  value is found for the central stream, for which the surface velocity is mainly underestimated.

The surface velocity field  $|\mathbf{u}_s|$  for  $C_L = 31.56 \text{ Pa}^{-2} \text{ m a}^{-1}$ , is shown in Figure 5.41(a). The difference between the simulated ( $C_L = 31.56 \text{ Pa}^{-2} \text{ m a}^{-1}$ ) and the reference surface velocity field, thus  $|\mathbf{u}_{s,\text{ref}}| - |\mathbf{u}_s|$ , is shown in Figure 5.41(b).

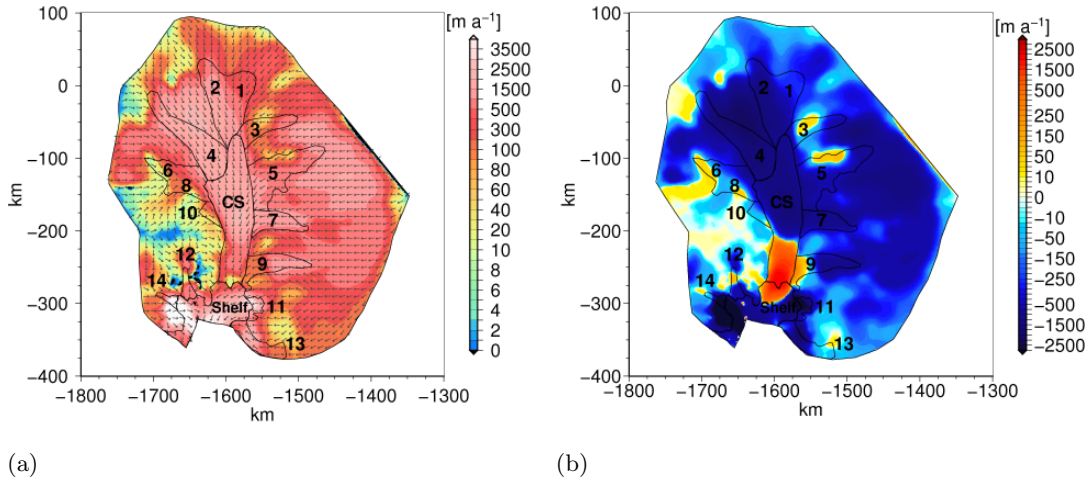


Figure 5.41: (a)  $|\mathbf{u}_s|$  and (b)  $|\mathbf{u}_{s,\text{ref}}| - |\mathbf{u}_s|$  for  $C_L = 31.56 \text{ Pa}^{-2} \text{ m a}^{-1}$

The surface flow field for  $C_L = 31.56 \text{ Pa}^{-2} \text{ m a}^{-1}$  is dominated by very high velocities (Figure 5.41(b)), which is also reflected in the difference to the reference simulation (Figure 5.41(b)), where an overestimation is found in a major part of the entire region. Only the central stream area in the vicinity of the grounding line is slower than for the reference simulation, indicated by the red region in Figure 5.41(b).

This strong overestimation of the velocities is also reflected in the  $\text{RMS}_{\mathbf{u}_s}$  values in Figures 5.39(a) and (b). On the  $\text{RMS}_{\mathbf{u}_s}$  values for tributaries 3, 6, 8 and 10 are  $< 500 \text{ m a}^{-1}$ .

The overall flow pattern can not be reproduced with the method of using the two parameter roughness index  $\{\xi_2, \eta_2\}$  in the sliding law. Still some interesting features arise,

which will be discussed in the following.

#### 5.5.4 Discussion

In this section we test the applicability of a theory developed by *Li et al.* (2010) to the region of Pine Island Glacier, that connects a two parameter roughness index  $\{\xi_2, \eta_2\}$  to the basal sliding law. We rewrite the equations from *Li et al.* (2010), by partly using information of the original ideas from *Weertman* (1957), and extend the sliding law with a temperature function, to apply it as a boundary condition in our flow model. We define a constant sliding parameter  $C_L$ , over which a parameter study is conducted.

The results of the surface flow field show certain features. The central stream in all the simulations from this section is partitioned into a faster flowing upper part, and a slower flowing lower part, in the vicinity of the ice shelf. The speed reduction towards the ice shelf was already found in simulations of the preceding two sections, but is here even stronger pronounced. However, the faster flowing upper part in the simulations conducted here, resembles much more the observed velocity field, as was the case in the simulations with constant sets of parameters within the sliding law (Section 5.3).

No single value for  $C_L$  could be found, that reproduces the surface velocity field of Pine Island Glacier with all its features. For higher  $C_L$  values, that reproduce the velocities in the central stream in a better manner, the velocities in the slower flowing area around tributaries 3, 5, 7 and 9, located to the South of the main stream, are simulated much too high (refer to Figure 5.40(a)). Additionally, the area around tributary 14 behaves slightly different to most other tributaries. It speeds up much faster for much lower values of  $C_L$ . This was already found in the previous section, Section 5.4, and is related to the low roughness measures  $\xi$ ,  $\xi_2$  and  $\eta_2$  in that region.

It has to be noted here, that the method developed by *Li et al.* (2010), which is based on the theory from *Weertman* (1957), is strictly speaking only valid for hard bed sliding, as discussed in Section 5.1.1. Since we showed in Section 5.3.2, that an area of weak bed is suspected below some parts of the central stream of Pine Island Glacier, the method by *Li et al.* (2010) should strictly speaking not be applied here. Thus it is somewhat surprising, that the method seems to work best in reproducing the surface velocity field in the area of the suspected weak bed.

Thus, despite the inability of a complete reproduction of the surface flow field of Pine Island Glacier with the method presented here, it still resulted in a surface flow structure, that reveals some important features.

## 5.6 Discussion

In this chapter we approached the challenge of formulating an appropriate sliding law for the simulation of the flow field of Pine Island Glacier from 3 different angles. Our starting point is hereby always a Weertman-type sliding law, as discussed in Section 5.1.1 and shown in Eq. (5.6).

The first approach, described in Section 5.3, is to take constant sets of sliding parameters, that have previously successfully been applied in sliding laws for other areas. Even though the flow field structure could not be reproduced with this approach, it let us conclude, that the reduced effective pressure  $N_b = \rho_i g H - p_w$  is of major importance for an appropriate sliding law formulation for Pine Island Glacier.

Our second approach, described in Section 5.4, is based to the original formulation of the Weertman-type sliding law, in which the basal sliding parameter  $C_b$  is connected to, among other things, the basal roughness. We take a data set of the basal roughness below Pine Island Glacier (*Rippin et al., 2011*), and match the spatial variation of its field and a defined range of the basal sliding parameter  $C_b$ . The procedure is conducted for 3 different formulations, with a varying impact of the basal effective pressure. The results produce a surface flow field, that resembles in its main features the observed field. Although the fingered structure of the tributaries is not as clearly visible, the fast flowing main stream entering the ice shelf, is.

The last approach is based on a method from *Li et al. (2010)*, which they theoretically developed, and is tested here for its applicability to Pine Island Glacier. The method relates a two parameter roughness index  $\{\xi_2, \eta_2\}$  to the obstacle dimension and spacing of Weertman's original sliding formulation, described in Section 5.1.1. Simulations are conducted, in which a parameter study over an unconstrained sliding parameter  $C_L$  is carried out. The resulting surface flow fields show high velocities in the area of low driving stress in the upper central stream. However, the velocity in the lower central stream reduces towards the grounding line, which contradicts the observed surface velocity pattern.

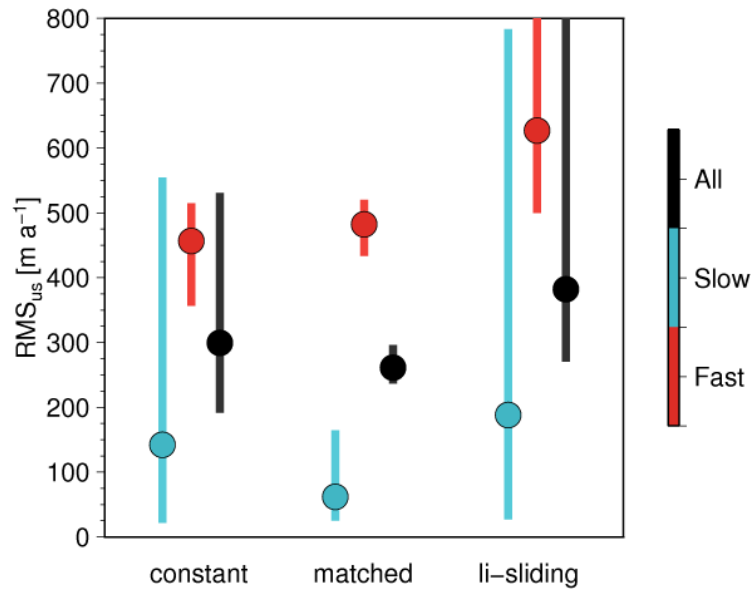


Figure 5.42: Compilation of  $\text{RMS}_{u_s}$  values from the three sections, with the mean value shown as a filled circle and the range of values shown in the wide bar.

The  $\text{RMS}_{u_s}$  deviations from the simulated to the reference surface velocity field are calculated for all simulations. To distinguish the fast flowing central stream with all its tributaries, which is dominated by basal sliding, as shown in Figure 4.30, from the slower flowing remainder of the domain, a partitioning is introduced as shown in Figure 5.6(b). The  $\text{RMS}_{u_s}$  values for all simulations, subdivided into the regions "Fast", "Slow" and

“All“, are shown in Figure 5.42. The designations ”constant“, ”matched“ and ”li-sliding“ refer to the results from Sections 5.3, 5.4 and 5.5, respectively. Each filled circle here refers to the mean value of a region and section, while the coloured bar behind it gives the range of values obtained with the according method.

The  $\text{RMS}_{u_s}$  values, shown in Figure 5.42 thus suggest, that the closest fit of the simulated to the reference surface velocities is achieved, for all regions ”Fast“, ”Slow“ and ”All“, with the method that uses constant sets of parameters, demonstrated in Section 5.3. Although, the smallest  $\text{RMS}_{u_s}$  values for the ”Slow“ regions are with  $\sim 25 \text{ m a}^{-1}$ , for all 3 methods, very close to each other. The smallest spread of  $\text{RMS}_{u_s}$  values, for the regions ”Fast“, ”Slow“ and ”All“, is reached with the matching method, treated in Section 5.4.

The reproduction of the absolute values of the surface flow field, as also discussed in the previous chapter, in Section 4.2.2, is a challenge. The  $\text{RMS}_{u_s}$  values stand for the deviations to the reproduction. We also already emphasised at various occasions in this chapter, that also the qualitative structure of the flow field is of major importance. With qualitative structure we mean the reproduction of fast flowing streams and slower flowing regions. So now, stepping away from the error measure of  $\text{RMS}_{u_s}$  values, when comparing the qualitative surface flow field structure, it is by far best reproduced by the matching method, described in Section 5.4.

One of the major achievements of this technique is, that it brings some of the original physical meaning, of representing the basal roughness, back into the sliding law. The formulation is thus not solely dependent on control methods. This finding is especially important in a changing basal environment. *Smith et al.* (2012) describe a process of rapid subglacial erosion beneath Pine Island Glacier, which could lead to a change in the roughness measure below the glacier. The rapid increase of RES profiles at Pine Island Glacier make the roughness measure, possibly also the temporal change of it, more widely available.



## Chapter 6

### Conclusions and outlook

The aim of this study was to advance our knowledge about the internal dynamics, basal motion and thermal structure of Pine Island Glacier, a fast flowing outlet glacier in the West Antarctic Ice Sheet. The glacier is located in an area of the West Antarctic Ice Sheet, where the bedrock is in many regions well below the sea level. Additionally, the bed slopes down from the grounding line towards the inland of the glacier. On this kind of setting the marine ice sheet instability hypothesis is based, which postulates an intrinsically unstable condition *Vaughan* (2008). In the past decades Pine Island Glacier was observed to have undergone various changes, including acceleration, thinning and grounding line retreat. Additionally, rapid subglacial erosion of a marine sediment basin below the glacier is suspected (*Smith et al.*, 2012). The future behaviour of the glacier is important for estimates of global eustatic sea level rise, as Pine Island Glacier alone holds enough ice above flotation, to raise global sea level by 0.52 m, if fully melted (*Vaughan et al.*, 2006).

A variety of external factors can influence the internal dynamics of the glacier, and therefore being important for its future behaviour. These external factors include the temperature of the atmosphere at the surface, accumulation, melt rates, the geothermal heat flux at the base and mechanical basal conditions, as for example the existence of rough bedrock or smooth marine sediments. While the conditions at the surface are nowadays assessable in reasonable temporal and spatial resolution, with use of remote sensing techniques, the conditions at the base still remain widely unknown, due to the difficult accessibility.

Therefore we aim to define the recent state of important basal conditions at Pine Island Glacier, with use of a thermo-mechanically coupled 3D full-Stokes ice flow model. In glacier dynamic studies, the coupling of the temperature field to the flow dynamics is of high importance. Higher internal ice temperatures lead to a stronger internal deformation. Additionally, as ice is believed to slide over its base only at interface temperatures near or at the local melting point, the sliding behaviour is also sensitively influenced by the temperature distribution. Furthermore, the consideration of all stress terms, as done in the here presented full-Stokes model, is especially important when simulating processes in the vicinity of the grounding line. The coupled ice flow model is implemented in the commercial Finite Element Method software COMSOL Multiphysics<sup>®</sup>. The software COMSOL has previously already been successfully applied to the study of glaciological questions (e.g. *Humbert*, 2010; *Rückamp*, 2011). We advanced and extended the application to a coupled ice sheet - ice shelf system in three dimensions. The implementation and validation of the coupled flow model is conducted as part of this study.

The results of the application of the validated coupled flow model to the region of Pine Island Glacier, are divided into two parts. In the first part, the dominant local mechanisms driving the flow of Pine Island Glacier are investigated. This is of interest

because the surface flow field is dominated by a complex structure of various tributaries feeding into a fast flowing main stream. In a changing environment, the tributaries might react differently to external changes. Additionally the information can be of interest for planning of measurement surveys in the area. Our results are validated along the observed surface velocity field of Pine Island Glacier, representing the surface flow structure in the years 2007 to 2009 (*Rignot et al.*, 2011). We carefully declare our results to be a likely present setting, as the complex glacial system can not uniquely be defined with a diagnostic experimental set up (*Raymond and Gudmundsson*, 2009). Still we can exclude unlikely, and emphasise the more likely settings. To our knowledge it is the first full-Stokes flow model to successfully solve fully-coupled for the glacier flow and temperature field of Pine Island Glacier in three dimensions.

Our results show, that large areas at the base of the glacier are temperate, with temperatures at the pressure melting point. At the same time the thickness of the temperate basal layer is suspected to be very small in most areas. Only the area around a small tributary feeding into the ice shelf, tributary 11, shows a wider area of a temperate layer thickness  $> 70$  m. Tributaries 4 and 6, feeding into the upper part of the central stream, are separated by a band of cold ice at the base, suggesting a temperature control of the flow field in that area. In some fast streaming areas the finding of a temperate base is strongly coupled to the inclusion of a friction heating term. This could suggest support of a deceleration, if initiated due to other factors, like for example a change in the basal mechanical conditions in that area. An increased geothermal heat flux around the location of a suspected sub volcanic centre below Pine Island Glacier (*Corr and Vaughan*, 2008) is not suspected to alter the flow structure significantly, as the structure of the temperate ice at the base seems to be reasonably stable in our simulations. This is not including the effect of change in the effective pressure, who's importance will be emphasised below. We identify the data set from Purucker 2012 (updated version of *Fox Maule et al.*, 2005) for the geothermal heat flux below Pine Island Glacier to be the likely best representation of actual conditions.

Basal sliding is identified to be the dominant mechanism for fast flow at Pine Island Glacier. Formulation of an appropriate sliding law to be used as a basal boundary condition in ice flow models is one of the big challenges in present numerical glaciological studies. Therefore, in the second part of this study, we focus on the formulation of an appropriate sliding law for Pine Island Glacier. As a starting point, we test the applicability of formulations, that have been successfully applied in other areas. These formulations consist of constant parameter sets in a Weertman-type sliding law. The results show, that a reduced effective pressure is necessary to be included in the basal sliding law, to simulate the transition from grounded to floating ice in the central stream appropriately. All tested formulations with constant parameter sets though are not able to reproduce the upper part of the fast flowing central stream, and generally the fingered structure of the flow field. This is partly due to an area with very low basal stress in the middle of the central stream, where a Weertman-type sliding law with constant parameter sets can not produce high basal velocities. This challenge is usually met by the use of control methods, that produce a spatially varying basal sliding parameter, accounting for the differences in the surface flow field. Our reference simulation was conducted with a similar approach. In a next step we want to include a measured physical quantity into the formulation of the basal sliding law.

The structure of the low in driving stress partially correlates with the structure of the

---

basal roughness below Pine Island Glacier, as derived by *Rippin et al.* (2011). Therefore a marine sediment basin is likely present, where weak till can not support the basal drag of the fast flowing ice, being in a state of plastic failure. This motivates our attempt to include some of the original physical meaning of the basal sliding parameter  $C_b$  in a sliding law, by matching the structure of the basal roughness with a relevant range of values. The results show a much better representation of the surface flow field, with a fast flowing central stream. Although, an area of very low roughness adjacent to the slow flowing part of the ice shelf, leads to an overestimation of flow velocities in that area. The method we introduce here, thus, although promising, needs to be extended to include other locally relevant factors, to reproduce the observed surface velocity field at Pine Island Glacier. An important role hereby can likely be tributed to the subglacial water system, not modelled explicitly in this study. The importance of the effective pressure in a sliding formulation emphasises this.

Another method of including information about the basal roughness in the basal sliding formulation is based on a theory by *Li et al.* (2010). This theory relates a two parameter roughness index, representing the amplitude and frequency of the roughness, to Weertman's original obstacle dimension and spacing. The thus formulated sliding law, which leaves one parameter to adjust, is applied to Pine Island Glacier. The resulting flow field structure shows high velocities in the upper part of the central stream, but low velocities in the lower part, towards the ice shelf. The sliding law, as formulated here, does not include the effective water pressure yet.

As an outlook for interesting questions to be addressed in the future, we will in the following make some suggestions. The fully coupled ice flow model should be extended even further. Shear margins should be included in the ice flow model, connecting damage with the enhancement factor. Also the connection of basal roughness and sliding should be analysed further. The Li-sliding formulation should be extended with the effective water pressure. Possibly the speed reduction in the central stream towards the ice shelf could be regulated. In the future it would be worthwhile to couple a hydrological model to it, as the effective pressure was shown to be very important to the sliding behaviour. Additionally, the internal deformation of the underlying till could be modelled explicitly. Also the implementation of grounding line motion is meaningful. If successfully included, prognostic studies could be conducted. The prognostic studies would focus on decadal changes, as the full-Stokes model is not applicable to much longer periods due to computational constraints. For Pine Island Glacier this is of interest, as changes are observed even in a decadal time scale. The thermal state, especially in the region where a significant temperate layer was found, could be verified with help of RES profiles.

We want to conclude with a few final remarks. The present state of the internal temperature and flow structure of Pine Island Glacier was successfully simulated. The results show a predominantly cold glacier, with a big part of the base being temperate. The flow field in the central stream and the numerous tributaries is dominated by basal sliding. Our formulation of the basal sliding law emphasises the connection between sliding velocity and basal roughness, as parts of the complex observed surface flow structure could be reproduced. The present dynamics and temperature structure of the glacier are of major importance for its future behaviour. A thermo-mechanically coupled model, as we presented here, is essential for the inference of interrelations between the thermal regime, the basal roughness structure and the flow and sliding conditions.



# Appendix A

## A.1 Integration theorems

### A.1.1 Reynold's transport theorem

$$\frac{dg}{dt} = \frac{\partial g}{\partial t} + \text{div}(g\mathbf{u}) \quad (\text{A.1})$$

### A.1.2 Integral formula of Gauss - Divergence theorem

$$\int_{\Omega} (\text{div} f) \, dx = \oint_{\partial\Omega} f \cdot \mathbf{n} \, da \quad (\text{A.2})$$

### A.1.3 Integration by parts - Green-Gauss theorem

$$\int_{\Omega} \left( -w \frac{\partial F}{\partial x} \right) dx = \int_{\Omega} \left( \frac{\partial w}{\partial x} F - \frac{\partial}{\partial x} (wF) \right) dx \quad (\text{A.3})$$



# Bibliography

- Alley, R., 1992: Flow-law hypotheses for ice-sheet modeling. *J. Glaciol*, **38**(129), 245–256.
- Alley, R. B., I. Joughin, et al., 2012: Modeling ice-sheet flow. *Science*, **336**(6081), 551–552.
- Aschwanden, A., E. Bueller, C. Khroulev, and H. Blatter, 2012: An enthalpy formulation for glaciers and ice sheets. *Journal of Glaciology*, **58**(209), 441–457.
- Bamber, J. L., J. L. Gomez-Dans, , and J. A. Griggs, 2009: A new 1km digital elevation model of the Antarctic derived from combined satellite radar and laser data – Part 1: Data and methods. *The Cryosphere*, **3**, 101–111.
- Bamber, J. L., R. E. M. Riva, B. L. A. Vermeersen, and A. M. LeBrocq, 2009: Reassessment of the Potential Sea-Level Rise from a Collapse of the West Antarctic Ice Sheet. *Science*, **324**, 901–903.
- Baral, D. R., K. Hutter, and R. Greve, 2001: Asymptotic Theories of Large-Scale Motion, Temperature, and Moisture Distribution in Land-Based Polythermal Ice Sheets: A Critical Review and New Developments. *Applied Mechanics Reviews*, **54**, 215.
- Barnes, P., D. Tabor, and J. Walker, 1971: The friction and creep of polycrystalline ice. *Proceedings of the Royal Society of London. A. Mathematical and Physical Sciences*, **324**(1557), 127–155.
- Benn, D. I. and D. J. A. Evans, 2010: *Glaciers and Glaciation*. Hodder Arnold Publication, 2nd edition.
- Bentley, C. R. and N. A. Ostenson, 1961: Glacial and subglacial topography of West Antarctica. *Journal of Glaciology*, **3**(29), 882–912.
- Bindschadler, R., 1983: The importance of pressurized subglacial water in separation and sliding at the glacier bed. *Journal of Glaciology*, **29**(101), 3–19.
- Bindschadler, R., 2006: The environment and evolution of the West Antarctic ice sheet: setting the stage. *Philosophical Transactions of the Royal Society A*, **364**, 1583–1605.
- Bindschadler, R. A., 2002: History of lower Pine Island Glacier, West Antarctica, from Landsat imagery. *Journal of Glaciology*, **48**(163), 536–544.
- Bingham, R. G., E. C. King, A. M. Smith, and H. D. Pritchard, 2010: Glacial geomorphology: Towards a convergence of glaciology and geomorphology. *Progress in Physical Geography*, **34**(3), 327–355.
- Bingham, R. G. and M. J. Siegert, 2009: Quantifying subglacial bed roughness in Antarctica: implications for ice-sheet dynamics and history. *Quaternary Science Reviews*, **28**(3-4), 223–236.

- Björnsson, H., 1988: Hydrology of ice caps in volcanic regions.
- Blankenship, D., R. Bell, S. Hodge, J. Brozena, J. Behrendt, and C. Finn, 1993: Active volcanism beneath the West Antarctic ice sheet and implications for ice-sheet stability.
- Blatter, H., 1995: Velocity and stress fields in grounded glaciers: a simple algorithm for including deviatoric stress gradients. *Journal of Glaciology*, **41**(138), 333–344.
- Blatter, H., R. Greve, and A. Abe-Ouchi, 2010: A short history of the thermomechanical theory and modelling of glaciers and ice sheets. *Journal of Glaciology*, **56**(200), 1087–1094.
- Blatter, H. and K. Hutter, 1991: Polythermal conditions in Arctic glaciers. *Journal of Glaciology*, **37**(126), 261–269.
- Bohlander, J. and T. Scambos, 2007: Antarctic coastlines and grounding line derived from MODIS Mosaic of Antarctica (MOA). *National Snow and Ice Data Center. Digital media. Accessed 24 April 2008.*, **Boulder, Colorado USA**.
- Bougamont, M., S. Tulaczyk, and I. Joughin, 2003: Response of subglacial sediments to basal freeze-on 2. Application in numerical modeling of the recent stoppage of Ice Stream C, West Antarctica. *Journal of Geophysical Research*, **108**(B4), 2223.
- Boulton, G. and R. Hindmarsh, 1987: Sediment deformation beneath glaciers: rheology and geological consequences. *Journal of Geophysical Research*, **92**(B9), 9059–9082.
- Boulton, G. S. and D. Dent, 1974: The nature and rates of post-depositional changes in recently deposited till from south-east iceland. *Geografiska Annaler. Series A. Physical Geography* 121–134.
- Boulton, G. S. and A. S. Jones, 1979: Stability of temperate ice caps and ice sheets resting on beds of deformable sediment. *Journal of Glaciology*, **24**, 29–43.
- Budd, W. and T. Jacka, 1989: A review of ice rheology for ice sheet modelling. *Cold Regions Science and Technology*, **16**(2), 107–144.
- Budd, W. and D. Jenssen, 1987: Numerical modelling of the large-scale basal water flux under the West Antarctic Ice Sheet. In *Dynamics of the West Antarctic Ice Sheet*, Van der Veen, C.J., O. J., editor. Kluwer, Dordrecht, 293–320.
- Bueler, E., 2008: Lessons from the short history of ice sheet model intercomparison. *The Cryosphere Discussions*, **2**(3), 399–412.
- Bueler, E., J. Brown, and C. Lingle, 2007: Exact solutions to the thermomechanically coupled shallow ice approximation: effective tools for verification. *Journal of Glaciology*, **53**(182), 499–516.
- Christoffersen, P. and S. Tulaczyk, 2003: Response of subglacial sediments to basal freeze-on 1. Theory and comparison to observations from beneath the West Antarctic Ice Sheet. *Journal of Geophysical Research*, **108**(B4), 2222.
- Clarke, G., 1987: A short history of scientific investigations on glaciers. *Journal of Glaciology* 4–24.

- Clarke, G., 2005: Subglacial processes. *Annual Review of Earth and Planetary Sciences*, **33**, 247–276.
- Clarke, G., G. Cross, and C. Benson, 1989: Radar imaging of glaciovolcanic stratigraphy, Mount Wrangell caldera, Alaska: interpretation model and results. *Journal of Geophysical Research*, **94**(B6), 7237–7249.
- Comiso, J. C., 2000: Variability and Trends in Antarctic Surface Temperatures from In Situ and Satellite Infrared Measurements. *Journal of Climate*, **13**, 1674–1696.
- COMSOL, 2008: COMSOL Multiphysics Reference Guide. *COMSOL AB, Vers. 3.5a*.
- COMSOL, 2012a: COMSOL Multiphysics Reference Guide. *COMSOL AB, Vers. 4.3a*.
- COMSOL, 2012b: COMSOL Multiphysics User’s Guide. *COMSOL AB, Vers. 4.3a*.
- Cornford, S., D. Martin, D. Graves, D. Ranken, A. Le Brocq, R. Gladstone, A. Payne, E. Ng, and W. Lipscomb, 2012: Adaptive mesh, finite volume modeling of marine ice sheets. *Journal of Computational Physics* 529–549.
- Corr, H. F. J., C. S. M. Doake, A. Jenkins, and D. G. Vaughan, 2001: Investigations of an “ice plain” in the mouth of Pine Island Glacier, Antarctica. *Journal of Glaciology*, **47**(156), 51–57.
- Corr, H. F. J. and D. G. Vaughan, 2008: A recent volcanic eruption beneath the West Antarctic ice sheet. *Nature Geoscience*, **1**(2), 122–125.
- Cuffey, K. M. and W. S. B. Paterson, 2010: *The Physics of Glaciers*. Butterworth-Heinemann, 4th edition.
- Dahl-Jensen, D., N. Gundestrup, S. Gogineni, and H. Miller, 2003: Basal melt at North-GRIP modeled from borehole, ice-core and radio-echo sounder observations. *Annals of Glaciology*, **37**(1), 207–212.
- Dalziel, I. W. D. and D. H. Elliot, 1982: West Antarctica: Problem child of Gondwanaland. *Tectonics*, **1**(1), 3–19.
- Dalziel, I. W. D. and L. A. Lawver, 2001: The lithospheric setting of the West Antarctic ice sheet. *The West Antarctic Ice Sheet: Behavior and Environment*, **77**, 29–44.
- Deeley, R. M. and P. H. Parr, 1914: The Hintereis Glacier. *Philosophical Magazine*, **27**, 153–176.
- Dierckx, M. and J.-L. Tison, 2013: Marine ice deformation experiments: an empirical validation of creep parameters. *Geophysical Research Letters* 1–5.
- Docquier, D., L. Perichon, and F. Pattyn, 2011: Representing Grounding Line Dynamics in Numerical Ice Sheet Models: Recent Advances and Outlook. *Surveys in Geophysics*, **32**, 417–435.
- Durand, G., O. Gagliardini, B. de Fleurian, T. Zwinger, and E. L. Meur, 2009: Marine Ice-Sheet Dynamics: Hysteresis and Neutral Equilibrium. *Journal of Geophysical Research*, **114**, F03009.

- Durand, G., O. Gagliardini, L. Favier, T. Zwinger, and E. le Meur, 2011: Impact of bedrock description on modeling ice sheet dynamics. *Geophysical Research Letters*, **38**(20), L20501.
- Durand, G., O. Gagliardini, T. Zwinger, E. L. Meur, and R. C. A. Hindmarsh, 2009: Full-Stokes modeling of marine ice-sheets: influence of the grid size. *Annals of Glaciology*, **50**(52), 109–114.
- Durran, D. R., 2010: *Numerical methods for fluid dynamics: With applications to geophysics*, volume 32. Springer.
- Duval, P., 1977: The role of the water content on the creep rate of polycrystalline ice. *Isotopes and impurities in snow and ice*, **118**, 29–33.
- Echelmeyer, K., 1987: Direct observation of basal sliding and deformation of basal drift at sub-freezing temperatures. *Journal of Glaciology*, **33**(113).
- Echelmeyer, K. A., W. D. Harrison, C. Larsen, and J. E. Mitchell, 1994: The role of the margins in the dynamics of an active ice stream. *Journal of Glaciology*, **40**(136), 527–538.
- Engelhardt, H., 2004: Ice temperature and high geothermal flux at Siple Dome, West Antarctica, from borehole measurements. *Journal of Glaciology*, **50**(169), 251–256.
- Engelhardt, H., N. Humphrey, B. Kamb, and M. Fahnestock, 1990: Physical conditions at the base of a fast moving Antarctic ice stream. *Science*, **248**, 57–59.
- Engelhardt, H. and B. Kamb, 1998: Basal sliding of ice stream B, West Antarctica. *Journal of Glaciology*, **44**(147), 223–230.
- Favier, L., O. Gagliardini, G. Durand, and T. Zwinger, 2012: A three-dimensional full Stokes model of the grounding line dynamics: effect of a pinning point beneath the ice shelf. *The Cryosphere*, **6**(1), 101–112.
- Flowers, G. E., H. Björnsson, and F. Palsson, 2003: New insights into the subglacial and periglacial hydrology of Vatnajökull, Iceland, from a distributed physical model. *Journal of Glaciology*, **49**(165), 257–270.
- Fowler, A. C., 1986: A sliding law for glaciers of constant viscosity in the presence of subglacial cavitation. *Proceedings of the Royal Society of London. A. Mathematical and Physical Sciences*, **407**(1832), 147–170.
- Fox Maule, C., M. E. Purucker, N. Olsen, and K. Mosegaard, 2005: Heat Flux Anomalies in Antarctica Revealed by Satellite Magnetic Data. *Science*, **309**(5733), 464 – 467.
- Fretwell, P., H. Pritchard, D. Vaughan, J. Bamber, N. Barrand, R. Bell, C. Bianchi, R. Bingham, D. Blankenship, G. Casassa, et al., 2013: Bedmap2: improved ice bed, surface and thickness datasets for Antarctica. *The Cryosphere Discussions*, **7**, 376–393.
- Gagliardini, O., D. Cohen, P. Råback, and T. Zwinger, 2007: Finite-element modeling of subglacial cavities and related friction law. *Journal of Geophysical Research*, **112**(F2), F02027.

- Gagliardini, O., F. Gille-Chaulet, and M. Montagnat, 2009: A review of anisotropic polar ice models: from crystal to ice-sheet flow models. *Low Temperature Science*, **68**(Supplement), 149–166.
- Gladstone, R. M., V. Lee, J. Rougier, A. J. Payne, H. Hellmer, A. L. Brocq, A. Shepherd, T. L. Edwards, J. Gregory, and S. L. Cornford, 2012: Calibrated prediction of Pine Island Glacier retreat during the 21st and 22nd centuries with a coupled flowline model. *Earth and Planetary Science Letters*, **333-334**, 191–199.
- Gladstone, R. M., V. Lee, A. Vieli, and A. J. Payne, 2010: Grounding line migration in an adaptive mesh ice sheet model. *Journal of Geophysical Research*, **115**(F4), F04014.
- Gladstone, R. M., A. J. Payne, and S. L. Cornford, 2012: Resolution requirements for grounding-line modelling: sensitivity to basal drag and ice-shelf buttressing. *Annals of Glaciology*, **53**(60), 97–105.
- Glen, J., 1952: Experiments on the deformation of ice. *Journal of Glaciology*, **2**, 111–114.
- Glen, J. W., 1955: The creep of polycrystalline ice. *Proceedings of the Royal Society of London. A. Mathematical and Physical Sciences*, **228**(1175), 519–538.
- Gramelsberger, G., 2010: *Computereperimente - Zum Wandel der Wissenschaft im Zeitalter des Computers*. transcript Verlag, Bielefeld.
- Greve, R., 1997: Application of a polythermal three-dimensional ice sheet model to the Greenland ice sheet: response to steady-state and transient climate scenarios. *Journal of Climate*, **10**(5), 901–918.
- Greve, R., 2005: Relation of measured basal temperatures and the spatial distribution of the geothermal heat flux for the Greenland ice sheet. *Annals of Glaciology*, **42**(1), 424–432.
- Greve, R. and H. Blatter, 2009: *Dynamics of ice sheets and glaciers*. Springer.
- Groh, A., H. Ewert, M. Scheinert, M. Fritsche, A. Rülke, A. Richter, R. Rosenau, and R. Dietrich, 2012: An Investigation of Glacial Isostatic Adjustment over the Amundsen Sea Sector, West Antarctica. *Global and Planetary Change*, **98-99**, 45–53.
- Gudmundsson, G. H., 2003: Transmission of basal variability to a glacier surface. *Journal of Geophysical Research*, **108**(B5), 2253.
- Gudmundsson, G. H., 2011: Ice-stream response to ocean tides and the form of the basal sliding law. *The Cryosphere*, **5**, 259–270.
- Gudmundsson, G. H., J. Krug, G. Durand, L. Favier, and O. Gagliardini, 2012: The stability of grounding lines on retrograde slopes. *The Cryosphere Discussions*, **6**, 2597–2619.
- Hindmarsh, R. C. A., 1993: Qualitative dynamics of marine ice sheets. *Ice in the Climate System I*, **12**, 68–99.
- Hindmarsh, R. C. A., 1996: Stability of ice rises and uncoupled marine ice sheets. *Annals of Glaciology*, **23**, 94–104.

- Holland, D. M. and A. Jenkins, 1999: Modeling thermodynamic ice-ocean interactions at the base of an ice shelf. *Journal of Physical Oceanography*, **29**(8), 1787–1800.
- Hooke, R., 1981: Flow law for polycrystalline ice in glaciers: comparison of theoretical predictions, laboratory data, and field measurements. *Reviews of Geophysics*, **19**(4), 664–672.
- Hooke, R. L., 2005: *Principles of Glacier Mechanics*. Cambridge University Press.
- Horwath, M. and R. Dietrich, 2009: Signal and error in mass change inferences from GRACE: the case of Antarctica. *Geophysical Journal International*, **177**, 849–864.
- Hubbard, B., M. Siegert, and D. McCarroll, 2000: Spectral roughness of glaciated bedrock geomorphic surfaces: implications for glacier sliding. *Journal of Geophysical Research*, **105**(B9), 21295–21303.
- Hughes, T., 1973: Is the West Antarctic ice sheet disintegrating? *Journal of Geophysical Research*, **78**(33), 7884–7910.
- Hughes, T. J., 2000: *The finite element method: linear static and dynamic finite element analysis*. Dover Publications.
- Humbert, A., 2006: Numerical simulations of the ice flow dynamics of Fimbulisen. *FRISP Report*, **17**, 67–78.
- Humbert, A., 2010: The temperature regime of Fimbulisen, Antarctica. *Annals of Glaciology*, **51**(55), 56–64.
- Humbert, A., T. Kleiner, C. Mohrholz, C. Oelke, R. Greve, and M. Lange, 2009: A comparative modeling study of the Brunt Ice Shelf/Stancomb-Wills Ice Tongue system, East Antarctica. *Journal of Glaciology*, **55**(189), 53–65.
- Hutter, K., 1983: *Theoretical glaciology: material science of ice and the mechanics of glaciers and ice sheets*. Reidel.
- Hutter, K. and K. Jöhnk, 2004: *Continuum methods of physical modeling: continuum mechanics, dimensional analysis, turbulence*. Springer.
- Huybrechts, P. and J. de Wolde, 1999: The dynamic response of the Greenland and Antarctic ice sheets to multiple-century climatic warming. *Journal of Climate*, **12**(8), 2169–2188.
- Iken, A., 1981: The effect of the subglacial water pressure on the sliding velocity of a glacier in an idealized numerical model. *Journal of Glaciology*, **27**, 407–421.
- IPCC-AR3, 2001: *The scientific basis. Contribution of working group I to the third assessment report of the Intergovernmental Panel on Climate Change*. Cambridge University Press: Cambridge, United Kingdom.
- IPCC-AR4, 2007: *Contribution of Working Group I to the Fourth Assessment Report of the Intergovernmental Panel on Climate Change*. Cambridge University Press, Cambridge, United Kingdom and New York, NY, USA,.

- Jacka, T. and W. Budd, 1989: Isotropic and anisotropic flow relations for ice dynamics. *Annals of Glaciology*, **12**, 81–84.
- Jacobs, S. S., H. H. Hellmer, and A. Jenkins, 1996: Antarctic ice sheet melting in the Southeast Pacific. *Geophysical Research Letters*, **23**(9), 957–960.
- Jacobs, S. S., A. Jenkins, C. F. Giulivi, and P. Dutrioux, 2011: Stronger ocean circulation and increased melting under Pine Island Glacier ice shelf. *Nature Geoscience*, **4**, 519–523.
- Jamieson, S. S., A. Vieli, S. J. Livingstone, C. Ó. Cofaigh, C. Stokes, C.-D. Hillenbrand, and J. A. Dowdeswell, 2012: Ice-stream stability on a reverse bed slope. *Nature Geoscience*, **5**, 799–802.
- Jenkins, A., P. Dutrioux, S. S. Jacobs, S. D. McPhail, J. R. Perrett, A. T. Webb, and D. White, 2010: Observations beneath Pine Island Glacier in West Antarctica and implications for its retreat. *Nature Geoscience*, **3**(7), 468–472.
- Johnson, C., 2009: *Numerical Solution of Partial Differential Equations by the Finite Element Method*. Dover Publications, Inc., Mineola, New York.
- Jordan, T., F. Ferraccioli, D. Vaughan, J. Holt, H. Corr, D. Blankenship, and T. Diehl, 2009: Aerogravity evidence for major crustal thinning under the Pine Island Glacier region (West Antarctica). *Geological Society of America Bulletin*, **122**(5–6), 714–726.
- Joughin, I. and R. B. Alley, 2011: Stability of the West Antarctic ice sheet in a warming world. *Nature Geoscience*, **4**, 506–513.
- Joughin, I., D. R. MacAyeal, and S. Tulaczyk, 2004: Basal shear stress of the Ross ice streams from control method inversions. *Journal of Geophysical Research*, **109**(B9), 1–62.
- Joughin, I., B. E. Smith, and D. M. Holland, 2010: Sensitivity of 21st century sea level to ocean-induced thinning of Pine Island Glacier, Antarctica. *Geophysical Research Letters*, **37**, L20502.
- Joughin, I. R., E. Rignot, C. E. Rosanova, B. K. Lucchitta, and J. Bohlander, 2003: Timing of Recent Accelerations of Pine Island Glacier, Antarctica. *Geophysical Research Letters*, **30**(13), 28–31.
- Joughin, I. R., S. Tulaczyk, J. L. Bamber, D. D. Blankenship, J. W. Holt, T. A. Scambos, and D. G. Vaughan, 2009: Basal conditions for Pine Island and Thwaites Glaciers, West Antarctica, determined using satellite and airborne data. *Journal of Glaciology*, **55**(190), 245–257.
- Kamb, B., 1970: Sliding motion of glaciers: theory and observations. *Reviews of Geophysics and Space Physics*, **8**(4), 673–728.
- Kamb, B., 2001: Basal zone of the west Antarctic ice streams and its role in lubrication of their rapid motion. In *The West Antarctic Ice Sheet, behavior and environment*, Alley, R. B. and Bindshadler, R. A., editors. AGU, 157–199.

- Karlsson, N. B., D. M. Rippin, D. G. Vaughan, and H. F. J. Corr, 2009: The internal layering of Pine Island Glacier, West Antarctica, from airborne radar-sounding data. *Annals of Glaciology*, **50**, 141–146.
- Katz, R. F. and M. G. Worster, 2010: Stability of ice-sheet grounding lines. *Proceedings of the Royal Society A: Mathematical, Physical and Engineering Science*, **466**(2118), 1597–1620.
- King, E. C., J. Woodward, and A. M. Smith, 2004: Seismic evidence for a water-filled canal in deforming till beneath Rutford Ice Stream, West Antarctica. *Geophysical Research letters*, **31**(20), L20401.
- Klauke, S., 2006: Numerische Modellierung eines Antarktischen Eisschild-Schelfeis-Systems- Riiser-Larsen und Einzugsgebiet. Master's thesis.
- Kleiner, T., 2010: *Entwicklung eines dreidimensionalen numerischen full-Stokes-Fließmodells und seine Anwendung auf ein Inland-Schelfeisystem der Antarktis im Bereich des westlichen Droning Maud Lands*. PhD thesis, Universität Münster.
- Kleiner, T. and A. Humbert, 2014: Numerical simulations of major ice streams in western Dronning Maud Land, Antarctica, under wet and dry basal conditions. *Journal of Glaciology*, **60**(220), 215–232.
- Landvik, J. Y., S. Bondevik, A. Elverhoi, W. Fjeldskaar, J. Mangerud, O. Salvigsen, M. Siegert, J. Svendsen, and T. Vorren, 1998: The last glacial maximum of Svalbard and the Barents Sea area: ice sheet extent and configuration. *Quaternary Science Reviews*, **17**(1-3), 43–75.
- Langel, R. and W. Hinze, 1998: *The magnetic field of the earth's lithosphere: the satellite perspective*. Cambridge University Press.
- Larour, E., J. Schiermeier, E. Rignot, H. Seroussi, M. Morlighem, and J. Paden, 2012: Sensitivity Analysis of Pine Island Glacier ice flow using ISSM and DAKOTA. *Journal of Geophysical Research*, **117**(F2), F02009.
- Le Brocq, A. M., A. J. Payne, and A. Vieli, 2010: An improved Antarctic dataset for high resolution numerical ice sheet models (ALBMAP v1). *Earth System Science Data*.
- Leng, W., L. Ju, M. Gunzburger, and S. Price, 2013: Manufactured solutions and the verification of three-dimensional Stokes ice-sheet models. *The Cryosphere*, **7**, 19–29.
- Lestringant, R., 1994: A two-dimensional finite-element study of flow in the transition zone between an ice sheet and an ice shelf. *Annals of Glaciology*, **20**(1), 67–72.
- Li, X., B. Sun, M. J. Siegert, R. G. Bingham, X. Tang, D. Zhang, X. Cui, and X. Zhang, 2010: Characterization of subglacial landscapes by a two-parameter roughness index. *Journal of Glaciology*, **56**(199), 831–836.
- Lliboutry, L., 1968: General theory of subglacial cavitation and sliding of temperate glaciers. *Journal of Glaciology*, **7**, 21–58.

- Lliboutry, L., 1971: Permeability, brine content and temperature of temperate ice. *Journal of Glaciology*, **10**, 15–29.
- Lliboutry, L., 1987: *Very Slow Flows of Solids: Basics of modeling in geodynamics and glaciology*. Martinus Nijhoff.
- Lliboutry, L., 1993: Internal melting and ice accretion at the bottom of temperate glaciers. *Journal of Glaciology*, **39**, 50–64.
- Lliboutry, L. and P. Duval, 1985: Various isotropic and anisotropic ices found in glaciers and polar ice caps and their corresponding rheologies. **3**(2), 207–224.
- MacAyeal, D. R., 1989: Large-scale ice flow over a viscous basal sediment- Theory and application to ice stream B, Antarctica. *Journal of Geophysical Research*, **94**(B4), 4071–4087.
- MacAyeal, D. R., 1992: The basal stress distribution of Ice Stream E, Antarctica, inferred by control methods. *Journal of Geophysical Research*, **97**(B1), 595–603.
- MacGregor, J. A., G. A. Catania, M. S. Markowski, and A. G. Andrews, 2012: Widespread rifting and retreat of ice-shelf margins in the eastern Amundsen Sea Embayment between 1972 and 2011. *Journal of Glaciology*, **58**(209), 458–466.
- Mercer, J., 1978: West Antarctic ice sheet and CO<sub>2</sub> greenhouse effect- A threat of disaster. *Nature*, **271**(5643), 321–325.
- Millero, F., 1978: Freezing point of sea water. *Eighth Report of the Joint Panel on Oceanographic Tables and Standards*. UNESCO, Paris.
- Morland, L., 1984: Thermomechanical balances of ice sheet flows. *Geophysical & Astrophysical Fluid Dynamics*, **29**(1-4), 237–266.
- Morland, L., 1987: Unconfined ice-shelf flow. *Dynamics of the West Antarctic Ice Sheet* 99–116.
- Morlighem, M., 2011: *Ice sheet properties inferred by combining numerical modeling and remote sensing data*. PhD thesis, Ecole Centrale Paris.
- Morlighem, M., E. Rignot, H. Seroussi, E. Larour, H. Ben Dhia, and D. Aubry, 2010: Spatial patterns of basal drag inferred using control methods from a full-Stokes and simpler models for Pine Island Glacier, West Antarctica. *Geophysical Research Letters*, **37**(14), L14502.
- Mothes, H., 1926: Dickenmessungen von Gletschereis mit seismischen Methoden. *Geologische Rundschau*, **17**(6), 397–400.
- Naish, T., R. Powell, R. Levy, G. Wilson, R. Scherer, F. Talarico, L. Krissek, F. Niessen, M. Pompilio, T. Wilson, L. Carter, R. DeConto, P. Huybers, R. McKay, D. Pollard, J. Ross, D. Winter, P. Barrett, et al., 2009: Obliquity-paced Pliocene West Antarctic ice Sheet oscillations. *Nature*, **458**, 322–328.
- Nerem, R. S., E. Leuliette, and A. Cazenave, 2006: Present-day sea-level change: A review. *Comptes Rendus Geoscience*, **338**(14), 1077–1083.

- Nitsche, F., S. Jacobs, R. Larter, and K. Gohl, 2007: Bathymetry of the Amundsen Sea continental shelf: Implications for geology, oceanography, and glaciology. *Geochemistry Geophysics Geosystems*, **8**, Q10009.
- Nye, J., 1953: The flow law of ice from measurements in glacier tunnels, laboratory experiments and the Jungfraufirn borehole experiment. *Proceedings of the Royal Society of London. A. Mathematical and Physical Sciences*, **219**(1139), 477–489.
- Nye, J., 1957: The distribution of stress and velocity in glaciers and ice-sheets. *Proceedings of the Royal Society of London. A. Mathematical and Physical Sciences*, **239**(1216), 113–133.
- Nye, J. F., 1969: The calculation of sliding of ice over a wavy surface using Newtonian viscous approximation. *Proceedings of the Royal Society, London*, **A311**(1506), 445–467.
- Park, J., N. Gourmelen, A. Shepherd, S. Kim, D. Vaughan, and D. Wingham, 2013: Sustained retreat of the Pine Island Glacier. *Geophysical Research Letters*, **40**, 1–6.
- Paterson, W., 1994: *The physics of glaciers*. Oxford, etc., Elsevier.
- Pattyn, F., 2000: Ice-sheet modelling at different spatial resolutions: focus on the grounding zone. *Annals of Glaciology*, **31**(1), 211–216.
- Pattyn, F., 2003: A new three-dimensional higher-order thermomechanical ice sheet model: Basic sensitivity, ice stream development, and ice flow across subglacial lakes. *Journal of Geophysical Research*, **108**(B8), 2382.
- Pattyn, F. and G. Durand, 2013: Why marine ice sheet model predictions may diverge in estimating future sea level rise. *Geophysical Research Letters*, **40**, 4316–4320.
- Pattyn, F., L. Perichon, A. Aschwanden, B. Breuer, B. de Smedt, O. Gagliardini, G. H. Gudmundsson, R. C. A. Hindmarsh, A. Hubbard, J. V. Johnson, T. Kleiner, Y. Konovalov, C. Martin, A. J. Payne, D. Pollard, S. Price, M. Rückamp, F. Saito, O. Soucek, S. Sugiyama, and T. Zwinger, 2008: Benchmark experiments for higher-order and full-Stokes ice sheet models (ISMIP-HOM). *The Cryosphere*, **2**, 95–108.
- Pattyn, F., L. Perichon, G. Durand, L. Favier, O. Gagliardini, R. Hindmarsh, T. Zwinger, T. Albrecht, S. Conford, D. Docquier, H. Gudmundsson, A. Humbert, T. Kleiner, E. Larour, D. Martin, M. Morlighem, A. Payne, M. Rückamp, N. Wilkens, et al., 2013: Grounding-line migration in plan-view marine ice-sheet models: results of the ice2sea MISIP3d intercomparison. *Journal of Glaciology*, **59**(215), 2163.
- Pattyn, F., C. Schoof, L. Perichon, R. Hindmarsh, E. Bueler, B. de Fleurian, G. Durand, O. Gagliardini, R. Gladstone, D. Goldberg, et al., 2012: Results of the Marine Ice Sheet Model Intercomparison Project, MISIP. *The Cryosphere*, **6**(3), 573–588.
- Payne, A. J. and D. J. Baldwin, 2000: Analysis of ice-flow instabilities identified in the EISMINT intercomparison exercise. *Annals of Glaciology*, **30**(1), 204–210.
- Payne, A. J., A. Vieli, A. P. Shepherd, D. J. Wingham, and E. Rignot, 2004: Recent dramatic thinning of the largest West Antarctic ice stream triggered by oceans. *Geophysical Research Letters*, **31**, L23401.

- Peters, M. E., D. D. Blankenship, and D. L. Morse, 2005: Analysis techniques for coherent airborne radar sounding: Application to West Antarctic ice streams. *Journal of Geophysical Research*, **110**(B6), B06303.
- Pettersson, R., P. Jansson, and H. Blatter, 2004: Spatial variability in water content at the cold-temperate transition surface of the polythermal Storglaciären, Sweden. *Journal of Geophysical Research*, **109**(F2), F02009.
- Pfeffer, W. T., J. Harper, and S. O’Neel, 2008: Kinematic constraints on glacier contributions to 21st-century sea-level rise. *Science*, **321**(5894), 1340–1343.
- Pollack, H., S. Hurter, and J. Johnson, 1993: Heat flow from the Earth’s interior: analysis of the global data set. *Reviews of Geophysics*, **31**(3), 267–280.
- Pollard, D. and R. DeConto, 2012: A simple inverse method for the distribution of basal sliding coefficients under ice sheets, applied to Antarctica. *The Cryosphere Discussions*, **6**, 1405–1444.
- Pollard, D. and R. M. DeConto, 2009: Modelling West Antarctic ice sheet growth and collapse through the past five million years. *Nature*, **458**, 329–332.
- Pralong, A., 2005: *On the instability of hanging glaciers*. PhD thesis, Swiss Federal Institute of Technology, Zürich.
- Pritchard, H., S. Ligtenberg, H. Fricker, D. Vaughan, M. Van den Broeke, and L. Padman, 2012: Antarctic ice-sheet loss driven by basal melting of ice shelves. *Nature*, **484**(7395), 502–505.
- Raymond, M. J. and G. H. Gudmundsson, 2009: Estimating basal properties of ice streams from surface measurements: a non-linear Bayesian inverse approach applied to synthetic data. *The Cryosphere*, **3**(2), 265–278.
- Reddy, J. and D. Gartling, 2010: *The finite element method in heat transfer and fluid dynamics*. CRC.
- Rignot, E., 2001: Evidence for rapid retreat and mass loss of Thwaites Glacier, West Antarctica. *Journal of Glaciology*, **47**(157), 213–222.
- Rignot, E., 2002: Ice-shelf changes in Pine Island Bay, Antarctica, 1947-2000. *Journal of Glaciology*, **48**(161), 256.
- Rignot, E., 2006: Changes in ice dynamics and mass balance of the Antarctic ice sheet. *Philosophical Transactions of the Royal Society A*, **364**, 1637–1655.
- Rignot, E., 2008: Changes in West Antarctic ice stream dynamics observed with ALOS PALSAR data. *Geophysical Research Letters*, **35**(12), L12505.
- Rignot, E., J. Mouginot, and B. Scheuchl, 2011: Ice flow of the Antarctic ice sheet. *Science*, **333**(6048), 1427–1430.
- Rignot, E. J., 1998: Fast recession of a West Antarctic glacier. *Science*, **281**(5376), 549–551.

- Rippin, D., J. Bamber, M. Siegert, D. Vaughan, and H. Corr, 2006: Basal conditions beneath enhanced-flow tributaries of Slessor Glacier, East Antarctica. *Journal of Glaciology*, **52**(179), 481–490.
- Rippin, D., D. Vaughan, and H. Corr, 2011: The basal roughness of Pine Island Glacier, West Antarctica. *Journal of Glaciology*, **57**(201), 67–76.
- Rückamp, M., 2011: *Eisgeometrie und Fließdynamik der subpolaren Eiskappe von King George Island (Antarktis)*. PhD thesis, Universität Münster.
- Scambos, T. A., J. Bohlander, C. Shuman, and P. Skvarca, 2004: Glacier acceleration and thinning after ice shelf collapse in the larsen b embayment, antarctica. *Geophysical Research Letters*, **31**(18), L18402.
- Scherer, R. P., A. Aldahan, S. Tulaczyk, G. Possnert, H. Engelhardt, and B. Kamb, 1998: Pleistocene Collapse of the West Antarctic Ice Sheet. *Science*, **281**, 82–85.
- Schmeltz, M., E. Rignot, T. K. Dupont, and D. R. Macayeal, 2002: Sensitivity of Pine Island Glacier, West Antarctica, to changes in ice-shelf and basal conditions: a model study. *Journal of Glaciology*, **48**(163), 552–558.
- Schoof, C., 2005: The effect of cavitation on glacier sliding. *Proceedings of the Royal Society A: Mathematical, Physical and Engineering Science*, **461**(2055), 609–627.
- Schoof, C., 2007a: Ice sheet grounding line dynamics: Steady states, stability, and hysteresis. *Journal of Geophysical Research*, **112**, F03S28.
- Schoof, C., 2007b: Marine ice-sheet dynamics. Part 1. The case of rapid sliding. *Journal of Fluid Mechanics*, **573**, 27–56.
- Schweizer, J., 1989: Friction at the base of a glacier. *Mitteilungen der Versuchsanstalt fuer Wasserbau, Hydrologie und Glaziologie der ETH Zuerich*, **101**.
- Scott, J. B. T., G. H. Gudmundsson, A. M. Smith, R. G. Bingham, H. D. Pritchard, and D. G. Vaughan, 2009: Increased rate of acceleration on Pine Island Glacier strongly coupled to changes in gravitational driving stress. *The Cryosphere*, **3**, 125–131.
- Seddik, H., R. Greve, T. Zwinger, F. Gillet-Chaulet, and O. Gagliardini, 2012: Simulations of the Greenland ice sheet 100 years into the future with the full Stokes model Elmer/Ice. *Journal of Glaciology*, **58**(209), 427–440.
- Sergienko, O., R. Bindschadler, P. Vornberger, and D. MacAyeal, 2008: Ice stream basal conditions from block-wise surface data inversion and simple regression models of ice stream flow: Application to Bindschadler Ice Stream. *Journal of Geophysical Research*, **113**(F4), F04010.
- Shapiro, N. M. and M. H. Ritzwoller, 2004: Inferring surface heat flux distributions guided by a global seismic model: particular application to Antarctica. *Earth and Planetary Science Letters*, **223**, 213–224.
- Shepherd, A., E. R. Ivins, A. Geruo, V. R. Barletta, M. J. Bentley, S. Bettadpur, K. H. Briggs, D. H. Bromwich, R. Forsberg, N. Galin, et al., 2012: A Reconciled Estimate of Ice-Sheet Mass Balance. *Science*, **338**(6111), 1183–1189.

- Shepherd, A. P., D. J. Wingham, and E. Rignot, 2004: Warm ocean is eroding West Antarctic Ice Sheet. *Geophysical Research Letters*, **31**, L23402.
- Shreve, R., 1972: Movement of water in glaciers. *J. Glaciol*, **11**(62), 205–214.
- Smith, A., C. Bentley, R. Bingham, and T. Jordan, 2012: Rapid subglacial erosion beneath Pine Island Glacier, West Antarctica. *Geophysical Research Letters*, **39**(12), L12501.
- Smith, A. M., 2007: Subglacial bed properties from normal-incidence seismic reflection data. *Journal of Environmental & Engineering Geophysics*, **12**(1), 3–13.
- Smith, A. M., T. A. Jordan, F. Ferraccioli, and R. G. Bingham, 2013: Influence of subglacial conditions on ice stream dynamics: Seismic and potential field data from Pine Island Glacier, West Antarctica. *Journal of Geophysical Research*, **118**(4), 1471–1482.
- Steinemann, S., 1954: Results of Preliminary Experiments on the Plasticity of Ice Crystals. *Journal of Glaciology*, **2**(16), 404–412.
- Stenoien, M. D. and C. R. Bentley, 2000: Pine Island Glacier, Antarctica: A study of the catchment using interferometric synthetic aperture radar measurements and radar altimetry. *Journal of Geophysical Research*, **105**(B9), 21761–21779.
- Taylor, J., M. J. Siegert, A. J. Payne, and B. Hubbard, 2004: Regional-scale bed roughness beneath ice masses: measurement and analysis. *Computers & Geosciences*, **30**(8), 899–908.
- Thomas, R. and C. Bentley, 1978: A model for Holocene retreat of the West Antarctic ice sheet. *Quaternary Research*, **10**(2), 150–170.
- Timmermann, R., A. Le Brocq, T. Deen, E. Domack, P. Dutrieux, B. Galton-Fenzi, H. Hellmer, A. Humbert, D. Jansen, A. Jenkins, A. Lambrecht, K. Makinson, F. Niederjager, F. Nitsche, O. A. Nøst, L. H. Smedsrud, and W. H. F. Smith, 2010: A consistent data set of Antarctic ice sheet topography, cavity geometry, and global bathymetry. *Earth System Science Data*, **2**(2), 261–273.
- Tulaczyk, S., W. B. Kamb, and H. F. Engelhardt, 2000: Basal mechanics of Ice Stream B, West Antarctica 2. Undrained plastic bed model. *Journal of Geophysical Research*, **105**, 483–494.
- van der Meer, J. J., J. Menzies, and J. Rose, 2003: Subglacial till: the deforming glacier bed. *Quaternary Science Reviews*, **22**(15-17), 1659–1685.
- Van der Veen, C., 1987: Longitudinal stresses and basal sliding: a comparative study. In *Dynamics of the West Antarctic Ice Sheet*. Springer, 223–248.
- van der Veen, C., 1999: Evaluating the performance of cryospheric models 1. *Polar Geography*, **23**(2), 83–96.
- van der Veen, C., 2002: Polar ice sheets and global sea level: How well can we predict the future? *Global and Planetary Change*, **32**(2), 165–194.

- Vaughan, D., A. Smith, H. Corr, A. Jenkins, C. Bentley, M. Stenoien, S. Jacobs, T. Kellogg, E. Rignot, and B. Lucchitta, 2001: A review of Pine Island Glacier, West Antarctica: Hypotheses of instability vs. observations of change. *Antarctic Research Series*, **77**, 237–256.
- Vaughan, D. G., 2008: West Antarctic Ice Sheet collapse - the fall and rise of a paradigm. *Climatic Change*, **91**, 65–79.
- Vaughan, D. G., H. F. J. Corr, F. Ferraccioli, N. Frearson, A. O'Hare, D. Mach, J. W. Holt, D. D. Blankenship, D. L. Morse, and D. A. Young, 2006: New Boundary Conditions for the West Antarctic ice sheet: Subglacial topography beneath Pine Island Glacier. *Geophysical Research Letters*, **33**(9), L09501.
- Vieli, A. and A. J. Payne, 2003: Application of control methods for modelling the flow of Pine Island Glacier, West Antarctica. *Annals of Glaciology*, **36**(1), 197–204.
- Vieli, A. and A. J. Payne, 2005: Assessing the ability of numerical ice sheet models to simulate grounding line migration. *Journal of Geophysical Research*, **110**, 1–18.
- Walker, J. and J. Geissman, 2009: Geologic Time Scale. *Geological Society of America*.
- Weertman, J., 1957: On the sliding of glaciers. *Journal of Glaciology*, **3**, 33–38.
- Weertman, J., 1974: Stability of the junction of an ice sheet and an ice shelf. *Journal of Glaciology*, **13**, 3–11.
- Weis, M., R. Greve, and K. Hutter, 1999: Theory of shallow ice shelves. *Continuum Mechanics and Thermodynamics*, **11**(1), 15–50.
- Wingham, D. J., A. J. Ridout, R. Scharroo, R. J. Arthern, and C. K. Shum, 1998: Antarctic Elevation Change from 1992 to 1996. *Science*, **282**, 456–458.
- Wingham, D. J., D. W. Wallis, and A. P. Shepherd, 2009: Spatial and temporal evolution of Pine Island Glacier thinning, 1995–2006. *Geophysical Research Letters*, **36**(17), L17501.

## Acknowledgements

Als erstes möchte ich mich bei Angelika Humbert bedanken, die diese Dissertation betreut hat. Ich habe, durch ihre ständige Bereitschaft ihr Wissen zu teilen und zu diskutieren, sehr viel gelernt. Ihre sehr freundliche und immer motivierende Art hat mir speziell während der Durststrecken sehr geholfen.

Mein Dank gilt auch Jörn Behrens, der bereit war das Zweitgutachten zu übernehmen, und mich außerdem in technischen Fragen und generell motivierend unterstützt hat.

Detlef Quadfasel möchte ich danken, dass er der Chair meines Advisory Panels war, sowie Mitglied der Prüfungskommission. Lars Kaleschke und Matthias Hort möchte ich ebenfalls danken, dass sie Teil der Prüfungskommission waren.

Thomas Kleiner gilt mein Dank für die ständige Bereitschaft meine Fragen zu beantworten oder zu diskutieren. Auch die Hilfe bei technischen Komplikationen weiß ich sehr zu schätzen.

Martin Rückamp und Olga Sergienko danke ich für die Hilfe und den Erfahrungsaustausch im Umgang mit COMSOL.

Bei David Rippin möchte ich mich für das zur Verfügung stellen der Rauigkeitsdaten bedanken, und bei Anne LeBrocq für die Geometrie-Daten des Pine Island Gletschers. Dem Central IT Service möchte ich danken für die Hilfe und Geduld mit COMSOL. Und dem AWI möchte ich danken, dass ich meine Modellläufe dort durchführen konnte und für die Übernahme der Flugkosten nach San Francisco.

Thomas, Martin, Florian, Werner und Johannes B. danke ich für das Korrekturlesen dieser Arbeit.

Diese Arbeit wurde ermöglicht durch das Exzellenzcluster 'CliSAP' (EXC177), Universität Hamburg, finanziert durch die Deutsche Forschungsgemeinschaft (DFG). Die Graduiertenschule SICSS hat mir den Besuch diverser Konferenzen ermöglicht, dafür möchte ich mich bedanken.

Johannes Lohse und Sebastian Beyer möchte ich für die immer nette Atmosphäre im Büro danken. Und auch Doreen, Johannes B., Florian, Martin und Thomas gilt mein Dank, für den allgemein sehr netten Umgang in der Arbeitsgruppe.

Laura danke ich für unsere Fahrgemeinschaft und die ausführlichen Kaffeerunden, die den Einstieg in den Tag angenehm gemacht haben. Außerdem möchte ich ganz herzlich der Mittagscrew danken.

Ein ganz spezieller Dank gilt meiner Familie Anke, Carsten, Anna und Kjen.

Und natürlich ganz besonders Alex, der mit sehr viel Unterstützung und Geduld den Prozess von Anfang bis Ende als mein "Erstbetreuer" begleitet hat.

## **Eidesstattliche Erklärung**

Hiermit versichere ich, dass ich diese Arbeit selbständig verfasst habe und keine anderen als die angegebenen Quellen und Hilfsmittel benutzt habe.

Nina Wilkens